Imperial College London

Development of optical projection tomography for mesoscopic 3-D biomedical imaging

Lingling Chen

Photonics Group

Department of Physics

Imperial College London

Supervised by Paul M. W. French & James McGinty & Christopher Dunsby.

2014

Thesis submitted in partial fulfilment of the requirements for the degree of Doctor of Philosophy (PhD)

Imperial College London

Abstract

Optical projection tomography (OPT) is an exciting technique for imaging "mesoscopic" (1 – 10 mm) samples at a high resolution, providing three-dimensional (3-D) absorption and/or fluorescence distributions of chromophores in optically transparent specimens. This thesis describes the study, development and application of OPT technology for potential applications in biomedical research including developmental biology, tissue analysis (e.g. for histopathology), the study of disease mechanisms and therapies, dosimetry and drug discovery.

The thesis begins with an introduction to fluorescence, fluorescence lifetime imaging (FLIM) and OPT and then describes the experimental configurations and characterisation of in-house developed intensity-based OPT instruments. Using the measured characteristics of specific OPT set-ups, different tomographic reconstruction approaches for OPT are investigated through modelling and experiments and the achievable image quality and speed are compared to the performance obtained with the standard reconstruction algorithm.

The development of OPT using a novel angular multiplexing technique is then discussed. This employs multiple imaging systems in parallel that can acquire OPT data sets simultaneously. Their performances using different focusing arrangements to image either shifted focal planes or a common focal plane in the sample is investigated and shown to provide faster imaging with improved spatial resolution. The latter configuration is demonstrated to offer the capability to track feature motions such as cell trajectories with a time lapse resolution limited by the frame rate of the cameras and to provide 3-D feature tracking with significantly reduced light dose compared to standard OPT.

The application of OPT and its extension to incorporate wide-field time-gated FLIM, referred as FLIM-OPT, to a range of biological specimens is then discussed, including fixed and chemically cleared tissues and live animal models. These experiments demonstrate the efficacy of OPT as a 3-D imaging tool for biomedical research. The potential efficacy of FLIM-OPT to read out Förster resonance energy transfer (FRET) is then demonstrated, including in live zebrafish embryos. Thus OPT is shown to provide a 3-D tomographic imaging technique able to yield structural and functional information in intact organisms.

Acknowledgements

Firstly, I would like to thank my supervisors Paul French, James McGinty and Chris Dunsby for giving me the opportunity to work on this PhD project and more importantly, for all the help, guidance, encouragement and support over the three years. I would also like to extend my thanks to other staff members and post-docs I have worked closely. In particular, I should mention Mark Neil for his incisive advice on Fourier Optics and Sunil Kumar for his practical help in the lab (always finding things and fixing my LabView program). I must thank the help of Martin and Simon in the Optics workshop. Without their expertise, none of the work would have been possible. A special thanks to Margaret Dallman, Paul Frankel, Guy Rutter and Gordon Stamp from Biology and Medicine, who provided zebrafish and tissue samples used in the experiments presented in Chapter 3, 4, 5 and 6.

To my friends and colleagues here at Imperial I have shared my time with; Meng, Hugh, Hugo, Joao, Natalie, Dom, Romain, Sean, Doug, both Alexs, both Lionels, James, Cliff, Ian, Anca, Sergio, Rakesh, Yuriy, Martin, Gordon, Vincent, Ben, Tim, Ed, Carlos, Robbie, Rob, Emma, Gabs, Amp, Noemi, Mercedes and probably many others. Together you have made the last three years thoroughly enjoyable. Thanks go to all of you.

I would also like to thank my close friends outside of Imperial – particularly Jie, Xi, Yiqin, Ying for your friendship and remote caring over the last three years. A special thanks to LL as well. Without your support, my writing up would certainly not have been this enjoyable. Most importantly, I would like to thank my parents. You were always supportive (emotionally and financially) and encouraging. A huge thank you for invaluable emotional support over the years.

Finally, I would like to acknowledge a Lee Family Scholarship for my PhD studentship.

To my family

Author declaration

All the work presented within this thesis is my own with the exception of the following:

- The development of the software used to fit the fluorescence lifetime data was undertaken by Sean Warren of the Photonics group, Imperial College London.
- The old OPT and FLIM-OPT system was originally developed by Dr. James McGinty of the Photonics group, Imperial College London.
- The old OPT acquisition software, FLIM acquisition software used to acquire data in Chapter 3, 6 was originally developed by Dr. Clifford Talbot and Dr. James McGinty of the Photonics group, Imperial College London.
- The biomedical samples used in Chapter 3, 4, 5 & 6 were from Prof. Margaret Dallman (zebrafish), Department of Life Sciences, Imperial College London; Dr. Paul Frankel (zebrafish), Department of Medicine, University College London; Prof. Guy Rutter (mouse pancreas), Department of Medicine, Imperial College London; Prof. Gordon Stamp (mouse tissues), Department of Medicine, Imperial College London.

'The copy right of this thesis rests with the author and is made available under a Creative Commons Attribution Non-Commercial No Derivative licence. Researchers are free to copy, distribute or transmit the thesis on the condition that they attribute it, that they do not use it for commercial purpose and that they do not alter, transform or build upon it. For any reuse or redistribution, researchers must clear to others the licence terms of this work'

Contents

Abstract 1

Acknowledgements 2

Author declaration 4

List of Figures 9

List of Tables 18

List of Videos 19

Abbreviations 20

Chapter 1: Thesis Overview 22

Chapter 2: Background overview of fluorescence and 3-D mesoscopic imaging 24

2.1. Fluorescence 24

2.2. Physical properties of fluorescence 26

2.2.1. Intensity 26

2.2.2. Absorption and emission spectra 27

2.2.3. Fluorescence lifetime 28

2.3. Fluorescence imaging 30

2.3.1. Intensity imaging 30

2.3.2. Spectrally resolved fluorescence imaging 30

2.3.3. Temporally resolved fluorescence imaging 30

2.4. Time-resolved Fluorescence imaging techniques 31

2.4.1. Time-domain FLIM: Time-correlated single photon counting (TCSPC) 31

2.4.2. Time-domain FLIM: Wide-field time-gated FLIM 32

2.4.3. Wide-field frequency-domain FLIM 34

2.4.4. Fluorescence lifetime data fitting 35

2.5. Time gating acquisition using a GOI 36

2.5.1. GOI design 37

2.5.2. Time gating 38

2.6. Förster resonance energy transfer (FRET) 39

2.7. 3-D mesoscopic imaging techniques 41

2.7.1. Light sheet microscopy 43
2.7.2. Optical projection tomography (OPT) 48
2.7.3. Scanning laser optical tomography (SLOT) 55
2.8. Numerical analysis of spatial resolution in OPT and SPIM 56
2.9. Standard FBP algorithms for parallel beam projections 60
2.10. Conclusions 64
Chapter 3: Optimising reconstructed OPT images 65
3.1. Determination of the MTF of OPT system 66
3.1.1. Imaging system 66
3.1.2. MTF characterisation 68
3.2. Reconstruction based on the standard FBP algorithm 72
3.2.1. Materials 72
3.2.2. Acquisition procedure and settings 72
3.2.3. Evaluation methods 74
3.2.4. Ramp filter 74
3.2.5. Standard FBP reconstruction results and discussions 75
3.3. MTF-mask filtering reconstruction 77
3.3.1. MTF-mask filter 78
3.3.2. MTF-mask filtering reconstruction results and discussion 80
3.4. MTF deconvolution reconstruction 86
3.4.1. MTF-deconvolution filter 86
3.4.2. MTF-deconvolution reconstruction results and discussion 88
3.5. Conclusions 91
Chapter 4: Angular multiplexing OPT to improve image quality 93
4.1. Shifted focal plane dual-axis OPT system 93
4.1.1. Imaging setup 96
4.1.2. Sample preparation 96
4.1.3. Acquisition settings and procedure 96
4.1.4. Reconstruction procedure 97
4.1.5. Results and discussion 97

4.1.6. Further improvement in acquisition procedure 100
4.2. Demonstration of four-axis OPT system 101
4.2.1. Imaging setup 101
4.2.2. Sample preparation and acquisition settings 102
4.2.3. Reconstruction procedure 102
4.2.4. Results and discussion 103
4.3. Conclusions 106
Chapter 5: Angular multiplexing OPT to achieve triangulation of dynamic samples 107
5.1. Preface 107
5.2. Simulation 108
5.2.1. 3-D localisation information extraction 108
5.2.2. Results and discussion 110
5.3. Initial demonstration of 3-D cell migration mapping within zebrafish 111
5.3.1. Imaging setup 112
5.3.2. Sample preparation and mounting 112
5.3.3. Acquisition settings and procedure 113
5.3.4. 3-D localisation information extraction 113
5.3.5. Results and discussion 114
5.4. Conclusions 117
Chapter 6: Biomedical applications of intensity and lifetime OPT 118
6.1. Demonstration of biomedical tissues 118
6.1.1. Pancreas specimens 118
6.1.2. Label-free OPT of *ex vivo* tissue samples for histopathology research 121
6.2. *In vivo* imaging of zebrafish 124
6.2.1. *In vivo* FLIM-OPT 125
6.2.2. FRET in zebrafish 134
6.2.3. Time-lapse global imaging of cancer in juvenile and adult zebrafish 140
6.3. Conclusions 144
Chapter 7: Conclusions and outlook 146
7.1. Conclusions of thesis 146

7.2. Future work 148
Publications 149
Presentations 150
References 151
Appendix I: Excitation sources for fluorescence intensity and lifetime imaging 160
Mercury arc lamp 160
Super-continuum source 160
Appendix II: FLIM-OPT microscope system characterisation 163

List of Figures

Figure 2.1: A Jabloński Diagram outlining the possible transitions in a molecule. Here the ground state is denoted S_0 , the first and the second excited singlet states are denoted S_1 and S_2 and the first triplet state is denoted T_1. Each level also illustrates a number of vibrational levels. Transitions between all of these finely spaced levels results in the observed broad absorption/ emission (fluorescence) curves.

Figure 2.2: Schematic showing excitation and emission transitions between the ground and first excited electronic state of a molecule and illustrating the concept of mirror image rule and "Stokes" shift.

Figure 2.3: Simplified diagram illustrating TCSPC (stop-start). DM – dichroic mirror, TAC – time-to-amplitude convertor, ADC – analogue-to-digital convertor, PMT – photon multiplying tube.

Figure 2.4: Simplified time gating scheme (2 time gates). After excitation with ultra-short pulses of light, the intensity in two time gates (gate 1 and gate 2) is measured and then used to calculate the lifetime.

Figure 2.5: Time gated FLIM scheme (multiple time gates). After excitation with ultra-short pulses, the resultant fluorescence decay is sampled at different delay points.

Figure 2.6: Illustration of frequency domain FLIM. The sample is excited by a modulated light source and the lifetime may then be extracted by measurement of the induced phase shift and demodulation.

Figure 2.7: Schematic of a time-gated wide-field FLIM system. DM – dichroic mirror; GOI – gated optical intensifier; PC – personal computer. (This figure is adapted from [9].)

Figure 2.8: Schematic of a single plate GOI (MCP – micro-channel plate).

Figure 2.9: Representations of acquired gated data with respect to a single excitation pulse and fluorescence decay as well as the acquisition process. (This figure is adapted from [9].)

Figure 2.10: Principle of Forster Resonance Energy Transfer between donor and acceptor.

Figure 2.11: FRET efficiency curve as a function of donor-acceptor distance (R) for arbitrary value of R_0. R_0 - Förster radius.

Figure 2.12: FRET detection through lifetime changing.

Figure 2.13: The concept behind fluorescence light sheet microscopy. In light sheet microscopy, illumination and detection are performed through two distinct optical paths. The illumination axis is arranged orthogonal to the detection axis. The most common

implementation is to generate a sheet of laser light that selectively illuminates the sample in the focal plane of the detection optics from one side. (This figure is adapted from [41].)

Figure 2.14: Illustration of different light sheets. (a) In SPIM, a static light sheet is formed by spreading a laser beam in the vertical dimension with dedicated optics. (b) In DSLM, a virtual light sheet is generated by rapidly scanning vertically a Gaussian laser beam. Both of them are with varying thickness due to the nature of Gaussian beam. (c) A Bessel beam can be scanned to obtain more uniform light sheet. Although the core of Bessel beam is thin and long, it is surrounded by a series of rings. (d) Two-photon Bessel beam can be employed and the excitation only occurs in the centre of the beam to further get a thin and uniform light sheet.(This figure is adapted from [41].)

Figure 2.15: Illustration of different illumination and detection techniques. (a) one-sided illumination/one-sided detection, (b) two-sided illumination/one-sided detection; (c) sequential multiview imaging and (d) two-sided illumination/two-sided detection.

Figure 2.16: Illustration of the trade-off in OPT between achievable lateral resolution and sample size as the resolution improves proportionally with the NA while the DOF scales inversely with the square of the NA of the imaging lens.

Figure 2.17: Schematic of the most common and convenient OPT setup on how to mitigate the trade-off between sample size and achievable resolution. This illustration is on a cross-sectional plane (X-Y plane). DOF – depth of field, ϕ: sample diameter.

Figure 2.18: Diagram of OPT. The specimen is supported in a refractive index matched medium (e.g. BABB, an agarose gel, water) and is rotated to a series of angular positions. Both transmission and absorption light can be collected by an optical system and recorded by an imaging detector (e.g. a CCD).

Figure 2.19: (a) An OPT raw projection image (2-D wide-field fluorescence image of a mouse embryo) at one orientation. (b) The sinogram for a particular X-Y plane (while line illustrating in (a)). (c) The corresponding "filtered" sinogram (after employing a ramp filter in the frequency domain). (d) The corresponding reconstructed cross-sectional image.

Figure 2.20: The schematic setup of SLOT. A photo diode is used to capture transmitted light. FL – fluorescence filter. PMT – photon multiplying tube. (This figure is adapted from [36].)

Figure 2.21: Gaussian beam width as a function of the axial distance z. ω_0: beam waist; b: depth of focus; Z_R: Rayleigh range.

Figure 2.22: Theoretical lateral and axial (sectioned) resolution of SPIM and OPT for samples on the scale of 1-30 mm. The lateral and the axial resolution of SPIM are shown as the red circles and the red dotted lines and the lateral and the axial resolution of OPT shown as

the blue dots. Indeed, OPT has isotropic resolution and thus, the blue dots are the same and cannot be distinguished in this figure. (λ -500 nm, n_{bath} - 1.3)

Figure 2.23: A slice of an object, i(x,y), and its parallel projection $P_\theta(r)$, which is taken by measuring a set of parallel rays, from an angle of θ.

Figure 3.1: Schematic of in-house developed intensity-based OPT microscope system. O – objective, AP – aperture, L1 – condenser lens, F1 – excitation filter, DM – dichroic mirror, L2 – tube lens, F2 – emission filter, M – mirror.

Figure 3.2: Photograph of intensity-based OPT microscope system.

Figure 3.3: Transmitted light (a) in-focus (0 μm) and (b) defocus (200 μm) images of a scalpel blade with the NA of 0.07.

Figure 3.4: (a) The measured ESF is plotted as discrete data points. The fit to these points is illustrated by the red solid line. The linear correlation coefficient between these two is 0.9999. (b) The corresponding MTF at this position from the analytical method, shown as the red solid line, and from the numerical Fourier transform procedure, shown as data points.

Figure 3.5: Three pairs of MTFs at the different positions from the analytical method, shown as the lines, and the numerical Fourier transform procedure, shown as data points. MTF1 is the MTF in focus; MTF2 and MTF3 are for 70 and 200 μm defocus, respectively.

Figure 3.6: MTFs as a function of defocus (z) for different effective NAs (0.09, 0.07, 0.06, 0.05, 0.04 and 0.03) of the 1×1 binning intensity-based OPT microscope system. (1040×1040, Δk_x = 0.596 mm^{-1}, Δy = 1.6125 μm, the vertical scale -838.5 – 838.5 μm and the horizontal scale -309.92 – 309.92 mm^{-1}). These measurements were not limited by camera pixel size.

Figure 3.7: Schematic of the intensity-based OPT "standard" acquisition procedure.

Figure 3.8: Schematic of radial and tangential resolution used to evaluate the image quality.

Figure 3.9: (a) A simulated object and (b) its corresponding smeared unfiltered backprojection (i.e. 2-D) at one orientation; (c) 2-D ramp filter and (d) 2-D backprojection at one angle with this ramp filter applied in the reconstruction process. (effective NA of 0.07 for the OPT system; 1040×1040 pixels, Δk_x = 0.596 mm^{-1}, Δx, Δy = 1.6125 μm; the scale of x,y is -838.5 – 838.5 μm and the scale of k_x is -309.92 – 309.92 mm^{-1})

Figure 3.10: The experimental (a) raw sinogram for the central plane of the beads and (b) corresponding reconstructed X-Y image of (a) with the standard FBP algorithm. The results were reconstructed from 360 projections (i.e. a 1º interval) for an effective NA of 0.07. Scale bar, 200 μm.

Figure 3.11: Line plots and Top-hat convolved Gaussian fits through the (a) radial and (b) tangential axis of the reconstructed off-axis bead in Fig. 3.10, where the points correspond to the reconstructed data and the lines to the fits. The off-axis bead is located 334 μm away from the axis of rotation.

Figure 3.12: (a) 2-D binary MTF-mask filter, (b) 2-D ramp filter, (c) the combination of the MTF-mask filter and 2-D ramp filter and (d) backprojection at one angle with the MTF-mask filter and ramp filter applied in the reconstruction process from the same simulated raw data in Fig. 3.9. (effective NA of 0.07 for the OPT system; 1040×1040 pixels, Δk_x = 0.596 mm^{-1}, Δx, Δy = 1.6125 μm; the scale of x,y is -838.5 – 838.5 μm and the scale of k_x is -309.92 – 309.92 mm^{-1})

Figure 3.13: The simulated (a) standard FBP reconstruction and (b) the background for (a). The simulated (c) MTF-mask filtered reconstruction and (d) the background for (c). The results were reconstructed from 90 projections (i.e. a 4º interval) for an effective NA of 0.07. The background images were obtained by removing the beads in the corresponding reconstructed images. The images of the background are on the same intensity scale to show the difference. Scale bar, 200 μm.

Figure 3.14: The experimental (a) standard FBP reconstruction and (b) the background for (a). The experimental (c) MTF-mask filtered reconstruction and (d) the background for (c). The results were reconstructed from 90 projections (i.e. a 4º interval) for an effective NA of 0.07. The background images were obtained by removing the beads in the corresponding reconstructed images. The images of the background are on the same intensity scale to show the difference. Scale bar, 200 μm.

Figure 3.15: (a) Simulated (S) and experimental (E) correlation results of standard FBP and MTF-mask filtered reconstructions for an effective NA of 0.07. (b) Experimental correlation results for different effective NAs (0.06, 0.07, 0.09), with standard FBP correlations as the dotted lines and the MTF-mask filtered reconstruction correlations as the solid lines (three dotted lines are similar and cannot be distinguished in this figure and thus black colour is used to represent them).

Figure 3.16: (a, b, c, d) Standard FBP reconstruction and (e, f, g, h) MTF-mask filtered reconstruction of a zebrafish embryo with an effective NA of 0.07 from 360 projections (i.e. a 1º interval), 180 projections (i.e. a 2º interval), 120 projections (i.e. a 3º interval) and 90 projections (i.e. a 4º interval) respectively. Scale bar, 200 μm.

Figure 3.17: (a) 2-D MTF-deconvolution filter, (b) 2-D ramp filter, (c) the combination of the MTF-deconvolution filter and the 2-D ramp filter and (d) backprojection at one angle with the MTF-deconvolution and the ramp filter applied in the reconstruction process from the same simulated data in Fig. 3.9. (effective NA of 0.07 for the OPT system; 1040×1040

pixels, $\Delta k_x = 0.596$ mm^{-1}, Δx, $\Delta y = 1.6125$ μm; the scale of x,y is -838.5 – 838.5 μm and the scale of k_x is -309.92 – 309.92 mm^{-1})

Figure 3.18: Plots through the radial directions of (a) the off-axis bead and (b) the near-axis bead and the tangential axes of (c) the off-axis bead and (d) of the near-axis bead simulated results with an effective NA of 0.07 respectively. Obj – object; Decon – deconvolution; Non-decon – standard and MTF-mask filtering. (off-axis bead located 334 μm away from the axis of rotation; near-axis bead located 103 μm away from the axis of rotation.)

Figure 3.19: The experimental results for (a) standard FBP reconstruction; (b) deconvolution reconstruction (Scale bar, 200 μm) from 360 projections (i.e. a 1º interval) for an effective NA of 0.07 with (c) and (d) showing the magnified reconstructions respectively (Scale bar, 100 μm).

Figure 3.20: The experimental results for (a) standard FBP reconstruction; (b) deconvolution reconstruction of zebrafish embryo with an effective NA 0.07 from 360 projections (i.e. a 1º interval). The images are on the same intensity scale to show the difference. Scale bar, 200 μm.

Figure 4.1: Schematic of "standard" OPT system setup. DOF – depth of field, EF – emission filter, AP – aperture, L1 and L2 – tube lens, ϕ – sample diameter.

Figure 4.2: Schematic of dual axis OPT system setup (inset shows optimal DOFs and the focal planes of two imaging systems). DOF – depth of field, EF – emission filter, AP – aperture, L1 and L2 – tube lens, FP – focal plane, ϕ – sample diameter.

Figure 4.3: Reconstructed X-Y and X-Z image slices of a bead (located 0.43 mm from the axis of rotation) acquired with the standard OPT system (a, b) and the dual axis OPT system (c, d). Scale bar, 20 μm.

Figure 4.4: Line plots and Gaussian fits through the Y axis of the reconstructed bead in Fig. 4.3 for the dual axis (D, red line) and the standard (S, black lines) single axis OPT systems showing (a) normalised and (b) relative line intensity data.

Figure 4.5: Maximum intensity projections of the 3-D reconstruction of a 54 dpf zebrafish tail acquired with (a) the dual axis and (b, c) the standard single axis OPT plotted for comparison with absolute intensity (a, b) and normalised intensity (a, c) scales; (d) intensity line profiles from figures (a, b) as indicated (arrows), where the standard OPT intensity data has been multiplied by 2 for clarity. Scale bar, 0.5 mm.

Figure 4.6: Schematic of using one camera demonstrating four axis OPT system setup. DOF – depth of field, FP – focal plane, ϕ – sample diameter.

Figure 4.7: Reconstructed X-Y and X-Z image slices of a bead acquired from the standard single axis OPT acquisition (a, b), the dual axis OPT acquisition (c, d) and the four axis OPT acquisition (e, f). Scale bar, 20 μm.

Figure 4.8: Line plots and Gaussian fits through the X axis of the reconstructed bead in Fig. 4.7 for the four axis (F, red line), the dual axis (D, black line) and the standard single axis (S, blue lines) OPT acquisitions showing (a) normalised and (b) relative line intensity data.

Figure 5.1: The raw two sequential projections from a typical OPT acquisition of live LysC:GFP zebrafish embryo at 3 dpf in fluorescence based on the intensity-based OPT system. Arrows indicate a moving cell which would not be accurately reconstructed. Scale bar, 500 μm.

Figure 5.2: The raw corresponding orthogonal projections from (a) 0° view and (b) 90° view as the simulated volume rotated at different time points. White arrows indicate the bead reconstructed in Fig. 5.3 while red arrows indicate another bead in the same plane at Time 0.

Figure 5.3: Reconstructed X-Y image slices of a bead from pairs of orthogonal projections at different time points. Artefacts (green arrows) could potentially be produced when more than one bead is present in the same Z plane but can be identified by using the consistency of full time-lapse information. White and red arrows indicate the beads shown in Fig. 5.2 with the same colour.

Figure 5.4: The comparison of the simulated movements from the original object volumes and the coarse reconstructions respectively at X-Y projection view by adding 20 time points together. Artefacts (arrows) could be produced in the reconstruction when more than one bead is present in the same Z plane.

Figure 5.5: 3-D traces of bead motion over the 20 time points with solid lines corresponding to the original object movements and the points to the localisation information extracted from the coarse 3-D reconstructions.

Figure 5.6: Schematic of dual image acquisition system setup (inset shows the common focal plane of two orthogonal imaging axes on the axis of rotation).EF – emission filter, AP – aperture, L1 and L2 – tube lens, FP – focal plane, ϕ – sample diameter.

Figure 5.7: A ROI of (a) a raw fluorescence projection and (b) the corresponding segmented image of the 2 dpf LysC: GFP mitfa-/- roy-/- zebrafish embryo at one angle. Scale bar, 100 μm.

Figure 5.8: Wide-field transmission image of 2 dpf LysC: GFP mitfa-/- roy-/- zebrafish at one orientation (white box shows the initial ROI).Scale bar, 0.25mm.

Figure 5.9: Wide-field time-lapse fluorescence images of the ROI indicated in Fig. 5.8 from 0° view. Scale bar, 100 μm.

Figure 5.10: Wide-field time-lapse fluorescence images of the ROI indicated in Fig. 5.8 from 90° view. Scale bar, 100 μm.

Figure 5.11: 3-D traces of cell migration in ROI indicated in Fig. 5.8 over 360 seconds in a model of wound inflammation in the 2 dpf LysC: GFP zebrafish embryo based on pairs of orthogonal projections.

Figure 5.12: 3-D cell migration mapping in the tissue from (a) X-Z and (b) Y-Z view at 0, 180, 360 second time point in a model of wound inflammation in the 2 dpf LysC: GFP zebrafish embryo based on pairs of orthogonal projections (see Video 5.1). Red lines correspond to the previous movements while white lines correspond to latest movement from the last time point. Scale bar, 100 μm.

Figure 6.1: Photograph of in-house developed intensity-based macroscope OPT system.

Figure 6.2: Maximum intensity projections of the 3-D reconstruction of two 16-week-old mice pancreas and beta cell volume. Alexa 594 goat anti-guinea pig antibody was applied in order to visualise insulin-positive staining, shown in red. Scale bar, 2 mm.

Figure 6.3: Maximum intensity projections from two opposite views of the 3-D reconstruction of a mice lung and heart with (a, b) showing blue channel (excitation centred 470 nm), (c, d) showing green channel (excitation centred 530 nm) and (e, f) showing merged two-channels (see Video 6.1). Scale bar, 5 mm.

Figure 6.4: Maximum intensity projections from two views of the 3-D reconstruction of a female mouse urogenital sinus (UGS) showing merged two-channels (see Video 6.2). Scale bar, 5 mm.

Figure 6.5: Schematic of in-house developed FLIM-OPT microscope system. O – objective, AP – aperture, L1 – condenser lens, F1 – excitation filter, DM – dichroic mirror, L2 – tube lens, F2 – emission filter, M – mirror; GOI – gated optical intensifier. (The GOI is coupled to a CCD through the use of two infinity focussed opposing camera lens of focal length of 50 mm and 35 mm.)

Figure 6.6: Photograph of the major components of the detection unit (GOI/HRI and CCD coupling).

Figure 6.7: Photograph of (a) in-house developed FLIM-OPT microscope system and (b) the corresponding spectral filtered illumination based on an ultrafast fibre-laser-pumped super-continuum source.

Figure 6.8: A single projection of a live LysC:GFP zebrafish embryo (confirmed by observing heart beat during acquisition) in (a) transmission and in (b) fluorescence based on the intensity-based OPT system. Scale bar, 500 μm.

Figure 6.9: Schematic of the FLIM-OPT “standard” acquisition procedure.

Figure 6.10: Maximum intensity projections of (a) a 3-D fluorescence intensity reconstruction and (b) the combined fluorescence (red) and absorption (grey) intensity reconstruction of a live LysC:GFP transgenic zebrafish embryo 3 dpf. Scale bar, 500 μm.

Figure 6.11: Maximum intensity projections of 3-D fluorescence lifetime reconstructions on a continuous colour scale of a live LysC:GFP transgenic zebrafish embryo 3 dpf from two orthogonal orientations. Scale bar, 500 μm.

Figure 6.12: A fluorescence lifetime histogram showing two clear populations corresponding to GFP and autofluorescence.

Figure 6.13: Maximum intensity projections of 3-D fluorescence lifetime reconstructions on a discrete colour scale of a live LysC:GFP transgenic zebrafish embryo 3 dpf (see Video 6.3) from two orthogonal orientations (corresponding to Fig. 6.11). Scale bar, 500 μm.

Figure 6.14: The basic structure of a single-chain FRET-based biosensor. The scheme shows the YFP and the CFP fluorophores conjugating the biosensor. Activation of ligand module results in an interaction between the sensor and the ligand. This in turn alters the FRET efficiency. The graphs illustrate the expected relative fluorescence lifetime of CFP for the inactive and active states of the biosensor.

Figure 6.15: A description and a diagram of (a) the CFP-only probe for the non-FRET signal; (b) the YFP-only probe as a no donor control probe for background and bleedthrough monitoring; (c) the linked CFP/YFP probe for the High-FRET signal between the two adjoining proteins;(d) constitutively active probe that contains the Rac1 protein with a mutation in its binding site that renders it constantly active (i.e. High-FRET). The four probes here described are four control probes used in the experiment.

Figure 6.16: 3-D transmitted light reconstructions and the fluorescence lifetime images of 24 hpi zebrafish embryos with different control probes: (a) the CFP-only probe (no FRET); (b) the linked CFP-YFP probe (High FRET); (c) the constitutively active probe (High FRET) and their corresponding lifetime histograms.

Figure 6.17: 3-D fluorescence lifetime images of 48 hpi zebrafish embryos with different probes: (a) the CFP-only probe (no FRET); (b) the linked CFP-YFP probe (High FRET); (c) the constitutively active probe (High FRET); (d) the experimental Rac probe and their corresponding lifetime histograms.

Figure 6.18: (a) Wide-field fluorescence image and (b) maximum intensity projection image of 3-D fluorescence OPT reconstruction of a live 30 dpf Casper:Fli-EGFP zebrafish with transplanted Tag-RFP U87MG tumour cells (see Video 6.4). Scale bar, 5 mm.

Figure 6.19: 3-D time-lapse fluorescence images of a double-transgenic zebrafish at Day (a) 5, (b) 13, (d) 20, (d) 40 and (e) 53 after the initial tumour inducement with (h-j) correspond to the

corresponding separate tumour volumes at each time point. The fish was 50 dpf on the day the longitudinal experiment began (Day 0). (The transparent mutant Casper zebrafish line crossed to the double-transgenic reporter line expressing GFP-labelled tumours and a mCherry vasculature (Tg Casper: KDR-mCherry: Tet on GFP-V12Kras) was utilised.) Scale bar, 5 mm.

Figure 8.1: Schematic of ultrafast fibre-laser-pumped super-continuum source (SC-400-2, Fianium Ltd) [149].

Figure 8.2: (a) The measured ESF of FLIM-OPT microscope system is plotted as discrete data points. The fit to these points is illustrated by the red solid line. The linear correlation coefficient between these two is 0.9999. (b) The corresponding MTF at this position from the analytical method, shown as the red solid line, and the numerical Fourier transform procedure, shown as data points.

Figure 8.3: Three MTFs at different binning parameters for the same NA shown in Fig. 8.2 (a) from the analytical method, shown as the black dots for 1×1 binning, the red squares for 2×2 binning, and the blue solid line for 4×4 binning.

Figure 8.4: MTFs as a function of defocus (z) for different effective NAs (0.13, 0.07, 0.06, 0.05, 0.04 and 0.03) of the 4×4 binning FLIM-OPT microscope system. (260×260, Δk_x = 0.596 mm^{-1}, Δy = 6.45 μm, the vertical scale -838.5 – 838.5 μm and the horizontal scale -77.48 – 77.48 mm^{-1}).

Figure 8.5: MTFs as a function of defocus (z) for (a)intensity-based OPT microscope system and (b) FLIM-OPT microscope system. (NA 0.07, 1×1 binning, 1040×1040, Δk_x = 0.596 mm^{-1}, Δy = 1.6125 μm, the vertical scale -838.5 – 838.5 μm and the horizontal scale -309.92 – 309.92 mm^{-1}).

List of Tables

Table 3-1: The analytic values for the resolution at best focus and DOF for different effective NAs of the OPT system.

Table 3-2: The radial and tangential FWHM of the reconstructed beads for different effective NAs of 0.06, 0.07 and 0.09 with the standard FBP reconstruction method (near-axis bead located 103 μm away from the axis of rotation; off-axis bead located 334 μm away from the axis of rotation; average bead diameter 14.8±0.13 μm).

Table 3-3: The average background from the standard FBP and the MTF-mask filtering reconstruction for different effective NAs of 0.06, 0.07 and 0.09 (all data based on 90 experimental angular projections).

Table 3-4: The radial and tangential FWHM of reconstructed beads for different effective NAs with the MTF-mask filtering approach. (near-axis bead located 103 μm away from the axis of rotation; off-axis bead located 334 μm away from the axis of rotation; average bead diameter 14.8±0.13 μm)

Table 3-5: The radial and tangential FWHM of reconstructed off-axis beads with different reconstruction approaches for an effective NA of 0.07. (FBP – standard FBP reconstruction; MTF-mask – MTF-mask filtered reconstruction; MTF-deconvolution – MTF-deconvolution reconstruction; off-axis bead located 334 μm away from the axis of rotation; average bead diameter 14.8±0.13 μm)

Table 4-1: The FWHM of the standard and dual projection OPT reconstructions for beads at different locations.

Table 4-2: The FWHM of the standard, the dual axis and the four axis OPT reconstructions for the bead in Fig. 4.7 (1.92 mm away from the rotation axis).

Table 4-3: The FWHM of the standard, the dual axis and the four axis OPT reconstructions for the bead locating at 0.65mm away from the rotation axis.

Table 4-4: The FWHM of the standard, the dual axis and the four axis OPT reconstruction for the bead locating at 1.09 mm away from the rotation axis.

Table 6-1: Maximum frames per second for CCD (Clara, Andor technology plc) [135]. Full frame: 1392×1040.

List of Videos

Video 5.1: 3-D neutrophil cell migration mapping in the tissue for 360 seconds in a model of wound inflammation in the 2 dpf LysC: GFP zebrafish embryo based on pairs of orthogonal projections. Red lines correspond to the previous movements while white lines correspond to latest movement from the last time point.

Video 6.1: 3-D fluorescence OPT reconstruction of a mice lung and heart with blue channel (excitation centred 470 nm) and green channel (excitation centred 530 nm) merged.

Video 6.2: 3-D fluorescence OPT reconstruction of a female mouse urogenital sinus (UGS) with blue channel (excitation centred 470 nm) and green channel (excitation centred 530 nm) merged.

Video 6.3: 3-D fluorescence lifetime reconstructions on a discrete colour scale of a 3 dpf live LysC:GFP transgenic zebrafish embryo.

Video 6.4: 3-D fluorescence OPT reconstruction of a live 30 dpf Casper:Fli-EGFP zebrafish with transplanted Tag-RFP U87MG tumour cells.

Abbreviations

ADC	Analogue-to-digital convertor
BABB	Benzyl alcohol/benzyl benzoate
CCD	Charge-coupled device
CLSM	Confocal laser scanning microscopy
CW	Continuous wave
DAQ	Data acquisition
DM	Dichroic mirror
DOF	Depth of field
dpf	Days post-fertilisation
DSLM	Digital scanned laser light-sheet fluorescence microscopy
ESF	Edge spread function
FBP	Filtered backprojection
FEP	Fluorinated Ethyline Propylene
FLIM	Fluorescence lifetime imaging
FOV	Field of view
FRET	Förster resonance energy transfer
FWHM	Full width half maximum
FWM	Four-wave mixing
GFP	Green fluorescent protein
GOI	Gated optical intensifier
GPU	Graphic processor units
HILO	Highly inclined and laminated optical sheet
hpi	Hour post injection

HRI	High rate imager
LSF	Line spread function
LSM	Laser scanning microscopy
MI	Modulation instability
MIP	Maximum intensity projection
MTF	Modulation transfer function
MRI	Magnetic resonance imaging
NA	Numerical aperture
OPFOS	Orthogonal-plane fluorescence optical sectioning
OPM	Oblique plane microscopy
OPT	Optical projection tomography
PMT	Photon multiplying tube
PSF	Point spread function
ROI	Region of interest
sCMOS	Scientific complementary metal-oxide-semiconductor
SLOT	Scanning laser optical tomography
SNR	Signal-to-noise ratio
SPECT	Single-Photon Emission Computed Tomography
SPIM	Selective plane illumination microscopy
TAC	Time-to-amplitude convertor
TCSPC	Time correlated single photon counting
UGS	Urogenital sinus
UV	Ultraviolet

Chapter 1: Thesis Overview

This thesis primarily concerns the development and applications of optical projection tomography (OPT) and aims to illustrate the potential of such mesoscopic three-dimensional (3-D) imaging technology for biomedical research (e.g. fundamental biological research, drug discovery, etc.). OPT has been extended to incorporate wide-field fluorescence lifetime imaging (FLIM) instrumentation, referred as FLIM-OPT, providing 3-D fluorescence lifetime imaging. The tomographic reconstruction process has been developed to incorporate the measured characteristics of the optical system, providing more realistic reconstructed images. OPT has also been developed to incorporate an angular multiplexing technique, employing multiple imaging systems in parallel to acquire OPT data sets simultaneously focussed at different planes within the sample. This approach has been adapted to multiple image acquisitions at orthogonal projection angles focussed at the rotation axis, enabling rapid time-lapse 3-D feature tracking at the camera frame rate.

Chapter 2 introduces the basic concepts of fluorescence and its characteristics that may be measured including intensity, excitation and emission spectrum and lifetime. It also describes various approaches to obtain quantitative information from fluorescence imaging and introduces the theoretical background and common implementations of Förster Resonance Energy Transfer (FRET) measurements. There follows a review of the current 3-D optical imaging techniques for mesoscopic samples (e.g. small animals, embryos and engineered tissues), including the most common implementations and the applications of these imaging techniques, including OPT and light sheet microscopy. A comparison of spatial resolution for "standard" OPT and selective plane illumination microscopy (SPIM) is presented. The standard filtered back projection (FBP) algorithm for parallel-beam projection from the mathematical basis is introduced as this is key to understanding OPT.

Chapter 3 describes the development and evaluation of modified tomographic reconstruction techniques incorporating the optical characteristics measured for our OPT system. In the standard FBP algorithm, only a ramp filter in the weighting process is used. However, a spatial frequency modulation is applied by the optical system in OPT resulting from the diffraction of focussed light. The OPT system is characterised by experimentally determining the modulation transfer functions (MTFs) as a function of defocus for different effective collection numerical apertures (NAs). The development and evaluation of modified computational reconstruction programme to incorporate the optical characteristic information (i.e. experimentally determined MTFs) using either MTF-mask filtering or deconvolution of the MTF is then presented, which includes the generation of filters and the investigation on how these modified reconstruction techniques can improve image quality for different acquisition strategies, i.e. reduced angular sampling or highly sampled acquisitions.

Chapter 4 describes the development of an angular multiplexing technique for OPT with a view to ameliorating the trade-off between sample size and spatial resolution. This entails using dual optical imaging channels acquiring data simultaneously focused on shifted planes in the sample. The proof of principle

extension to OPT with four multiplexed projections is then presented. The improved average spatial resolution and increased light collection efficiency of this multiplexed OPT approach is evaluated.

Chapter 5 describes the development of angular multiplexing OPT to achieve triangulation of dynamic samples. The dual-axis OPT from the last chapter is extended to conduct simultaneous image acquisition at orthogonal projection angles during an OPT "scan" as a means to obtain 3-D mapping information with higher time resolution than the total sample rotation time. By processing image data from pairs of orthogonal projections, this approach is shown to enable 3-D tracking of the motion of specific features such as cells within a sample.

Chapter 6 describes various *ex vivo* and *in vivo* biomedical applications of OPT and FLIM-OPT on fixed tissues and live organisms. First, the application to fixed tissues to readout morphology for histopathology-based research is presented. Then applications of OPT and FLIM-OPT to live zebrafish are discussed, including the first demonstration of FLIM-OPT to distinguish between exogenous labels and background autofluorescence with similar spectral properties but different lifetime values, the first demonstration of FLIM-OPT as a 3-D tomographic imaging platform for mapping protein-protein interactions via FRET in live zebrafish embryos, and the demonstration of the potential of OPT for longitudinal 3-D global imaging of tumour generation and progression in intact live juvenile/adult zebrafish. These experiments illustrate how OPT and FLIM-OPT can spatially and temporally resolve dynamic events in 3-D and indicate their potential as a 3-D imaging platform for biological and pharmacological research on live disease models.

Finally, **Chapter 7** concludes the thesis, summarising the progress achieved and results obtained. It then discusses the future potential of OPT technology.

Chapter 2: Background overview of fluorescence and 3-D mesoscopic imaging

Fluorescence imaging is now a common and important tool for monitoring biological and chemical systems. In this chapter, the concepts of fluorescence and the photo-physics behind it will be introduced, specifically its use in conjunction with different contrast mechanisms, namely intensity, spectral and lifetime imaging. There is an increasing trend in biomedical research toward *in situ* studies employing 3-D imaging techniques. For samples in "mesoscopic" (1 – 10 mm) regime, such as small animals, animal embryos and engineered tissues, a variety of imaging techniques have been developed. The second half of the chapter outlines the common 3-D mesoscopic optical imaging techniques and reviews the work in this field with respect to fluorescence imaging. The standard FBP algorithm for parallel-beam projection from the mathematical basis is introduced as this is key to understanding OPT. Topics covered include:

- Physical properties of fluorescence
- Fluorescence imaging techniques
- FLIM and FRET
- Introduction to mesoscopic imaging
- Light sheet microscopy
- Optical projection tomography (OPT)
- Numerical analysis of spatial resolution in OPT and selective plane illumination microscopy (SPIM)
- Standard FBP algorithm

2.1. Fluorescence

The general definition of fluorescence is the emission of a photon corresponding to the radiative transitions from an excited electronic state to the ground state, where the two states have the same spin multiplicity, i.e. singlet to singlet or triplet to triplet. Indeed, fluorescence is just one of the transitions which can occur within a molecule and such electronic transitions are "allowed" in quantum mechanics because the states involved in the transitions have the same spin multiplicity. The most common form of fluorescence is the transition between the first excited and ground singlet electronic state. The absorption and emission of light between different energy levels and a number of other processes involved in fluorescence are nicely visualised through a Jabloński diagram [1], shown in Fig. 2.1.

The Jabloński diagram illustrates a simplified view of the different electronic states of a fluorescent atom or molecule (fluorophore) and the transitions between them. The singlet ground and first excited states are depicted by S_0, S_1. At each of the states, the fluorophore can occupy one of a number of vibrational energy

levels. All the states are arranged vertically by energy level. For simplicity, only four vibrational energy levels are shown for each electronic state in Fig. 2.1.

Following Boltzmann statistics, it can be considered that essentially all molecules will be found in a vibrational level of the electronic ground state (S_0) at room temperature and standard pressure. When a molecule absorbs a photon with appropriate energy, an electron is excited from the ground state to a particular higher vibrational level of an excited electronic state. The process of this absorption is rapid, on the order of 10^{-15} s (fs).

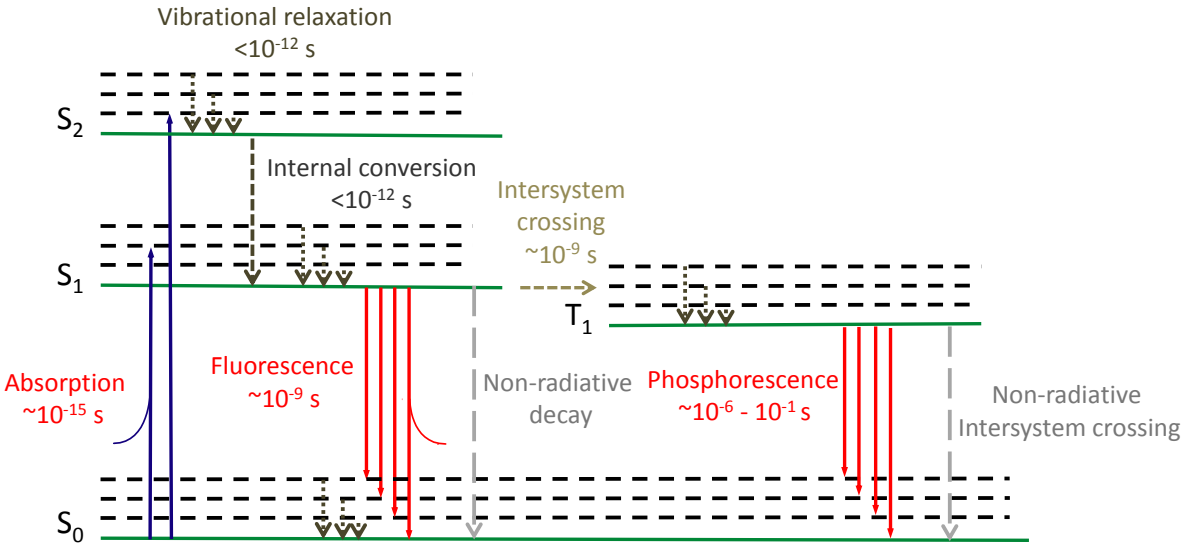


Figure 2.1: A Jabloński Diagram outlining the possible transitions in a molecule. Here the ground state is denoted S_0 , the first and the second excited singlet states are denoted S_1 and S_2 and the first triplet state is denoted T_1. Each level also illustrates a number of vibrational levels. Transitions between all of these finely spaced levels results in the observed broad absorption/ emission (fluorescence) curves.

Once excited, the electron will then rapidly (< 10^{-12} s (ps)) relax to the lowest vibrational level of S_1 via the processes known as *vibrational relaxation* and *internal conversion*. After promotion to an excited state, electrons will relax to the lowest vibrational energy level in this state, known as vibrational relaxation. It is also possible for electrons to decay non-radiatively from one state to another, where two states have the same spin multiplicity (e.g. $S_2 – S_1$), known as internal conversion. The lowest vibrational level of S_1 is the starting point for fluorescence emission, non-radiative decay or transition to the lowest triplet state. From here, the electron can decay to the ground state via fluorescence with the emission of a photon. This process is termed *fluorescence*, which typically takes place on the 10^{-9} s (ns) scale. Another route between S_1 and S_0 is by internal conversion, i.e. non-radiative. Generally, it occurs on a longer time scale (i.e. on the ns scale) than that from higher excited states to S_1 due to the increased energy gap. Alternatively, if the electron decays to the lowest triplet state via intersystem crossing, there is only a relatively low possibility for the radiative transition from T_1 to S_0 due to the "spin forbidden" state transition between triplet-singlet states in quantum

mechanics. This radiative transition requires spin conversion (i.e. a flip in spin from +1/2 to -1/2 or vice versa) and is named *phosphorescence*. It is a very slow process with typical lifetime ranging from milliseconds to seconds, much longer than the fluorescence process. Because of this long phosphorescence lifetime, some photochemical reactions, which are important in understanding photobleaching effects, may occur during this period.

From the Jabloński diagram, it is clear that fluorescence always originates from the same energy level (the lowest vibrational level of S_1), irrespective of which energy level the molecules are first excited in to. This leads to a shift of the fluorescence (emission) spectrum to a longer wavelength, or lower energy, relative to the absorption spectrum (Stokes shift) [1, 2]. A Stokes shift is almost universal for fluorescent molecules. One common cause for it is the rapid decay to the lowest vibrational level of S_1.

2.2. Physical properties of fluorescence

When a fluorescent signal is observed, it is desirable to make quantitative measurements to study and characterise the fluorescent structures in the sample. A fluorescent signal can be characterised by a number of properties including the intensity, spectrum and lifetime. Each one of them is dependent on the underlying electronic configuration of the fluorophore. It is noted that this configuration may be affected by changes in the local environment. Therefore, through the quantitative measurements of these properties it is possible to determine the fluorescent species and probe the local environment.

2.2.1. Intensity

The fluorescence intensity (I) refers to the number of emitted photons, or in other words, refers to how bright the sample is. As such it is inherently linked to the quantum yield (η) of the sample, which is also known as the emission efficiency. It is, in essence, a relative measure of the efficiency with which a given sample emits fluorescence photons. It is defined as the ratio of the number of emitted photons (N_e) to the number of absorbed photons (N_a) and can also be described as the fraction of fluorophores which decay through emission in terms of radiative (k_r) and non-radiative (k_{nr}) decay rates as shown below:

$$\eta = \frac{N_e}{N_a} = \frac{k_r}{k_r + k_{nr}} \qquad 2\text{-}1$$

The non-radiative decay rates include, but are not limited to, the rate of intersystem crossing and internal conversion. The quantum yield varies according to the local fluorophore environment since the non-radiative decay rate is a function of the molecular interactions with the environment. The quantum yield also varies according to the changes in the radiative decay rate. In addition to quantum yield, fluorescence intensity is proportional to the concentration of fluorophores in a sample. If the quantum yield is uniform within a sample, intensity measurements can determine the concentration of fluorophores; on the other hand, if the

concentration is uniform, the variations in fluorescence intensity provide the information of quantum yield changes, which may indicate molecular interactions.

Measurements of fluorescence intensity are the most common form of measurement in fluorescence imaging. However, problems may occur when attempting to make quantitative measurements due to the generally unknown concentration of the fluorophores and the sensitivity of the intensity-based measurements to the effects of the collection efficiency, the spatial variation in excitation, scattering and absorption of both excitation light and emitted fluorescence as well as background signals.

2.2.2. Absorption and emission spectra

The wavelength of the emitted fluorescence is another quantity that can be used to characterise the signal and may be used to distinguish between different molecules in the sample. It depends directly on the energy gap between the initial and final energy levels as described below (Plank's law):

$$\lambda_{em} = \frac{hc}{\Delta E} \qquad 2\text{-}2$$

where h is Planck's constant, c the velocity of light in vacuum and ΔE the energy gap between the two states involved in the emission process. The same rule also applies to the absorption wavelength. The wavelength of an emitted or absorbed photon depends on the energy level configuration of the fluorophore and also partially depends on the local fluorophore environment. Since there are a number of rotational and vibrational energy levels residing within each electronic level, emission from the lowest vibrational energy level of the S_1 state may occur to any of a number of vibrational levels within the ground state. This leads to a spread of energies and as a consequence, broad fluorescence emission spectra are typically a few tens of nm wide. Conversely, excitation from the ground state may occur to any of a number of excited levels, which yield the fluorescence absorption spectra.

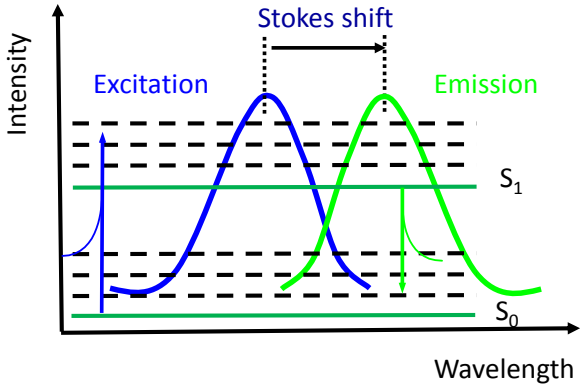


Figure 2.2: Schematic showing excitation and emission transitions between the ground and first excited electronic state of a molecule and illustrating the concept of mirror image rule and "Stokes" shift.

Figure 2.2 shows a schematic of excitation transitions from the lowest vibrational state of S_0 into different vibrational states of S_1 and emission from the lowest vibrational state of S_1 down to different vibrational states of S_0 on the left and right respectively. Typically, the fluorescence emission spectrum has a similar profile to the absorption spectrum, which is known as the mirror image rule. The reason for this can be explained by the same transitions being involved in both absorption and emission, and the similar vibrational structure of the states. However, although mirror image rule is often true, especially when the absorption represents S_0 to S_1 transitions, there are still many exceptions (e.g. biphenyl) [1]. The deviations from the mirror image rule often indicate geometric rearrangements and excited state reactions.

To extract quantitative information, the most basic approach is to ratio two different wavelength channels assuming that all the unwanted variations (e.g. illumination efficiency, collection efficiency, scattering, etc.) will cancel out. There are then more complex approaches which try to fit or decompose complex spectra into relative contributions from "pure" spectra (i.e. specific fluorophores).

2.2.3. Fluorescence lifetime

Fluorescence lifetime is the characteristic time of the decay process from an excited state to the ground state. It is defined as the average time that an electron remains in an upper energy level prior to its return to the ground state. This lifetime of the excited state is governed by the reciprocal of the sum of rates that depopulate it, as shown below

$$\tau = \frac{1}{k_r + k_{nr}} \qquad 2\text{-}3$$

where k_r is the radiative decay rate and k_{nr} is the non-radiative decay rate. The non-radiative decay rate is given by the sum of rate constants, described below

$$k_{nr} = k_{ic} + k_{iscp} + k_q[q] \qquad 2\text{-}4$$

where k_{ic} is the rate constant of internal conversion, k_{iscp} the rate of intersystem crossing to the triplet state, and $k_q[q]$ the possible quenching due to interactions with other molecules where $[q]$ is the concentration of quenchers [3]. In general, fluorescence lifetime is on the order of nanosecond (1ns ~ 100 ns). The intrinsic lifetime, τ_n, is the lifetime of the fluorophore in the absence of non-radiative processes, $1/k_r$.

Consider the excitation of a single fluorescent species with a δ-function pulse of light (an infinitely short pulse of light), resulting in an initial population (N_0) of fluorophores in the excited state. Then, the population of the excited state will decay according to

$$\frac{\partial N(t)}{\partial t} = -(k_r + k_{nr})N(t) \qquad 2\text{-}5$$

where $N(t)$ is the number of excited molecules at a time t following excitation. Recalling the lifetime of the excited state $\tau = (k_r + k_{nr})^{-1}$ and $N(t) = N_0$ at $t = 0$ and considering the fluorescence intensity $I(t)$ is proportional to the excited state population, the intensity of fluorescence, $I(t)$ at time t following excitation, emitted from this population of fluorophores will decay exponentially over time from its initial intensity of I_0, given by

$$I(t) = I_0 \exp\left[-\frac{t}{\tau}\right] \qquad 2\text{-}6$$

Thus, fluorescence lifetime is the average time required for the emitted fluorescence intensity to decrease to 1/e from its initial value.

So far, the text above just describes a single exponential decay process. In practice, the presence of multiple fluorophore species or multiple states arising from interactions with the local environment may result in more complex fluorescence decay profiles, which can be modelled by a N-component multi-exponential decay model. Typically a linear sum of multiple exponentials is used to fit complex fluorescence decay data. The intensity profile of a sample which follows a multi-exponential decay is given by,

$$I(t) = I_0 \sum_{i=1}^{N} c_i \exp\left[-\frac{t}{\tau_i}\right] \qquad 2\text{-}7$$

where each pre-exponential amplitude is represented by the weighting value c_i, each decay constant by τ_i. The pre-exponential amplitudes are normalised.

Even when a multi-exponential decay has been acquired and the values of lifetimes and pre-exponential factors determined, a single lifetime value (i.e. mean lifetime) can also be useful to describe the decay. This typically takes the form of the intensity weighted mean fluorescence lifetime defined by,

$$\tau_{mean} = \frac{\sum_{i=1}^{N} c_i \tau_i^2}{\sum_{i=1}^{N} c_i \tau_i} \qquad 2\text{-}8$$

The fluorescence lifetime of a fluorophore is an inherently ratiometric quantity as it is determined by the intensity decay over time and not by the absolute intensity value. This makes lifetime measurements less susceptible to artefacts introduced by varying fluorophore concentrations or excitation intensity fluctuations.

2.3. Fluorescence imaging

2.3.1. Intensity imaging

The simplest implementation of fluorescence microscopy is measuring the steady-state intensity of the signal. The image is obtained by recording the fluorescence signal emitted from each point within the sample. Depending on the specific experiment, the intensity measurement can indicate yield information on location or possibly provide more quantitative information on fluorophore concentration or fluorophore quantum efficiency.

However, absolute quantitative intensity measurements are difficult to achieve, especially in biological samples which often involve multiple absorbing and scattering event and have multiple fluorescent species. The intensity measurements are also sensitive to the collection efficiency, the variation in labeling efficiency and the spatial variation in excitation.

2.3.2. Spectrally resolved fluorescence imaging

The vibrational and rotational structures in the excited and the ground electronic states of fluorophores result in characteristic excitation and emission spectra for them. In addition, these spectral characteristics can be modulated (e.g. by solvent-solute interaction) and used to indicate local environment information.

Through the control of the excitation wavelength, particular fluorophores can be selectively excited in multiply labelled systems or a particular endogenous molecule can be chosen. Acquisition at particular wavelengths can be used to separate out different fluorophores into separate spectral channels [4].

Hyperspectral imaging is beyond discrete wavelength/band-selection measurements. The full spectrum is spread and sampled along a spatial dimension by using a dispersive element (e.g. grating, prism). Then the spatially dispersed spectrum is often incorporated into an instrument (e.g. spectrograph) including an array or imaging detector, which allows the full spectrum to be recorded of a single point or a line [5]. Alternatively, it can be realised by using scanning filters (e.g. fabry-perot, acoustic-optic, electro-optic). In this case the spectral information is recorded sequentially and at each time the full spatial information is recorded.

2.3.3. Temporally resolved fluorescence imaging

Fluorescence lifetime is defined as the average time during which a fluorophore remains in an excited state prior to its return to the ground state. Fluorescence lifetime imaging (FLIM) can use measured lifetimes to generate contrast in images of fluorophores with similar emission spectra but different lifetime values. It is an intrinsically ratiometric imaging technique and this ratiometric nature makes measuring fluorescence lifetime a more robust way to extract quantitative information from the sample, such as the rate of energy transfer, the rate of excited state reactions and the details about interactions with the local environment (e.g. pH, temperature, etc.). Thus, accurate and rapid lifetime measurement methods are experiencing extensive interest. Although it is not straightforward to measure lifetime because typical values are on the ns time-scale, requiring the use of pulsed or modulated sources, high-speed electronic devices and detectors, a great

deal of effort has been directed towards developing reliable techniques for lifetime measurements. Especially recent advances in ultrafast laser technology and in high-speed imaging detectors are prompting researchers to investigate the potential of fluorescence lifetime measurements. A more detailed description of the different techniques employed to measure the fluorescence lifetime can be found in the next section.

2.4. Time-resolved Fluorescence imaging techniques

As already described, FLIM is an intrinsic ratiometric imaging technique that measures the average relaxation time of excited fluorophores in a sample. The techniques employed to measure the fluorescence lifetime can be performed in the time and frequency domain according to whether the lifetime information is derived from the direct measurements of fluorescence intensity decay profiles as a function of time delay following pulsed excitation or from the measurements of phase difference between a modulated excitation signal and the resulting modulated emitted fluorescence signal. What follows in this section is an outline of both approaches and the most common forms of their implementation as well as the common methods of data analysis.

2.4.1. Time-domain FLIM: Time-correlated single photon counting (TCSPC)

Time correlated single photon counting (TCSPC) is the most common and photon-efficient implementation of time-domain fluorescence lifetime measurement techniques. As the name indicates, it involves measuring the arrival times of individual photons with respect to a pulsed excitation source. A start signal for each pulse is produced by irradiating a photodiode with light from the pulsed excitation source. This start signal initialises a linear voltage ramp in a time-to-amplitude convertor (TAC). Then, the detection of a fluorescence photon emitted from the sample stops the linear voltage ramp. The magnitude of the output voltage, which is generated in the TAC and is proportional to the time between start and stop signals, is then converted to a time signal through an analogue-to-digital convertor (ADC). This makes it possible to calculate the arrival time of the photon. A histogram of photon arrival times is then built up by detecting a large number of photons over repeated pulses of the excitation source. This histogram represents the decay profile of the emitted fluorescence from the sample [1]. The fluorescence lifetime information can then be extracted from this dacay profile in a number of ways (e.g. fitting an exponential curve (sub-section 2.4.4) or implementing phasor analysis [6]). As TCSPC is a single point technique, 2-D FLIM information can then be achieved by scanning the excitation beam across the sample and collecting a decay curve at each pixel.

TCSPC is a highly photon-efficient method of measuring lifetimes. However, the main drawback is the low acquisition speed. This is partly due to the scanning process (typically pixel by pixel) which is inherently slow and also due to the low photon count rate which is essentially limited by the "dead time" of the system's electronics and more importantly, by the need to avoid the effect of "pulse pile-up", where multiple photons arrive at the detector for a single excitation pulse. The dead time of a TCSPC system refers to the time requried for the TAC to reset ready for the next detection period. Any other photons arriving during this

dead time are not recorded. As the system is limited to detecting the first arriving photon, if many photons are emitted after each laser pulse then only the early photons are detected. Therefore, TCSPC requires the detection of a single photon per excitation pulse since pulse pile-up results in a bias of the measured lifetime towards a shorter value. In order to avoid this effect, excitation intensities need to be sufficiently low such that only one fluorescence photon is detected for every 50-100 pulses [1]. The requirement of detecting less than one fluorescence photon in a detection period results in many detection periods where no photons are recorded and thus, there is no stop signal in each of these periods. To address this issue, the TAC is equipped with a condition of "out-of-range" that automatically resets the TAC before the next detection period. This, however, is not desirable in high repetion rate systems (> 50 MHz). Therefore, TCSPC often works in a reverse stop-start mode, in which the arrival of the subsequent laser pulse acts as the stop signal thus avoiding the TAC being constantly reset. The principles of stop-start TCSPC are illustrated in Fig. 2.3.

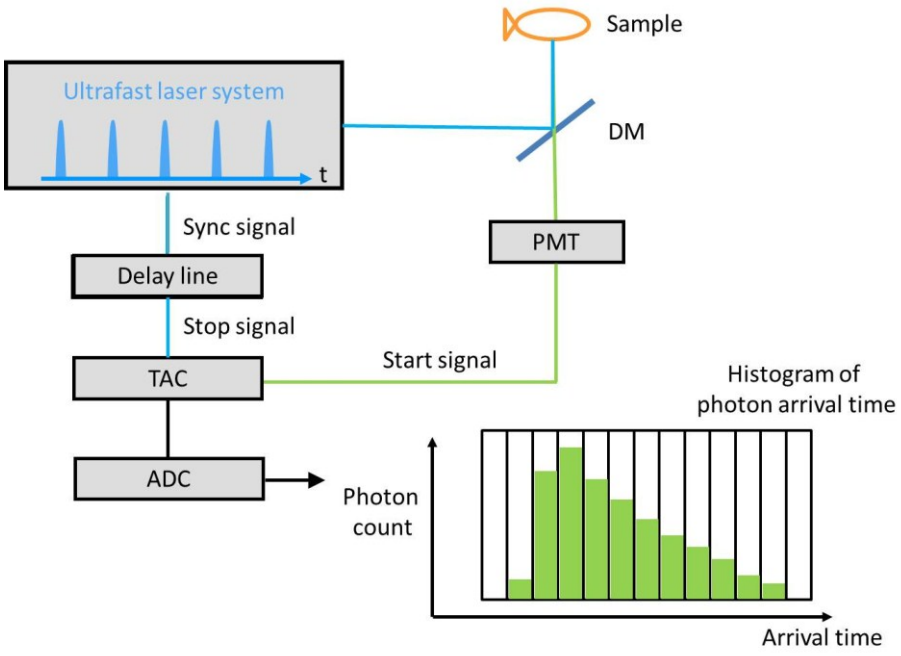


Figure 2.3: Simplified diagram illustrating TCSPC (stop-start). DM – dichroic mirror, TAC – time-to-amplitude convertor, ADC – analogue-to-digital convertor, PMT – photon multiplying tube.

2.4.2. Time-domain FLIM: Wide-field time-gated FLIM

Wide-field time-gated FLIM, rather than measuring the arrival times of fluorescence photons (e.g. TCSPC), measures the number of photons detected during a number of temporal windows at different delays with respect to the excitation pulses [7, 8]. It permits the simultaneous collection of fluorescence decay data from all image pixels and hence can be considered as a time-efficient FLIM technique. It is achieved by implementing gated optical intensifiers (GOIs) as a means of gating the emitted fluorescence onto the detector (e.g. a charge-coupled device (CCD), a scientific complementary metal-oxide-semiconductor

(sCMOS)) with respect to the excitation pulses. The GOI acts as a very fast shutter in front of the detector to take "snapshots" of the decaying fluorescence at distinct time positions with respect of the excitation pulses using a delay generator. The fluorescence decay profile can then be fitted to these samples and the lifetime information extracted. Typical gate widths vary from 100-1000 ps while the gate separation is typically on the order of nanoseconds [9-11].

Figure 2.4 shows the simplest case of determining the lifetime for a single exponential decay, in which the intensities are acquired in two gates positioned at different time delays. The ratio of the sampled intensity can be used to calculate the fluorescence lifetime, given by

$$\tau = \frac{\Delta T}{\ln\left(I_1 / I_2\right)} \qquad 2\text{-}9$$

where ΔT is the time offset between the start of the two gates and I_1 and I_2 are the sampled intensities in the corresponding gates respectively. The data collection and analysis are under the assumption of two equal-width gates [12] and this can be the basis of rapid lifetime determination.

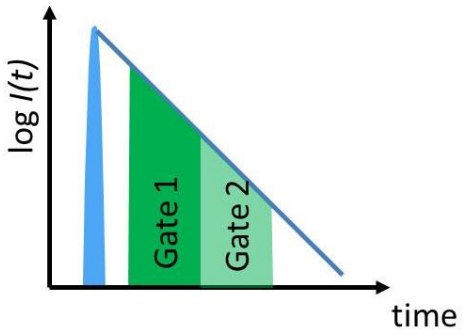


Figure 2.4: Simplified time gating scheme (2 time gates). After excitation with ultra-short pulses of light, the intensity in two time gates (gate 1 and gate 2) is measured and then used to calculate the lifetime.

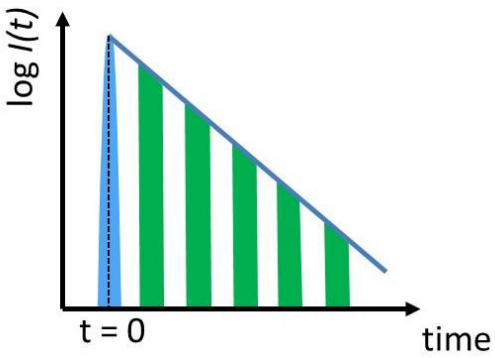


Figure 2.5: Time gated FLIM scheme (multiple time gates). After excitation with ultra-short pulses, the resultant fluorescence decay is sampled at different delay points.

In order to extract the lifetime of complex decay profiles, it is necessary to employ more than two time gates in FLIM measurements, as illustrated in Fig. 2.5. After acquisition, the data can be fitted to a multi-exponential decay mode to calculate the lifetime components and their corresponding contributions (i.e. fractions).

Wide-field time-gated FLIM is a relatively fast technique since information from all pixels is recorded in parallel. However, it has a lower photon efficiency compared to TCSPC [10]. A more detailed description of the workings of the GOI and implementation of wide-field time-gated FLIM can be found in section 2.5.

2.4.3. Wide-field frequency-domain FLIM

In frequency-domain FLIM the sample is illuminated with a sinusoidally modulated laser (typically in the MHz range) excitation source. The resultant (i.e. modulated) emission from the sample is the convolution between the fluorescence decay and the sinusoidal excitation, resulting in a sinusoidally varying fluorescence emission [1]. This emission is modulated at the same frequency as the source, but with a phase shift and a reduction in the modulation depth with respect to the excitation due to the finite fluorescence lifetime under investigation. The fluorescence emission is typically collected by the conjunction of a modulated image intensifier in front of a detector (e.g. a CCD). By acquiring a number of measurements at different phase shifts the sinusoidal emission can be reconstructed.

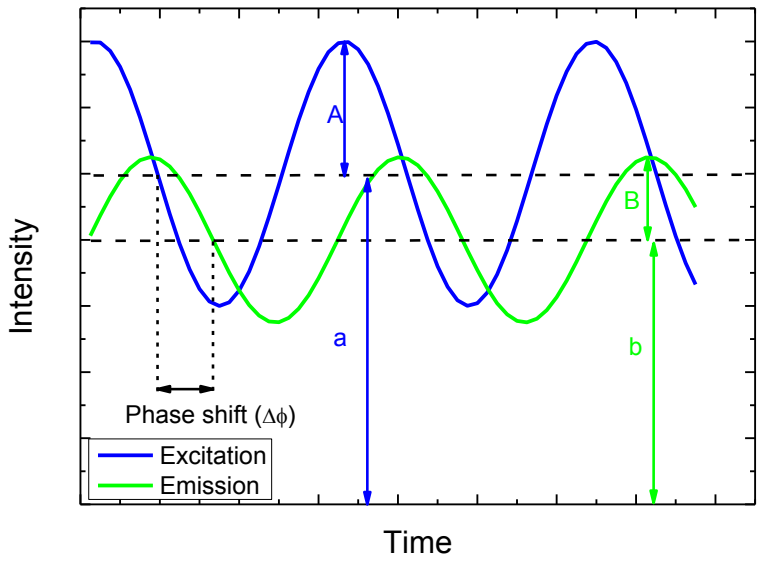


Figure 2.6: Illustration of frequency domain FLIM. The sample is excited by a modulated light source and the lifetime may then be extracted by measurement of the induced phase shift and demodulation.

The induced phase shift and demodulation between the excitation and the emission, as shown in Fig. 2.6, can then be measured and then the lifetime value (for a single exponential decay profile) calculated, given by

$$\tau_\phi = \frac{\tan(\Delta\phi)}{\omega} \qquad 2\text{-}10$$

$$\tau_m = \sqrt{\frac{1-m^2}{m^2\omega^2}} \qquad 2\text{-}11$$

where τ_ϕ is the phase lifetime, $\Delta\phi$ the induced phase shift, ω the modulated circular frequency, τ_m the modulation lifetime and m is defined as the ratio of the sinusoidal amplitude to the mean signal for the emission and excitation respectively, given by

$$m = \frac{B/b}{A/a} = \frac{B}{A}\cdot\frac{a}{b} \qquad 2\text{-}12$$

where A, a, B and b are defined in Fig. 2.6.

It is noted that if the fluorescence lifetime is purely single exponential, the phase lifetime and the modulation lifetime are identical. Away from this ideally simple case the calculated lifetimes differ. This difference can be used to indicate a complex decay profile, although it cannot be used to quantify the complexity.

The optimal excitation modulation frequency is given by $1/10\tau$, where τ is the fluorescence lifetime under investigation [13]. According to this, modulation frequencies are typically in the range of 10 – 100 MHz for lifetimes of 1-10 ns. Although the frequency-domain FLIM technique is less intuitive, the use of the modulated excitation sources (continuous wave (CW) light sources in combination with optical modulators) and detectors made it economically preferable to time-domain techniques.

2.4.4. Fluorescence lifetime data fitting

In order to extract fluorescence lifetime information, the fluorescence lifetime data must be analysed once the data has been acquired. The typical way to achieve this is fitting the acquired lifetime data to a particular model which follows the form of an exponential decay, as illustrated in Eq. 2-7. The extent to which the model agrees with the acquired data can be determined by the goodness-of-fit parameter, χ^2, given by

$$\chi^2 = \sum_{i=1}^{N} \frac{\left(I_i - f(t_i)\right)^2}{\sigma_{I_i}^2} \qquad 2\text{-}13$$

where I_i are the measured data points, $f(t_i)$ the function used to fit the data and σ_{Ii} the error associated with each data point. The iterative fitting process is then employed to find the minimum of χ^2 numerically (i.e. non-linear least squares fitting).

In the case of shot noise limited data (e.g. single exponential photon counting data), the expected error is the square root of the measured value (i.e. $\sigma_I = \sqrt{I}$) and consequently, the χ^2 function can be simplified to

$$\chi^2 = \sum_{i=1}^{N} \frac{\left(I_i - f\left(t_i\right)\right)^2}{I_i} \qquad 2\text{-}14$$

or

$$\chi^2 = \sum_{i=1}^{N} \frac{\left(I_i - f\left(t_i\right)\right)^2}{f\left(t_i\right)} \qquad 2\text{-}15$$

which are known as Nyman's (divided by the measured intensity) and Pearson's (divided by the fitting value) χ^2 respectively. In this work, the Pearson's test was implemented in the in-house developed fitting software.

2.5. Time gating acquisition using a GOI

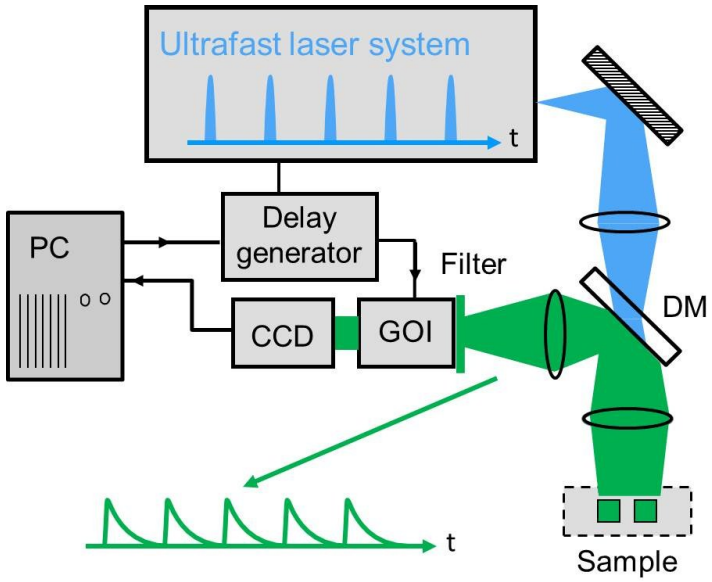


Figure 2.7: Schematic of a time-gated wide-field FLIM system. DM – dichroic mirror; GOI – gated optical intensifier; PC – personal computer. (This figure is adapted from [9].)

In wide-field time-gated fluorescence lifetime measurements, a number of gated intensity measurements with respect to the excitation pulses are acquired with the fluorescence lifetime calculation performed afterwards using an appropriate fitting technique. In this thesis the wide-field time-gated FLIM technology based on a GOI coupled to a CCD was employed, as shown in Fig. 2.7. This section provides an overview of the time gating technique and describes the basic construction of the detection unit.

2.5.1. GOI design

To implement FLIM in an OPT system, a wide-field time domain detection unit consisting of a GOI, providing gain and ultra-short gate widths, coupled to a CCD was employed to record gated images. The use of GOI to perform time-gated FLIM measurements has been widely demonstrated and characterised (e.g. gain voltage, gate width, vignetting, etc.) [14, 15].

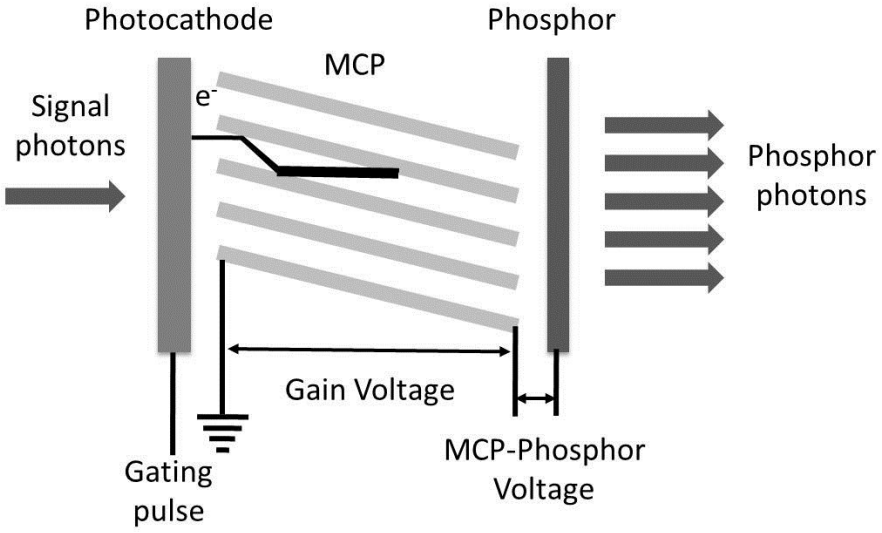


Figure 2.8: Schematic of a single plate GOI (MCP – micro-channel plate).

A basic schematic of a single micro-channel plate (MCP) GOI is depicted in Fig. 2.8. The GOI consists of three main components – a photocathode, a MCP and a phosphor screen. The collected fluorescence is directed onto the photocathode of the GOI. Each photon that is incident on the photocathode has a probability to generate an electron via the photoelectric effect. The efficiency of this mechanism is defined as the quantum efficiency of the device and is a function of the incident wavelength. Those electrons are then accelerated across the MCP (a single MCP in Fig. 2.8, but can also be a double MCP) by an applied voltage. The signal is amplified due to the coating of a secondary electron emission film on the MCP to maximise secondary emission of electrons. The voltage across the MCP can be adjusted and is described as the gain voltage. The resultant amplified electron signal from the MCP is then converted to a photon signal at the phosphor screen. When the GOI is "off" a small positive voltage is applied to the photocathode while when it is switched "on" a negative voltage is applied to the photocathode, accelerating the photoelectrons towards the MCP. This negative voltage, in gated mode, is repetitively applied. This results a train of gated amplification periods, the width of which is controlled by the gating pulse. Therefore, a GOI can be thought of as an ultra-fast shutter with amplification. The image produced by the phosphor screen can be transferred to a recording device (e.g. a CCD).

2.5.2. Time gating

For the wide-field time-gated FLIM acquisition technique, a number of linearly spaced time gated wide-field images are recorded with respect to the excitation pulses. Each gated image is actually a summation of many amplified gated events incident on the GOI at the laser repetition rate and integrated by a recording device (e.g. CCD). The intensifier gate delays are adjusted by employing a computer-controlled electronic delay line that is synchronised to the excitation laser repetition rate.

Performing wide-field time-gated FLIM requires the GOI to be triggered at the repetition rate of the pulsed laser source (40 MHz in this work) via a temporal delay box. This delay box is used to shift the gate with respect to the reference trigger signal (i.e. the signal synchronised to the excitation laser). The temporal position of the gate with respect to the reference trigger signal defines the delay time. The recording device is then triggered by the acquisition programme and integrates the signal from the GOI for a user-defined period (referred to as integration time) over many excitation pulses. After the integration, the recording device is read out and the delay box switches to the next time delay position (i.e. time gate shift relative to the excitation pulses). This process is repeated for a user-defined number of gates. Figure 2.9 shows a fluorescence decay and acquired gate positions with respect to a single excitation pulse and represents the data exported to the sequential fitting process. It also depicts the acquisition process. By acquiring a series of images at different time delay positions, the acquisition of several sampled gated fluorescence images are obtained and therefore, the fluorescence lifetime information can be extracted by using a fitting technique.

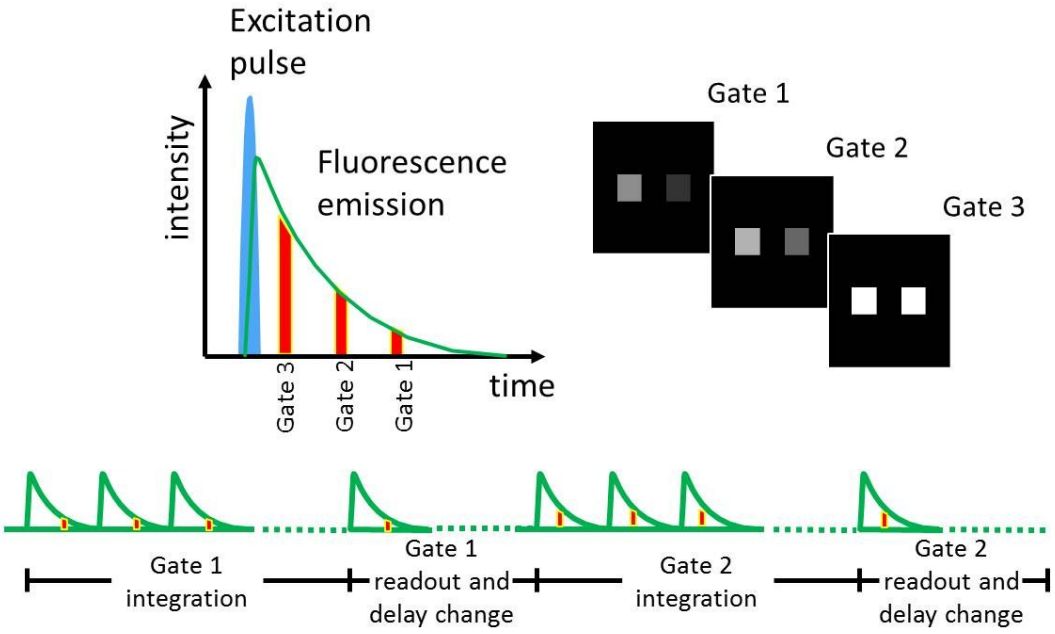


Figure 2.9: Representations of acquired gated data with respect to a single excitation pulse and fluorescence decay as well as the acquisition process. (This figure is adapted from [9].)

2.6. Förster resonance energy transfer (FRET)

Förster Resonance Energy Transfer (FRET) is a mechanism describing the energy non-radiatively transferring from an excited state of one fluorophore (called the "donor") to another fluorophore (called the "acceptor") via dipole-dipole coupling [16]. For this photo-physical process to occur, the two fluorophores have to fulfil a number of criteria [17]. Firstly, the absorption spectra of the acceptor must have sufficient overlap with the emission spectra of the donor. This permits the potential pathway for the energy to transfer. Secondly, the separation between the donor and acceptor must be sufficiently small (≤ 10 nm) for the energy transfer to occur. Thirdly, the transition dipole moments of the donor and acceptor must be favourably aligned. Figure 2.10 illustrates the principle of FRET between donor and acceptor.

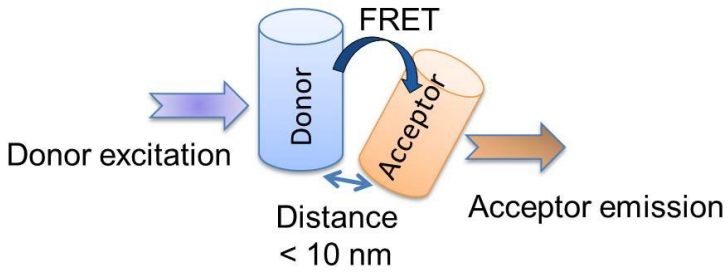


Figure 2.10: Principle of Forster Resonance Energy Transfer between donor and acceptor.

Förster [16] showed that the rate of energy transfer (k_T) was inversely proportional to the sixth power of the distance between the donor and acceptor, given by

$$k_T = \frac{1}{\tau_D}\left(\frac{R_0}{R}\right)^6 \qquad 2\text{-}16$$

where R is the distance between the donor and acceptor, τ_D the fluorescence lifetime of the donor without the acceptor present and R_0 the Förster radius, which characterises the distance at which the efficiency of energy transfer drops to 50%.

The efficiency of energy transfer, E, is defined as the fraction of photons the donor absorbs that are transferred to the acceptor [1],

$$E = \frac{k_T}{k_T + k_r + k_{nr}} = \frac{k_T}{k_T + 1/\tau_D} \qquad 2\text{-}17$$

Substituting Eq. 2-16 in Eq. 2-17, then FRET efficiency can be written as

$$E = \frac{R_0^6}{R_0^6 + R^6} \qquad 2\text{-}18$$

Figure 2.11 illustrates the FRET efficiency curve as a function of donor-acceptor separation for arbitrary value of R_0. When the separation between the donor and acceptor is equal to the Förster radius, the FRET efficiency drops to 50%. As the separation increases the FRET efficiency quickly drops off to approach 0. The sensitivity of FRET efficiency to changes in distance between the donor and acceptor has led to FRET being known as a "spectroscopic ruler" [18].

It is noted that the energy transfer occurs between the donor and the acceptor at a length scale (≤ 10 nm) far beyond the diffraction limit (typically hundreds of nanometres) but colocalisation/interaction of them can still be inferred through energy transfer. This makes FRET a particularly useful tool in biomedical application to quantify molecular dynamics (e.g. monitor the interaction of proteins, probe signalling pathways, etc.).

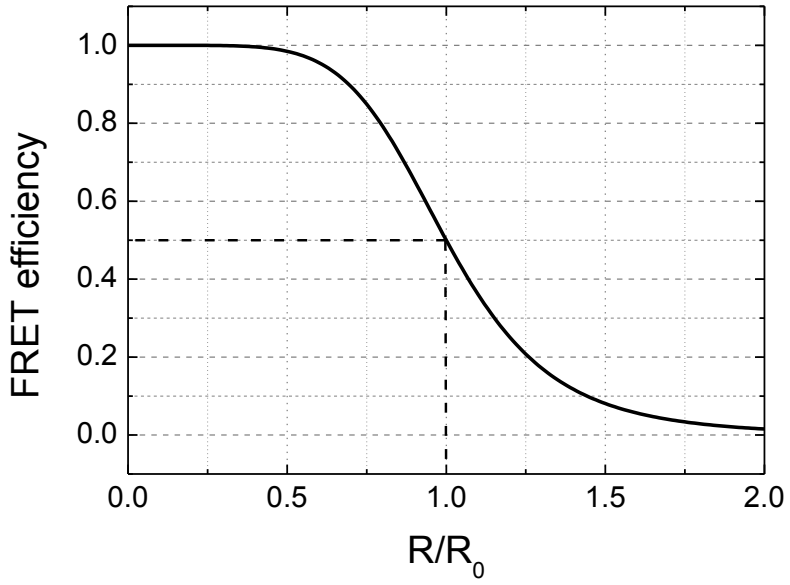


Figure 2.11: FRET efficiency curve as a function of donor-acceptor distance (R) for arbitrary value of R_0. R_0 - Förster radius.

To measure the transfer of energy indicative of FRET, a variety of ways have been developed, including intensity measurement [19], spectral measurements [20, 21], fluorescence polarisation measurements [22] and fluorescence lifetime measurements [23, 24].

In this thesis, FLIM is employed as the platform to measure FRET induced change in the fluorescence lifetime of a donor to indicate energy transfer. FRET provides an extra de-excitation pathway for the donor and therefore the lifetime of the donor is reduced when there is energy transfer, given by

$$\tau_{DF} = \frac{1}{k_r + k_{nr} + k_T} \qquad 2\text{-}19$$

as shown in Fig. 2.12.

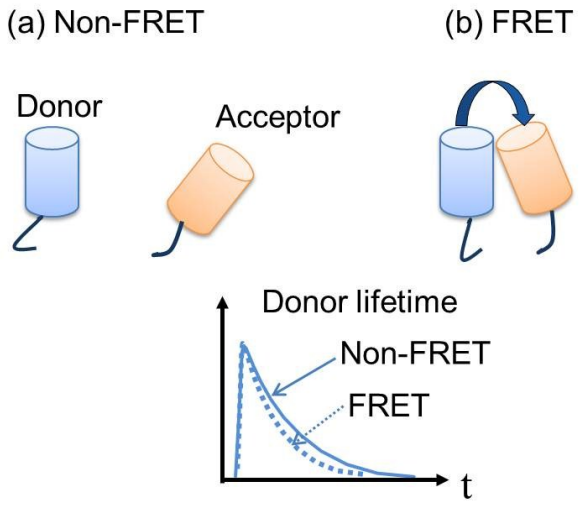


Figure 2.12: FRET detection through lifetime changing.

Since FLIM is an intrinsically ratiometric imaging technique, it has the potential to provide more quantitative measurements than intensity based imaging [24] and so FLIM is an increasingly useful tool of FRET imaging.

2.7. 3-D mesoscopic imaging techniques

More than ever, biological and biomedical research depends heavily on imaging instrumentation. Today, biomedical research is progressing from studies of mono-layers of cells on glass to *in situ* measurements of biological systems, both *ex vivo* and *in vivo*, and thus there is an increasing demand in applying 3-D imaging techniques to map the structural and functional information throughout samples.

Microscopic magnetic resonance imaging (μMRI), which is an imaging technique that uses a magnetic field and pulses of radio waves to visualise internal structures of the body, is capable of imaging live embryos in 3-D during development. It makes use of the property of nuclear magnetic resonance to image nuclei of atoms inside the body. It suffers a number of drawbacks, such as the fact that the strength of the magnet increases with the required resolution, and that the typical achievable resolution is not sufficient to identify all the tissues or organs within an embryo. More importantly, it is not an optical technique and thus, it cannot image the distributions of commonly used staining/fluorescence labelling techniques. These limitations make

MRI more useful for specimens ≥ 1 cm in diameter and less attractive for mesoscopic (1 – 10 mm) and microscopic specimens (< 1 mm in diameter).

At the other end of the size scale are the well-established imaging techniques - confocal/multiphoton laser scanning microscopy (LSM) [25, 26] - which provide optically sectioned images, or the 3-D structure of a sample can be obtained at high resolution by physically sectioning it (e.g. for histopathology-based research). The achievable lateral resolution is then limited by the imaging instrumentation (e.g. the NA of the objective and the imaging wavelength) and the axial resolution is determined by the thickness of the sections. However, precise physical cutting, mounting, imaging and registration make the whole process very time-consuming and labour-intensive. More importantly, physical sectioning precludes the possibility of *in vivo* imaging due to its very nature. Hence, optical sectioning has been proposed for 3-D *in vivo* fluorescence microscopy. Confocal microscopy produces an optically sectioned image by rejecting the light generated outside the focal plane with a pinhole in front of the detector [2, 25]. The NA determines the thickness of the optical section that is imaged. It is very efficient at generating 3-D images of specimens that have been fluorescently labelled.

However, one of the significant drawbacks for confocal microscopy is the potential photobleaching as the excitation is not axially confined (i.e. the whole depth of specimen is exposed to the excitation even when a single optical section being collected). This issue can be addressed by employing multiphoton LSM [26, 27], in which intense infrared light is concentrated at the focus of the objective such that multiple photons can be simultaneously absorbed to excite the sample. The probability of multiphoton excitation decays quickly away from the focal plane; thus, the probability of photobleaching is reduced by selectively exciting only the section at the focal plane and thus, the total number of fluorophore excitations required to image a specimen is reduced. The signal collection efficiency can also be improved, especially in scattering samples, without the need for a detector pinhole. The use of infrared wavelength leads to deeper tissue penetration depth (up to 700 μm [27]) compared to single photon excitation but reduces the resolution compared to single-photon confocal microscopy. In addition, high power laser pulses are required, and thus over time the sample may suffer from the detrimental effects of light (e.g. nonlinear effects associated with phototoxicity). Ultimately, thermal damage can impose a practical limit on the depth and speed of multiphoton fluorescence imaging.

In a common confocal LSM, the illumination and detection axes typically overlap in an antiparallel manner (epifluorescence arrangement). The use of a single lens with a limited numerical aperture (NA) results in an anisotropic point spread function (PSF). This PSF is elongated along the optical axis. To address this issue, the confocal theta microscope, in which the illumination and detection axes are orthogonal point-by-point, has been developed, providing a more isotropic PSF and a resulting improvement in resolution [28-32].

Although confocal/multiphoton LSM can provide improved contrast and optical sectioning compared to wide-field microscopes, they suffer from limited penetration depth. They are typically applied to specimens up to a few hundred microns in thickness (usually much less than that) and as such, are often employed for exploring subcellular distributions of fluorophores within small groups of cells. It is inherently slow raster

imaging as the focal spot is required to scan across the sample to build up the final image pixel by pixel. Therefore, acquiring full 3-D data sets can be very time-consuming and may not be practical for larger samples (e.g. whole embryos).

Therefore, there is an imaging gap between confocal/multiphoton LSM and MRI. The size and opacity of whole embryos (typically a few millimetres in size) make it especially challenging to achieve high resolution (a few to tens of micron) at the depth of several hundred microns to millimetres inside intact embryos. In order to visualise the 3-D structures of samples in this "mesoscopic" regime, such as small animals, embryos and engineered tissues, a variety of optical imaging techniques have been developed including optical projection tomography (OPT) [33], light sheet microscopy (e.g. selective plane illumination microscopy (SPIM) [34] and ultramicroscopy [35]) and scanning laser optical tomography (SLOT) [36]. What follows below is an outline of above methods and the various forms of their implementation.

2.7.1. Light sheet microscopy

Light sheet microscopy or imaging, which uses a sheet of laser light (e.g. by optically confining light to a single slice) with a well-defined thickness, is a form of optical sectioning imaging that allows the sample to be left intact and alive in contrast to physical sectioning. It is a fluorescence imaging technique that uses a focused light-sheet to selectively illuminate the specimen from the side at the focal plane of the imaging system. It restricts the excitation to the plane of interest and consequently, fluorescence is excited only in the desired plane.

This light-sheet idea has been widely adapted in orthogonal-plane fluorescence optical sectioning (OPFOS) for fluorescently stained samples [37], in 3-D light scanning macrography for surface scanning of flies [38] and in thin light-sheet microscopy for aquatic microbes [39]. For modern biology, the idea has been widely adapted in SPIM [34, 40-42], Ultramicroscopy [35, 43-45], digital scanned laser light-sheet fluorescence microscopy (DSLM) [46], objective coupled planar illumination microscopy [47], multidirectional SPIM [48-50], highly inclined and laminated optical sheet (HILO) microscopy [51] and oblique plane microscopy (OPM) [52]).

2.7.1.1. Concept and components

The concept behind fluorescence light sheet microscopy techniques is to selectively illuminate the specimen from the side in a well-defined volume around the focal plane of the detection path. In light sheet microscopy, illumination and detection are performed through two distinct optical paths. The illumination axis is arranged orthogonal to the detection axis. Although there are different implementations of this idea (e.g. SPIM, HILO, OPM), the general principles remain the same and illustrated in Fig. 2.13. The most common implementation is to generate a sheet of laser light that selectively illuminates the sample in the focal plane of the detection optics from one side.

Generally, a light sheet microscopy consists of five basic units including (1) illumination (generation of an appropriate light sheet), (2) excitation (laser), (3) detection, (4) movement (translation and rotation) and (5) control (acquisition and processing) [53].

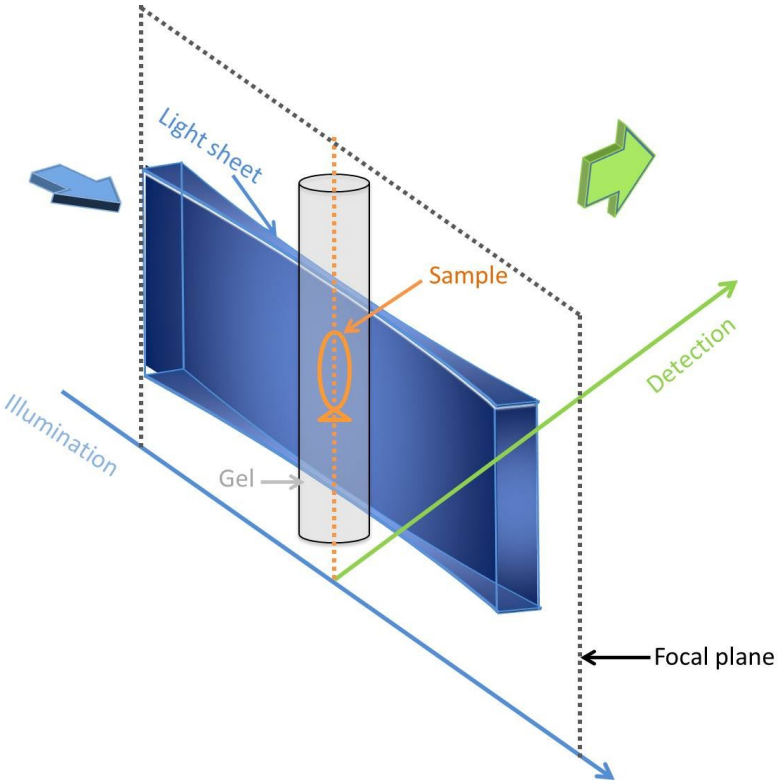


Figure 2.13: The concept behind fluorescence light sheet microscopy. In light sheet microscopy, illumination and detection are performed through two distinct optical paths. The illumination axis is arranged orthogonal to the detection axis. The most common implementation is to generate a sheet of laser light that selectively illuminates the sample in the focal plane of the detection optics from one side. (This figure is adapted from [41].)

Generating a light sheet

It is of crucial importance for the performance of the microscope to generate an appropriate light sheet. The properties of the light sheet are valued from the thickness, uniformity and its ability to penetrate tissue. In SPIM, diffraction limits the dimensions of the light sheet and the achievable thickness depends on the field of view (FOV) it illuminates and is discussed in detail in section 2.8. Theoretically, the lateral resolution is equivalent to that in a wide-field microscope, which is given by the NA of the objective lens and the wavelength of the fluorescence. The axial resolution is determined by the light sheet thickness in the case of the low NA detection system. It is noted that SPIM is the wide-field version of confocal theta microscopy as the focal plane of the detection optics is illuminated from the side.

There are different ways to generate light sheets, as illustrated in Fig. 2.14. In SPIM, the combination of cylindrical optics and the objective lens are used to generate a sheet of light of varying thickness. This light sheet is a static light sheet produced by collimating a beam in one dimension and focusing it in another dimension. The waist of the light sheet is positioned in the centre of the FOV. Alternatively, the sheet of light can be formed by focusing a laser beam to a single line and then rapidly scanning it vertically. This concept was introduced in DSLM by using a Gaussian laser beam [46]. It is noted that both light sheets in SPIM and DSLM suffer from a varying thickness due to the nature of Gaussian beam propagating. To obtain a more uniform light sheet, a Bessel beam, with a feature of thin and long focus, was introduced to scan vertically [54]. Although the core of Bessel beam is thin and long, the central maximum is surrounded by a series of rings. This would result a relatively thick light sheet. In order to further achieve a very thin and uniform light sheet, two-photon Bessel beam illumination was introduced and the excitation only occurs in the centre of the beam where the intensity is sufficiently high. By scanning this beam vertically, a very thin light sheet (< 1 μm) was generated for small FOV such as for 3-D subcellular imaging [55]. In addition, the penetration depth of light is expected to be increased due to the Bessel beam's persistent propagation properties.

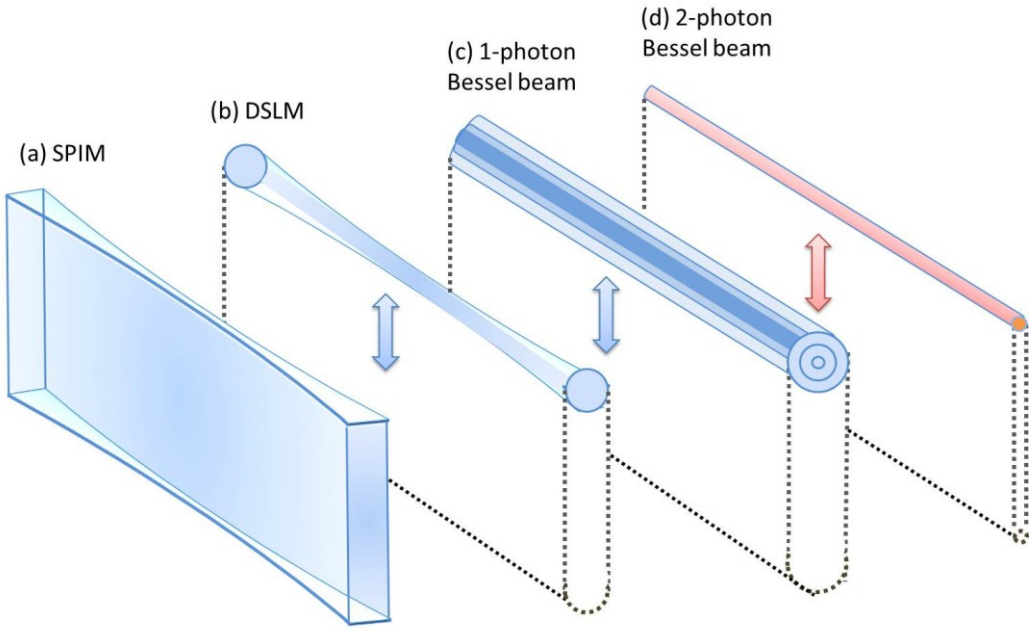


Figure 2.14: Illustration of different light sheets. (a) In SPIM, a static light sheet is formed by spreading a laser beam in the vertical dimension with dedicated optics. (b) In DSLM, a virtual light sheet is generated by rapidly scanning vertically a Gaussian laser beam. Both of them are with varying thickness due to the nature of Gaussian beam. (c) A Bessel beam can be scanned to obtain more uniform light sheet. Although the core of Bessel beam is thin and long, it is surrounded by a series of rings. (d) Two-photon Bessel beam can be employed and the excitation only occurs in the centre of the beam to further get a thin and uniform light sheet.(This figure is adapted from [41].)

Excitation, detection, movement and control

In light sheet microscopy, illumination and detection are performed through two distinct and orthogonal optical paths. Practical realisations are diverse and adapted to the sample of interest (e.g. size, magnification, immersion medium) [40, 41]. Typically, the volumes imaged with light sheet microscopy are appropriate for millimetre-sized samples with low NA objectives and for smaller-sized samples (e.g. single cells), and volumes similar to those that can be achieved by confocal LSM techniques with medium-to-high NA objectives.

The excitation and the detection unit in light sheet microscopy are similar to that of a wide-field fluorescence microscopy. The excitation unit provides collimated laser beams from several laser lines (e.g. at 488, 514, 543, 633 nm) or from super-continuum sources. The detection unit consists of an objective lens, a tube lens, an emission filter and a detector (e.g. a CCD).

The 3-D image stacks can be acquired by quickly moving the specimen over the desired axis (i.e. along the optical axis of the detection system) when the optical arrangement is fixed. Alternatively, when the specimen is fixed, the image stacks can be acquired by simultaneously moving the light sheet and the focal plane. Sample rotation can be implemented to determine the optimal view angle [42]. It also allows the acquisition of image stacks along different directions, which can be used to obtain sequential multi-view acquisitions [56, 57].

In the initial and most common SPIM setup, one-sided illumination/one-sided detection is employed, as shown in Fig. 2.15 (a). However, this illumination light entering the sample from one side can be attenuated as it penetrates the sample, which results in a loss in excitation and the corresponding fluorescence on the far side. In addition, although scattering within the plane of illumination does not affect the light sheet quality, the scattering along the axis of detection will lead to a spread of the light sheet and therefore a loss in optical sectioning and axial resolution.

To compensate for the attenuation, two-sided illumination/one-sided detection can be employed, as shown in Fig. 2.15 (b), in which the light illuminates the sample from opposing sides [35, 48], thereby increasing the overall penetration of the illumination light. Sequential multiview imaging can also be employed, in which the sample is rotated and image stacks are sequentially acquired from different view angles (typically 4-12), as shown in Fig. 2.15 (c), to increase the overall penetration depth of the light [56, 57]. Subsequently, the individual image stacks are registered and fused, achieving a single dataset with high-resolution information inherited from individual image stacks [58, 59]. Although it increases the image quality, this sequential multiview imaging is inherently slow and thus less attractive to capture fast processes in live specimens. It may result in spatiotemporal artefacts that constrain quantitative analysis (e.g. the reconstruction of cell tracks). These artefacts could be eliminated by simultaneous multiview imaging for light sheet microscopy [49, 50], in which two illumination and two detection objective lenses that are focused on the sample from four different directions are employed [60], as shown in Fig. 2.15 (d). The detection objective lenses are focused on the common focal plane and this plane is in turn illuminated by the two opposing light sheets.

The two-sided illumination and two-sided detection form four individual imaging braches. These four image stacks are sufficient to yield to a 3-D all-around view of a specimen without rotation. This allows *in toto* fluorescence imaging of specimens with subcellular resolution at a high imaging speed (e.g. allow faithful tracking of nuclei and cell shape change) [49, 50].

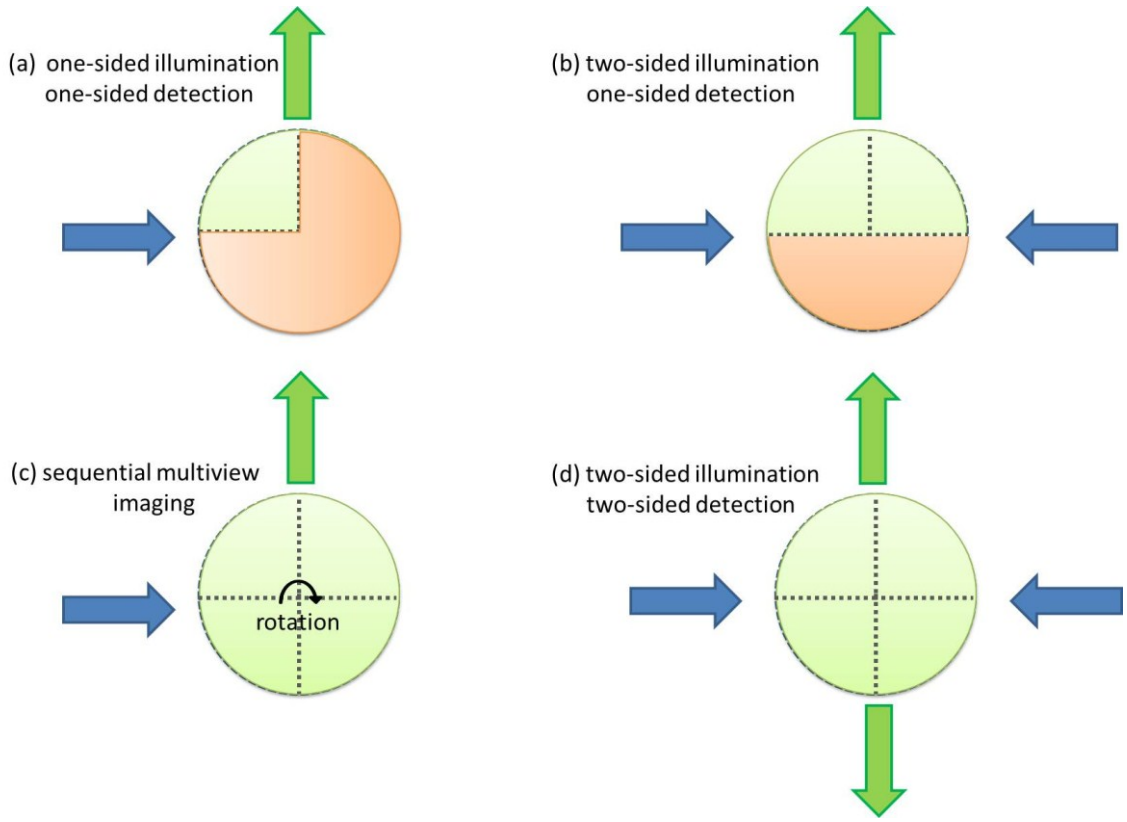


Figure 2.15: Illustration of different illumination and detection techniques. (a) one-sided illumination/one-sided detection, (b) two-sided illumination/one-sided detection; (c) sequential multiview imaging and (d) two-sided illumination/two-sided detection.

In HILO microscopy, a single lens is used for oblique light-sheet illumination and detection. The incident laser beam is highly inclined by a large refraction and is laminated as a thin optical sheet at the specimen side, which results in a narrow FOV [51]. OPM is similar to HILO technique but with extended FOV by employing extensive optics [52].

2.7.1.2. Light sheet microscopy's applications

Light sheet microscopy is suited for a number of applications, from fixed to live imaging. The ability to image an entire embryo in 3-D at high speeds is of importance for developmental studies in which cells are tracked over hours along paths across the whole embryo.

Light sheet microscopes can be built up and adapted to a wide range of sample sizes, from single cells to whole embryos (e.g. zebrafish [42, 48, 61], medaka [34], *Drosophila* [49, 50, 62]). The imaging of 3-D cell

cultures primarily benefit from low photobleaching [63]. The imaging of complex organisms and live samples primarily benefit from optical sectioning.

2.7.2. Optical projection tomography (OPT)

OPT [33, 64, 65], also known as optical computed tomography (CT) [66], is another exciting optical technique for imaging mesoscopic samples at a high resolution in 3-D. 'Tomography' (except optical coherence tomography) covers forms of imaging that involves solving an inverse problem – finding the cross-sectional structure of an object from the observations when illuminating the object from many different angles. Fundamentally, tomographic imaging deals with reconstructing cross-sectional images from their projections. Mathematical transformations or computer models must be used to recover the 3-D structure of the specimen from the observed external measurements that are based on the interaction of the specimen and the illumination (e.g. X-rays, visible light, ultrasound, and magnetic resonance). This is in contrast to techniques that directly read out the internal structure, such as confocal LSM and light sheet microscopy (by optical sectioning).

The idea of optical CT was introduced in 1996 to obtain 3-D dose distributions based around a laser scanning system coupled to a photodiode detector [66]. A wide-field version was also developed by incorporating a light source coupled to a CCD [67]. Since then, both versions have been developed [68-75]. For modern biology, Sharpe *et al.* developed a microscopy technique that used OPT to produce high-resolution 3-D images of both fluorescent and non-fluorescent biological specimens in 2002 [33]. This technique combined chemical clearing, fluorescence imaging and projection tomography.

Compared to optical sectioning techniques, OPT uses a very different approach. OPT maximizes the depth of field (DOF) of the imaging system rather than minimising the DOF to obtain (i.e. for confocal LSM, light sheet microscopy) a precise focal plane within the sample. This results in an image with an "in focus" view through the whole specimen and as a consequence, the raw data do not explicitly contain depth information. Instead, OPT relies on acquiring images of the sample from many different projection angles, and then using computer models or mathematics transformations to calculate the cross-sectional images. What follows in this sub-section is the brief introduction of the concept of OPT and the most common form of its implementation, a number of developments and various applications.

2.7.2.1. Concept and configuration

OPT is the optical analogue of X-ray CT, in which the 3-D structure (i.e. a stack of X-Y slices) of a rotating sample is reconstructed from a series of wide-field 2-D projections (i.e. X-Z images). For tomographic reconstruction, a standard filtered backprojection (FBP) algorithm is typically employed [76], which is based on the parallel-beam projection assumption. This standard FBP algorithm will be discussed in detail in section 2.9.

A key advantage of OPT compared to X-ray CT for imaging biological tissue is the use of optical radiation with its rich spectroscopic contrast, including absorption and fluorescence (i.e. fluorescence intensity and

fluorescence lifetime [77, 78]). This 3-D global visualisation in both transmission and fluorescence modes features an advantage for localising the structures of interest in the whole specimen (e.g. elucidating the anatomical and molecular complexity of organogenesis [79]). Unfortunately, compared to X-rays, the longer wavelength of optical radiation also leads to stronger optical diffraction and scattering, both of which compromise the assumption of parallel-beam projection in the standard FBP algorithm. In OPT, the optical projection images are acquired such that they approximate parallel beam projections through the sample at different projection angles. This is achieved by accommodating the constraints imposed by diffraction-limited imaging and addressing the issues of scattering.

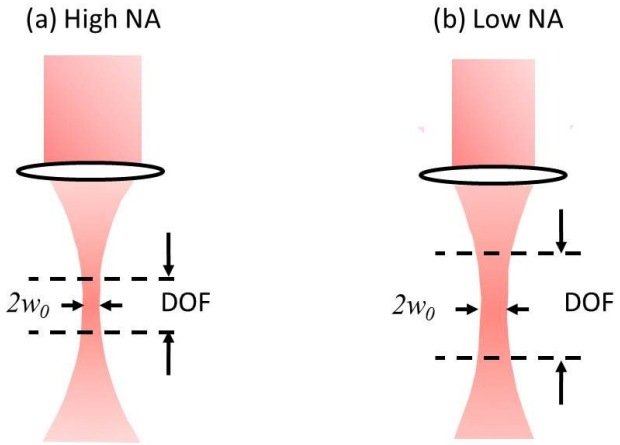


Figure 2.16: Illustration of the trade-off in OPT between achievable lateral resolution and sample size as the resolution improves proportionally with the NA while the DOF scales inversely with the square of the NA of the imaging lens.

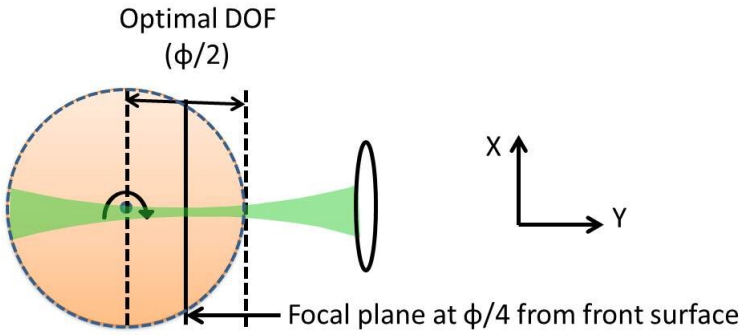


Figure 2.17: Schematic of the most common and convenient OPT setup on how to mitigate the trade-off between sample size and achievable resolution. This illustration is on a cross-sectional plane (X-Y plane). DOF – depth of field, ϕ : sample diameter.

The constraints imposed by diffraction-limited imaging result in a trade-off in OPT between achievable lateral resolution and sample size as the resolution improves proportionally with the NA (in the case of the

pixels of the imaging detectors sampling the image sufficiently) while the DOF scales inversely with the square of the NA of the imaging lens, as illustrated in Fig. 2.16. This resolution-size trade-off will be discussed in detail in section 2.8.

In order to accommodate the constraints, OPT is generally configured such that the volume to be imaged is confined within the DOF of the imaging system, thereby approximating parallel-beam projection. The most common and convenient scheme for OPT to mitigate the trade-off is to arrange the DOF to extend through half of the sample by locating the focal plane a quarter of the way into the sample rather than at the axis of rotation, as shown in Fig. 2.17. This results in the front half of the sample being imaged under the parallel-beam projection approximation, which interrogates the entire sample during the course of a full rotation (i.e. 360°). In this configuration, two opposite images are actually focused on different regions of the specimen. Consequently, an image from one direction is not an exact mirror image of a view from the opposite direction and thus, does not contain the same information. Therefore, it is necessary to acquire angular projections over a full rotation, i.e. 360°, to achieve a high-quality reconstruction.

In order to avoid the issue of scattering, it is necessary to apply OPT to optically transparent samples that either have been rendered transparent by chemical clearing or that are inherently transparent. Scattering occurs at refractive index mismatches in a sample. For less transparent and larger organisms, chemical clearing is required, transforming intact tissue into an optically transparent construct. The original and most common method in OPT is replacing water in the sample with a high refractive index solvent (i.e. 1:2 mixture of benzyl alcohol and benzyl benzoate (BABB) with refractive index of 1.56) and thus, reducing light scattering [33]. In this case, chemical clearing is indeed refractive index matching. It does not involve any chemical action between the chemical solvent and the sample. There are a number of high refractive index solvents (e.g. BABB, dibenzyl ether (index of 1.56), methyl salicylate (index of 1.52), etc.) that can be used for chemical clearing. However, these optical clearing agents quench fluorescent protein emission since these proteins require water molecules to fluorescence. Therefore, they are typically used for optical clearing after antibody staining. Recently, a water-based optical clearing agent, SeeDB, was reported without quenching many types of fluorescent dyes, including fluorescent proteins and lipophilic neuronal tracers [80]. Alternatively, a technology termed as CLARITY was reported for the transformation of intact tissue into a nanoporous hydrogel-hybridisation form that is fully assembled but optically transparent and macromolecule-permeable [81]. The optical clearing in this process is achieved by removing lipids non-destructively. The main drawback for chemical clearing is the fact that it is inherently fatal to live organisms and therefore precludes the possibility of *in vivo* imaging.

As there is an increasing demand in translating studies of biological processes at the cellular level from monolayer cell cultures to live organisms, it is interesting to apply OPT to small live organisms that are inherently transparent – particularly those that can be genetically manipulated to serve as disease models (e.g. zebrafish). However, as small organisms grow, they typically become more opaque and consequently,

the scattering leads to a reduction in image quality. Most *in vivo* optical imaging experiments on zebrafish have been confined to embryos up to 3 days post-fertilisation (dpf), which retain high transparency.

A basic configuration for OPT is illustrated in Fig. 2.18. The specimen is suspended in a refractive index matched medium to reduce the scattering. This results in light propagating through the specimen in approximately straight lines. The specimen is maintained within the medium, rotated to a series of angular positions (typically ≥ 360 steps) and a projection image is captured at each angle. Both transmission and absorption projection data can be collected via an optical system and recorded by an imaging detector (e.g. a CCD).

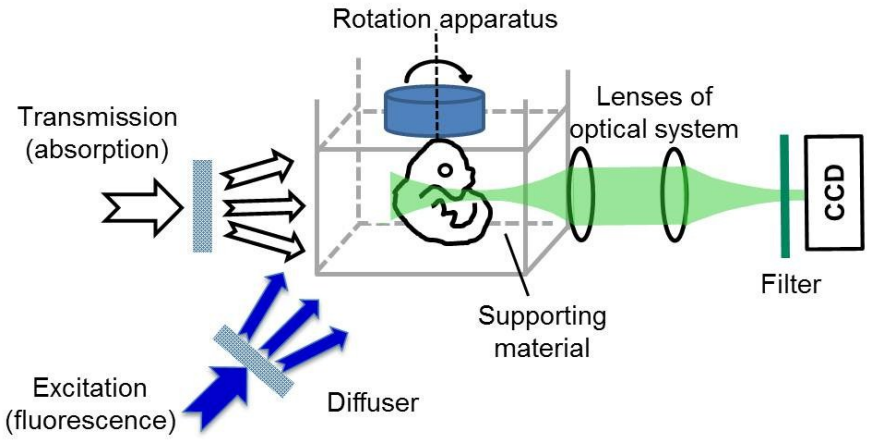


Figure 2.18: Diagram of OPT. The specimen is supported in a refractive index matched medium (e.g. BABB, an agarose gel, water) and is rotated to a series of angular positions. Both transmission and absorption light can be collected by an optical system and recorded by an imaging detector (e.g. a CCD).

After a series of 2-D projections (X-Z images) are acquired at different angles, the standard FBP algorithm is typically used for tomographic reconstruction [76], although iterative reconstruction techniques have also been developed [82] (especially in the case of a reduced number of projections). Figure 2.19 (a) shows an example raw projection at one orientation (2-D wide-field fluorescence image of a mouse embryo). For a particular cross-sectional plane (i.e. X-Y plane) of the sample, as indicated by the dotted line in Fig. 2.19 (a), this makes up the sinogram (X-θ image) for this plane, as shown in Fig. 2.19 (b). From the sinogram, the signal function (e.g. fluorescence intensity) in this cross-sectional plane can be recovered by employing the standard FBP algorithm, which includes two parts: the filtering part, which is a simple weighting of each projection in frequency space, and the backprojection part, which finds the elemental reconstructions by adding together the inverse Fourier transform of each weighted projection at the corresponding projection angle. Figure 2.19 (c) and (d) show the "filtered" sinogram (after employing a ramp filter in frequency domain) and the corresponding reconstructed cross-sectional image respectively from the raw data shown in Fig. 2.19 (b).

It is also noted that the wavelength used for OPT is of importance in achieving a high quality image. As specimens become more opaque or more absorbing, short visible wavelengths penetrate less, leading to a reduced contribution from deeper structures. Shifting the wavelength up to infrared can suppress autofluorescence and improve the image quality.

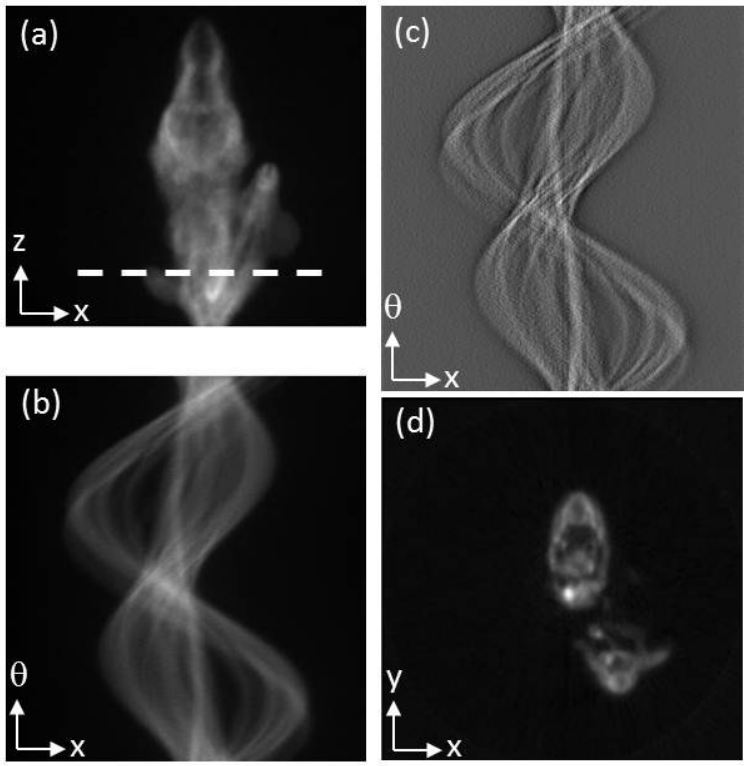


Figure 2.19: (a) An OPT raw projection image (2-D wide-field fluorescence image of a mouse embryo) at one orientation. (b) The sinogram for a particular X-Y plane (while line illustrating in (a)). (c) The corresponding "filtered" sinogram (after employing a ramp filter in the frequency domain). (d) The corresponding reconstructed cross-sectional image.

To visualise the 3-D reconstructed data sets from OPT, the same visualisation techniques used in similar imaging technique such as MRI can be employed. In this thesis, the commercial 3-D visualisation software Volocity (PerkinElmer) is used. Virtual sections can be viewed at any orientation and the specimen can also be rendered as a 3-D object.

2.7.2.2. OPT's developments

Two fundamental limits that restrict the application of OPT are imaging speed and achievable resolution. The potential to apply OPT to "mesoscopic" samples for biomedical research, particularly for *in vivo* imaging, has prompted increasing interest in optimizing the image quality and resolution and minimizing the image data acquisition time.

Image quality can be degraded by artefacts resulting from system misalignment, system aberrations, intensity-based signal variations and tissue absorption properties. Methods have been described to correct or suppress such artefacts [83-86]. For *in vivo* imaging, the artefacts may result from the specimen movement and a set of mathematical methods have been developed for motion correction [87, 88].

Image quality can also be degraded by the deviations from the parallel-beam projection assumption that underlies the standard FBP algorithm. These deviations arise when OPT is implemented with relatively high NA optics, for which rays at a range of angles with respect to the optical axis are collected. For high resolution OPT, there is a trade-off between increasing the NA to improve the in-focus lateral resolution and reducing the NA to increase the DOF in order to ensure that the whole sample is in reasonable focus (i.e. that the lateral resolution does not vary significantly along the optical axis). A typical situation for many biomedical applications, especially for larger samples, is the DOF of the imaging system being less than the sample radius. In this case, OPT is undertaken with samples that extend beyond the confocal parameter (Rayleigh range) of the imaging lens and so the reconstructed resolution becomes increasingly anisotropic away from the axis of rotation. Building on ideas developed for single-photon emission computed tomography [89], this distance-dependent resolution has been accounted for by applying an appropriate deconvolution filter to the raw projection data based on a computationally generated PSF [90]. The key effect is to correct for the frequency modulation applied to the signal by the optical system and therefore to improve the achieved spatial resolution. The OPT reconstruction can also be modified in other ways to take into account the optical characteristic of the imaging system [91], which will be discussed in detail in Chapter 3.

One way to address the resolution-size trade-off issue is to extend the DOF for a given NA by axially scanning the focal plane through the sample [92, 93] and thus introducing the "pseudoprojection" idea. In other words, to translate the sample with respect to the focal plane such that different portions of the sample are sequentially imaged "in focus". This also helps to achieve uniform collection efficiency throughout a sample that is larger than the DOF of the imaging system and to realise higher spatial resolution imaging over larger volumes. Although the simplest OPT configuration does not provide subcellular resolution, this scanning focal plane method provided a significant spatial resolution improvement for OPT of smaller samples (with the resolution of 0.38 μm for a sample with the size of 50 μm) [93]. For larger specimens, the trade-off can be mitigated by introducing an angular multiplexing technique in OPT [94], which will be discussed in detail in Chapter 4.

As an optical imaging technique, OPT is fundamentally limited by light scattering. To address the effect of light scattering, experimental methods have been described such as introducing time-gated imaging techniques [95, 96] and polarization selection techniques [97] in OPT to select ballistic photons. In addition, alternative algorithms to obtain relatively good-quality reconstructions for more scattering specimens have been developed [97, 98]. These developments make OPT particularly attractive in relatively large and more scattering specimens.

Due to the nature of "seeing the whole sample in every view", OPT potentially provides information with much higher time-lapse resolution and lower light dose on the sample by tracking the movement of features during an acquisition. For example, an OPT setup is able to provide the information to track the movement of features (e.g. neutrophil migration) by acquiring just pairs of orthogonal images and then calculating the 3-D coordinates of the moving features. This extension will be discussed in detail in Chapter 5. This is in contrast to optical sectioning imaging techniques which require scanning over the whole sample to obtain the full information at each time point.

OPT can be extended to FLIM-OPT by incorporating wide-field FLIM instrumentation. Our group (McGinty *et al.*) described a FLIM-OPT system and demonstrated the application of this technique to a fixed and optically cleared mouse embryo [77]. FLIM-OPT is based on the wide-field acquisition of a series of time-gated fluorescence intensity images at different time delay positions with respect to the excitation pulses at each angle of projection. From these raw projections, a number of time-resolved 3-D intensity volumes can be reconstructed and followed by fitting of the fluorescence decay in each voxel to produce a 3-D reconstruction of the fluorescence lifetime distribution. This technique makes the final results insensitive to intensity variations due to the ratiometric nature of FLIM. In the original experiment, FLIM was able to distinguish between the labelled fluorescence (i.e. Alexa-488-labelled neurofilament) and the autofluorescence from the heart and dorsal aorta of a mouse embryo. The application of FLIM-OPT to live animal models will be discussed in detail in Chapter 6. The further development by using FLIM-OPT to localise protein-protein interactions via FRET will also be discussed.

2.7.2.3. OPT's applications

OPT can be applied to reconstruct the absorption and/or fluorescence distributions in optically transparent specimens and can be applied to a wide range of sample sizes from sub-mm to cm scales. It was originally used on a fixed mouse embryo after chemical clearing [33]. Since then, due to its relatively simple optical configuration, the high resolution, fluorescence/absorption modes in the mesoscopic regime, it has a number of applications on fixed specimens (e.g. human tissue, chick limb, mouse pancreas) which have been rendered transparent by chemical clearing [99-105]. It has also been extended into the field of live imaging on relatively transparent samples (e.g. *C. elegans*, *D. melanogaster*, *Danio rerio*) [78, 85, 87, 88, 91, 97, 106-108]. Practical realisations of OPT can be diverse and can be adapted to a wide range of sample sizes, from group of cells to whole embryos.

Because OPT can obtain both absorption and fluorescence profiles, it is able to utilise a wealth of different staining techniques for gene-expression analysis [65]. This gene-expression study primarily benefits from the ability of OPT to provide an overview of expression patterns for a number of specimens relatively rapidly. OPT has important applications for morphology and histopathology-based research as a convenient non-invasive 3-D imaging technique, especially in the growing field of mouse models of disease. For example, OPT allows accurate localisation and measurement of beta cell mass, which is a prerequisite for interpretation of biomedical results for diabetes research (e.g. Type 2 diabetes disease). Another significant

application of OPT is to help study disease mechanisms and potential therapies in live organisms due to its ability to do time-lapse imaging of entire transparent animal models (e.g. zebrafish embryo, juvenile transgenic zebrafish which can maintain transparency) in 3-D and its potential to be extended to FLIM-OPT [77, 78, 109]. This FLIM-OPT extension measures 3-D lifetime information and can be utilised to provide functional information for the investigation of 3-D biological processes *in vivo*. These applications will be discussed in detail in Chapter 6.

2.7.2.4. Comparison with light sheet microscopy

Fluorescence light sheet microscopy features the advantages of relatively higher acquisition speed over OPT. However, this technique is limited to fluorescence imaging and typically requires a different and relatively complicated optical configuration compared to that of a standard microscope. It also requires a critical optical alignment. In contrast, OPT can provide the reconstructed absorption and/or fluorescence distributions in specimens. For the configuration, OPT can be implemented on a standard wide-field microscope with just minor modifications and the corresponding optical alignment is much less critical.

With regard to the achievable resolution, for a given sample size, although light sheet microscopy could provide higher lateral resolution (due to the high NA imaging lens), it has anisotropic resolution, which could potentially make the analysis of 3-D images difficult, while OPT has isotropic spatial resolution due to its rotational scanning. A detailed numerical analysis of the "standard" spatial resolution of OPT and SPIM by following a number of formulae describing the different behaviour of the most common form for those two techniques will be discussed in section 2.8.

Both light sheet microscopy and OPT can be practically realised in diverse versions and adapted to samples of interest (size, magnification, immersion medium). As optical imaging techniques, both of them are fundamentally limited by light scattering. However, OPT has the potential to more readily adapt to scattering specimens using a similar experimental imaging configuration and incorporating more complex reconstruction algorithms. In the limit OPT tends to diffuse tomography.

2.7.3. Scanning laser optical tomography (SLOT)

Scanning laser optical tomography (SLOT) [36] is a line scanning version of OPT. As discussed before, in OPT the NA is typically reduced to increase the DOF in order to ensure that the whole sample is in reasonable focus during the acquisition. The reduction of NA, especially when imaging larger specimens (e.g. mouse tissues with the size of a few centimetres), not only affects the resolution but also causes the system to be accompanied by a significant decrease of light collection efficiency. To address this efficiency issue, a laser scanner is introduced in OPT and this version is referred as SLOT. Figure 2.20 shows the schematic setup of a SLOT (adapted from [36]).

The scanning position of the focal spot determines the source of fluorescence emission and this allows the fluorescence photons to be collected via simple high NA optics onto a point detector (e.g. single element photon multiplying tube) rather than a camera. Fluorescence light is collected by a lens system consisting of

two plano-convex lenses, which redirects the light to the detector. One projection image is then formed by scanning the focal point across the sample and integrating the detector at each point. This scanning process results a significant increase in the light collection efficiency. However, it also results a long acquisition time. This makes SLOT more suitable for relatively large optically cleared samples [36, 110] which are sensitive to photobleaching or phototoxicity.

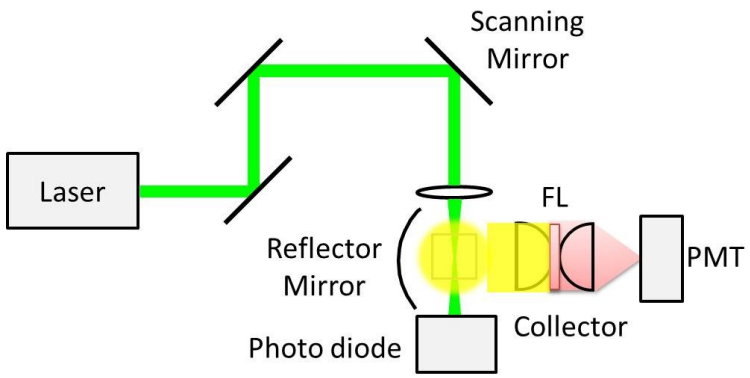


Figure 2.20: The schematic setup of SLOT. A photo diode is used to capture transmitted light. FL – fluorescence filter. PMT – photon multiplying tube. (This figure is adapted from [36].)

2.8. Numerical analysis of spatial resolution in OPT and SPIM

The last section briefly outlined the 3-D imaging techniques commonly used in mesoscopic biomedical research, especially highlighting OPT and SPIM (a common form of light sheet microscopy) and their advantages, disadvantages, applications and limitations. Although these discussions illustrated the differences between them (e.g. configuration, spatial resolution, efficiency), they did not adequately quantify the strength of the rotational scanning (for OPT) or discuss properly the differences between the image formation properties of OPT and SPIM instruments. In this section, a number of formulae describing the different behaviour of the most common form of these two instruments will be presented and a numerical analysis of the "standard" spatial resolution of these systems will then be discussed.

Consider a sample with a volume of X^3. The resolution of an optical system is the necessary minimum separation between two objects such that their corresponding images can still be resolved via the optical system. According to the Rayleigh criterion, this separation is limited by the 2-D PSF at best focus of the optical system, which is the Airy diffraction pattern (for circular exit pupils). The radius of the disk, r_{Airy}, is defined as the radius to the first dark ring, given by,

$$r_{Airy} = \frac{0.61\lambda}{NA} \qquad 2\text{-}20$$

where λ is the wavelength of light, *NA* the numerical aperture of the imaging system. It is noted that the 2-D PSF is just the cross section of the 3-D PSF of the optical system and varies as a function of distance between the object and the focal plane. Consequently, Eq. 2-20 applies only at the focal plane (best focus) of the optical system. The resolution here is indeed lateral resolution in the plane perpendicular to the optical axis.

DOF is a charateristic of the axial focussing properties of an optical system. It is measured parallel to the opical axis. Objects which are located within the DOF of the optical system are considered to be in reasonable focus (i.e. the lateral resolution does not vary significantly along the optical axis). In practice, the range of pixel number and density for image sensors is limited (i.e. not significantly beyond the sampling limit of the PSF) and the DOF does not just depend on the NA and imaging wavelength but is related by [90]

$$DOF = n_{bath}\left(\frac{\lambda}{NA^2} + \frac{e}{M_a \cdot NA}\right) \qquad 2\text{-}21$$

where n_{bath} is the refractive index of the medium in which the specimen is immersed, λ the wavelength of light, e the pixel size of the imaging detector and M_a the lateral magnification of the imaging system.

According to the Nyquist criterion of sampling frequency, the Airy disk must be sampled with a detector spacing less than half of the radius. This is required so that the image is diffraction limited (not pixel limited). This requires that the pixel size satisfies

$$\frac{e}{M_a} \le \frac{r_{Airy}}{2} \qquad 2\text{-}22$$

and making the substitutions into Eq 2-21, the maximum possible DOF is given

$$DOF_{\max} = n_{bath} \cdot \left(\frac{\lambda}{NA^2} + \frac{r_{Airy}}{2NA}\right) = n_{bath} \cdot \frac{\lambda}{NA^2}\left(1 + 0.305\right) \qquad 2\text{-}23$$

Therefore,

$$DOF_{\max} = 1.305 n_{bath} \frac{\lambda}{NA^2} \qquad 2\text{-}24$$

Equations 2-20 and 2-24 indicate the conventional trade-off between increasing the NA to improve the in-focus lateral resolution and reducing the NA to increase the DOF. In a typical OPT system, in which the trade-off is actually mitigated by arranging for the DOF of the imaging system to extend through half of the sample by locating the focal plane a quarter of the way into the sample rather than focusing at the axis of rotation. This relationship is described by

$$DOF \ge 0.5X \qquad 2\text{-}25$$

As a result, the relationship between a given sample size and image resolution (considering OPT has isotropic resolution due to its rotational scanning) including lateral (R_L) and axial (R_Z) resolution in OPT is expressed by

$$NA \le \sqrt{\frac{2.61 n_{bath} \cdot \lambda}{X}} \qquad 2\text{-}26$$

$$R_L = R_Z = 0.61\frac{\lambda}{NA} \ge 0.61\lambda\sqrt{\frac{X}{2.61 n_{bath} \cdot \lambda}} = \sqrt{\frac{0.143\lambda \cdot X}{n_{bath}}} \qquad 2\text{-}27$$

For light sheet microscopy, it is preferable to have the light sheet as thin as possible and uniform across the field of view. However, how thin the illuminated volume can be is limited by diffraction. In a "standard" SPIM system, cylindrical optics are used to generate a sheet of varying thickness. The light converges towards the sample and diverges away from it. Considering a Gaussian beam used in SPIM, shown in Fig. 2.21,

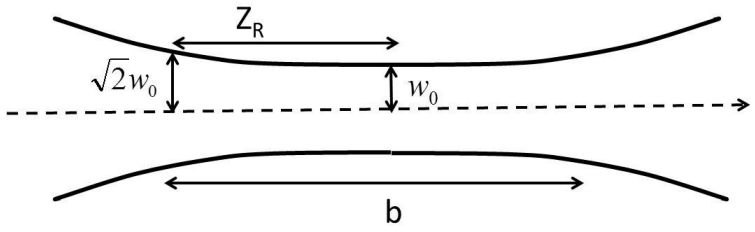


Figure 2.21: Gaussian beam width as a function of the axial distance z. ω_0: beam waist; b: depth of focus; Z_R: Rayleigh range.

The relationships between Rayleigh range (Z_R), depth of focus (b) and beam waist (ω_0) are given respectively by

$$Z_R = \frac{\pi\omega_0^2}{\lambda} \qquad 2\text{-}28$$

$$b = 2Z_R = 2\frac{\pi\omega_0^2}{\lambda} \qquad 2\text{-}29$$

The waist of the light sheet is located in the centre of the FOV. In "standard" SPIM, the sample needs to be located within the depth of focus b to ensure the light sheet is reasonably uniform across the whole sample, which indicates $b \ge X$, then

$$X \le \frac{2\pi\omega_0^2}{\lambda} \qquad 2\text{-}30$$

In order to obtain an image with no out-of-focus blur, the DOF of the detection objective should be at least the thickness of the light sheet,

$$DOF \ge 2\omega_0 \qquad 2\text{-}31$$

As a result, the relationships between a given sample size and image resolution for SPIM are described by

$$NA \le \sqrt[4]{\frac{2\pi \times 1.305^2 n_{bath}^2 \cdot \lambda}{4X}} = \sqrt[4]{\frac{2.6751 n_{bath}^2 \cdot \lambda}{X}} \qquad 2\text{-}32$$

$$R_L = 0.61\frac{\lambda}{NA} \ge 0.61\lambda \Big/ \sqrt[4]{\frac{2.6751 n_{bath}^2 \cdot \lambda}{X}} = \sqrt[4]{\frac{0.052\lambda^3 \cdot X}{n_{bath}^2}} \qquad 2\text{-}33$$

$$R_Z = 2\omega_0 \ge 2\sqrt{\frac{\lambda \cdot X}{2\pi}} = \sqrt{\frac{2\lambda \cdot X}{\pi}} \qquad 2\text{-}34$$

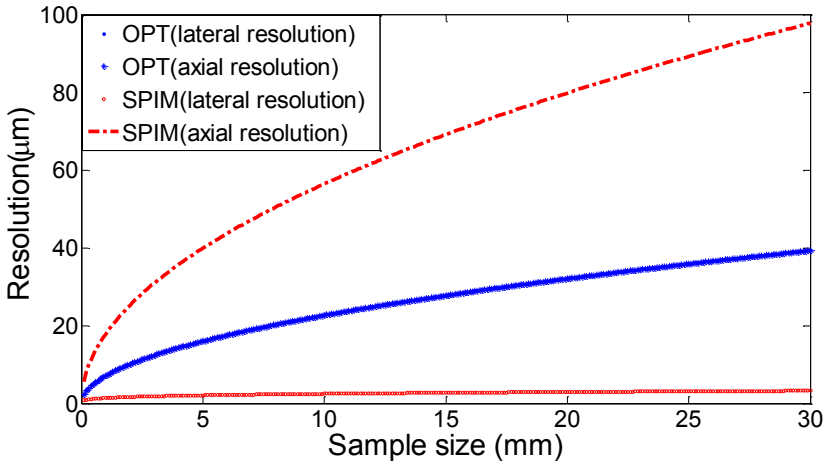


Figure 2.22: Theoretical lateral and axial (sectioned) resolution of SPIM and OPT for samples on the scale of 1-30 mm. The lateral and the axial resolution of SPIM are shown as the red circles and the red dotted lines and the lateral and the axial resolution of OPT shown as the blue dots. Indeed, OPT has isotropic resolution and thus, the blue dots are the same and cannot be distinguished in this figure. (λ -500 nm, n_{bath} - 1.3)

Figure 2.22 shows the optimal lateral and the sectioned (axial) resolution of SPIM and OPT when imaging samples on 1 mm - 3 cm scale with the lateral and the axial resolution of SPIM as the red circles and the red dotted lines respectively and the lateral and the axial resolution of OPT as the blue dots. Indeed, OPT has isotropic resolution and as a result the blue dots are the same and cannot be distinguished in this figure.

Although for a given sample size, the best lateral resolution of SPIM is higher than that of OPT, the sectioned resolution of SPIM is lower than the axial resolution of OPT. This also indicates that SPIM has an anisotropic resolution, which becomes worse as the given sample size increases. In practice, to achieve a more isotropic resolution in a SPIM system, the NA of the detection objective is often reduced, and/or the sample can be rotated such that the depth of focus (b) only covers part of the sample.

In conclusion, this section has discussed a numerical analysis of the "standard" spatial resolution of OPT and SPIM by following a number of formulae describing the different behaviour of the most common form of these two instruments. It has shown that for a given sample size, although SPIM could provide higher lateral resolution, it has anisotropic resolution, which could potentially make the analysis of 3-D images difficult, while OPT has isotropic spatial resolution due to its rotational scanning.

2.9. Standard FBP algorithms for parallel beam projections

Ideally, projections are a set of integrated measurements of some sample property (e.g. absorption, fluorescence) along straight lines through the object and referred to as line integrals. The key to tomographic reconstruction is the Fourier Slice Theorem, which relates the 1-D Fourier transform of the projection data to the 2-D Fourier transform of the object cross section. The Fourier Slice Theorem will be derived by finding the Fourier transform of a projection taken along straight-ray lines. The reconstruction algorithm based on this straight-ray projection assumption is known as the FBP algorithm.

As the name indicates, there are two essential aspects of FBP: the filtering part, which is a simple weighting of each projection in frequency space, and the backprojection part, which finds the elemental reconstructions by adding together the inverse Fourier transform of each weighted projection at the corresponding projection angle. Generally, the complete FBP algorithm can be divided into four steps: Fourier transform of the measured projection data, multiplication by the weighting filter, inverse Fourier transform of the filtered projections and summation over the image plane (the backprojection process). The backprojection process is named as such since it can be visualised as the smearing of each filtered projections over the image plane [76]. It is noted that the specific FBP reconstruction algorithm used depends on the type of projection data measured, for example the standard FBP algorithm is used with parallel beam projection data and the weighted FBP algorithm is used with fan beam data.

The standard FBP algorithm for parallel-beam projection is derived by first considering how projections of an object are formed through line integrals, as shown in Fig. 2.23. A line integral is the integral of some property (e.g. absorption, fluorescence) of the object along the line. Taking one slice of the object, which is represented by a 2-D function $i(x,y)$, a line integral $P_\theta(r)$ ($r = x\cdot\cos\theta + y\cdot\sin\theta$) is defined as

$$P_\theta(r) = \int_{(\theta,r)line} i(x,y)ds = \int_{-\infty}^{\infty}\int_{-\infty}^{\infty} i(x,y)\delta(x\cos\theta + y\sin\theta - r)dxdy \qquad 2\text{-}35$$

The function $P_\theta(r)$ is known as the Radon transform of the function $i(x,y)$. A projection is formed by combing a set of line integrals. The simplest projection is a collection of parallel ray integrals, which is known as parallel-beam projection.

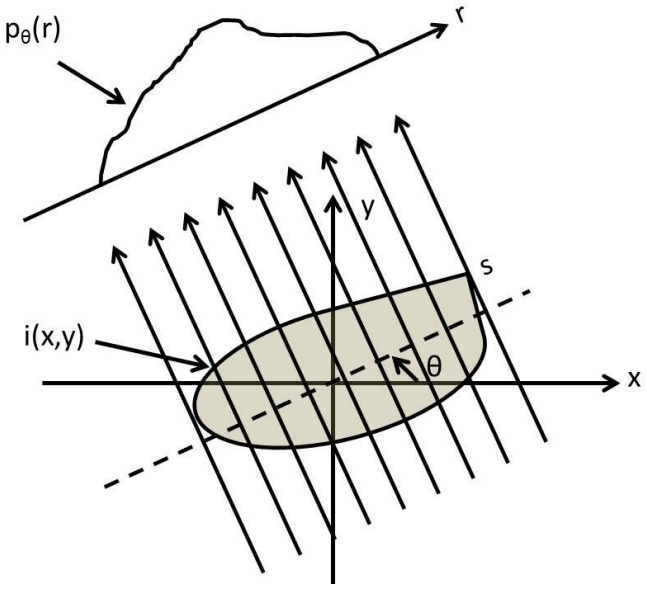


Figure 2.23: A slice of an object, i(x,y), and its parallel projection $P_\theta(r)$, which is taken by measuring a set of parallel rays, from an angle of θ.

The Fourier Slice Theorem is derived by taking the 1-D Fourier transform of a parallel projection. It is noted that this is equivalent to a radial line in the 2-D Fourier transform of the original object. The 2-D Fourier transform of the object function is defined as

$$I(k_x,k_y)=\int_{-\infty}^{\infty}\int_{-\infty}^{\infty} i(x,y)e^{-i2\pi\left(xk_x+yk_y\right)}dxdy \qquad 2\text{-}36$$

The Fourier transform of a projection $P_\theta(r)$ at an angle θ is given by

$$S_\theta(\omega)=\int_{-\infty}^{\infty} P_\theta(r)e^{-i2\pi\omega r}dr \qquad 2\text{-}37$$

The simplest example is given for a projection at θ = 0 (i.e. along the y dimension). Consider the Fourier transform of the object along the line in the frequency domain given at $k_y = 0$, then the Fourier transform is simplified to

$$I(k_x,0)=\int_{-\infty}^{\infty}\int_{-\infty}^{\infty} i(x,y)e^{-i2\pi xk_x}dxdy \qquad 2\text{-}38$$

This integral then can be split into two parts,

$$I(k_x,0)=\int_{-\infty}^{\infty}\left[\int_{-\infty}^{\infty} i(x,y)dy\right]e^{-i2\pi xk_x}dx \qquad 2\text{-}39$$

It is noted that the term in brackets can be recognised as the equation for a projection along lines of constant x. Substituting Eq. 2-35 in Eq. 2-39, then

$$I(k_x,0)=\int_{-\infty}^{\infty} P_{\theta=0}(x)e^{-i2\pi xk_x}dx \qquad 2\text{-}40$$

The right-hand side of Eq. 2-40 represents the 1-D Fourier transform of the projection $P_{\theta=0}$. This relationship is the simplest form of the Fourier Slice Theorem. It is clear that this is independent of the orientation between the object and the coordinate system.

Furthermore, considering the (r,s) coordinate system to be a rotated version of the original (x,y) system and substituting Eq. 2-35 in Eq. 2-37, then

$$S_\theta(\omega)=\int_{-\infty}^{\infty}\int_{-\infty}^{\infty} i(x,y)e^{-i2\pi\omega(x\cos\theta+y\sin\theta)}dxdy \qquad 2\text{-}41$$

The right-hand side of Eq. 2-41 represents the 2-D Fourier transform at an angle θ,

$$S_\theta(\omega)=I(\omega,\theta)=I(\omega\cos\theta,\omega\sin\theta) \qquad 2\text{-}42$$

This relationship is on a more solid foundatation and is the essence of parallel-beam projection tomography. It proves the Fourier Slice Theorem, which relates the 1-D Fourier transform of a projection to a single radial line of the 2-D Fourier transform of the objent. This provides a simple conceptual model of tomography – given the Fourier transform of each projection at sufficient angle sampling the projections could be assembled into a complete estimate of the Fourier transform of the object and then simply inverted to obtain an estimate of the object.

The algorithm which is widely deployed in almost all applications of parallel-beam projection tomography is the standard FBP algorithm. It is straightforward since each projection represents a nearly independent measurement of the object by finding the Fourier transform of the projection and then using the Fourier Slice Theorem. It is noted that the projections are nearly independent because the background (i.e. the DC term in the frequency domain) is the common information in the Fourier transforms of the different projections at different angles. It is also noted that low spatial frequencies at one oritation may be seen as higher spatial frequencies in another.

Recalling the formula for the inverse Fourier transform, the 2-D object function *i(x,y)*, can then be expressed as

$$i(x,y) = \int_{-\infty}^{\infty}\int_{-\infty}^{\infty} I(k_x,k_y) e^{i2\pi(xk_x+yk_y)} dk_x dk_y \qquad 2\text{-}43$$

Exchanging the rectangular coordinate system in the frequency domain, (k_x, k_y), for a polar coordinate system, (ω, θ), by making the following substitutions,

$$k_x = \omega\cos\theta \qquad k_y = \omega\sin\theta \qquad dk_x dk_y = \omega d\omega d\theta$$

The inverse Fourier transform in a polar system can be described as

$$i(x,y) = \int_{0}^{2\pi}\int_{0}^{\infty} I(\omega,\theta) e^{i2\pi\omega(x\cos\theta+y\sin\theta)} \omega d\omega d\theta \qquad 2\text{-}44$$

The integral can be split into two by considering θ from 0º to 180º and from 180º to 360º, and then using the property

$$I(\omega,\theta+180) = I(-\omega,\theta) \qquad 2\text{-}45$$

Eq. 2-44 then can be written as

$$i(x,y) = \int_{0}^{\pi}\left[\int_{-\infty}^{\infty} I(\omega,\theta)|\omega| e^{i2\pi r\omega} d\omega\right] d\theta \qquad 2\text{-}46$$

Substituting Eq. 2-42 in Eq. 2-46 (i.e. substituting the Fourier transform of the projection at θ for the 2-D Fourier transform of the object), Eq. 2-46 can be written as

$$i(x,y) = \int_{0}^{\pi}\left[\int_{-\infty}^{\infty} S_\theta(\omega)|\omega| e^{i2\pi r\omega} d\omega\right] d\theta \qquad 2\text{-}47$$

The term in brackets can be recognised as a filtering operation, where the frequency response of the filter is given by $|\omega|$ (i.e. the ramp filter); therefore, the resulting projection from this operation can be called a "filtered projection". Then, the resulting projections for different angles θ are added to form the estimate of *i(x,y)*. In the reconstruction process, each filtered projection is backprojected or smeared across a 2-D image plane at the corresponding acquisition angle.

In order to approximate straight-ray projection, in OPT the specimen is suspended in a refractive index matched medium and as a consequence light will propagate in straight lines due to index matching (i.e. no refractive scattering). Furthermore, imaging system must be arranged such that approximately parallel rays only are imaged (i.e. the "effective" DOF covers the volume to be imaged). Therefore, the standard FBP algorithm can be typically used for tomographic reconstruction in OPT. It is noted that this OPT

reconstruction process (i.e. using the FBP algorithm) can be modified to take into account the optical characteristics of the imaging system, which will be discussed in more detail in Chapter 3 [90, 91].

2.10. Conclusions

This chapter has provided an introduction to the basic concepts of fluorescence and its main physical properties and particularly how to utilise fluorescence for biomedical applications. The fluorescence signal can be described in terms of intensity, absorption and/or emission spectra and lifetime, all of which are not only defined by the molecular structure but also affected by the local fluorophore environment. A number of the common implementations of fluorescence imaging were outlined, particularly the common methods for fluorescence lifetime measurements (TCSPC, wide-field time-gated and frequency domain). The technique of FRET was also introduced since it allows information on the energy transfer between appropriately labelled proteins (donor-acceptor). This phenomenon is of significance since the interaction between the donor and the acceptor happens at a length scale far beyond the diffraction limit but through energy transfer colocalisation/interaction can still be inferred. The method of measuring FRET by using FLIM was also introduced as well as its potential advantages.

This chapter has also reviewed the current 3-D optical imaging techniques for mesoscopic samples, including OPT, light sheet microscopy and SLOT. The concept, the most common implementations, the developments and the applications for these imaging techniques were outlined as well as the comparison between them.

A numerical analysis of the "standard" spatial resolution of OPT and SPIM was discussed by following a number of formulae describing the different behaviour of the most common form for those two instruments. It described that for a given sample size, although SPIM could provide higher lateral resolution, the resolution is anisotropic, which could potentially make the analysis of 3-D images difficult, while OPT has isotropic spatial resolution due to its rotational scanning.

The standard FBP algorithm was derived from the mathematical basis of tomography with non-diffraction sources to recover the cross-sectional images of an object from the projection data. The assumption on parallel-beam projection that underlies the standard FBP algorithm was discussed.

The remainder of this thesis utilises some of the techniques introduced in this chapter (i.e. fluorescence imaging, wide-field time-gated FLIM, FRET and OPT), particularly OPT, in studies. The thesis primarily aims at the development of OPT for 3-D mesoscopic biomedical imaging.

Chapter 3: Optimising reconstructed OPT images

This chapter is concerned with the investigation of modified OPT reconstruction techniques that account for the optical characteristics (i.e. the modulation transfer function (MTF)) of the imaging system by either MTF-mask filtering or deconvolution by the MTF [91].

Initially, the in-house developed intensity-based OPT microscope system is characterised by experimentally determining the MTFs for different effective collection NAs of the system as a function of defocus to quantify the additional spatial frequency modulation applied by the use of focussed optical radiation with its associated instrumentation in OPT. Typically, the standard FBP algorithm is deployed for computed tomographic reconstruction. In practice, however, the use of focussed optical radiation with its associated instrumentation limits the applicability of the standard FBP algorithm, which assumes parallel-beam projection. To accommodate non-parallel light imaging in OPT, modified reconstruction techniques incorporating the MTF information of the system by using the experimentally determined MTFs as either mask filters or deconvolution filters are investigated. First, a 2-D binary filter based on the MTF frequency cut-off is employed as an additional filter during backprojection reconstruction, which restricts the high frequency information to the region around the focal plane and progressively decreases the spatial frequency bandwidth with defocus. This MTF-mask filter helps to suppress "streak" artefacts in OPT data acquired with a reduced number of projections (i.e. at reduced angular sampling), thereby facilitating faster OPT acquisitions while maintaining reasonable quality reconstructions. It is of significant interest to achieve reasonable quality images with a reduced number of angular projections (i.e. under sampling) because this will reduce the overall light dose on the sample - and therefore any photobleaching or phototoxic effects - and improve time-lapse resolution, e.g. for *in vivo* imaging. In addition, this reduced number of acquired projections will lead to a reduction in storage space required for a data set and its reconstruction time. The experimentally determined MTF can also be used to produce an appropriate deconvolution filter that can be employed to correct for any spatial frequency modulation applied by the imaging system. The MTF-deconvolution approach provides improved resolution reconstructions for high-angular-sampling OPT acquisitions. Topics in this chapter include:

- Optical characterisation of OPT systems by experimentally determining MTFs as a function of defocus
- Discussion on image reconstruction based on the standard FBP algorithm
- Modified OPT reconstruction incorporating MTF-mask filtering
- Modified OPT reconstruction incorporating MTF-deconvolution

3.1. Determination of the MTF of OPT system

3.1.1. Imaging system

The in-house developed intensity-based OPT microscope system utilising both transmitted light and epifluorescence imaging was built on a standard inverted wide-field microscope (IX-71, Olympus UK Ltd). Figure 3.1 shows a schematic of this intensity-based OPT system. A 4x objective (UPLFLN4X, Olympus UK Ltd) was employed in the experiments. The choice of filter cube was governed by the sample. For example, a standard GFP filter cube (GFP-3035B-OMF, Laser 2000 Ltd) was chosen for GFP-label imaging (e.g. a fluorescent Casper:Fli-EGFP transgenic zebrafish). Appropriate apertures (AP) positioned directly behind the objective defined the diameter of the back aperture, and were used to adjust the effective collection NA of the system. Images including transmitted and fluorescence images were recorded on a CCD camera (Clara, Andor Technology plc, 1040×1392, 6.45 μm pitch size, cooled to -20 ºC) via a tube lens (U-CMAD3, Olympus UK Ltd).

A custom-built chamber was fabricated to hold the small tube-mounted samples (e.g. zebrafish embryos or bead phantoms in short lengths of translucent Fluorinated Ethyline Propylene (FEP) tubing) in a refractive index-matched environment and to allow stable sample rotation without unnecessary movement. Figure 3.2 shows the basic features of the intensity-based OPT microscope system, including white-light transmission imaging, an illumination port for excitation by an external source (i.e. a mercury arc lamp or an ultrafast fibre-laser-pumped super-continuum source in this work, described in Appendix I), an imaging port, a custom-built chamber and a rotation stage.

The focusing arrangement in this chapter was configured such that the focal plane of the imaging system and the axis of rotation were coincident. For this coincident arrangement, all parts of sample will pass through the focal plane twice over the full rotation (i.e. 360º) and the region around the focal plane (or the axis of rotation) will be always maintained at "best focus". There are other possible focusing arrangements (e.g. focusing the imaging systems at shifted planes in the sample, which will be discussed in Chapter 4). For those arrangements, the front half of the sample is imaged under the parallel-beam projection approximation, which interrogates the entire sample during the course of a full complete rotation but objects located between the axis of rotation and the nearest focal plane to the axis of rotation will never be imaged at "best focus" (i.e. will not pass through the focal planes).

Although the work described in this chapter used the coincident optical arrangement, the ideas expressed are applicable to other arrangements. It is noted that, for the coincident optical arrangement, it is only necessary to acquire angular projections over 180º when imaging absorption coefficients in transmission. However, for fluorescence tomography, this is not the case if there is a spatial variation in excitation intensity or fluorescence absorption (inner filter effect) across the sample.

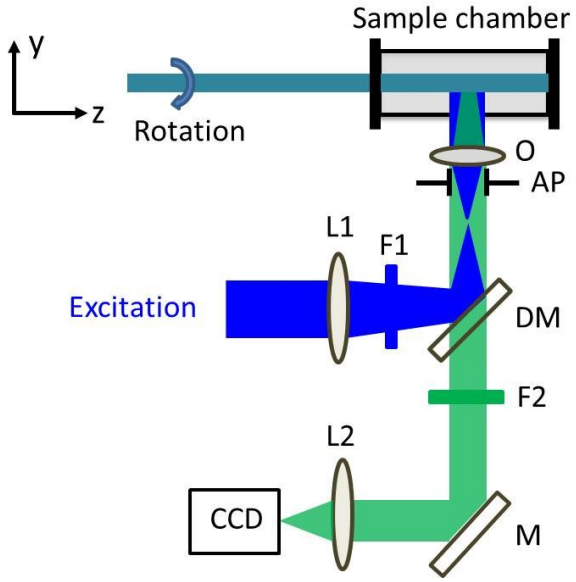


Figure 3.1: Schematic of in-house developed intensity-based OPT microscope system. O – objective, AP – aperture, L1 – condenser lens, F1 – excitation filter, DM – dichroic mirror, L2 – tube lens, F2 – emission filter, M – mirror.

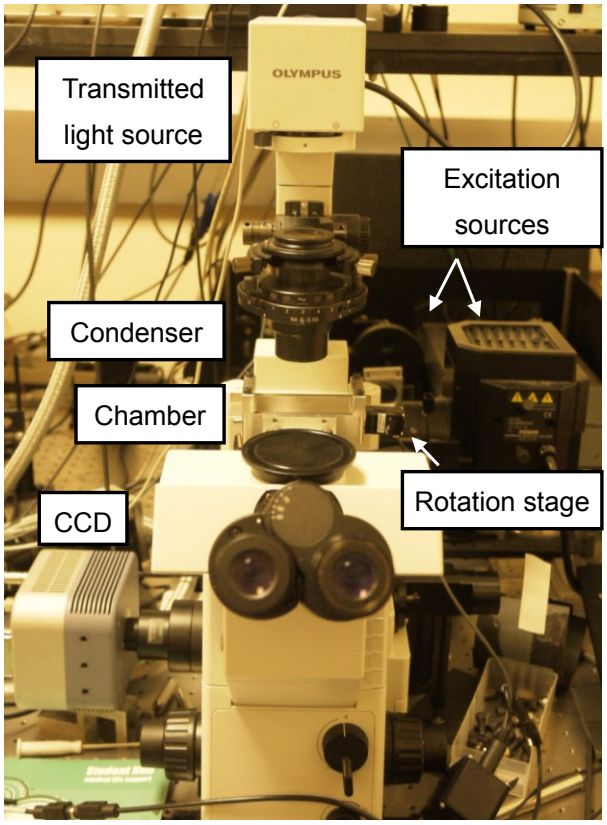


Figure 3.2: Photograph of intensity-based OPT microscope system.

3.1.2. MTF characterisation

As described in Chapter 2, the key advantage of OPT compared to X-ray CT is the use of optical radiation in biological tissues with its rich spectroscopic contrast, including absorption and fluorescence. However, the use of focussed optical radiation with its associated instrumentation in "high magnification" OPT limits the applicability of parallel-beam projection. In order to quantify this additional spatial frequency modulation applied by the focussing optical system, the OPT system is characterised by experimentally determining the MTFs for different effective collection NAs of the optical imaging system as a function of defocus. This MTF information can be used to understand the trade-off between the spatial resolution and sample size and therefore used to optimise the configuration of the system and further incorporated to modify the reconstruction process.

The 1-D MTF, which is the Fourier transform of the line spread function (LSF), is a parameter that characterises the spatial resolution properties of an imaging system. The straightforward approach to measuring the MTF of an optical system is to image a sub-resolution slit, obtain the LSF and then calculate the MTF through the Fourier transform method. However, this method is sensitive to noise. Yin *et al.* reported an analytic method to determine the MTF in a digital system by imaging a slit and analysing its digitized image [111]. In this case, a 10 μm slit was adequate for the resolution. However, considering the small pixel dimension of the detection camera (e.g. 6.45 μm in the CCD used in this work) and the achievable optical resolution in OPT (e.g. a few μm), a 10 μm slit was too large for an accurate MTF measurement. Boone *et al.* extended this method by using the edge spread function (ESF) instead of the LSF [112]. The ESF, which is the integral of the LSF, was measured by imaging a sharp discontinuity (e.g. a knife-edge). The profile of the straight edge, the ESF, was fit by analytic equation and the fitting parameters were employed in an analytic expression of the MTF. This technique relies on oversampling a continuous knife-edge image. However, when it is applied to a digital imaging device with a finite pixel dimension, the image is not sampled sufficiently, which may introduce aliasing and therefore, significant errors in calculating the MTF.

To further address the sampling issue and obtain an accurate MTF, Gundy *et al.* extended the traditional knife-edge technique by tilting the knife-edge with respect to the CCD pixels [113]. This allows generation of a composite scan with a higher resolution than the sampling rate defined by the pixel size. What follows describes a tilted knife-edge technique used to determine the MTF for the different effective collection NAs of the OPT system as a function of defocus [91].

3.1.2.1. Methods

Transmitted light images of a scalpel blade mounted in the custom built chamber filled with water (i.e. the typical refractive-index matched medium in OPT applications, e.g. *in vivo* zebrafish embryo imaging) at an angle of ~9.5º relative to the vertical axis of the CCD were acquired. Figure 3.3 (a) and (b) show the transmitted light in-focus and defocus images with the NA of 0.07 respectively.

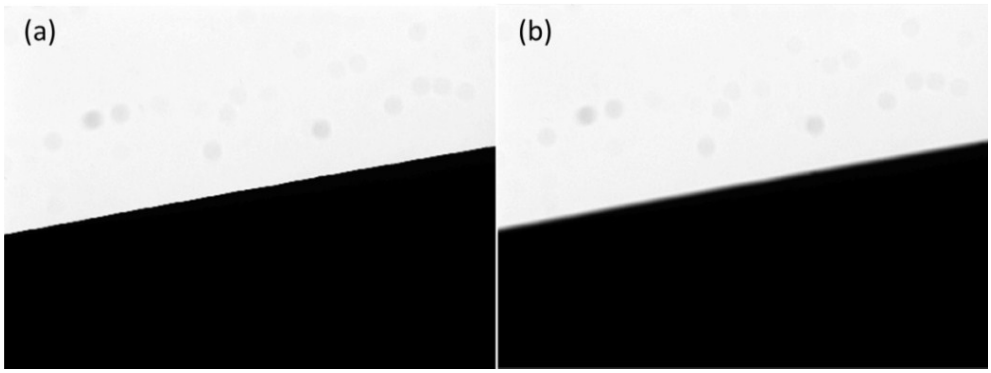


Figure 3.3: Transmitted light (a) in-focus (0 μm) and (b) defocus (200 μm) images of a scalpel blade with the NA of 0.07.

It is noted that the transmitted light images were based on incoherent white-light source since the targeted MTF was the incoherent MTF of the system considering the incoherent nature of fluorescence. The transmitted light images were acquired over a focus range of 2.4 mm (i.e. up to 1.2 mm either side of the in-focus image) and repeated for effective collection NAs in the range 0.03-0.09. The distance of the scalpel blade from the focal plane (i.e. best focus) was recorded by a plunge dial indicator (model #398877, RS Ltd). Average ESFs were determined from 10 bright field and 30 background images. The ~9.5º tilt facilitated an increased effective sampling of the knife-edge by interleaving 6 rows of pixels to produce a 1-D ESF. Figure 3.4 (a) illustrates the 1-D ESF from the in-focus blade image (Fig. 3.3 (a)).

Based on the analysis method (to obtain the analytical MTF from the fit of the corresponding ESF) by Boone *et al.* [112], an analytic equation representing the weighted sum of an error function and exponential recovery term was used to fit the measured ESFs, given by

$$ESF(x) = a \cdot \left[1 - \exp\left(-b \cdot |x - x_0|\right)\right] + c \cdot erf\left(d^{1/2} \cdot |x - x_0|\right) \qquad 3\text{-}1$$

where *erf* is the error function, defined as $erf(x) = \frac{2}{\sqrt{\pi}} \int_0^x e^{-t^2} dt$. The parameters from these fits were then used in an analytic expression to determine the MTF, given by

$$MTF(f) = \frac{c \cdot \exp\left(-\pi^2 f^2 / d\right) + a \cdot \left(1 + 4\pi^2 f^2 / b^2\right)^{-1}}{c + a} \qquad 3\text{-}2$$

Figure 3.4 (a) shows the measured in-focus ESF and the resulting fit for the imaging system (the blue dots and the red solid line respectively). The resultant MTF, determined by using both the analytic expression and the numerical Fourier transform procedure (i.e. numerical differentiation and Fourier transformation) are illustrated by the red solid line and the blue dots respectively in Fig. 3.4 (b).

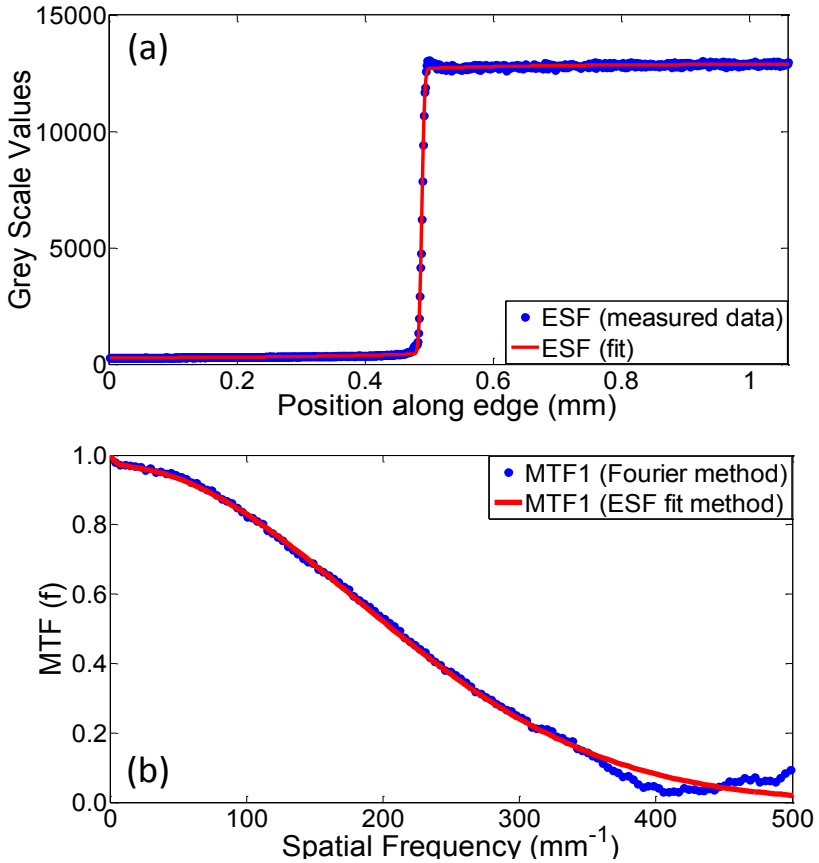


Figure 3.4: (a) The measured ESF is plotted as discrete data points. The fit to these points is illustrated by the red solid line. The linear correlation coefficient between these two is 0.9999. (b) The corresponding MTF at this position from the analytical method, shown as the red solid line, and from the numerical Fourier transform procedure, shown as data points.

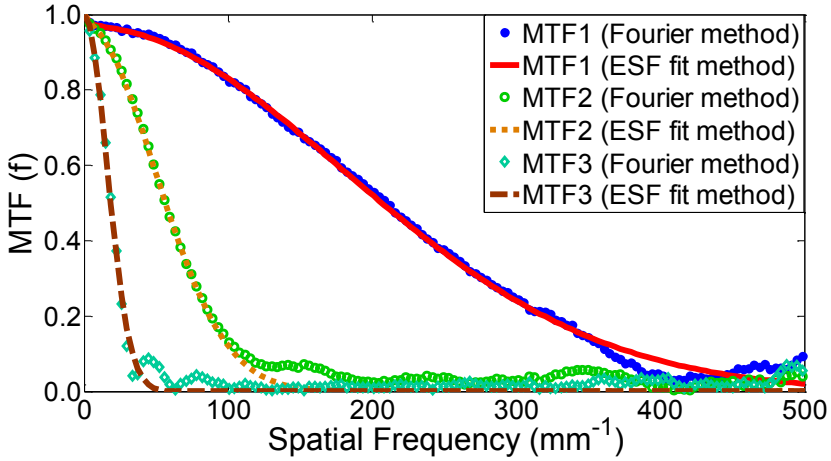


Figure 3.5: Three pairs of MTFs at the different positions from the analytical method, shown as the lines, and the numerical Fourier transform procedure, shown as data points. MTF1 is the MTF in focus; MTF2 and MTF3 are for 70 and 200 μm defocus, respectively.

The MTFs at different focal positions were analysed to obtain 1-D MTF information as a function of defocus. Figure 3.5 shows three pairs of MTFs at different positions (in-focus, 70 and 200 μm defocus) with the lines corresponding to the analytical method and the data points corresponding to the numerical Fourier transform procedure, visibly illustrating the reduction in the bandwidth of the transferred spatial frequencies as a function of defocus. These curves also illustrate the high correspondence between the conventional Fourier transform approach and the analytical method.

It is noted that in the ESF fitting process, a Gaussian-dominated model of the LSF was assumed and therefore also the resulting MTF. While this is not the correct functional form for the MTF of a 'perfect' lens with a circular aperture, the limiting resolution is dominated by the first minimum of an ideal in-focus MTF form. The cut-off frequency can be determined by fitting the assumed model to an ideal in-focus MTF, which results in an offset of 3.6%. Therefore, this value can be used as the frequency cut-off threshold for this MTF model. Considering this along with the noise associated with the ESF measurement, particularly at high spatial frequencies, it is sufficient to use the Gaussian-dominated approximation for the generation of 2-D MTFs (i.e. the 1-D MTFs as a function of defocus).

3.1.2.2. Results and discussion

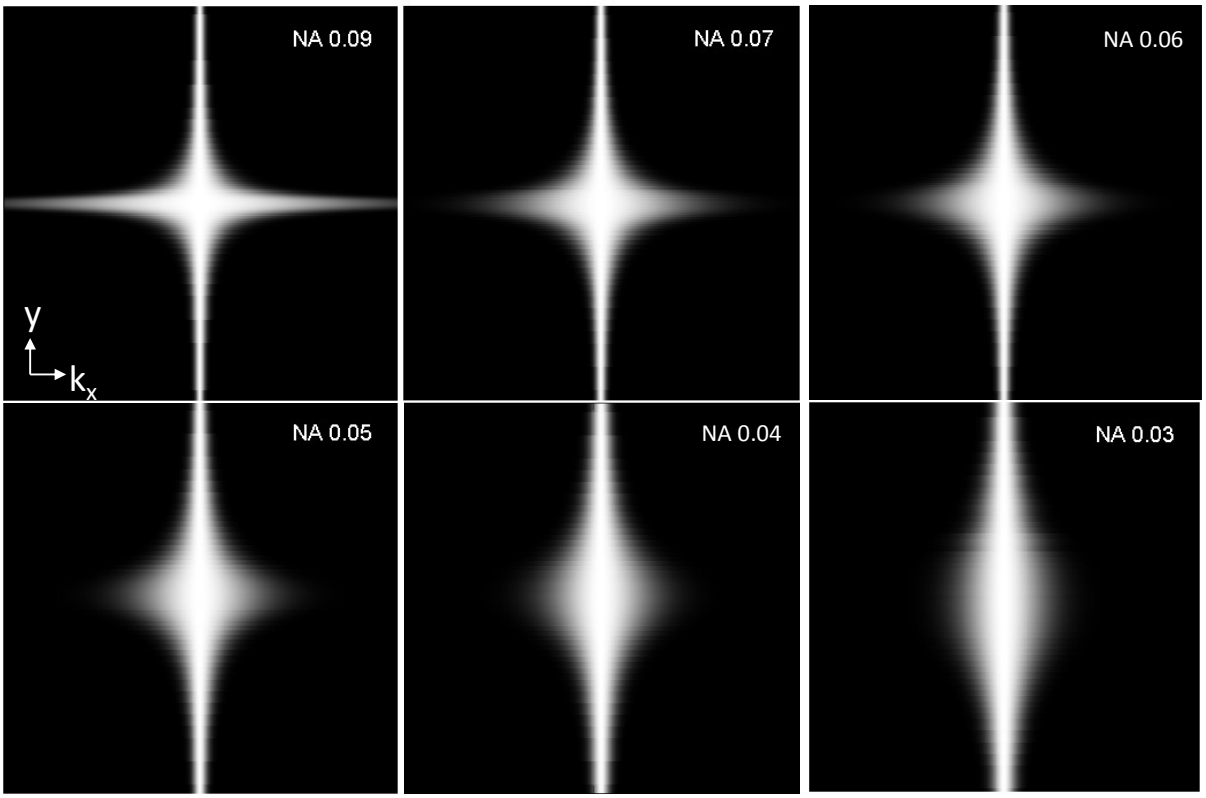


Figure 3.6: MTFs as a function of defocus (z) for different effective NAs (0.09, 0.07, 0.06, 0.05, 0.04 and 0.03) of the 1×1 binning intensity-based OPT microscope system. (1040×1040, Δk_x = 0.596 mm^{-1}, Δy = 1.6125 μm, the vertical scale -838.5 – 838.5 μm and the horizontal scale -309.92 – 309.92 mm^{-1}). These measurements were not limited by camera pixel size.

Figure 3.6 shows six 2-D MTFs (1040×1040) as a function of defocus for different effective NAs (0.09, 0.07, 0.06, 0.05, 0.04 and 0.03) of the 1×1 binning intensity-based OPT microscope system. The pixel dimension for the vertical axis (defocus distance) is 1.6125 μm and for the horizontal axis (spatial frequency) is 0.596 mm^{-1} (i.e. the vertical scale -838.5 – 838.5 μm and the horizontal scale -309.92 – 309.92 mm^{-1}), where the pixel size of the CCD camera is 6.45 μm and a 4x objective was used in the OPT microscope system (i.e. the magnification of 4). It is evident that as the NA decreases the in-focus bandwidth (i.e. lateral resolution) decreases and the DOF of the optical system increases. For a given sample size, an appropriate NA of the OPT system is required to balance the resolution and the DOF. It is noted that these measurements were not limited by the CCD camera pixel size.

3.2. Reconstruction based on the standard FBP algorithm

The reconstruction process recovers a stack of cross-sectional images of a sample from a series of projection images acquired at different projection angles. Ideally, projections would be a set of integrated measurements of some sample property (e.g. absorption, fluorescence) along straight lines through the object and referred to as line integrals. As discussed in section 2.9, the reconstruction algorithm based on the parallel-beam projection assumption is known as the standard FBP algorithm. This section illustrates the performance of the standard FBP reconstruction approach, which will be used as the reference for the following sections to evaluate the performance of modified reconstruction approaches.

3.2.1. Materials

To evaluate the performance of the different reconstruction methods, a bead phantom was used as a model sample. The phantom consisted of a low concentration suspension of fluorescent beads (F8844, Life Technologies Ltd) in 2% agarose, with an average bead diameter of 14.8±0.13 μm and excitation/emission maxima at 505/515 nm respectively. The phantom was drawn into short lengths of translucent FEP tubing (#06406-60, Cole-Palmer).

3.2.2. Acquisition procedure and settings

3.2.2.1. Intensity-based OPT acquisition procedure

OPT is based on the wide-field acquisition of a series of 2-D intensity images (absorption/fluorescence) at different projection angles. For intensity-based OPT acquisition, the programme starts with selecting the rotation stage and camera and then initialising and setting up the camera (e.g. binning, integration time, cooling) and the rotation stage. During the acquisition, the CCD is typically set to a single scan internal trigger mode and then triggered by the signal from the program for a user defined period (i.e. integration time). After the integration, the CCD is read out and the image is saved. After that, the rotation stage then

switches to the next angular position. This process is repeated for a user-defined number of angular steps. Figure 3.7 shows a schematic of the intensity-based OPT "standard" acquisition procedure.

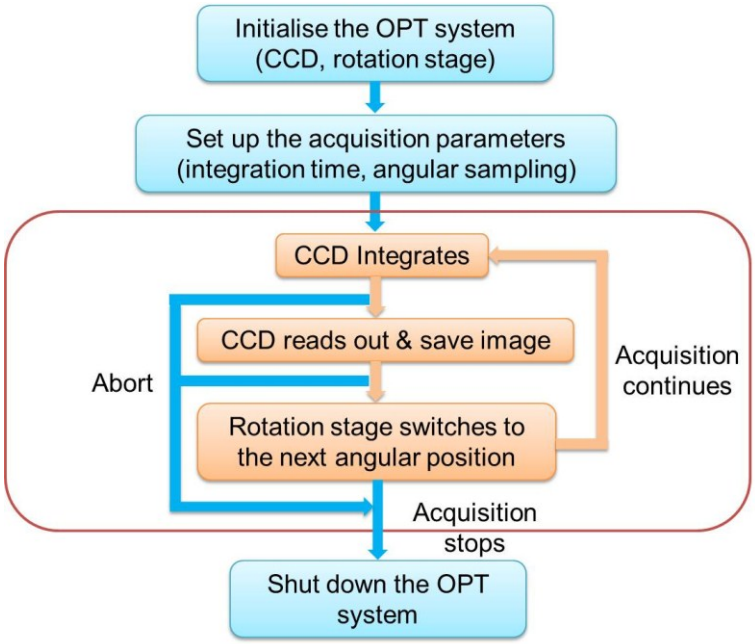


Figure 3.7: Schematic of the intensity-based OPT "standard" acquisition procedure.

3.2.2.2. Acquisition settings

A 4x objective (UPLFLN4X, Olympus UK Ltd) and a GFP filter cube (GFP-3035B-OMF, Laser 2000 Ltd) were employed. Three different apertures were positioned directly behind the objective, resulting in effective collection NAs of 0.06, 0.07 and 0.09. Images were formed on a CCD camera (Clara, Andor Technology plc). The analytic values for the resolution at best focus (r_{Airy}) and the DOF for different NAs of 0.06, 0.07 and 0.09, which were calculated using Eq. 2-20 and 2-21 respectively, are given in Table 3.1.

	NA 0.06	NA 0.07	NA 0.09
r_{Airy} (μm)	5.3	4.5	3.5
DOF (μm)	228	169	108

Table 3-1: The analytic values for the resolution at best focus and DOF for different effective NAs of the OPT system.

During a standard OPT acquisition, image data was acquired at equal angular intervals as the sample rotated (e.g. acquiring images every 1° over a full rotation). A typical exposure time for each frame of the bead

phantom was 100 ms (which filled the dynamic range of the CCD for the effective NA of 0.07). In practice, however, to enable the results from different effective NAs to be compared directly, the exposure time was adjusted to maintain a consistent signal-to-noise (SNR) ratio.

3.2.3. Evaluation methods

All reconstructed cross-sectional images were visually examined to directly evaluate the differences between the standard FBP reconstruction and the modified reconstructions. To further quantify the performances of the different reconstruction techniques, a line was plotted through the radial and tangential axes centred on the reconstructed beads, as illustrated in Fig. 3.8, and the full width half maxima (FWHM) of the reconstructed bead images were measured along the radial and tangential axes.

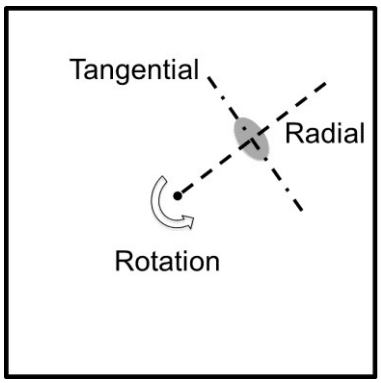


Figure 3.8: Schematic of radial and tangential resolution used to evaluate the image quality.

3.2.4. Ramp filter

Assuming a parallel-beam projection regime, each row of pixels in a recorded image can be considered as a 1-D projection (i.e. a sum along the optical axis of a 2-D slice through the sample). In the standard FBP reconstruction, a 1-D ramp filter is applied to each projection to correct for the sampling of the spatial frequency content of the object because of the rotational scanning geometry and the resulting repeatedly acquired background (i.e. the DC term in the frequency domain). The filtered projections are then backprojected or smeared across the 2-D image plane.

Alternatively, to directly compare with the modified reconstruction methods, this can be done by first smearing the unfiltered projection across the 2-D plane (X, Y – spatial), as indicated in Fig. 3.9 (b). Then a 1-D Fourier transform is applied across the dimension X to form a 2-D plane (K_x – spatial frequency, Y – spatial). After this, a 2-D ramp filter (K_x – spatial frequency, Y – spatial), which is indeed a smeared 1-D ramp filter as shown in Fig. 3.9 (c), is applied to correct for the sampling of the spatial frequencies. After the inverse 1-D Fourier transform across the dimension K_x, a smeared filtered projection across the 2-D image plane (X, Y – spatial) is achieved, as indicated in Fig. 3.9 (d).

Figure 3.9 (a) and (b) show a simulated object and its corresponding smeared unfiltered backprojection (i.e. 2-D) at one orientation while (c) and (d) show a normalized 2-D ramp filter and the corresponding filtered backprojection after applying this ramp filter. It is noted that the high spatial frequency components are present across the whole image plane without any restriction in this case. After the filtering, the set of such filtered projections would then be summed over the image plane at each corresponding acquisition angle to reconstruct the tomographic images (i.e. the 2-D cross sectional images of the object).

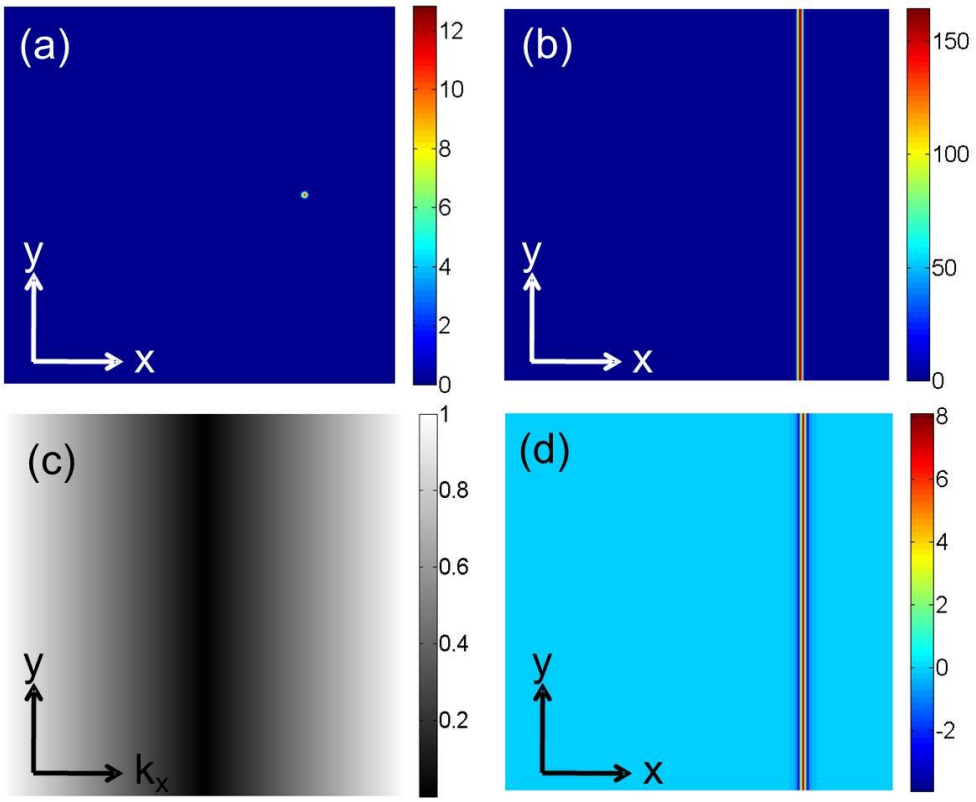


Figure 3.9: (a) A simulated object and (b) its corresponding smeared unfiltered backprojection (i.e. 2-D) at one orientation; (c) 2-D ramp filter and (d) 2-D backprojection at one angle with this ramp filter applied in the reconstruction process. (effective NA of 0.07 for the OPT system; 1040×1040 pixels, Δk_x = 0.596 mm^{-1}, Δx, Δy = 1.6125 µm; the scale of x,y is -838.5 – 838.5 µm and the scale of k_x is -309.92 – 309.92 mm^{-1})

3.2.5. Standard FBP reconstruction results and discussions

The reconstruction process produced a stack of cross-sectional (X-Y slice) images of the bead phantom for different effective collection NAs of 0.06, 0.07 and 0.09. To compare the results for different effective collection NAs, two beads located at different distances (i.e. 103 µm for the near-axis bead and 334 µm for the off-axis bead) from the axis of rotation were chosen. It is noted that these two beads were not in the same Z plane and therefore their sinograms were independent and reconstruction could be achieved separately for each bead. The sinograms of these two beads could also be combined computationally to give a more

complex object if desired. The reconstructions in this sub-section were achieved from the high-angular-sampling (i.e. 1º interval for the full rotation) experimental projection datasets by applying the standard FBP approach with the ramp filter.

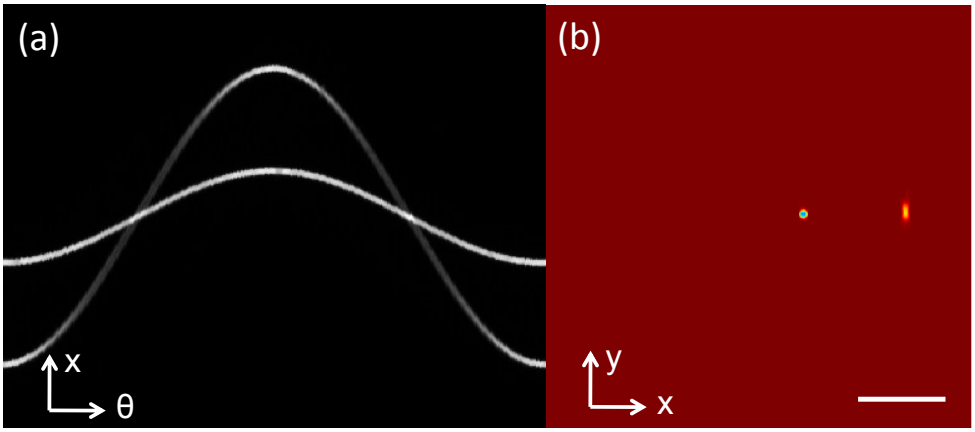


Figure 3.10: The experimental (a) raw sinogram for the central plane of the beads and (b) corresponding reconstructed X-Y image of (a) with the standard FBP algorithm. The results were reconstructed from 360 projections (i.e. a 1º interval) for an effective NA of 0.07. Scale bar, 200 μm.

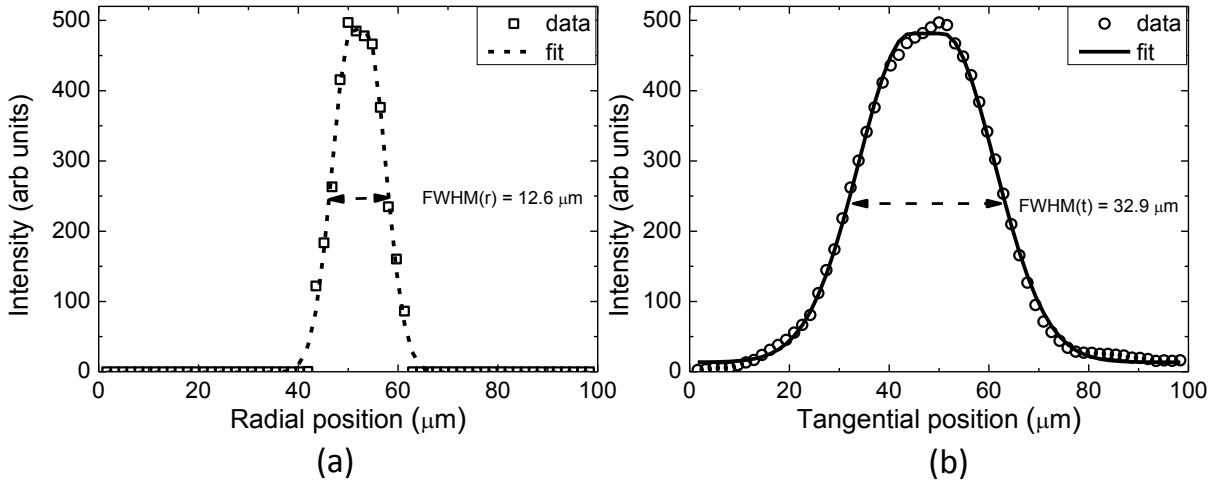


Figure 3.11: Line plots and Top-hat convolved Gaussian fits through the (a) radial and (b) tangential axis of the reconstructed off-axis bead in Fig. 3.10, where the points correspond to the reconstructed data and the lines to the fits. The off-axis bead is located 334 μm away from the axis of rotation.

Figure 3.10 (a) shows the combined raw sinogram for the central plane of the beads with an effective NA of 0.07 for the OPT system and (b) shows the corresponding reconstructed cross-sectional image (X-Y image) of the combined beads from the standard FBP reconstruction. The near-axis bead exhibits visually better tangential resolution than the off-axis bead. This can be explained by the fact that the off-axis bead for the

DOF produced by an NA of 0.07 did not remain in reasonable focus (i.e. within the DOF) during the whole acquisition. This difference is also confirmed by the line-sections through the radial and tangential axis of the reconstructed off-axis bead centre, as shown in Fig. 3.11 (a) and (b) respectively, with accompanying Top-hat convolved Gaussian fits providing the FWHM.

The radial and tangential FWHM of the reconstructed beads (near-axis and off-axis) for NAs of 0.06, 0.07 and 0.09 are given in Table 3-2. As expected, as the NA decreases the in-focus radial resolution (i.e. the best resolution) decreases as indicated by the increased FWHM of the near-axis bead. Similarly, as the NA decreases, the DOF increases as indicated by the reduced tangential FWHM of the off-axis bead. This illustrates the traditional trade-off in OPT between the achieved spatial resolution and the DOF. It is noted that at this magnification the imaging system operates just within the pixel sampling limit of the PSF (especially for the highest NA of 0.09, which operates at the Nyquist sampling limit) and therefore the curve fitting to the reconstructed bead diameter at higher NAs is sensitive to interpolation and pixel sampling.

FWHM (μm)	NA 0.06	NA 0.07	NA 0.09
Radial (near-axis)	16.2	15.9	15.4
Tangential (near-axis)	17.0	17.3	17.2
Radial (off-axis)	13.0	12.6	12.7
Tangential (off-axis)	25.9	32.9	45.1

Table 3-2: The radial and tangential FWHM of the reconstructed beads for different effective NAs of 0.06, 0.07 and 0.09 with the standard FBP reconstruction method (near-axis bead located 103 μm away from the axis of rotation; off-axis bead located 334 μm away from the axis of rotation; average bead diameter 14.8±0.13 μm).

3.3. MTF-mask filtering reconstruction

Two fundamental limits that restrict the application of OPT are imaging speed and spatial resolution. One important issue that limits imaging speed is the minimum number of angular projections required to adequately sample the subject and then to provide a reasonable tomographic reconstruction. This has been established in X-ray CT [76]. Adapting the standard equation for the number of projections required in the case of parallel-beam projection and assuming the spatial resolution is limited by diffraction (i.e. the NA of the optical system and the imaging wavelength), the required number of projections, *M*, for a low NA OPT system, is given by

$$M = \pi \cdot N = \frac{\pi \cdot D \cdot NA}{0.61\lambda} = \frac{\pi \cdot D}{r_{Airy}} \qquad 3\text{-}3$$

where N is the number of resolvable elements in the FOV or field of interest D given by the lateral resolution r_{Airy}. The typical value of M for the standard OPT system is ≥360 projections. Such fine angular sampling implies long data acquisition times with concomitant light dose on the sample. The image acquisition time is particularly extended for FLIM-OPT in which a series of time-gated fluorescence intensity images are required at each projection angle. Therefore, it is of significant interest to obtain reasonable quality images with a reduced number of projections (i.e. under sampling) as the reduced total number of acquired projections will reduce the overall light dose on the sample - and therefore any photobleaching or phototoxic effects - and improve time-lapse resolution, e.g. for *in vivo* imaging. In addition, the reduced number of acquired projections will lead to a reduction in storage space required for a data set and the reconstruction time. However, inadequate angular sampling can result in "streak" artefacts, i.e. unwanted high spatial frequency projected features that appear away from the focal region, in the reconstructed images when employing the standard FBP algorithm.

The aim of the following research is to maintain reasonable quality reconstructed images with a reduced number of acquired projections by modifying the standard OPT reconstruction process to incorporate the optical characteristic information (i.e. the MTF) as MTF-mask filtering. This is demonstrated by employing a 2-D binary filter based on the MTF frequency cut-off as an additional filter during backprojection reconstruction. This MTF-mask filter restricts the high frequency information to the region around the focal plane and progressively decreases the spatial frequency bandwidth with defocus. Therefore, it helps to suppress "streak" artefacts in OPT data acquired at reduced number of projections (i.e. reduced angular sampling), thereby facilitating faster OPT acquisitions and reducing the overall light dose on the sample.

3.3.1. MTF-mask filter

In the standard FBP reconstruction, a ramp filter is applied to each projection, as described in sub-section 3.2.4. The filtered projections are then back-projected at the corresponding acquisition angle and summed to reconstruct the cross section of the object. This process assumes parallel-beam projection, i.e. that the spatial frequencies transferred by the system are invariant along the projection direction. In order to account for the additional frequency modulation in the OPT system, a composite filter can be constructed from a combination of the 2-D ramp filter and the 2-D MTF-mask filter (i.e. the 2-D binary filter based on the MTF frequency cut-off).

The MTF-mask filter is a 2-D binary mask, which is generated from the experimentally determined MTF for the NA used in the acquisition. The MTF determination process assumes a Gaussian-dominated model of the MTF. Fitting the assumed Gaussian-dominated model to an ideal in-focus MTF results in a difference of 3.6% at the cut-off frequency and thus, the frequency cut-off threshold was set to 3.6% for this MTF model. The MTF-mask filter is then obtained by normalising the 2-D MTF by the frequency cut-off threshold, 3.6%, and then setting values above 1 to 1 and values below 1 to 0.

This filter is designed to appropriately restrict the spatial frequency components to regions from which the optical system could have transferred them. Using this filter as an additional filter in the reconstruction

reduces the high spatial frequency components away from the focal plane (i.e. only present in the region around the focal plane), thus a more realistic reconstruction may be achieved and "streak" artefacts suppressed at reduced angular sampling.

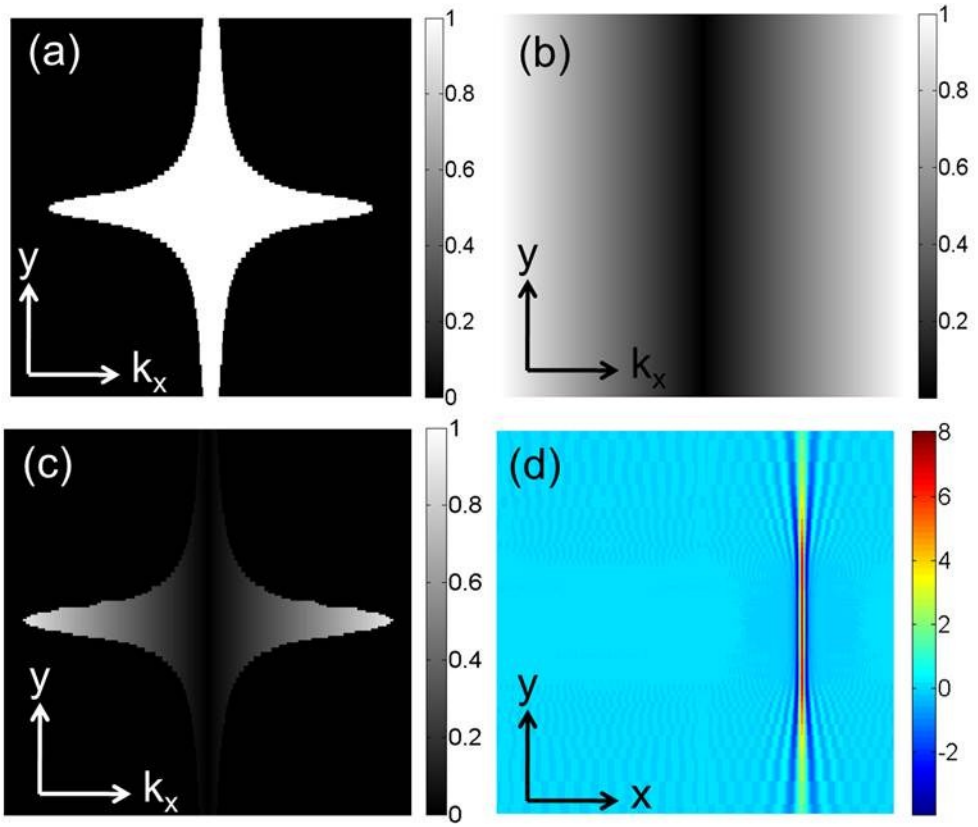


Figure 3.12: (a) 2-D binary MTF-mask filter, (b) 2-D ramp filter, (c) the combination of the MTF-mask filter and 2-D ramp filter and (d) backprojection at one angle with the MTF-mask filter and ramp filter applied in the reconstruction process from the same simulated raw data in Fig. 3.9. (effective NA of 0.07 for the OPT system; 1040×1040 pixels, Δk_x = 0.596 mm^{-1}, Δx, Δy = 1.6125 µm; the scale of x,y is -838.5 – 838.5 µm and the scale of k_x is -309.92 – 309.92 mm^{-1})

Figure 3.12 (a) shows the 2-D binary MTF-mask filter for an effective collection NA of 0.07 for the OPT system and (b) shows a normalised 2-D ramp filter. Figure 3.12 (c) shows the combination of the MTF-mask filter and the ramp filter applied in the reconstruction process and (d) shows the 2-D backprojection from the same simulated raw data in Fig. 3.9 but with the combined filter applied. Therefore the high spatial frequency components should only be present in the region from where the optical system could have transferred them. It is noted that the 2-D binary filter could potentially produce artefacts in the reconstruction, although the 2-D ramp filter tends to suppress the low spatial frequency components that might be generated as the MTF-mask filter narrows away from the focal plane. In addition, the averaging (i.e. summing up) of the backprojection process also tends to suppress such artefacts. In practice, the 2-D MTF-mask filter did not seem to produce discernible artefacts.

3.3.2. MTF-mask filtering reconstruction results and discussion

The same raw experimental dataset of the bead phantom was reconstructed with the MTF-mask filtering approach. The reconstruction process produced a stack of cross-sectional images of the bead phantom for effective collection NAs of 0.06, 0.07 and 0.09.

3.3.2.1. Simulation results

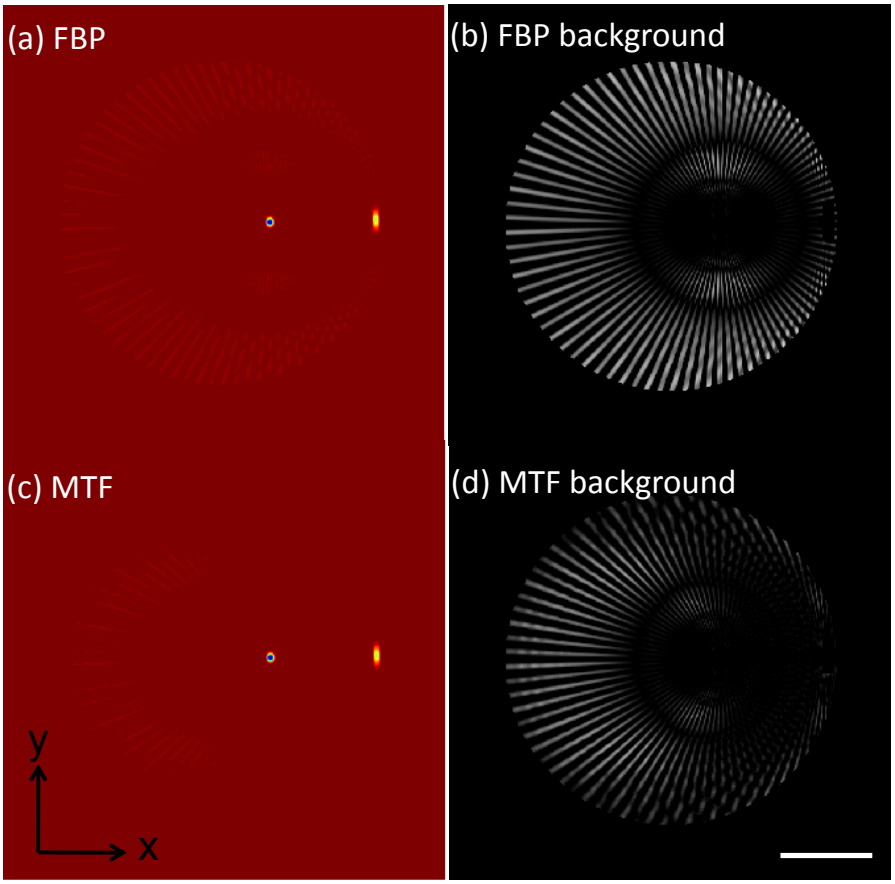


Figure 3.13: The simulated (a) standard FBP reconstruction and (b) the background for (a). The simulated (c) MTF-mask filtered reconstruction and (d) the background for (c). The results were reconstructed from 90 projections (i.e. a 4° interval) for an effective NA of 0.07. The background images were obtained by removing the beads in the corresponding reconstructed images. The images of the background are on the same intensity scale to show the difference. Scale bar, 200 µm.

To evaluate the performances between the standard FBP reconstruction technique and the modified reconstruction technique with the additional MTF-mask filter, a simulated dataset was generated for comparison with the experimental data. The simulated object consisted of two spherical beads of equal brightness at similar locations (i.e. 103, 334 µm) with respect to the axis of rotation to the beads measured in the corresponding experiments. The experimentally determined MTFs for different effective collection NAs were then used to numerically generate the corresponding projection data, which could be subsequently used for reconstruction by employing different filtering techniques (e.g. standard FBP, MTF-mask filtering

technique, etc.). It is noted that the simulation does not account for scattering, absorption, light propagation, spatial variation in excitation intensity and variation in collection efficiency, but serves only to model the defocus effects of the optical system (i.e. the MTF).

Figure 3.13 (a) shows the reconstruction of a simulated dataset using the standard FBP algorithm (i.e. the ramp filter only) and (b) shows the corresponding reconstruction with the beads removed to emphasise the background. Figure 3.13 (c) shows the reconstruction using the MTF-mask filtering technique (i.e. with the additional MTF-mask filter) and (d) shows the corresponding emphasized background. The dataset consisted of 90 projections (i.e. a 4º interval) for an effective NA of 0.07 of the OPT system. The reconstructions with the additional MTF-mask filter exhibit reduced "streak" artefacts of lower intensity compared to the reconstructions with the standard FBP algorithm.

3.3.2.2. Experiment results

Figure 3.14 shows the corresponding reconstructed and background images from experimental measurements. The experimental dataset consisted of 90 projections (i.e. a 4º interval) for an effective NA of 0.07 of the OPT system. To further evaluate the performances of the MTF- mask filtering technique, the reconstructions for NAs of 0.06, 0.07 and 0.09 using the standard FBP and MTF-mask filtering approach were analysed as the angular sampling was decreased.

The average value of the experimental background, which should be approximately zero, was calculated to evaluate the difference between the standard FBP and MTF-mask filtered reconstructions. Table 3-3 lists the values for different effective NAs (0.06, 0.07 and 0.09) and all data consisted of 90 experimental angular projections (i.e. a 4º interval). The reconstructions with the MTF-mask filtering approach exhibit significantly reduced background artefacts of lower intensity compared to the reconstructions with the standard FBP algorithm as the effective NA increases. This can be explained by the fact that as effective NA increases, the corresponding MTF-mask filter heavily restricts the high frequency components to the region around the focal plane and progressively decreases the spatial frequency bandwidth with defocus.

	NA 0.06	NA 0.07	NA0.09
Standard FBP	6.8 (100%)	5.3 (100%)	6.1 (100%)
MTF-mask FBP	5.0 (73.5%)	3.3 (62.3%)	1.7 (27.9%)

Table 3-3: The average background from the standard FBP and the MTF-mask filtering reconstruction for different effective NAs of 0.06, 0.07 and 0.09 (all data based on 90 experimental angular projections).

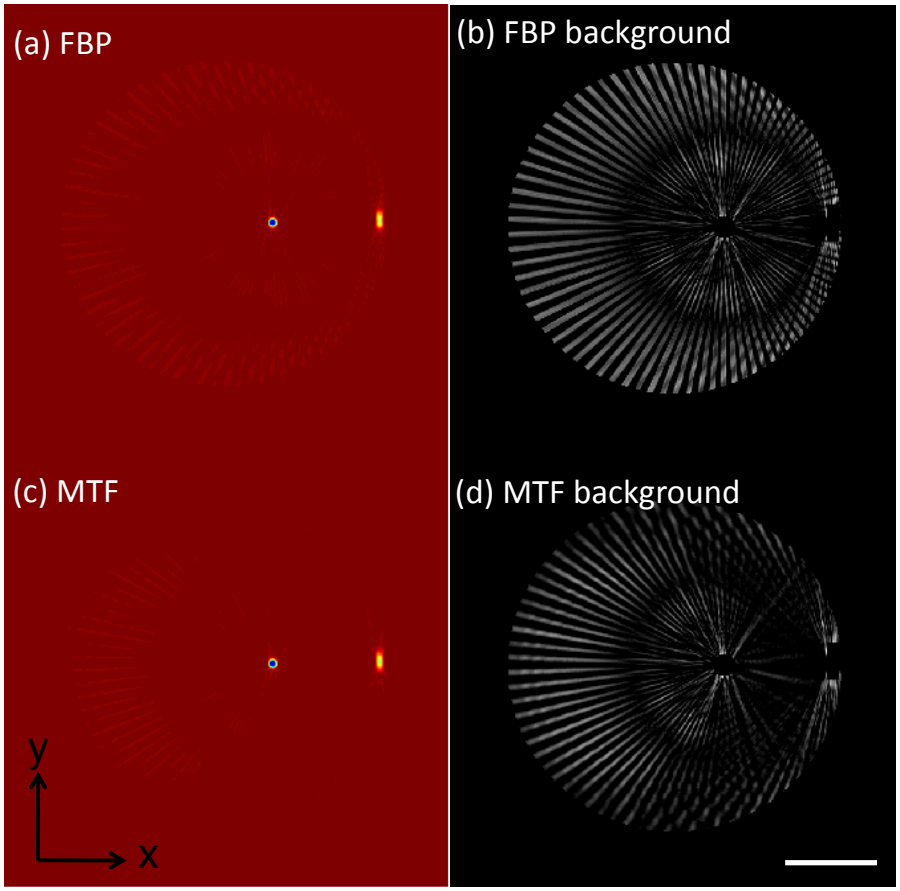


Figure 3.14: The experimental (a) standard FBP reconstruction and (b) the background for (a). The experimental (c) MTF-mask filtered reconstruction and (d) the background for (c). The results were reconstructed from 90 projections (i.e. a 4° interval) for an effective NA of 0.07. The background images were obtained by removing the beads in the corresponding reconstructed images. The images of the background are on the same intensity scale to show the difference. Scale bar, 200 µm.

To evaluate the reduction in reconstructed image quality when reducing the number of acquired projections, the correlation coefficients between the reconstructed images from low-angular-sampling and the highest-angular-sampling (i.e. a 1° interval in this experiment) were calculated to quantitatively indicate the reconstructed image quality at reduced angular sampling compared to that obtained using the highest-angular-sampling (i.e. the best reconstructed images, assumed to be closest to the real object). Figure 3.15 (a) shows the correlation coefficients between the reconstructed images from the lower angular-sampled projections and the best reconstruction (i.e. achieved from 360 projections) for an effective collection NA of 0.07, where the lines corresponds to the simulation results and the points to the experimental values. These curves illustrate how the MTF-mask filtering approach (i.e. using the MTF-mask filter as an additional filter in the reconstruction) can provide a better correlation with the reference images at a reduced number of projections by suppressing the "streak" artefacts. Therefore, the MTF-mask filtering approach should facilitate faster OPT acquisitions (i.e. under sampled acquisitions) while maintaining reasonable quality reconstructions. It is of significant interest because the reduced total number of acquired projections will reduce the overall light dose on the sample - and therefore any photobleaching or phototoxic effects - and

improve time-lapse resolution, e.g. for *in vivo* imaging. In addition, the reduced number of acquired projections will reduce the storage space required for a data set and its reconstruction time.

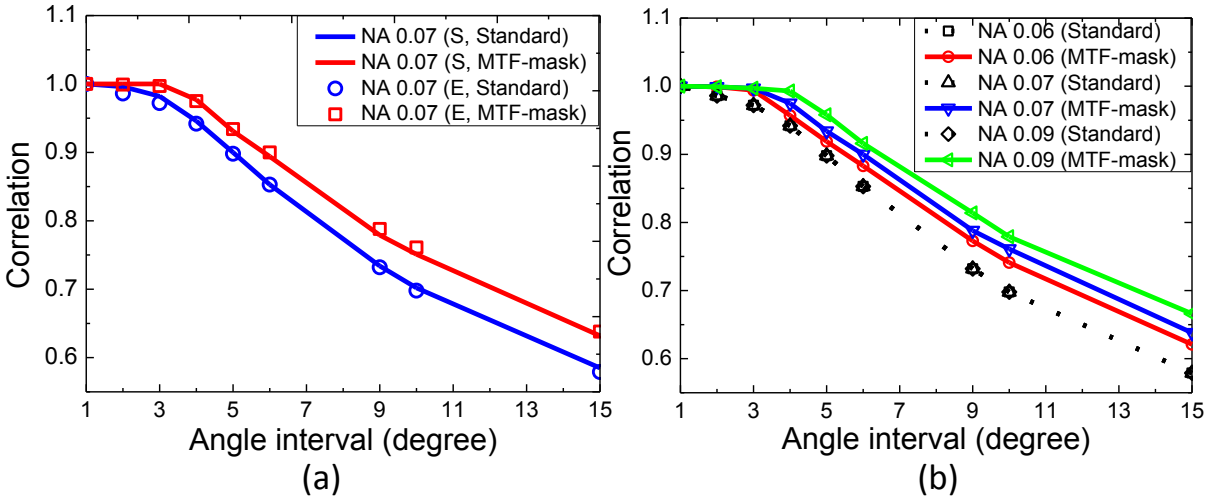


Figure 3.15: (a) Simulated (S) and experimental (E) correlation results of standard FBP and MTF-mask filtered reconstructions for an effective NA of 0.07. (b) Experimental correlation results for different effective NAs (0.06, 0.07, 0.09), with standard FBP correlations as the dotted lines and the MTF-mask filtered reconstruction correlations as the solid lines (three dotted lines are similar and cannot be distinguished in this figure and thus black colour is used to represent them).

To further evaluate the performance of the MTF-mask filtering reconstruction technique, the correlation coefficients between the reconstructed images from low-angular-sampling and the highest-angular-sampling were calculated for NAs of 0.06, 0.07 and 0.09 as the angular sampling was decreased. Figure 3.15 (b) shows the experimental correlation results for different effective NAs of 0.06, 0.07 and 0.09, in which the dotted lines corresponds to the correlation results with the standard FBP approach and the solid lines to the MTF-mask filtered reconstruction correlation results. It is noted that the three dotted lines indicating the standard FBP correlation coefficients are similar and cannot be distinguished in the figure. This is due to the fact that the standard FBP algorithm results in similar background structure for each NA (i.e. similar "streak" artefacts at reduced angular sampling) as it backprojects high frequency information across the whole image rather than the region around the focal plane. The correlation coefficients for higher NA MTF-mask filtered reconstructions decrease more slowly than those for the low NA at reduced angular sampling. This is due to the fact that the MTF-mask filter for the high NA suppresses the frequency components more aggressively. It is also noted that the correlation coefficient results shown here were performed with respect to the specific object (i.e. the bead phantom) chosen in the experiment for the corresponding NA of the OPT system. However, the trends are applicable to all samples. Once the appropriate NA is determined for a sample in OPT, the reconstruction quality using the MTF-mask filtering approach is always superior compared to the standard FBP approach at reduced angular sampling.

FWHM (μm)	NA 0.06	NA 0.07	NA 0.09
Radial (near-axis)	16.3	15.9	15.3
Tangential (near-axis)	17.0	17.3	17.2
Radial (off-axis)	13.3	12.4	12.6
Tangential (off-axis)	25.5	31.4	43.4

Table 3-4: The radial and tangential FWHM of reconstructed beads for different effective NAs with the MTF-mask filtering approach. (near-axis bead located 103 μm away from the axis of rotation; off-axis bead located 334 μm away from the axis of rotation; average bead diameter 14.8±0.13 μm)

To further analyse the resolution, the radial and tangential FWHM of the reconstructed beads with the MTF-mask filtering approach for different NAs are given in Table 3-4. Compared to the results with the standard FBP approach listed in Table 3-2, there is no significant difference between the FWHMs achieved using these two reconstruction techniques. This can be explained by the fact that MTF-mask filtering approach does not change the spatial frequency content of reconstructed objects directly, but rather suppresses high frequency "streak" artefacts particularly at reduced angular sampling.

In order to illustrate the impact of the modified reconstruction employing the MTF-mask filter on a biological sample, a Fli:GFP transgenic zebrafish embryo was imaged at 3 dpf to test the performance with an angular sampling interval of 1º (Fig. 3.16 (a, e)), 2º (Fig. 3.16 (b, f)), 3º (Fig. 3.16 (c, g)) and 4º (Fig. 3.16 (d, h)) with the interval becoming larger for improved imaging speed. Comparing Fig. 3.16 (b, c, d) and (f, g, h), the background streak artefacts are significantly suppressed by the modified reconstruction with the MTF-mask filtering approach. This approach provides a reconstructed image quality that is comparable to the standard FBP reconstruction with 1º interval sampling, shown in Fig. 3.16 (a), but at a portion (1/2, 1/3, 1/4) of the acquisition time and therefore a portion (1/2, 1/3, 1/4) of the overall light dose on the zebrafish embryo.

In conclusion, this section has demonstrated that it is possible to reduce the image acquisition time by reducing the number of acquired projections while maintaining reasonable image quality. This is achieved by modifying the standard OPT reconstruction process to incorporate the experimentally determined system optical characteristics by MTF-mask filtering. This MTF-mask filter restricts high frequency components to the region around the focal plane and progressively decreases the spatial frequency bandwidth with defocus. It helps to maintain the fidelity of reconstructions as the angular sampling is reduced. It is noted that, for complex objects, non-suppressed artefacts will not only affect the background but could also affect the reconstructed object itself.

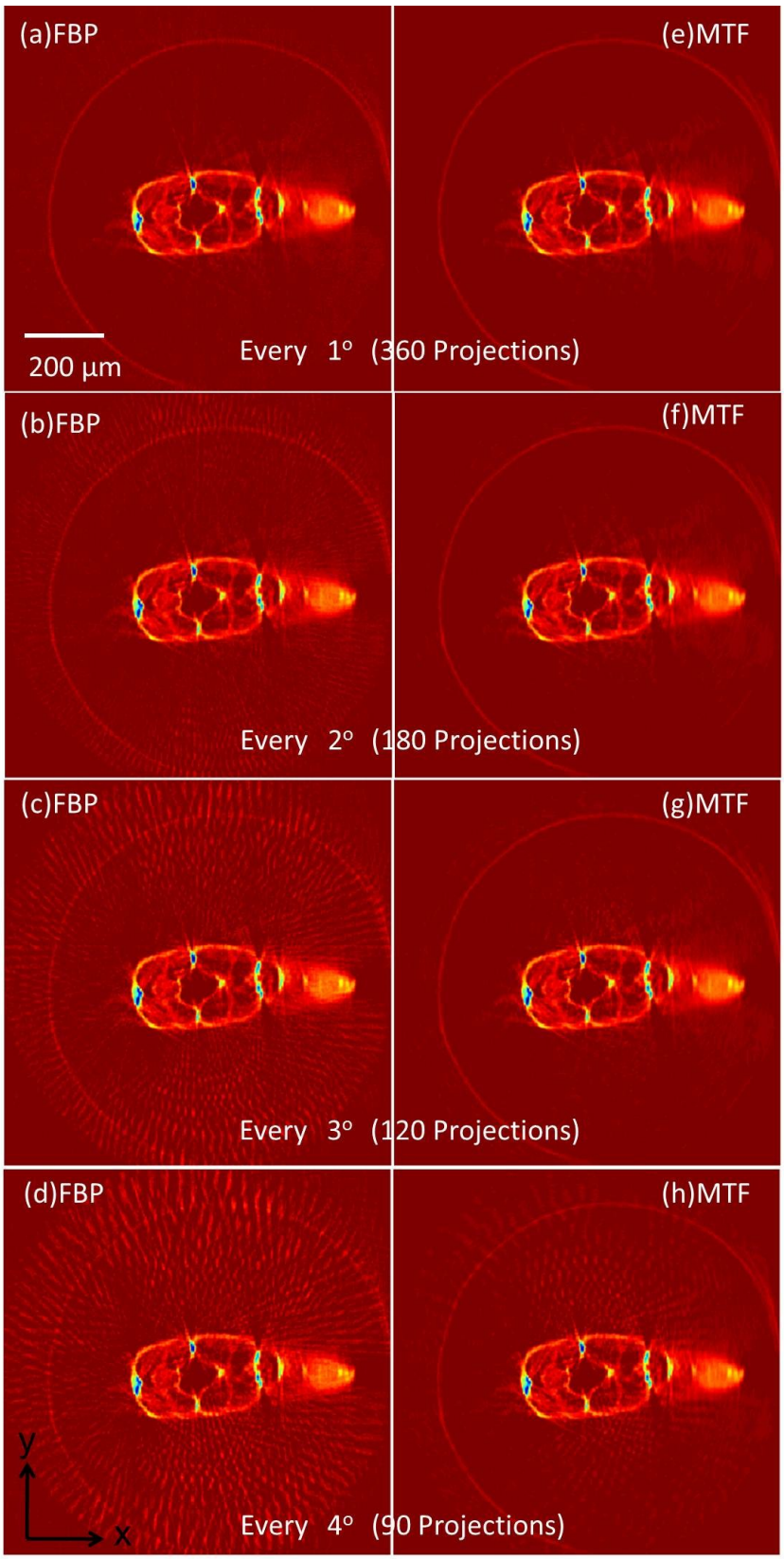


Figure 3.16: (a, b, c, d) Standard FBP reconstruction and (e, f, g, h) MTF-mask filtered reconstruction of a zebrafish embryo with an effective NA of 0.07 from 360 projections (i.e. a 1° interval), 180 projections (i.e. a 2° interval), 120 projections (i.e. a 3° interval) and 90 projections (i.e. a 4° interval) respectively. Scale bar, 200 µm.

3.4. MTF deconvolution reconstruction

Image quality can be degraded by the deviations from the parallel-beam assumption that underlies the standard FBP algorithm. These arise when OPT is implemented with relatively high NA optics, for which rays at a range of angles with respect to the optical axis are collected and so reconstructed images suffer from defocus blurring. OPT is typically undertaken with samples that extend beyond the DOF of the imaging systems and so the tangential resolution of the reconstructed images decreases radially away from the axis of rotation. Building on ideas developed for Single-Photon Emission Computed Tomography (SPECT) [89], this distance-dependent resolution can be addressed by applying an appropriate deconvolution filter to the raw projection data in order to correct for the frequency modulation applied to the signal by the optical system and therefore improve the achieved spatial resolution. In previous work this deconvolution filter has been based on a computationally generated PSF [90]. This section extends the above approach by modifying the standard FBP algorithm to incorporate a deconvolution filter based on the experimentally determined MTF for the effective collection NA of the optical imaging system. This experimentally derived deconvolution filter can be employed to realistically correct for the spatial frequency modulation applied by the imaging system and provide an improvement in the reconstructed image resolution for high-angular-sampling OPT acquisitions.

3.4.1. MTF-deconvolution filter

Using the notation adopted in [90], the deconvolution filter in the frequency domain can be visualised as a combination of two distinct components, given by

$$H_{deconv} = H_{W_\lim}^{-1} \cdot H_{Mm} \qquad 3\text{-}4$$

where $H_{W_\lim}^{-1}$ is the combination of a maximum limited recovery filter according to the experimentally determined MTF for a given effective NA and a Wiener filter to de-emphasize the noise while H_{Mm} is an edge-decaying MTF-mask filter.

It is necessary to employ the Wiener filter in this process since deconvolution can be highly sensitive to noise, especially in the high-frequency region. The Wiener deconvolution filter is described by

$$H_W^{-1} = \frac{H_M^* \cdot S_x}{|H_M|^2 \cdot S_x + S_u} \qquad 3\text{-}5$$

where H_M is the determined MTF, S_x is the signal power spectrum and S_u is the noise power spectrum.

In order to minimise the impact of noise in the information gaps in frequency space from the acquired data, the recovery filter is scaled by a weighting factor, given by [90]

$$H_{W_\lim}^{-1} = \begin{cases} \left|H_W^{-1}\right| : \left|H_W^{-1}\right| \le C_t \\ C_t + C_r\left(1 - \exp\left[-\dfrac{\left|H_W^{-1}\right| - C_t}{C_r}\right]\right) : \left|H_W^{-1}\right| > C_t \end{cases} \qquad 3\text{-}6$$

where C_t is the magnitude value at which the transition begins and C_r is the range used as a transition to the maximum magnitude. The common values for these parameters were selected empirically based on the suppression of high-frequency noise and background noise in the final reconstructed images and the values used in the deconvolution filter for this experiment were C_t =3, C_r =0.3, S_x=1, S_u=0.01.

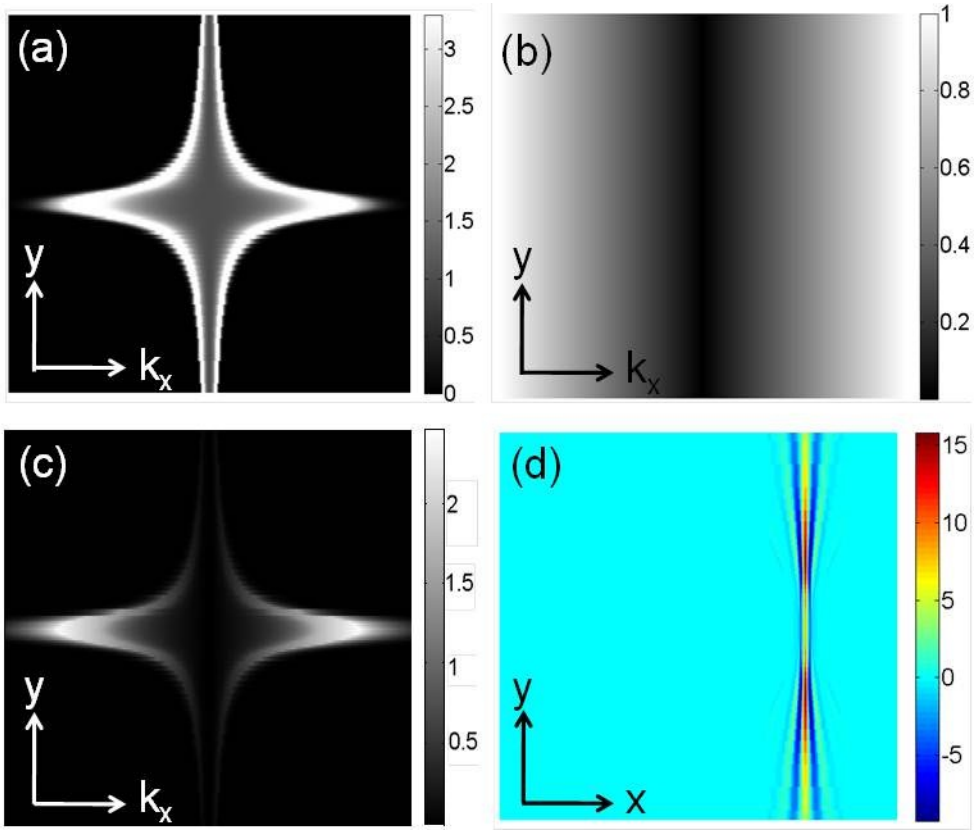


Figure 3.17: (a) 2-D MTF-deconvolution filter, (b) 2-D ramp filter, (c) the combination of the MTF-deconvolution filter and the 2-D ramp filter and (d) backprojection at one angle with the MTF-deconvolution and the ramp filter applied in the reconstruction process from the same simulated data in Fig. 3.9. (effective NA of 0.07 for the OPT system; 1040×1040 pixels, Δk_x = 0.596 mm^{-1}, Δx, Δy = 1.6125 μm; the scale of x,y is -838.5 – 838.5 μm and the scale of k_x is -309.92 – 309.92 mm^{-1})

The inverse filter emphasizes the high frequency components and may emphasize the frequencies beyond the bandlimit of the lens, i.e. dominated by noise. To explicitly de-emphasize the regions that contain no information (i.e. beyond the bandlimit) and may not be sufficiently de-emphasized by Wiener filter, the edge-decaying MTF-mask filter is generated by normalizing the MTF by a threshold value of 7% and setting values above 1 to 1 and then rolling down to zero. It is similar to MTF-mask filter described in the last

section, but increasingly suppresses the frequency components beyond the 7% threshold and reduces the sharpness of the edge. This is due to the considering of the sensitiveness of deconvolution to noise.

Figure 3.17 (a) shows the corresponding 2-D MTF-deconvolution filter for an effective collection NA of 0.07 of the OPT system and (b) shows a normalised 2-D ramp filter. Figure 3.17 (c) shows the combination of the MTF-deconvolution filter and the ramp filter applied in the reconstruction process and (d) shows the 2-D backprojection from the same simulated data in Fig. 3.9 but with this combined filter applied. Therefore the frequency modulation applied to the data by the imaging system can be realistically corrected.

3.4.2. MTF-deconvolution reconstruction results and discussion

The same raw experimental dataset of the bead phantom was reconstructed with the MTF-deconvolution approach. The reconstruction process produced a stack of cross-sectional images of the bead phantom for different effective collection NAs of 0.06, 0.07 and 0.09.

3.4.2.1. Simulation results

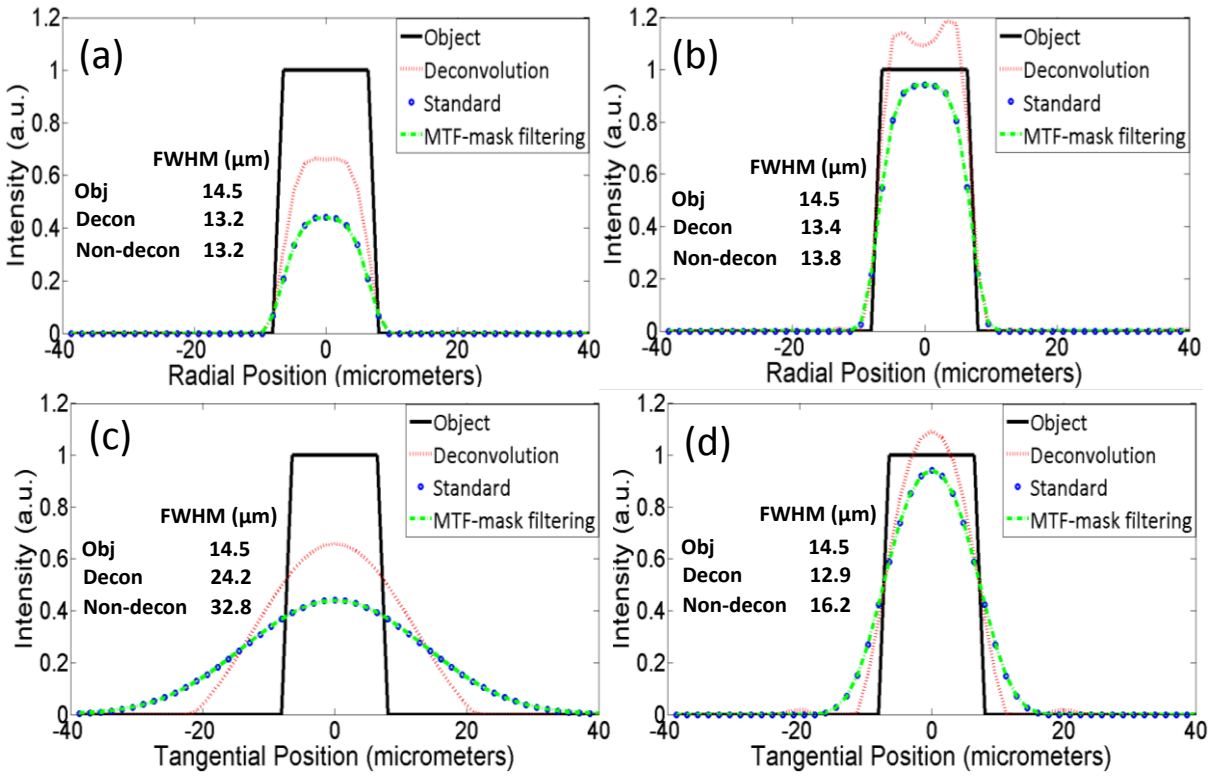


Figure 3.18: Plots through the radial directions of (a) the off-axis bead and (b) the near-axis bead and the tangential axes of (c) the off-axis bead and (d) of the near-axis bead simulated results with an effective NA of 0.07 respectively. Obj – object; Decon – deconvolution; Non-decon – standard and MTF-mask filtering. (off-axis bead located 334 µm away from the axis of rotation; near-axis bead located 103 µm away from the axis of rotation.)

To evaluate the performances of different reconstruction approaches, the same simulated dataset was employed for comparison with the experimental data, as described in sub-section 3.3.1. Figure 3.18 shows the radial and tangential line-sections (i.e. indicates the radial and tangential FWHM) of the reconstructed bead centres from the simulated bead projection data at an effective NA of 0.07 and a 1º angular sampling. The reconstructions were obtained with different reconstruction approaches, namely deconvolution, standard and MTF-mask filtering. As shown in Fig. 3.18 (c), the modified reconstruction with the additional MTF-deconvolution filter exhibits a noticeable improvement in resolution (i.e. reduced FWHM) compared to the non-deconvolved reconstructions (i.e. with the standard FBP and the MTF-mask filtering approach). The deconvolution process improves the resolution and increases the brightness of the reconstructed beads because it realistically corrects for the spatial frequency modulation applied by the imaging system. The reconstructed near-axis bead (i.e. the bead located 103 µm from the axis of rotation) exhibits higher contrast and improved tangential resolution than the reconstructed off-axis bead (i.e. the bead located 334 µm from the axis of rotation). This is due to the fact that the DOF for the NA of 0.07 did not allow the off-axis bead to stay in reasonable focus during the whole acquisition (i.e. did not transfer all the high frequency information all the time). It is also noted that there is no noticeable difference between the results achieved at a 1º angular sampling using the standard FBP approach and the modified MTF-mask filtering approach since the MTF-mask filter restricts the high frequency components to the region where the system has transferred them rather than changes the spatial frequency content of reconstructed objects directly.

3.4.2.2. Experiment results

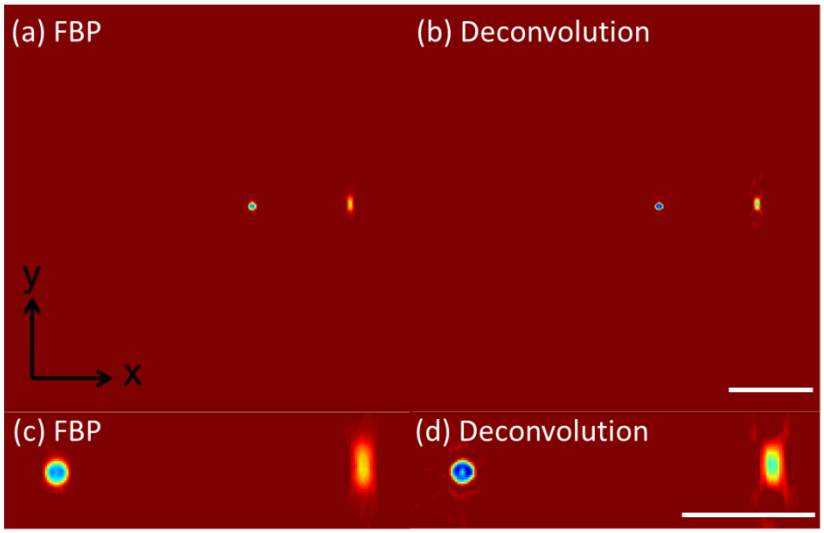


Figure 3.19: The experimental results for (a) standard FBP reconstruction; (b) deconvolution reconstruction (Scale bar, 200 µm) from 360 projections (i.e. a 1º interval) for an effective NA of 0.07 with (c) and (d) showing the magnified reconstructions respectively (Scale bar, 100 µm).

Figure 3.19 (a) and (b) show the images reconstructed from 360 angular projections (i.e. a 1º interval) by applying the standard FBP and the deconvolution approach respectively to experimental data acquired with

an effective NA of 0.07. The tangential extent of the reconstructed off-axis bead using deconvolution is visibly reduced, demonstrating the resolution improvement. The resolution improvement is also confirmed by the measured radial and tangential FWHM of the off-axis bead, as listed in Table 3-5, illustrating a ~24–28% improvement compared to the non-deconvolved reconstruction. Although some ringing is evident, it is not significantly detrimental to the reconstructed image for the high-angular-sampling acquisition.

In order to illustrate the impact of the modified reconstruction employing the additional MTF-deconvolution filter on a biological sample, the same raw experimental dataset of the zebrafish embryo, as described in section 3.3, was used for the reconstruction. Figure 3.20 (a) and (b) show the images reconstructed from the highest-angular-sampling (i.e. a 1° interval) dataset by applying the standard FBP and the MTF-deconvolution approach to the same zebrafish respectively. Comparing them on the same intensity scale, the deconvolved image exhibits improved contrast and resolution, both of which come from the more realistic correction for the spatial frequency modulation applied by the imaging system.

FWHM (µm)	FBP	MTF-mask	MTF-deconvolution
Radial (off-axis)	12.6	12.4	12.0
Tangential (off-axis)	32.9	31.4	23.9

Table 3-5: The radial and tangential FWHM of reconstructed off-axis beads with different reconstruction approaches for an effective NA of 0.07. (FBP – standard FBP reconstruction; MTF-mask – MTF-mask filtered reconstruction; MTF-deconvolution –MTF-deconvolution reconstruction; off-axis bead located 334 µm away from the axis of rotation; average bead diameter 14.8±0.13 µm)

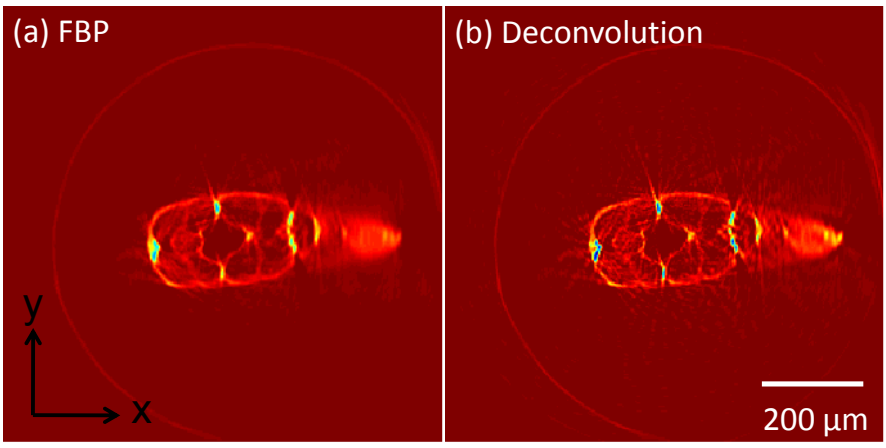


Figure 3.20: The experimental results for (a) standard FBP reconstruction; (b) deconvolution reconstruction of zebrafish embryo with an effective NA 0.07 from 360 projections (i.e. a 1° interval). The images are on the same intensity scale to show the difference. Scale bar, 200 µm.

It is noted that deconvolution involves increased amplification of spatial frequencies approaching the cut-off frequency since it is used to correct for the spatial frequency modulation applied by the imaging system. When reducing the acquired angular projections (i.e. reducing angular sampling), this will result in stronger "streak" artefacts and therefore, the image quality decreases rapidly. Thus, deconvolution is most appropriate for datasets acquired at a high angular sampling (e.g. the minimum required sampling as described in Eq. 3-3).

3.5. Conclusions

This chapter has described the investigation of modified OPT reconstruction methods incorporating the optical characteristics (i.e. the MTF) of the imaging system by either MTF-mask filtering or deconvolution of the MTF. It has demonstrated, for the first time, that a modified reconstruction process with MTF-mask filtering improves the reconstructed image quality by suppressing imaging artefacts that arise when the number of acquired projections is reduced and therefore, enables increased imaging speed and a reduced light dose. It has also demonstrated that a modified reconstruction process with MTF-deconvolution filtering provides improved spatial resolution reconstructions for high-angular-sampling OPT acquisitions by realistically deconvolving the spatial frequency modulation imposed by the imaging system on the acquired data.

The optical system was characterised by experimentally determining the MTFs for different effective collection NAs as a function of defocus to quantify the additional spatial frequency modulation applied by the use of focussed optical radiation with its associated instrumentation in OPT. The MTF information was obtained using the tilted knife-edge technique and an appropriate analytical equation. The MTFs illustrated that as the NA decreased, the in-focus bandwidth (i.e. lateral resolution) decreased and the DOF of the optical system increased as expected. For this intensity-based OPT microscope system, the experimentally measured MTFs also illustrated that the spatial resolution was limited by the diffraction limit (i.e. the NA of the optical system and the wavelength) for the NAs measured (0.09, 0.07, 0.06, 0.05, 0.04 and 0.03) rather than the camera pixel size.

The assumption of parallel-beam projection that underlies the standard FBP algorithm was discussed. In practice, however, the use of focussed optical radiation with its associated instrumentation limits the applicability of standard FBP algorithm in OPT. A bead phantom was used to quantify the performances of the reconstruction with the standard FBP algorithm. The reconstruction results illustrated the trade-off in OPT between the achieved spatial lateral resolution and the DOF and also showed that the tomographic images could be reasonably reconstructed from plane wavefronts as expected for the standard FBP when the DOF is comparable to the sample size.

A modified reconstruction method incorporating the MTF information of the system by employing the experimentally determined MTFs as mask filters was investigated. This approach was implemented by using

a 2-D binary filter based on the MTF frequency cut-off as an additional filter during the "filtering" process in the reconstruction. This MTF-mask filter restricts the high frequency information to the region around the focal plane and progressively decreases the spatial frequency bandwidth with defocus and therefore helps to maintain the fidelity of reconstructions as the angular sampling is reduced, thereby facilitating faster OPT acquisitions while maintaining reasonable quality reconstructions. The same bead phantom was used to quantify the performances of the modified reconstruction with this MTF-mask filtering approach, illustrating a reduction in the average background by approximately 72% for an NA of 0.09 and by approximately 38% for an NA of 0.07 compared to the standard FBP reconstruction. As a biological illustration, a Fli:GFP transgenic zebrafish embryo (3 dpf) was also imaged to demonstrate the improved imaging speed (proportional to the acquisition time) by using the MTF-mask filtered reconstruction. This investigation is of significant interest because the reduced total number of acquired projections will reduce the overall light dose on the sample - and therefore any photobleaching and/or phototoxic effects - and improve the time-lapse resolution. In addition, the reduced total number of acquired projections will lead in a reduction in the space needed to store the data set and its reconstruction time.

The modified reconstruction method incorporating the MTF information of the system by employing the experimentally determined MTFs as deconvolution filters was also investigated. The deconvolution filter was employed to realistically correct for the spatial frequency modulation applied by the imaging system. The same bead phantom was used to quantify the performances of modified reconstruction with the MTF-deconvolution filtering approach, illustrating an improvement of ~24–28% in the reconstructed image resolution for an NA of 0.07 with high-angular-sampling (i.e. a 1° interval) OPT acquisitions compared to the non-deconvolved reconstructions (i.e. with the standard FBP and the MTF-mask filtering approach). As a biological illustration, the same Fli:GFP transgenic zebrafish embryo dataset at high-angular sampling (i.e. a 1º interval) was also reconstructed with the MTF-deconvolution approach, illustrating the improved resolution and contrast. However, it should be noted that since the deconvolution is used to correct for the spatial frequency modulation by the imaging system, it involves increased amplification of spatial frequencies approaching the cut-off frequency. For reduced angular sampling, this will result in stronger "streak" artefacts and thus, the image quality decreases rapidly. Therefore, deconvolution is most appropriate for datasets acquired at a high angular sampling (e.g. the minimum required sampling as described in Eq. 3-3).

It is noted that although the work described in this chapter operated through modifying the standard FBP reconstruction to incorporate the experimentally determined MTF information. This MTF information can also be incorporated in other reconstruction techniques, e.g. algebraic reconstruction techniques [82].

Chapter 4: Angular multiplexing OPT to improve image quality

The previous chapter has described a development by modifying OPT reconstruction techniques that account for the optical characteristics (i.e. the MTF) of the imaging system. This chapter is concerned with an experimental development of OPT by introducing an angular multiplexing technique that can improve the resolution and the light collection efficiency by ameliorating the trade-off between NA and sample thickness.

Initially, angular multiplexing OPT is demonstrated by employing dual optical imaging channels acquiring data simultaneously at two orthogonal projection angles, focused on shifted planes in the sample [94]. The extension to four axis OPT is also demonstrated by employing one imaging system sequentially acquiring four data sets at shifted focal planes. This development improves the average spatial resolution for a given sample while increasing the light collection efficiency, thereby enabling increased acquisition speed and reduced light dose. Topics in this chapter include:

- Development of dual axis OPT system at shifted focal plane
- Demonstration of four axis OPT system at shifted focal plane

4.1. Shifted focal plane dual-axis OPT system

The potential to apply OPT to "mesoscopic" samples for biomedical research, particularly for *in vivo* imaging, has prompted increasing interest in optimizing the image quality and resolution and minimizing the image data acquisition time [83-88, 90, 93, 98, 114], as discussed in sub-section 2.7.2.

Image quality can be degraded by the deviations from the parallel-beam projection assumption that underlies the standard FBP algorithm. These arise when OPT is implemented with a relatively high NA optics, which are generally desirable for fluorescence imaging because the light collection efficiency and the lateral resolution increase with NA. For high resolution OPT there is a trade-off between increasing the NA to improve the in-focus lateral resolution and reducing the NA to increase the DOF in order to ensure that the whole sample is in reasonable focus. In the case when the DOF of the imaging system is comparable to the diameter of the sample, the tomographic images are reconstructed from plane wavefronts as expected for the standard FBP. However, OPT is typically undertaken with samples that extend beyond the confocal parameter (Rayleigh range) of the imaging lens and so the tangential resolution of the reconstructed images decreases radially away from the axis of rotation. In the commonly implemented case when the DOF is matched to the radius of the sample, as depicted in Fig. 4.1, all of the sample will be in focus for part of its revolution and an image of approximately uniform spatial resolution can still be reconstructed. In this work, this experimental configuration is referred to as the 'standard' single axis OPT, in which the trade-off is actually mitigated by arranging for the DOF of the imaging system to extend through half of the sample by

locating the focal plane at 1/4 of the way into the sample rather than focusing at the axis of rotation. Therefore the front half of the sample is imaged under the parallel-beam projection approximation, which interrogates the entire sample during the course of a full rotation.

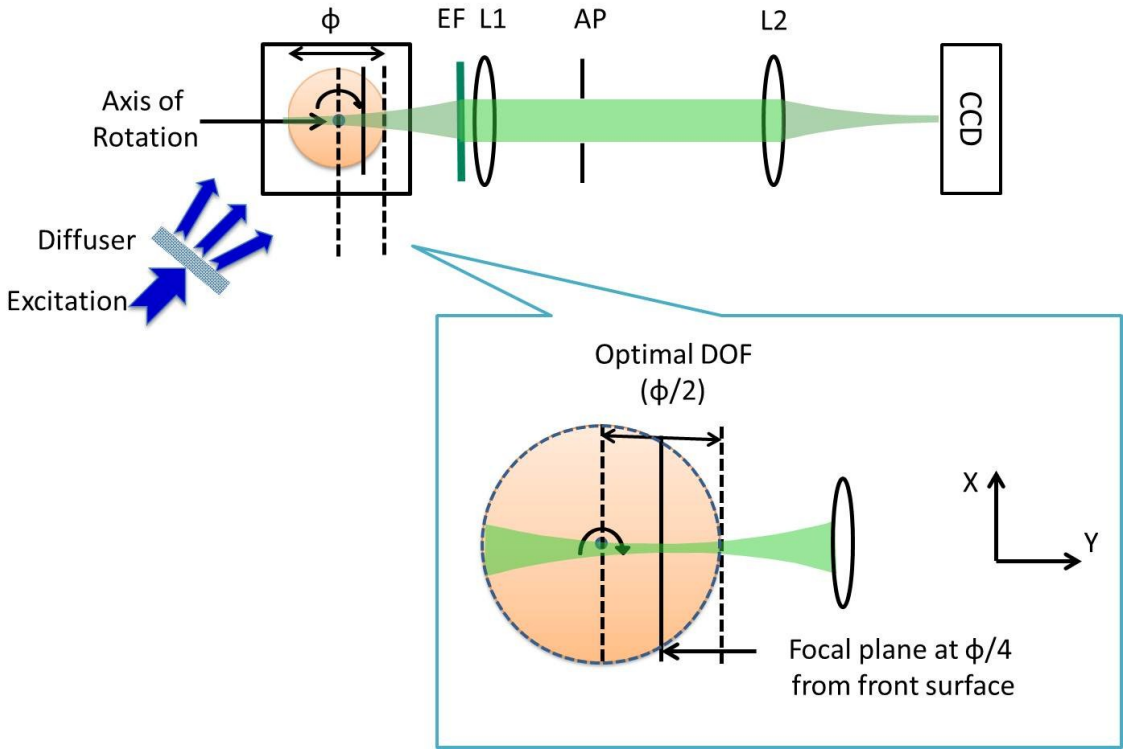


Figure 4.1: Schematic of "standard" OPT system setup. DOF – depth of field, EF – emission filter, AP – aperture, L1 and L2 – tube lens, ϕ – sample diameter.

However, in the case when the DOF is less than the sample radius, the reconstructed spatial resolution will decrease away from the focal plane. This situation is typical for many biomedical applications where high resolution is required but the sample is much greater than the DOF. One way to address this issue is to extend the DOF for a given NA by axially scanning the focal plane through the sample [92, 93]. This also helps to achieve uniform collection efficiency throughout a sample that is larger than the DOF of the imaging system and to realise higher spatial resolution imaging over larger volumes [93]. However, while this method can provide a significant spatial resolution improvement for OPT of smaller samples (hundreds of μm) [93], it is less attractive in the mesoscopic regime (1 – 10 mm) due to the larger focal scanning distances (~mm) required and the concomitant issues of scanning stability and speed. This may also add significantly to the total image acquisition time and increase the total light exposure for each tomographic image acquisition. Generally, it is always desirable to minimise the image acquisition time for experimental convenience, to be able to resolve dynamics and to minimise the exposure of the sample to optical radiation, which can result in photobleaching and phototoxicity.

The essence of the innovation of the following research is to ameliorate the trade-off between spatial resolution and sample thickness for relatively high NA OPT systems while simultaneously reducing the total image acquisition time and the corresponding light dose. The new idea is to achieve this by angular multiplexing, i.e. by acquiring image data from different depths at multiple projection angles simultaneously. To demonstrate this angular multiplexing OPT, dual optical imaging channels focused on shifted planes in the sample are employed, which acquire data simultaneously at two orthogonal angular projections [94], as illustrated in Fig. 4.2. This dual axis OPT improves the average spatial resolution while increasing the light collection efficiency, thereby enabling increased acquisition speed and reduced light dose.

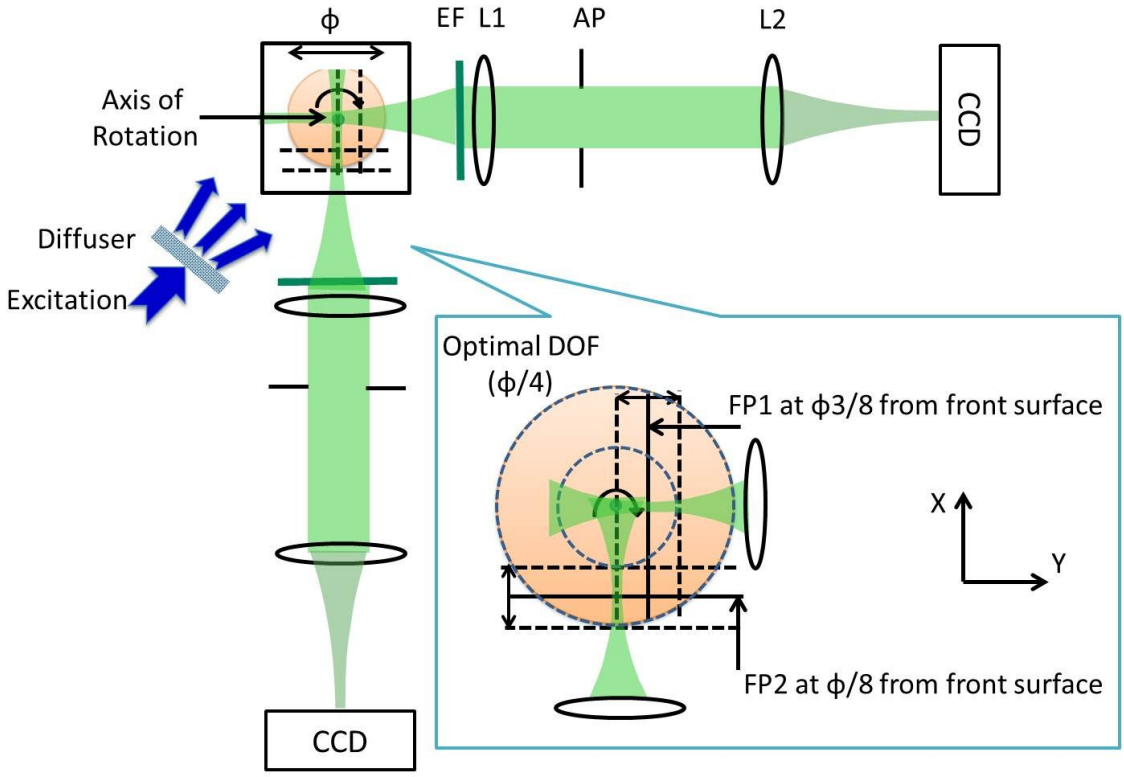


Figure 4.2: Schematic of dual axis OPT system setup (inset shows optimal DOFs and the focal planes of two imaging systems). DOF – depth of field, EF – emission filter, AP – aperture, L1 and L2 – tube lens, FP – focal plane, ϕ – sample diameter.

For a sample of a given size, this dual axis approach permits an increase in NA compared to the standard approach while maintaining the parallel-beam approximation if the DOF of each imaging channel extends throughout a quarter of the sample with the focal planes of the imaging channels being located at 1/8 and 3/8 respectively of the way into the sample along the radius, such that together they cover the front half of the sample. If the pixels of the imaging detector (e.g. CCD, sCMOS) can sample the image sufficiently such that the image resolution of the system is dominated by the optical resolution of the system, i.e. by the NA of the objective lens and the imaging wavelength, then the dual axis approach should permit a corresponding

improvement in spatial resolution by a factor of approximately √2 compared to the standard OPT configuration. Furthermore, it also should permit a corresponding improvement in light collection efficiency by a factor of approximately 4 due to the increased NA and the use of two imaging channels. However, in practice, the range of pixel number and density for image detectors is limited and then the DOF does not depend only on the NA of the objective lens and imaging wavelength but are related by Eq. 2-21. Therefore, the maximum image resolution improvement will not be realised unless the image is sufficiently sampled by the imaging detector, i.e. the pixels are adequately small compared to the PSF.

4.1.1. Imaging setup

The experimental configuration of dual axis OPT at shifted focal planes is depicted in Fig. 4.2. In brief, the sample was mounted under a rotation stage (T-NM17A200, Zaber Technologies Inc.) and suspended in a refractive-index matched environment (water in this experiment). The wide-field excitation was provided by a commercial 473 nm laser (Cobolt Blues^{TM}) incorporating a rotating diffuser. The fluorescence was imaged onto two CCD cameras (Clara, Andor Technology plc) using two imaging systems (L1: 25 mm achromatic doublet lens, L2: 50 mm achromatic doublet lens and an adjustable aperture) at orthogonal projection angles via appropriate emission filters (520 ± 17.5 nm). The effective collection NA was adjusted using the apertures (AP) in the back focal planes of lenses L1. The maximum FOV of the system, in which the lateral magnification was 2, was 3.35 × 4.49 mm^2.

4.1.2. Sample preparation

A cylindrical phantom of 3 mm diameter consisting of a low concentration suspension of fluorescent beads in 2% agarose, with an average bead diameter 4.2 μm and excitation/emission maxima at 505/515 nm respectively (F8859, Life Technologies Ltd), was used as a model sample. This bead phantom was suspended in a water-filled cuvette.

4.1.3. Acquisition settings and procedure

Image data was acquired on the "standard" single axis and the dual axis OPT systems described above using different apertures positioned in the back focal planes of lenses L1, resulting in an effective NA of 0.024 for the standard single axis OPT system with a DOF of 1.4 mm and an NA of 0.033 for each arm of the dual axis system, which gave a DOF of 0.78 mm. For the standard single axis OPT system, the focal plane was located at 0.69 mm from the axis of rotation axis while for the dual axis OPT system, the focal planes were located at 0.37 mm and 1.05 mm respectively from the rotation axis and thus, the imaging channels of the dual axis OPT system cover the same volume (i.e. the front half of the sample) as the standard OPT system under the parallel-beam projection approximation. During the acquisition for the bead phantom, image data was acquired at 0.9º angular intervals (i.e. 400 projections) as the sample rotated over a full rotation. The exposure time for each projection of the bead suspension was set 0.5 s for both systems.

The acquisition procedure for dual axis OPT system was adapted from the 'standard' procedure, as described in sub-section 3.2.2, to incorporate two CCD cameras. The acquisition settings and hardware control used an

in-house developed programme written in LabView 2010. Limited by the settings of the cameras, it was only possible to initialize/setup/query one camera at a time due to the internals of the Andor Software Development Kit (SDK), which gives the programmer access to the cameras. For a synchronised single scan, the CCDs were set to external trigger mode sequentially by the acquisition programme and then simultaneously externally triggered by a signal generator, which provided triggers at a user-defined period. After the integration, the CCDs were read out sequentially and the images were saved. After that, the rotation stage then switched to the next angular position. This process was repeated for a user-defined number of steps.

4.1.4. Reconstruction procedure

The standard FBP algorithm was applied for tomographic reconstruction. For the dual axis OPT system, two standard reconstructions were obtained from full raw projection data of each imaging channel using the FBP algorithm and then these two reconstructions were efficiently registered by cross-correlation [115]. The final tomographic reconstruction was achieved by adding two registered reconstructions together.

Alternatively, it could be achieved the other way round (i.e. to register the raw image data from two channels and add them together to form the "effective" sinograms first and then reconstruct the data using the FBP algorithm). Since the bead phantom (i.e. a simple structured sample) was used in the experiment, the achieved reconstructed results from these two methods were similar.

4.1.5. Results and discussion

The reconstruction process produced a stack of cross-sectional images of the bead phantom from the raw projection data for both systems. To compare the results for the standard single axis OPT and the dual axis OPT, a bead located 0.43 mm from the axis of rotation was chosen.

Figure 4.3 (a, b) show the resulting reconstructed images (X-Y and X-Z image slices) of this bead with the standard single axis OPT system while (c, d) show the corresponding reconstructed images with the dual axis OPT system. Since the beads, with an average diameter of 4.2 μm, are smaller than the optical resolution of both systems, these reconstructed images indicate the measured resolution of these OPT systems. The reconstructions of the dual axis OPT system directly exhibit improved spatial resolution and signal level.

The resolution improvement is also confirmed by the normalised line-sections through the Y axis of the reconstructed bead centre, as shown in Fig. 4.4 (a), with accompanying Gaussian fits providing FWHM of 13.4 μm and 10.8 μm for the standard and the dual axis OPT systems respectively. The significant improvement in signal level of the dual axis OPT system is also highlighted in Fig. 4.4 (b) by plotting the relative line intensity data. This signal level improvement results from both the ~3.8x increase in light collection efficiency and the improved resolution.

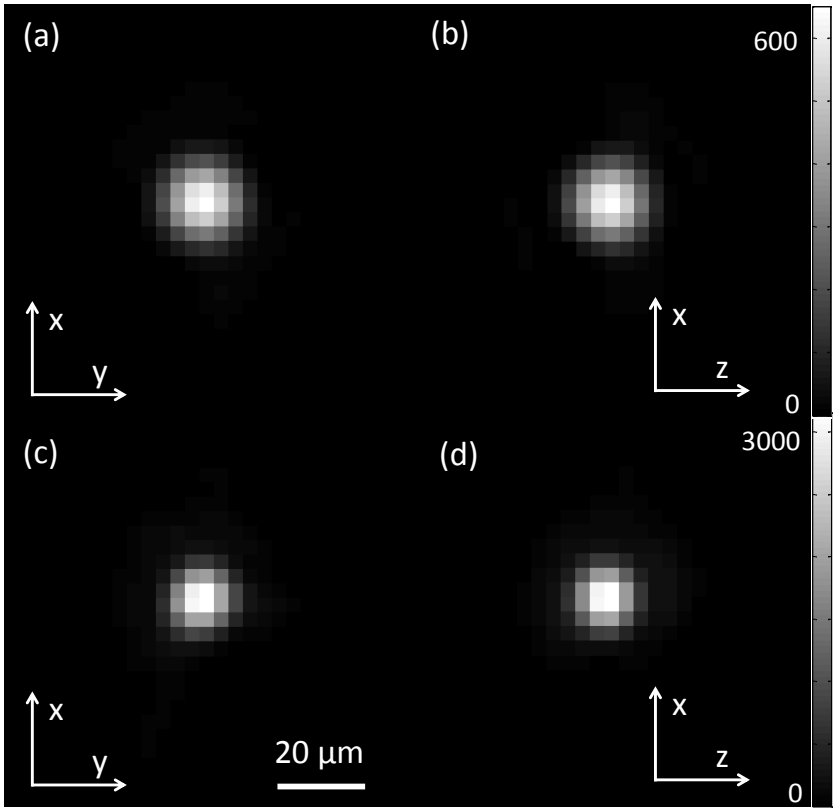


Figure 4.3: Reconstructed X-Y and X-Z image slices of a bead (located 0.43 mm from the axis of rotation) acquired with the standard OPT system (a, b) and the dual axis OPT system (c, d). Scale bar, 20 µm.

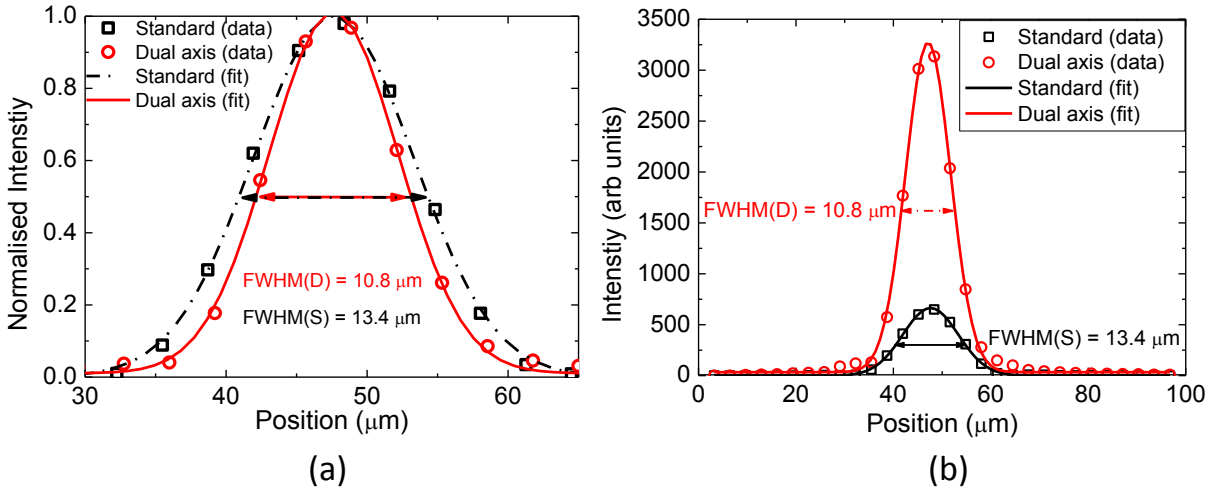


Figure 4.4: Line plots and Gaussian fits through the Y axis of the reconstructed bead in Fig. 4.3 for the dual axis (D, red line) and the standard (S, black lines) single axis OPT systems showing (a) normalised and (b) relative line intensity data.

To further analyse the resolution improvement, a number of beads at different distances from the axis of rotation (0.17, 0.34, 0.43, 0.65 and 0.98 mm) were analysed, as shown in Table 4-1. The measured average FWHM of these beads in the standard single axis and the dual axis OPT systems were 13.6±0.8 µm and

10.8±0.6 μm respectively, illustrating a ~20% improvement. The theoretical resolution at best focus, here defined as the lateral FWHM of Airy pattern of the imaging arm (i.e. limited by the NA of the objective lenses and the imaging wavelength), were 11.1 μm and 8.1 μm for the standard OPT with NA of 0.024 and the dual axis OPT with NA of 0.033 respectively. The observed values of the resolution are larger than the theoretical calculations. This can be explained by the fact that these OPT systems operate just within the sampling limit of the PSF and the reconstruction process involves interpolation. Nevertheless, a significant improvement in average spatial resolution and light collection efficiency has been demonstrated by using dual axis OPT focusing at shifted planes in the sample. This can be further improved by using imaging detectors with more resolution elements and an appropriate magnification.

	X (μm)		Y (μm)		Z (μm)	
	Standard	Dual-axis	Standard	Dual-axis	Standard	Dual-axis
Bead1 (0.17 mm)	13.8	10.6	13.7	10.3	13.1	10.4
Bead2 (0.34 mm)	13.7	10.6	13.6	11.3	12.9	10.2
Bead3 (0.43 mm)	13.6	11.0	13.4	10.8	13.1	10.4
Bead4 (0.65 mm)	12.2	10.9	14.6	10.9	14.0	11.1
Bead5 (0.98 mm)	15.4	12.7	12.7	10.4	14.0	11.2

Table 4-1: The FWHM of the standard and dual projection OPT reconstructions for beads at different locations.

To further illustrate the impact of the dual axis OPT system, the tail section of a fluorescent Casper:Fli-EGFP transgenic zebrafish was imaged at 54 dpf. Images were acquired at 200 angular projections over a full rotation with a CCD integration time of 0.1 s for both systems to maintain the total acquisition time at ~2.5 minutes (comprising 20 s of photon detection and 131 s of stage movement, CCD set-up and read out).

Figure 4.5 (a, b) show autoscaled MIPs of the 3-D reconstruction from the dual axis and the standard single axis OPT systems respectively while (c) shows the same MIP for the standard single axis OPT reconstruction displayed on the same intensity scale as (a). It is noted that unlike zebrafish embryos, mature fish exhibit significant optical scattering. Nevertheless, structures near the surface of the fish can be imaged, illustrating the significant improvement in the signal level and contrast for the dual axis OPT system. This improvement is also confirmed by the line-sections shown in Fig. 4.5 (d). The improved imaging efficiency could also be used to reduce the acquisition time of the dual axis OPT system to achieve the similar signal level of the standard approach, but with just a proportional reduction in illumination dose. It is noted that the orthogonal imaging systems could also be configured to collect light from the same sample volume, i.e. no shift in focal plane, to simply increase the imaging speed, e.g. for *in vivo* imaging.

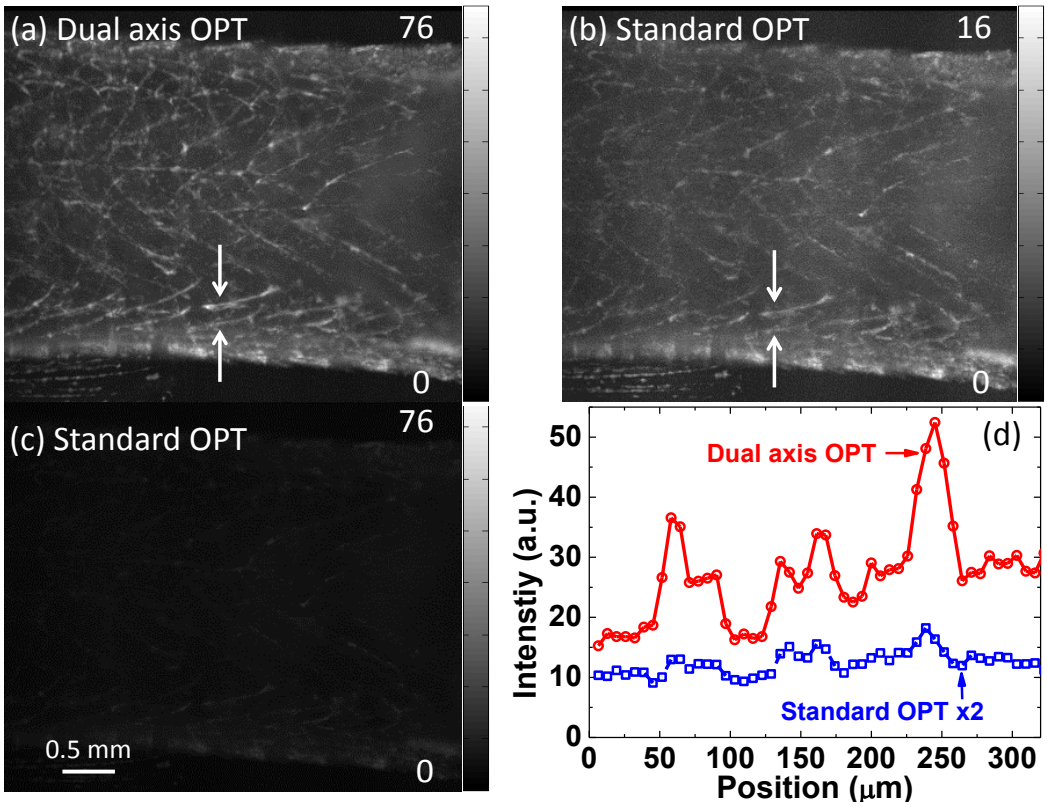


Figure 4.5: Maximum intensity projections of the 3-D reconstruction of a 54 dpf zebrafish tail acquired with (a) the dual axis and (b, c) the standard single axis OPT plotted for comparison with absolute intensity (a, b) and normalised intensity (a, c) scales; (d) intensity line profiles from figures (a, b) as indicated (arrows), where the standard OPT intensity data has been multiplied by 2 for clarity. Scale bar, 0.5 mm.

4.1.6. Further improvement in acquisition procedure

As described earlier in sub-section 4.1.3, the acquisition program could only sequentially initialize/setup/query one camera at a time due to the internals of the SDK, which slowed down the acquisition. In the fish tail imaging described in the last sub-section, each frame had an integration time of 0.1 s, leading to a total camera integration time (photon detection time) of 20 s. The remaining time of 131 s was due to the stage movement, rotational delay, CCD set-up and read out. This time can be significantly reduced by further developing the system and modifying the acquisition programme.

To facilitate a faster acquisition, two computers were used to run two CCD cameras separately. Each camera was controlled by software (Andor SOLIS) on each computer. The cameras were initialized and then set to operate in kinetic mode, which allowed the software to hold all the images during the acquisition and save them post acquisition, and in external trigger mode, which allowed the two cameras to simultaneously acquire images. The modified main LabView acquisition program only controlled the rotation stage and a multifunction data acquisition (DAQ) board (National Instruments USB-6008), which provided triggers at a user-defined period. After the integration for each frame, the rotation stage switched to the next angular position and the triggers were sent to the two cameras. This process was repeated for a user-defined number of steps. After the whole acquisition, the images were saved. The time for switching between the two

cameras, camera read out and image saving was significantly reduced. The response time from the rotation stage was also optimised. For the same acquisition settings for the fish tail imaging, in which each frame had an integration time of 0.1 s, leading to a total camera integration time of 20 s, the overall acquisition was reduced down to 45 s. The remaining time was only of 25 s due to the stage movement and triggering.

The reduced image acquisition time is of importance for experimental convenience, especially for *in vivo* imaging. It also consequently minimises the exposure of the sample to optical radiation, which can result in photobleaching and phototoxicity. It is noted that the exposure can also be minimised by employing a shutter to block the illumination when the cameras are not integrating.

4.2. Demonstration of four-axis OPT system

The last section has illustrated that a dual axis OPT system improves the average spatial resolution by ~20% while increasing the light collection efficiency by a factor of ~4 compared to the standard single axis OPT. This approach can be extended to more than two imaging axes, thereby further reducing the imaging acquisition time and corresponding light dose while improving the image resolution and enhancing the ability to image larger samples. This section demonstrates the proof of principle extension to four axis OPT by using one imaging system with an increased NA sequentially acquiring OPT data sets 4 times at shifted focal planes. For a sample of a given size, the DOF of each acquisition (to simulate each imaging channel) extends throughout 1/8 of the specimen with the focal planes of the acquisitions located at 1/16, 3/16, 5/16 and 7/16 respectively along the radius of the sample, such that together they cover the front half of the sample. This four axis approach can permit another increase in NA compared to the dual axis OPT while still maintaining the approximation to parallel-beam projection. If the pixels of the imaging detector sample the image sufficiently such that the image resolution of the system is dominated by the optical resolution of the system, then this four axis approach should permit a corresponding improvement in the resolution and the light collection efficiency by another factor of $\sqrt{2}$ and 4 respectively compared to the dual axis OPT configuration.

4.2.1. Imaging setup

Here four axis OPT is demonstrated by using one imaging system with an increased NA sequentially acquiring four datasets following the configuration depicted in Fig. 4.6. The setup was slightly modified from the configuration described in sub-section 4.1.1 by imaging the sample onto a sCMOS camera (Zyla, Andor Technology plc, 5.5 megapixel, 6.45 μm pixel size, cooled to 0 ºC) via the same imaging system increasing the maximum FOV of this system to 6.7×8.9 mm^2.

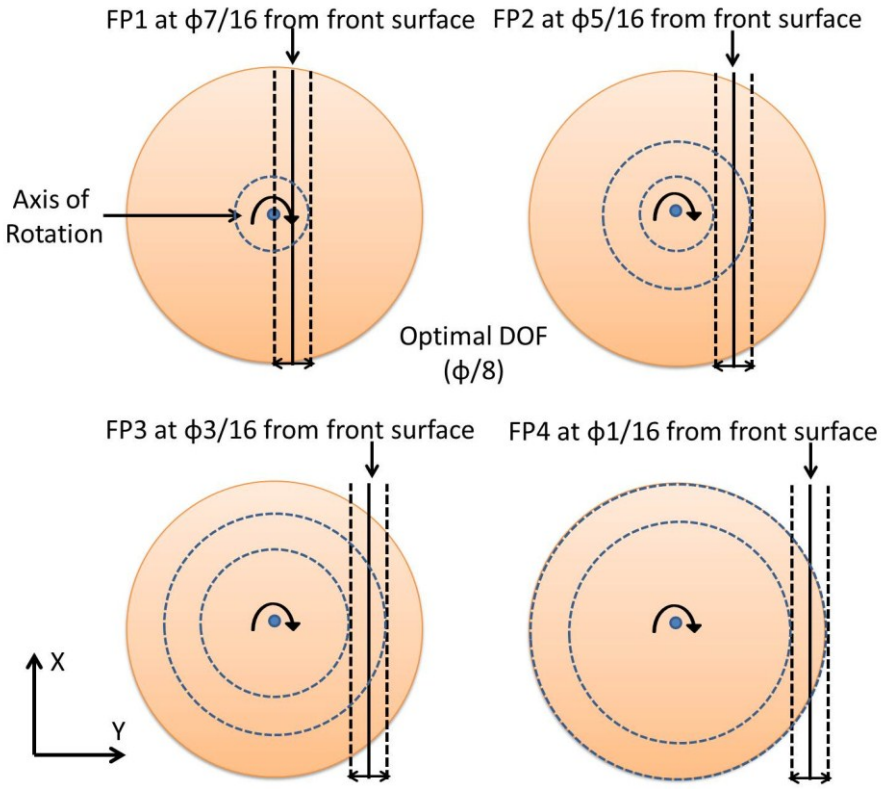


Figure 4.6: Schematic of using one camera demonstrating four axis OPT system setup. DOF – depth of field, FP – focal plane, ϕ – sample diameter.

4.2.2. Sample preparation and acquisition settings

A similar cylindrical bead phantom was prepared and used in the acquisition, but with a larger diameter of 5 mm. Image data was acquired with an NA of 0.017 for the standard single axis OPT system, which gave a DOF of 2.5 mm, with an NA of 0.025 for the dual axis OPT system, which gave a DOF of 1.3 mm, and with an NA of 0.037 for the four axis OPT system, which gave a DOF of 0.65 mm. For the standard single axis OPT system, the focal plane was located at 1.25 mm from the rotation axis; for the dual axis OPT system, the focal planes were located at 0.63 mm and 1.87 mm respectively from the rotation axis while for the four axis OPT system, the focal planes were located at 0.32 mm, 0.93mm, 1.56 and 2.18 mm respectively from the rotation axis. Therefore, together the effective acquisitions of all OPT systems cover the same volume (i.e. the front half of the sample) while maintaining the parallel-beam projection assumption. During the acquisition for the bead phantom, images were acquired sequentially at different focal planes by the sCMOS at 0.9º angular intervals (i.e. 400 projections) over a full rotation of the sample with 0.18 s integration time for each frame.

4.2.3. Reconstruction procedure

The standard FBP algorithm was applied for tomographic reconstruction. For four axis OPT system, the raw projections of each acquisition were efficiently registered by cross-correlation [115] first. After that, the sinograms were determined by selectively adding the effective sinograms for each acquisition. In this

process, effective sinograms were selected by only choosing the part within the DOF for each acquisition. Then, the standard FBP algorithm was applied for the final tomographic reconstruction.

4.2.4. Results and discussion

To compare the results for the standard single axis, the dual axis and the four axis OPT, a bead located 1.92 mm from the rotation axis was chosen.

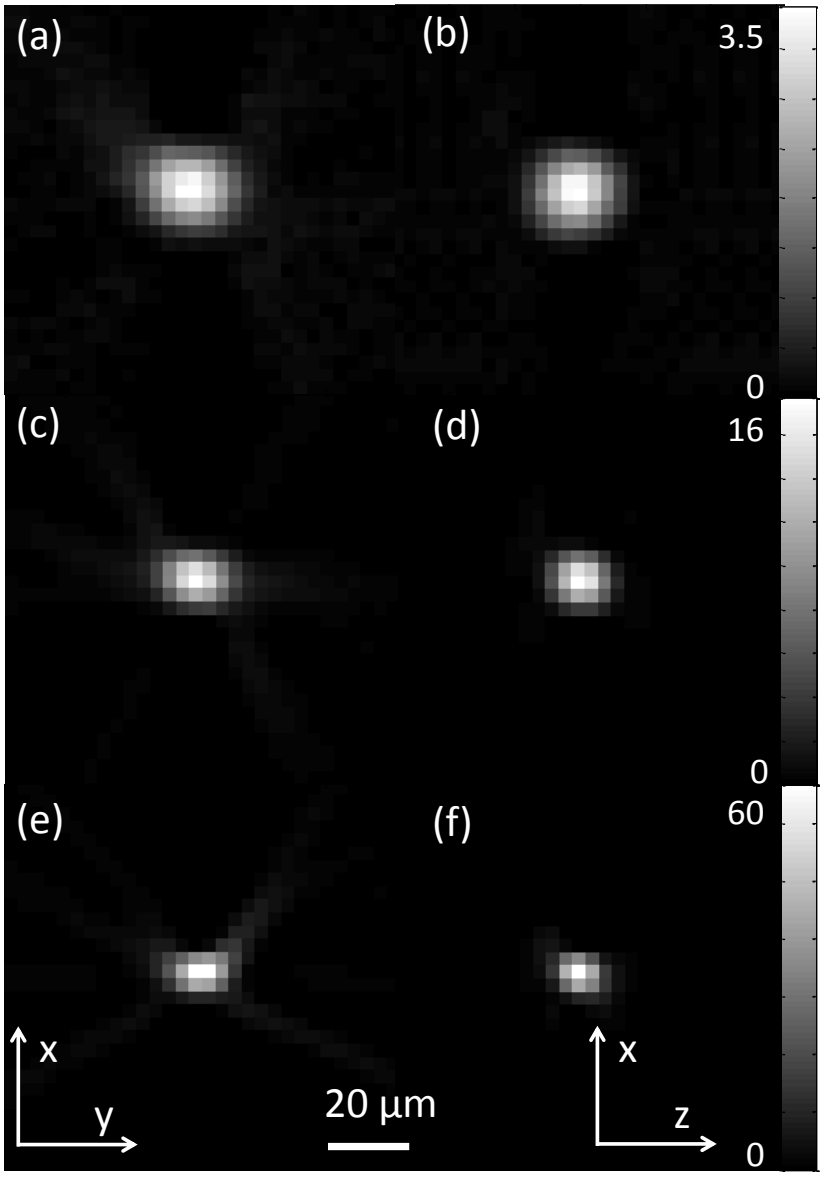


Figure 4.7: Reconstructed X-Y and X-Z image slices of a bead acquired from the standard single axis OPT acquisition (a, b), the dual axis OPT acquisition (c, d) and the four axis OPT acquisition (e, f). Scale bar, 20 µm.

Figure 4.7 (a, b) show the resulting reconstructed images (X-Y and X-Z image slices) of this bead from the standard OPT acquisition; (c, d) show the corresponding reconstructed images from the dual axis OPT

acquisition while (e, f) show the corresponding reconstructed images from the four axis OPT acquisition. Since the bead is smaller than the imaging resolution for all three OPT acquisitions, these reconstructed images indicate the measured resolution of these systems. The reconstructions of the four axis OPT acquisition directly exhibit improved spatial resolution and signal level compared to those of the dual axis and the standard single axis OPT acquisitions. The resolution improvement is also confirmed by the normalised line-sections through the X axis of the reconstructed bead centre, as shown in Fig. 4.8 (a), with accompanying Gaussian fits providing FWHM of 14.5 μm, 9.9 μm and 7.2 μm for the standard, the dual axis and the four axis OPT acquisitions respectively. The significant improvement of signal level for the four axis OPT acquisition is also highlighted in Fig. 4.8 (b) by plotting the relative line-sections through the reconstructed bead centre.

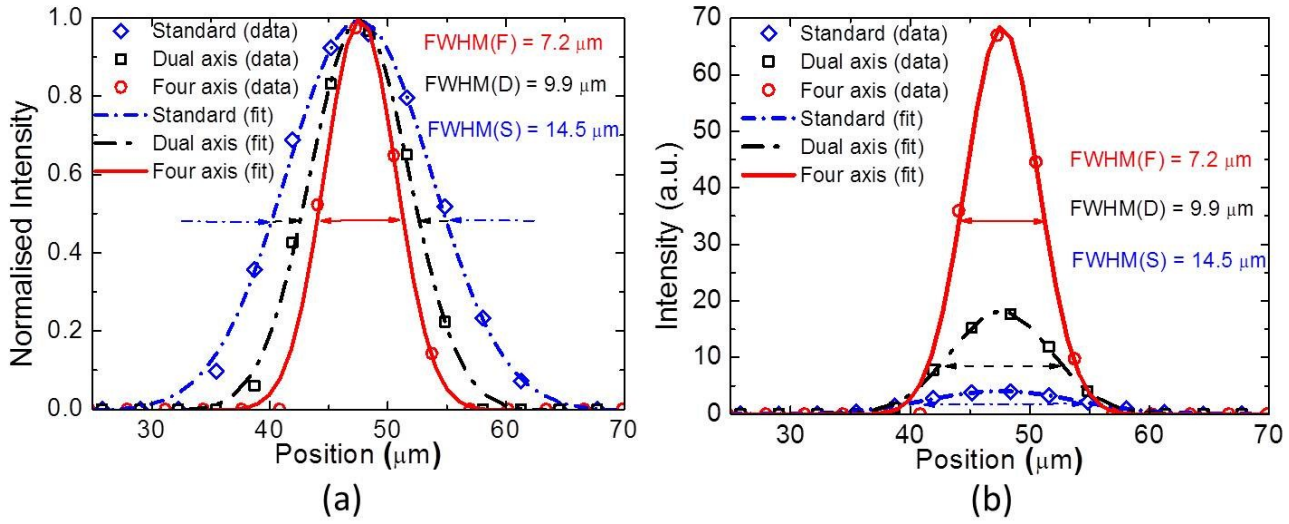


Figure 4.8: Line plots and Gaussian fits through the X axis of the reconstructed bead in Fig. 4.7 for the four axis (F, red line), the dual axis (D, black line) and the standard single axis (S, blue lines) OPT acquisitions showing (a) normalised and (b) relative line intensity data.

To further analyse the resolution improvement among different approaches, three beads at different distances from the axis of rotation (0.65, 1.09 and 1.92 mm) were analysed, as shown in Table 4-2,3,4. The measured average FWHM of these beads in the standard single axis, the dual axis and the four axis OPT acquisitions were 16.5±1.1 μm, 13.1±1.8 μm and 10.4±1.8 μm respectively, showing a further ~20% improvement for four axis OPT compared to the dual axis approach. The theoretical resolution at best focus, here defined as the FWHM of Airy pattern of the imaging arm, were 15.3 μm, 10.4 μm and 7.0 μm for the standard OPT with NA of 0.017, the dual axis OPT with NA of 0.025 and the four axis OPT with NA of 0.037 respectively. The observed values of the resolution are still larger than the theoretical calculations. This can also be explained by the same fact that these OPT systems operate just within the sampling limit of the PSF and the reconstruction process involves interpolation. Nevertheless, a further improvement in achieved average

spatial resolution and light collection efficiency for the four axis OPT compared to the dual axis OPT has been demonstrated.

FWHM (μm)	Standard (15.3) NA 0.017	Dual axis (10.4) NA 0.025	Four axis (7.0) NA 0.037
X	14.5	9.9	7.2
Y	17.1	14.2	11.4
Z	15.3	10.9	8.7

Table 4-2: The FWHM of the standard, the dual axis and the four axis OPT reconstructions for the bead in Fig. 4.7 (1.92 mm away from the rotation axis).

FWHM (μm)	Standard (15.3) NA 0.017	Dual axis (10.4) NA 0.025	Four axis (7.0) NA 0.037
X	15.7	13.7	11.4
Y	17.9	15.4	12.1
Z	16.9	14.4	11.6

Table 4-3: The FWHM of the standard, the dual axis and the four axis OPT reconstructions for the bead locating at 0.65mm away from the rotation axis.

FWHM (μm)	Standard (15.3) NA 0.017	Dual axis (10.4) NA 0.025	Four axis (7.0) NA 0.037
X	16.9	11.5	8.4
Y	17.0	13.9	11.4
Z	17.2	13.6	11.7

Table 4-4: The FWHM of the standard, the dual axis and the four axis OPT reconstruction for the bead locating at 1.09 mm away from the rotation axis.

In conclusion, angular multiplexing OPT leading to improved image resolution and light collection efficiency has been demonstrated by a multiple axis OPT system acquiring image data at shifted focal planes in the sample. This technique permits imaging with increased NA for a sample of a given size and thus, reducing the image acquisition time and corresponding light dose while improving the spatial resolution. It can be used to image absorption as well as fluorescence.

4.3. Conclusions

This chapter has introduced the development of OPT system by using an angular multiplexing technique. It has demonstrated that angular multiplexing OPT improves the average spatial resolution while increasing the light collection efficiency, thereby enabling increased acquisition speed and reduced light dose.

Angular multiplexing OPT was demonstrated by employing dual optical imaging channels, focused on shifted focal planes in the sample, acquiring data simultaneously at two orthogonal angular projections. This approach permitted imaging with increased NA for a given sample. A sub-resolution bead phantom was used to quantify the dual axis OPT performance compared to the "standard" approach, illustrating a ~20% improvement in achieved resolution and ~4x increase in light collection efficiency, thereby enabling increased acquisition speed and reduced light dose. The tail section of a fluorescent Casper:Fli-EGFP transgenic zebrafish (54 dpf) was also imaged to further illustrate the impact of the dual axis OPT system, illustrating the significant improvement in the signal level and contrast. The dual axis OPT system and the acquisition programme were further developed to facilitate a faster acquisition by significantly reducing the time for switching between two cameras, camera read out and imaging saving. This development is of significance for experimental convenience, especially for *in vivo* imaging since it is able to minimise the exposure of the sample to optical radiation, and therefore any photobleaching or phototoxic effects.

An extension to four-axis OPT by sequentially acquiring datasets using one camera focused at shifted planes was also demonstrated, illustrating a further ~20% improvement in achieved spatial resolution and ~4x increase in light collection efficiency compared to the dual axis approach.

In conclusion, angular multiplexing OPT permits imaging with increased NA for a sample of a given size and thus, reducing the image acquisition time and corresponding light dose while improving the spatial resolution. It is noted that it can be used to image absorption as well as fluorescence.

Chapter 5: Angular multiplexing OPT to achieve triangulation of dynamic samples

The previous chapter has described a development of OPT by introducing an angular multiplexing technique that improves the average spatial resolution while increasing the light collection efficiency. This chapter is concerned with the development of angular multiplexing OPT to achieve triangulation of dynamic samples. The dual-axis OPT configuration is extended to acquire images at orthogonal angles simultaneously such that features within the sample can be approximately localised in 3-D and thus, feature motion can be tracked with a time resolution of the acquisition frame rate rather than the total acquisition time for the full tomographic data set incorporating all angular projections. The use of orthogonal projections for 3-D time-lapse feature tracking with a higher time resolution and a reduced light dose is demonstrated and an initial demonstration of cell migration mapping within a zebrafish is presented. Topics in this chapter include:

- Simulation of angular multiplexing OPT to obtain 3-D time-lapse localisation information with a higher time resolution and a reduced light dose
- Demonstration of angular multiplexing OPT to obtain 3-D cell migration mapping within a zebrafish

5.1. Preface

Chapter 4 demonstrated angular multiplexing OPT (i.e. acquiring image data at multiple angular projections at shifted focal planes simultaneously) improves the average spatial resolution and the light collection efficiency, and thus can be used to facilitate a faster acquisition with reduced light dose. This has been initially demonstrated by dual axis OPT acquiring data sets at shifted focal planes in a sample simultaneously at orthogonal projections. This configuration can be extended to conduct multiple image acquisition at orthogonal projection angles such that features within the sample can be approximately localised in 3-D and thus, feature motion can be tracked with a time resolution equal to the acquisition frame rate. This is of importance since data sets presented in OPT typically represent “single time-point” acquisitions and therefore the time-lapse resolution is the total acquisition time for the full tomographic data set incorporating all angular projections. The position of features cannot be accurately reconstructed or even reconstructed at all if the features move a significant distance during this acquisition time, as shown in Fig. 5.1.

It is noted that static orthogonal projections can be used to approximately localise features in 3-D, especially in the case of features moving independently during the acquisition. However, the need for rotation rather than just orthogonal imaging is of importance when features are stationary over the acquisition. In this case, the artefacts cannot be removed for static orthogonal imaging, but can be easily removed for orthogonal imaging combined with rotation by using a standard FBP algorithm. In addition, the rotation can provide more angular information for the whole acquisition and therefore, may increase tracking accuracy. In this

chapter, the use of rotating orthogonal projections to track 3-D time-lapse feature motion is demonstrated and an initial demonstration of 3-D cell migration mapping within a zebrafish is presented.

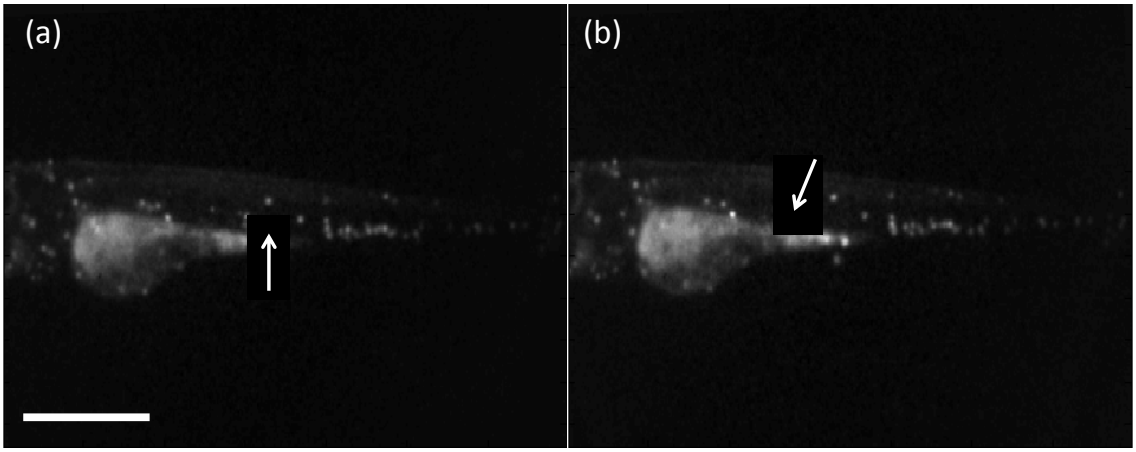


Figure 5.1: The raw two sequential projections from a typical OPT acquisition of live LysC:GFP zebrafish embryo at 3 dpf in fluorescence based on the intensity-based OPT system. Arrows indicate a moving cell which would not be accurately reconstructed. Scale bar, 500 µm.

5.2. Simulation

To evaluate the performance of tracking 3-D feature motion by using pairs of orthogonal projections, a simulated dataset was generated. The simulated sample consisted of 5 beads of equal brightness at different initial positions with independent velocities in 3-D. The raw corresponding orthogonal projections were generated as the simulated volume rotated at 1º angular intervals for 20 time points. The simulation does not account for scattering, absorption, light propagation, variation in collection efficiency or the defocus effects of the optical system, but serves only to model tracking time-lapse 3-D localisation information by using pairs of orthogonal projections.

5.2.1. 3-D localisation information extraction

Figure 5.2 (a) and (b) show a few projections at different time points at each angle (labelled as 0° and 90°) respectively. The 3-D reconstruction at each time point was determined by backprojecting two segmented orthogonal projections, which were obtained by generating a binary mask of the raw data, then finding the intersections of the structures. After the coarse reconstruction, the localisation information of the beads in the volume was extracted by cross-correlation using a "standard" simulated bead as a reference. Figure 5.3 shows reconstructed X-Y image slices of a bead from pairs of orthogonal projections at different time points, in which the white and red arrows indicate the beads shown in Fig. 5.2 with the same colour. These X-Y image slices of the 3-D reconstructions illustrate how the feature information can be approximately localised in the volume using a pair of orthogonal projections.

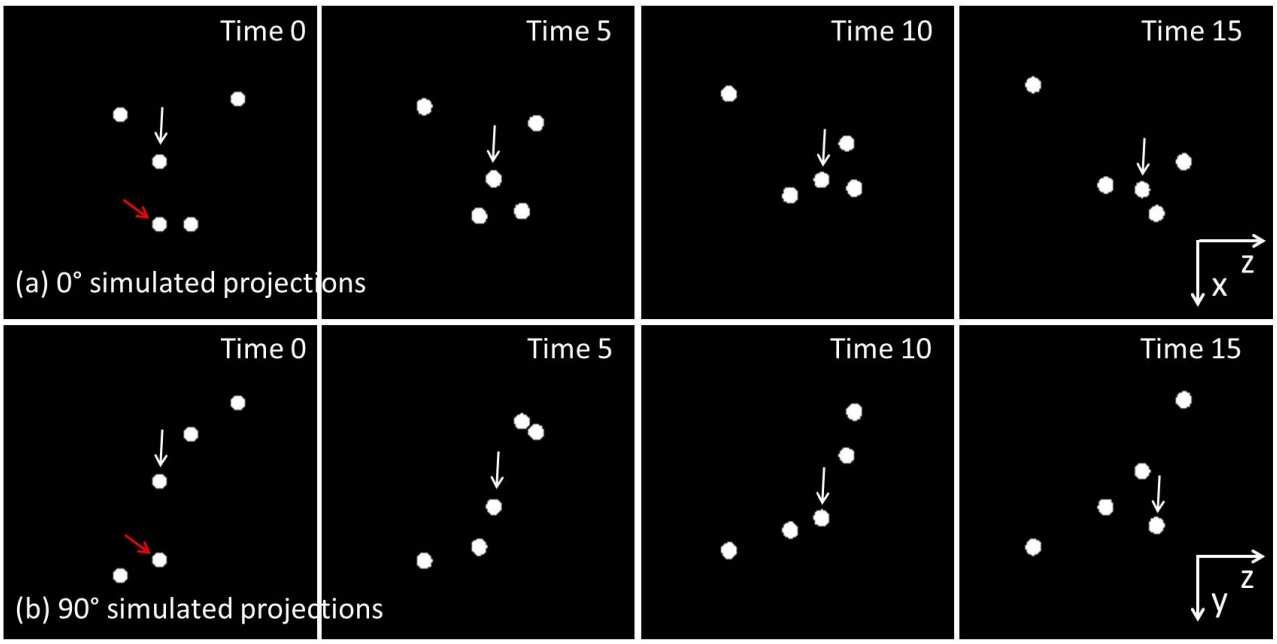


Figure 5.2: The raw corresponding orthogonal projections from (a) 0° view and (b) 90° view as the simulated volume rotated at different time points. White arrows indicate the bead reconstructed in Fig. 5.3 while red arrows indicate another bead in the same plane at Time 0.

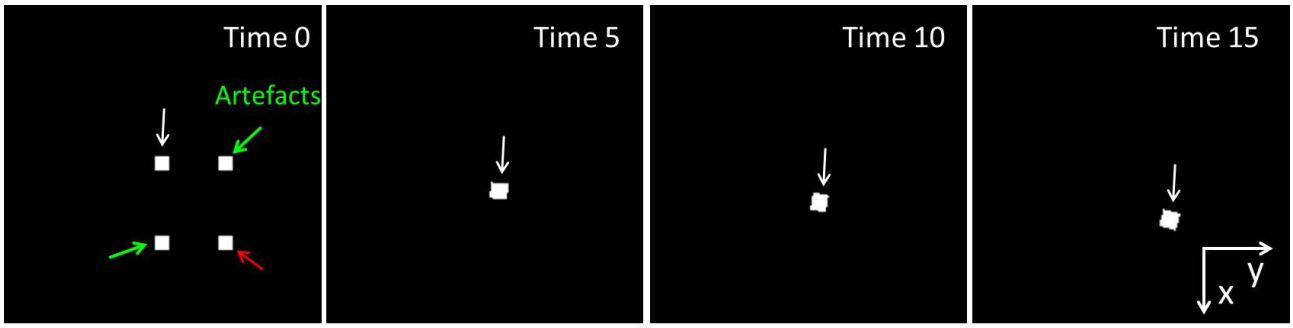


Figure 5.3: Reconstructed X-Y image slices of a bead from pairs of orthogonal projections at different time points. Artefacts (green arrows) could potentially be produced when more than one bead is present in the same Z plane but can be identified by using the consistency of full time-lapse information. White and red arrows indicate the beads shown in Fig. 5.2 with the same colour.

It is noted that using just a pair of orthogonal projections could potentially produce artefacts in the reconstruction when more than one bead is present in the same Z plane, as depicted in Fig. 5.2 and Fig. 5.3 (Time 0). This is due to the lost depth information in each projection. When these two objects (indicated by the white and red arrows in Fig. 5.2) are present in the same plane, the intersections of two backprojections at orthogonal angles produce two real objects (white and red arrows) and two artefacts (green arrows) from

the coarse reconstruction. Fortunately in practice, however, these artefacts can be removed by considering the consistency of the full time-lapse information. Considering the features in the sample move independently (e.g. cell migration), the artefacts may appear and disappear while the real features follow a continuous trace. Even if the features are stationary over the acquisition, the artefacts can be easily removed due to the rotation.

5.2.2. Results and discussion

The coarse reconstruction process produced a stack of cross-sectional (X-Y) binary images, indicating the intersections from pairs of orthogonal projection data at each time point. To further illustrate the potential artefacts introduced in this coarse reconstruction, Fig. 5.4 (a, b) show the comparison of the simulated movement from the object volumes and the coarse reconstructions respectively as an X-Y projection view by adding the 20 time points together.

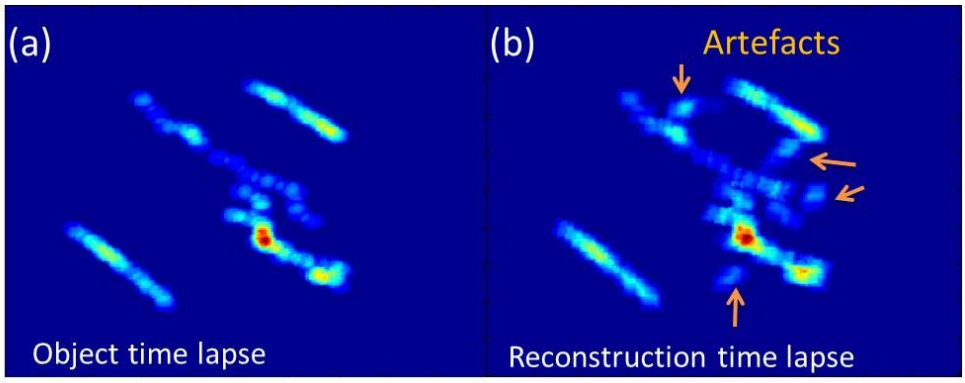


Figure 5.4: The comparison of the simulated movements from the original object volumes and the coarse reconstructions respectively at X-Y projection view by adding 20 time points together. Artefacts (arrows) could be produced in the reconstruction when more than one bead is present in the same Z plane.

The localisation results were extracted from the original bead volumes and the coarse reconstructions, after removing the artefacts, at different time points. Figure 5.5 shows 3-D traces of beads over the 20 time points, where the solid lines corresponds to the original movements and the points to the localisation information extracted from the coarse 3-D reconstructions. These curves illustrate how the feature motion can be tracked by using pairs of orthogonal projections and the consistency of the full time-lapse information of the features.

It is noted that increasingly complex features or movements in the volume will increase the difficulty in removing the artefacts and decrease the accuracy of the feature motion tracking by using just a pair of orthogonal projections at each time point. This, however, can be further improved by using more than two imaging axes, thereby reducing the artefacts potentially produced from the insufficient projections and enhancing the accuracy of motion tracking.

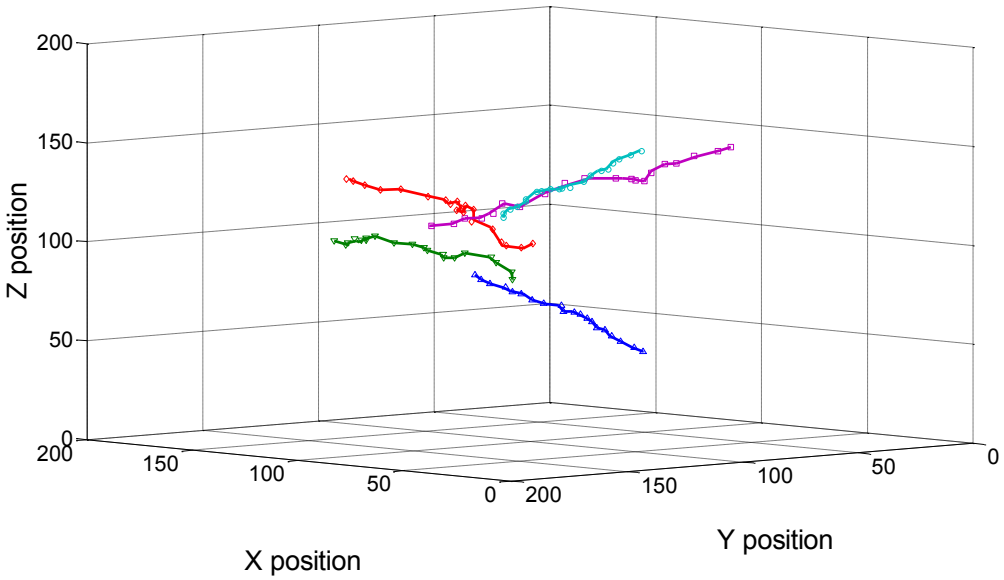


Figure 5.5: 3-D traces of bead motion over the 20 time points with solid lines corresponding to the original object movements and the points to the localisation information extracted from the coarse 3-D reconstructions.

5.3. Initial demonstration of 3-D cell migration mapping within zebrafish

The simulation results demonstrate the plausibility of tracking 3-D feature motion by using pairs of orthogonal projections with a time resolution of the individual frame rate rather than the total acquisition time for the full tomographic data set. This section demonstrates how to modify the dual axis OPT system to acquire orthogonal projections for tracking 3-D time-lapse feature motion and presents an initial demonstration of 3-D cell migration mapping within a zebrafish embryo.

An inflammatory response to tissue damage is conserved in almost all animal phyla. Inflammation, which is part of the complex biological response of vascular tissues to harmful stimuli, is a protective attempt by the organism to remove the stimuli and to initiate the healing process. Generally neutrophils, macrophages and their equivalents will be recruited to the wound site and may release signals that direct the healing process. This cell migration toward sites of tissue damage is of major significance because a clearer understanding of the inflammation response would be helpful in designing new therapies for tissue repair and controlling excessive inflammatory response. Typically, 3-D tracking in *in vivo* models requires a certain acquisition rate to obtain adequate information to achieve 3-D volumetric structure at each time point. The corresponding light dose may result in photobleaching or phototoxic effects. It is always desirable to minimise the acquisition time and the light dose for experimental convenience, especially for *in vivo* imaging or tracking. What follows demonstrates that it is plausible using a dual orthogonal projection acquisition system acquiring data simultaneously to provide 3-D cell migration mapping in a model of wound induced

inflammation in a zebrafish embryo with a sufficient time resolution and significantly reduced light dose, compared to time-lapse volumetric imaging.

5.3.1. Imaging setup

The setup was slightly modified from the configuration described in sub-section 4.1.1 by focusing the two imaging arms on a common plane. The experiment configuration of the dual image acquisition system, at orthogonal projection angles while focusing on the axis of rotation, is depicted in Fig. 5.6. A shutter (ThorLabs Inc, SH05), which was electronically controlled (ThorLabs Inc, apt-Solenoid controller), was positioned directly after the excitation laser to prevent light exposure on the sample when not acquiring projection images.

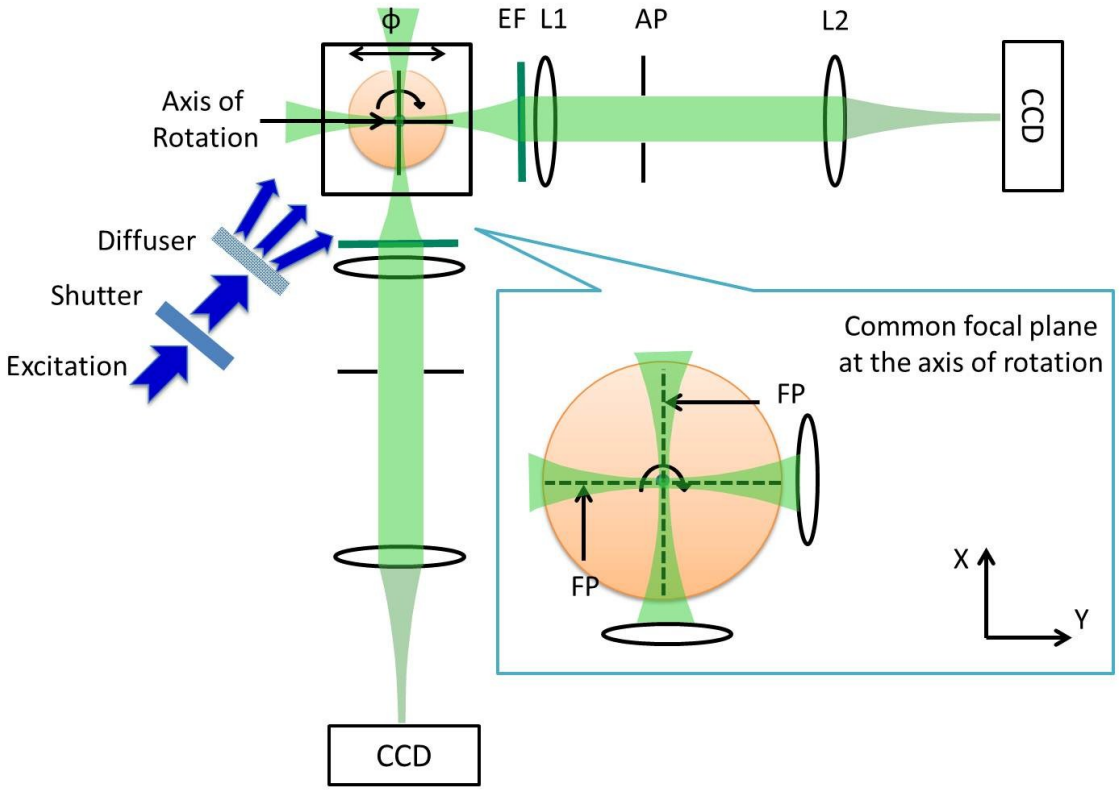


Figure 5.6: Schematic of dual image acquisition system setup (inset shows the common focal plane of two orthogonal imaging axes on the axis of rotation).EF – emission filter, AP – aperture, L1 and L2 – tube lens, FP – focal plane, ϕ – sample diameter.

5.3.2. Sample preparation and mounting

A transgenic zebrafish line (LysC: GFP mitfa-/- roy-/-) which is transparent and expresses GFP in neutrophils was used as an exemplar wound healing model for *in vivo* imaging of neutrophil recruitment to the site of damage. Embryos were raised in embryo medium (dechlorinated system water containing 0.0003% (v/v) methylene blue). Embryos at 2 dpf were embedded in 1% low melt point agarose, made from

embryo media, containing 0.3 mM MS-222 (Sigma) as an anesthetic. After anesthetization, they were drawn into translucent FEP tubing (06406-60, Cole-Palmer) with a refractive index similar to that of water that can be used in an index matched chamber for imaging applications. The translucent FEP tubing had inner and outer diameters of 0.8 and 1.6 mm respectively. Agarose was added to increase the viscosity of the water and prevent movement of the anaesthetized zebrafish embryo. A tail injury was induced 30 minutes before imaging to provide a stimulus and recruit the myeloid cells towards the wound site.

5.3.3. Acquisition settings and procedure

Image data was acquired on the dual orthogonal acquisition system described above using apertures positioned in the back focal planes of lenses L1, resulting in effective collection NA of 0.033 with a DOF of 0.78 mm. The resulting in-focus lateral resolution was ~11 μm. The focal planes of the two imaging arms were located at the axis of rotation. During the acquisition, image data was acquired at 0.9º angular intervals as the sample rotated with a certain time delay (15 s) between frames. Each frame had an integration time of 0.3 s for the fluorescence acquisition and 100 images (90º rotation) were acquired, which resulted in the acquisition times ~24 minutes. Both standard fluorescence and transmitted OPT data sets were also acquired with an integration time of 0.3 s and 1 s respectively at 0.9º angular intervals (i.e. a total of 400 projection images were recorded for each imaging arm) as the sample rotated over the full rotation. The total acquisition time for the OPT data sets was ~8 minutes and ~13 minutes for the standard fluorescence and transmitted light acquisitions respectively.

The acquisition procedure was adapted from the acquisition procedure used in the dual axis OPT system, described in sub-section 4.1.3, to include the shutter control. The shutter was open when the system was ready for a synchronised single scan. Then the CCDs were set to be simultaneously triggered by an external signal. After the acquisition, the shutter was closed and the rotation stage switched to the next angular position. This process was then repeated for a user-defined number of steps (e.g. 100 steps for each dataset). The process could be further developed by adapting the fast acquisition programme, described in sub-section 4.1.6, and thus, the acquisition time can be significantly reduced.

5.3.4. 3-D localisation information extraction

Ideally, the cells expressing GFP would have equal fluorescence brightness. In practice, however, the fluorescence intensity can be easily affected by the variable concentration of the fluorophores (e.g. expression level, clustering of cells, etc.), the effects of the collection efficiency (e.g. at different locations from the focal plane), the spatial variation in excitation, scattering and absorption of both excitation light and emitted fluorescence. Therefore, a local thresholding approach (Fiji, auto local threshold) was used to achieve image segmentation as an initial step of significance for further localisation information extraction. The threshold was computed for each pixel according to the "local" image intensity within a window of a certain radius around it. The implementation of Bernsen's thresholding method [116] was chosen, in which a circular window instead of a rectangular one was employed. This method employed a user-provided contrast threshold. If the local contrast was equal or above the contrast threshold, the threshold was set at the local

mid-grey value while if the local contrast was below the contrast threshold the neighbourhood was considered to consist only of one class and the pixel was set to background. Figure 5.7 (a) and (b) show a region of interest (ROI) in one raw fluorescence projection of the zebrafish embryo at one orientation and the corresponding segmented image using Bernsen's local thresholding method respectively. After the image segmentation, the adapting reconstruction and localisation information extraction approach as described in sub-section 5.2.1 was employed.

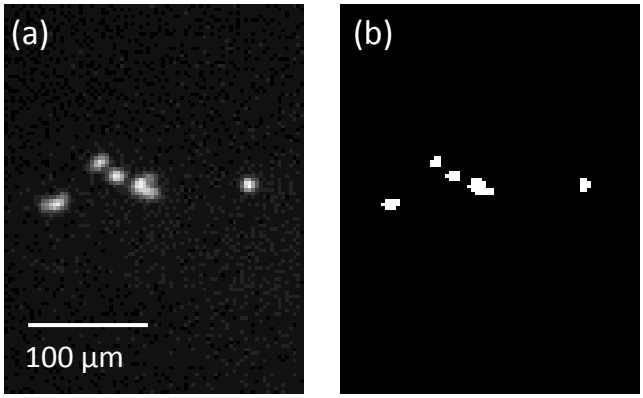


Figure 5.7: A ROI of (a) a raw fluorescence projection and (b) the corresponding segmented image of the 2 dpf LysC: GFP mitfa-/- roy-/- zebrafish embryo at one angle. Scale bar, 100 µm.

5.3.5. Results and discussion

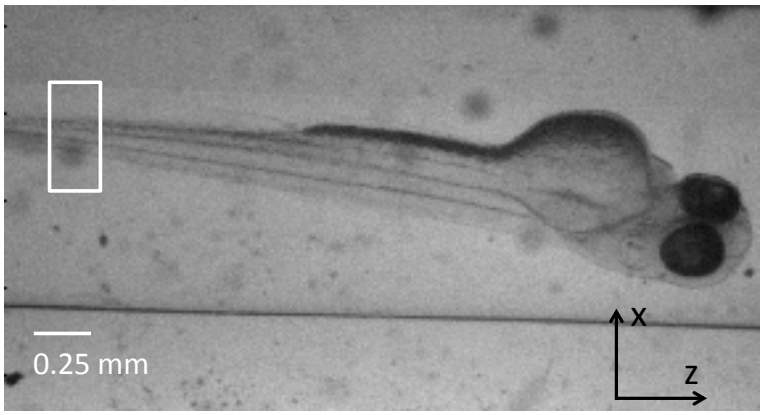


Figure 5.8: Wide-field transmission image of 2 dpf LysC: GFP mitfa-/- roy-/- zebrafish at one orientation (white box shows the initial ROI).Scale bar, 0.25mm.

The coarse reconstruction process produced a stack of cross-sectional binary images, indicating the intersections from pairs of orthogonal segmented projection data at each time point. Since the tail wound model was used in the experiment, the initial ROI was set to a section near the site of wound, indicated by

the white box in a wide-field transmission image of 2 dpf LysC: GFP mitfa-/- roy-/- zebrafish at one orientation in Fig. 5.8. Figure 5.9 and 5.10 show time-lapse orthogonal fluorescence projections of the ROI indicated in Fig. 5.8 for each arm (labelled as 0° and 90°) respectively. It is noted that these raw time-lapse fluorescence projections for each arm were not recorded from the same projection angle as the sample was rotated by an angular interval of 0.9º.

The cell localisation information was extracted from the angle-corrected coarse 3-D reconstruction at each time point. Considering the consistency of the full time-lapse information, the artefacts were then removed and pathways of cell migration were determined. Figure 5.11 shows corresponding time-lapse 3-D cell migration traces from the raw projection data as shown in Fig. 5.9 and 5.10.

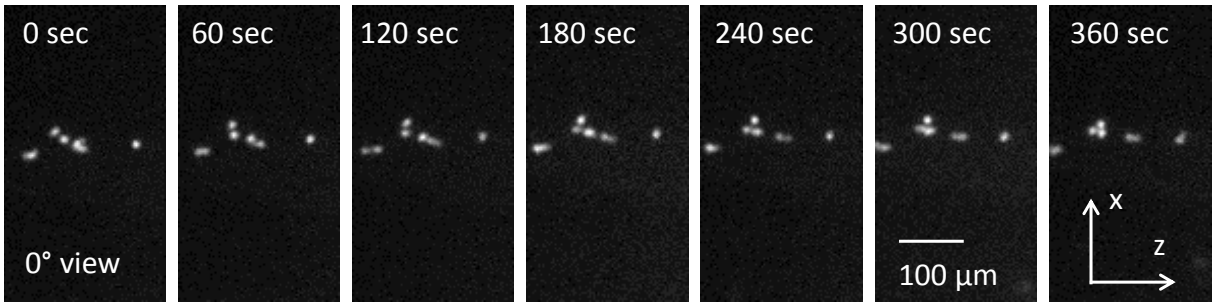


Figure 5.9: Wide-field time-lapse fluorescence images of the ROI indicated in Fig. 5.8 from 0° view. Scale bar, 100 µm.

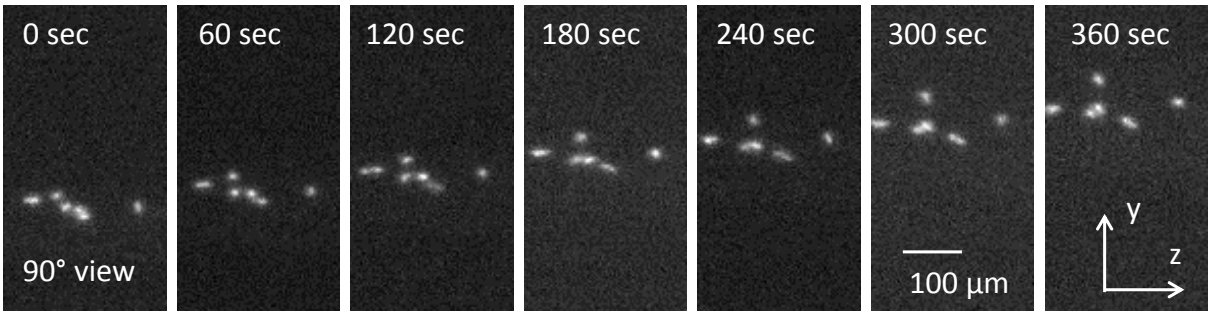


Figure 5.10: Wide-field time-lapse fluorescence images of the ROI indicated in Fig. 5.8 from 90° view. Scale bar, 100 µm.

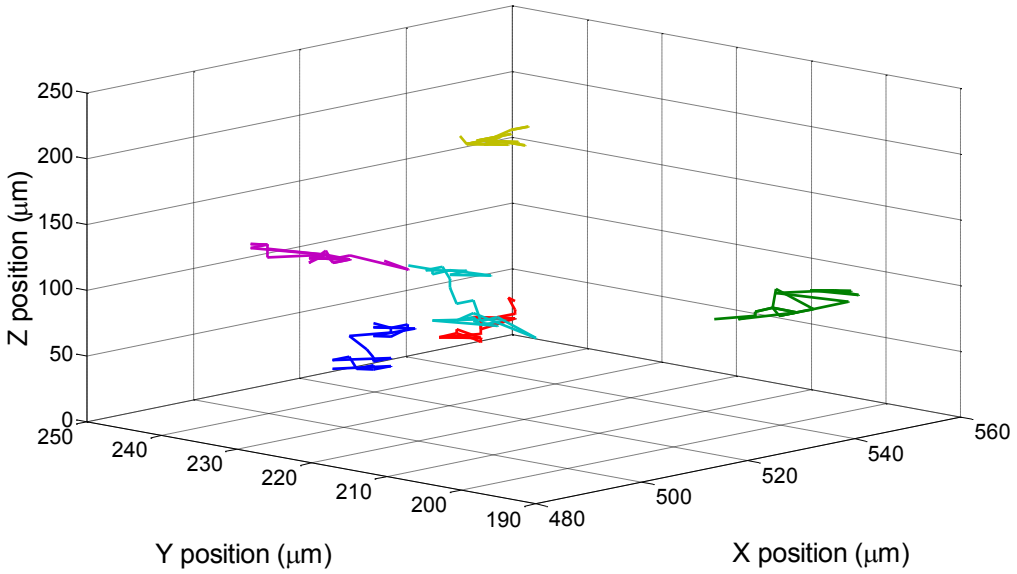


Figure 5.11: 3-D traces of cell migration in ROI indicated in Fig. 5.8 over 360 seconds in a model of wound inflammation in the 2 dpf LysC: GFP zebrafish embryo based on pairs of orthogonal projections.

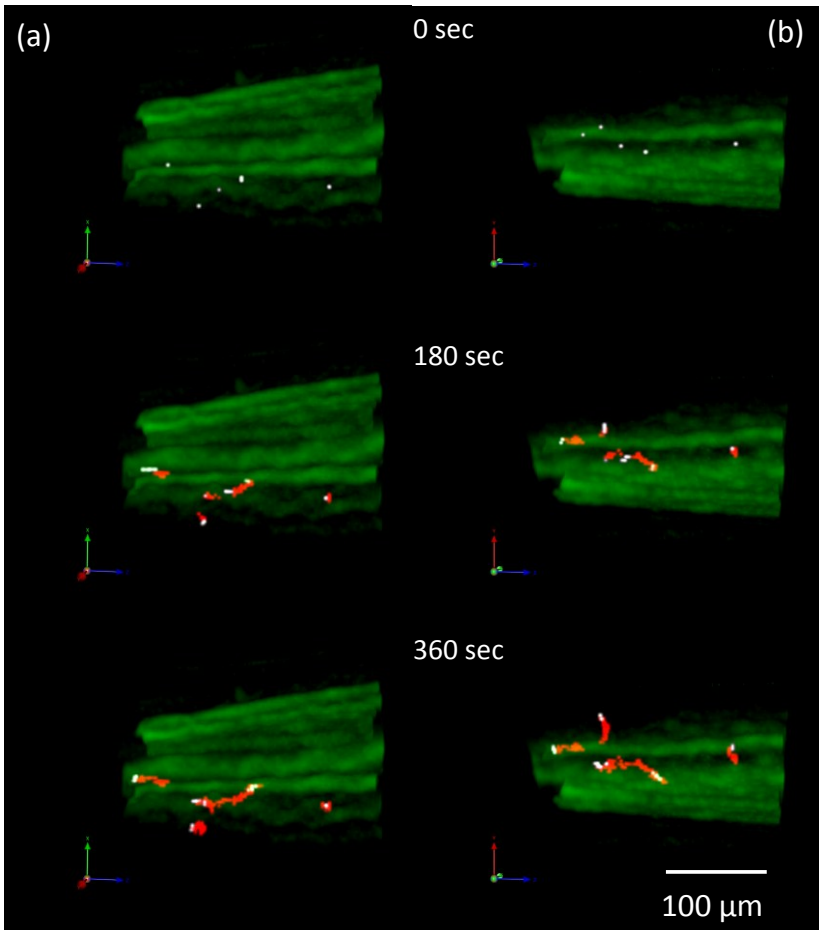


Figure 5.12: 3-D cell migration mapping in the tissue from (a) X-Z and (b) Y-Z view at 0, 180, 360 second time point in a model of wound inflammation in the 2 dpf LysC: GFP zebrafish embryo based on pairs of orthogonal projections (see Video 5.1). Red lines correspond to the previous movements while white lines correspond to latest movement from the last time point. Scale bar, 100 μm.

Figure 5.12 (Video 5.1) shows the migration mapping in the tissue at different time points from two views where red lines correspond to the previous movements while white lines correspond to latest movement from the last time point. These curves illustrate that the 3-D cell migration can be tracked by using pairs of orthogonal projections and the consistency of full time-lapse information. They reveal the local response of neutrophil to a wound signal.

In conclusion, this section has demonstrated the efficacy of using the dual orthogonal projection acquisition system focusing on a common plane and acquiring data simultaneously to track time-lapse feature motion with a sufficient time resolution equal to be the acquisition rate rather than the total acquisition time for the full tomographic data set and with a significantly reduced light lose, compared to time-lapse volumetric imaging. An initial demonstration of the 3-D cell migration mapping in a model of wound induced inflammation in the zebrafish embryo has been presented. The tracking accuracy for complex features and their motions in the biological organisms could be further improved by employing more than two imaging axes.

5.4. Conclusions

This chapter has introduced the development of OPT system by using an angular multiplexing technique to achieve multiple image acquisition for 3-D feature motion tracking. It has demonstrated the plausibility of using a dual orthogonal projection acquisition system acquiring data simultaneously to track time-lapse feature motion in a sample with a sufficient time resolution equal to be the acquisition rate and a significantly reduced light lose.

The dual image acquisition system at orthogonal projection angles was established by extending the configuration of the dual axis OPT system to focus the imaging channels on a common plane. The plausibility of using pairs of orthogonal projections and the consistency of full time-lapse information to track time-lapse feature motion at the frame rate was demonstrated via simulating independent bead movement in a volume. A model of wound induced inflammation of the LysC: GFP mitfa-/- roy-/- (express GFP in neutrophils) zebrafish embryo (2 dpf) was also imaged to further illustrate the impact of the dual image acquisition system at orthogonal angular projections, demonstrating 3-D cell migration mapping in the zebrafish embryo with a sufficient time resolution and a significantly reduced light dose, compared to time-lapse volumetric imaging.

Chapter 6: Biomedical applications of intensity and lifetime OPT

The previous three chapters have described the implementation and development of OPT microscope and macroscope systems. This chapter is concerned with the application of these OPT systems to biomedical samples and animal models. First, the application of the OPT macroscope system to biomedical tissues for morphology and histopathology research will be discussed, using the standard intensity-based OPT imaging technique to provide extrinsic (fluorescent dye) contrast and intrinsic (label-free) contrast of different tissue pathologies. The application of intensity-based OPT and FLIM-OPT to live zebrafish will also be discussed, including the feasibility of utilising FLIM-OPT to distinguish between multiple labels with similar spectral properties but different lifetime values, the feasibility of employing FLIM-OPT as a 3-D tomographic imaging platform for localisation of protein-protein interactions via FRET and the feasibility of applying OPT to obtain 3-D global imaging of tumour generation and progression in juvenile/adult zebrafish (weakly scattering regime). This chapter concludes with a discussion of the efficacy of OPT for *ex vivo* tissue samples and live animal models as a research tool. Topics in this chapter include:

- OPT of biomedical tissues for morphology and histopathology research
- Demonstration of FLIM-OPT of live zebrafish embryos
- 3-D localisation protein-protein interactions via FLIM FRET in zebrafish embryos
- 3-D global imaging of tumour progression in juvenile/adult zebrafish

6.1. Demonstration of biomedical tissues

OPT was originally applied to anatomical studies of fixed, cleared samples such as mouse embryos for research into development biology [64]. It is an increasingly useful tool for imaging and visualising organs and other biomedical tissue samples [64, 99, 100, 103, 117, 118]. 3-D OPT images can be formed using transmitted light (e.g. to map absorption coefficients) or using fluorescence radiation. Absorption contrast can arise from endogenous chromophores and exogenous labels or stains (e.g. the standard H&E stain). Fluorescence contrast can arise from exogenous labels including dyes or genetically expressed fluorescent proteins, or from endogenous fluorophores (e.g. collagen, elastin, NADH, etc.).

6.1.1. Pancreas specimens

Diabetes mellitus is a devastating disease and is a growing worldwide epidemic characterised by loss of insulin secretion. Affected individuals suffer from dysregulated glucose and lipid homeostasis and therefore complications including cardiovascular disease, blindness, kidney failure and cancer. The ability to accurately localise and measure beta cell mass is a prerequisite for interpretation of biomedical results for diabetes research.

OPT allows optical imaging in 3-D of relatively large tissues (up to tens of mm in each dimension) at high resolution (typically on the order of μm). Generally, the tissues are first rendered transparent by a chemical optical clearing and then embedded in agarose with biomedical targets being specifically labelled using dye-conjugated antibodies. OPT enables imaging of the intact 3-D structure (e.g. the intact pancreas) with many advantages (e.g. less time-consuming) compared to the serial capture of 2-D image slice data. It can provide 3-D reconstructions that enable quantitation of the number and localisation of insulin-containing beta cells within the pancreas [119-121].

This section mainly presents the application of OPT to pancreatic beta cell imaging, demonstrating the impact on mouse beta cell imaging for a collaborated experiment on Type 2 diabetes research [121].

6.1.1.1. Imaging system

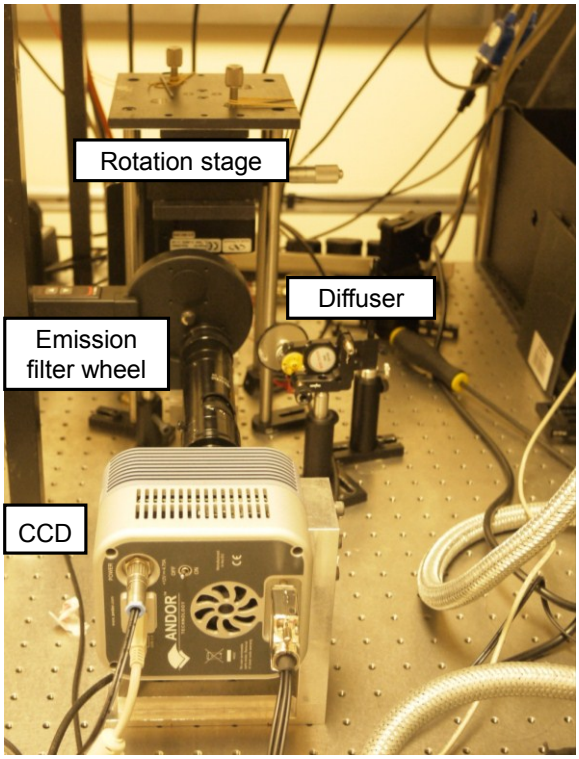


Figure 6.1: Photograph of in-house developed intensity-based macroscope OPT system.

The in-house developed OPT macroscope systems was used. Figure 6.1 shows the components of the in-house developed intensity-based OPT macroscope system. The camera lens (Optem Zoom 125C 12.5:1 Micro-Inspection Lens system with an Optem 1x Mini 299090 TV tube lens) formed an image onto the CCD (Clara, Andor Technology plc). The sample was mounted under a rotation stage (UE34CC, Newport Corp) and suspended in BABB. Wide-field excitation was provided by the spectrally filtered ultrafast fibre-laser-pumped super-continuum source (SC-400-2, Fianium Ltd) incorporating a rotating diffuser. The

magnification and the NA of the optical system were adjusted depending on the FOV required. The in-focus lateral resolution was ~25 μm.

6.1.1.2. Sample preparation and acquisition settings

Briefly, knockout mice (i.e. pancreas-specific Tcf7l2-null mice) for Type 2 diabetes research were prepared as described in [121]. To prepare for OPT imaging, whole pancreata were fixed in 4% (wt./vol.) paraformaldehyde at 4 °C for 2~3 hours, dehydrated, then frozen and de-frosted five times (-80 °C to room temperature). Pancreata were then blocked overnight in TBS-T containing 0.01% (wt./vol.) sodium azide and 10% (vol./vol.) serum and the samples were incubated overnight at 4 °C with guinea pig anti-swine insulin antibody (1:1000) dissolved in blocking buffer with extra 5% (vol./vol.) DMSO. Alexa 594 goat anti-guinea pig antibody was applied in order to visualise insulin-positive staining. Then, the sample was embedded in 1% (wt./vol.) agarose, dehydrated in methanol and cleared in BABB for OPT imaging.

All specimens were scanned using two fluorescent channels. The excitation and emission filters used for insulin-positive staining (beta cells) were 580 ± 15 nm and 650 ± 15 nm respectively and for autofluorescence (3-D shape of pancreata) signal were 480 ± 9 nm and 650 ± 15 nm respectively.

The "standard" intensity-based OPT acquisition procedure was applied, as described in sub-section 3.2.2, in which fluorescence images were acquired at 1° intervals as the sample rotated. The integration time for all the acquisitions was adjusted, depending on the signal level in the acquisition, to maximise the CCD dynamic range and therefore optimise the SNR in the reconstructions.

6.1.1.3. Results and discussion

The raw data for these two channels were reconstructed in a pair of 3D voxel data sets (voxel: μm 1:12.6). The reconstructions allow the distribution and total volume of insulin-positive areas to be assessed in pancreases. Figure 6.2 shows the 3-D OPT reconstructions of two 16-week-old mice pancreata from different experimental groups as representative examples, illustrating the accessibility of the distribution, size and number of insulin-positive cells. Beta cell volumes in μm^3 for each pancreas were measured using Volocity and given in Fig. 5 in [121], demonstrating OPT could provide quantitative information on the number and localisation of insulin-containing beta cells within the pancreas.

It is noted that intensity-based OPT provides mainly 3-D structural rather than quantitative information. These intensity measurements are susceptible to artefacts introduced by excitation intensity fluctuations or varying fluorophore concentrations. Nevertheless, the volume measurements are adequate rather than the accurate signal intensity measurements in this experiment. This work has demonstrated the application of OPT to pancreatic beta cell imaging, using the standard intensity-based imaging technique providing the 3-D reconstructions, in which the number and localisation of insulin-containing beta cells within the pancreas were established [121].

Type 2 diabetes usually involves defects in both insulin release and in hormone action. Both impaired glucose sensing by the beta cell and a loss of overall beta cell mass are involved in the decrease in beta cell function. However, the relative contributions of each for Type 2 diabetes remain unclear. Therefore, it is necessary to assess the contributions of cell loss versus function both prospectively and transversely in the diabetic population. It is noted that the existing requirement for extensive chemical treatment (i.e. to ensure that the sample has been rendered sufficiently transparent) and the introduction of antibodies limit this approach by precluding the possibility of monitoring beta cell mass prospectively in the developing embryonic pancreas. However, the development of an infrared-shifted fluorescent protein (IFP) in recent years, in principle, provides the possibility of performing OPT without the need to chemically clear the tissue [122]. The primordial rat pancreas, removed early in development, can be cultured *ex vivo* where pancreatic-islet like structures develop. Considering IFP along with the extension of discriminating against scattered light through a modified OPT configuration (e.g. structured illumination, polarisation gating, etc.) and more appropriate reconstruction algorithms, it may be possible to extend this approach to image more challenging (less transparent) samples and therefore may allow the appearance of beta cells to be monitored prospectively and over many weeks without chemical clearing.

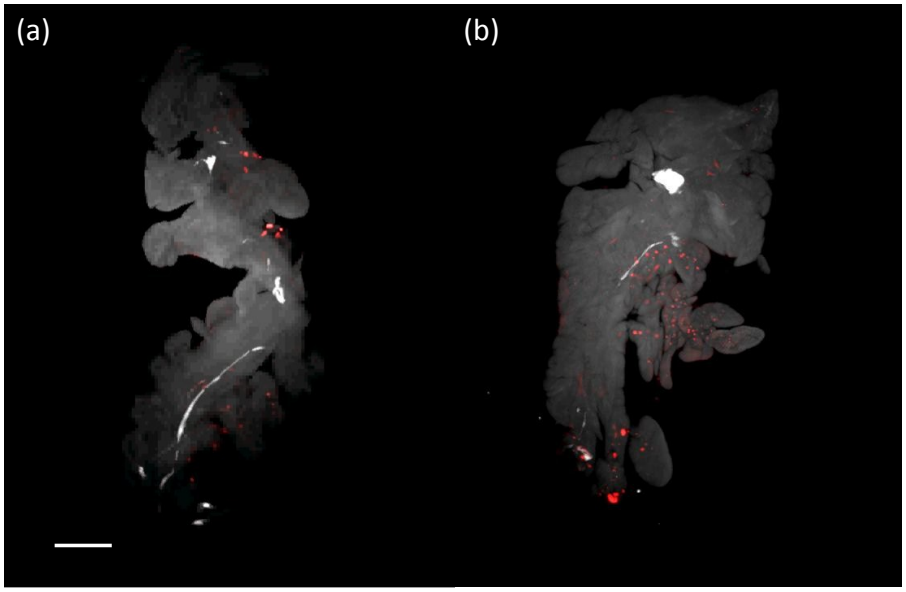


Figure 6.2: Maximum intensity projections of the 3-D reconstruction of two 16-week-old mice pancreas and beta cell volume. Alexa 594 goat anti-guinea pig antibody was applied in order to visualise insulin-positive staining, shown in red. Scale bar, 2 mm.

6.1.2. Label-free OPT of *ex vivo* tissue samples for histopathology research

One research topic of interest for OPT is its application to chemically cleared tissues for histopathology since OPT provides the opportunity to directly obtain "volumetric" 3-D images of intact samples rather than the standard approach of mechanically slicing them and combining images of each section to reconstruct 3-D

volumes. OPT is potentially preferable because mechanical "sectioning" is time-consuming, labour-intensive and is likely to damage delicate samples. In addition, for some "volumetric" samples which are irregularly shaped, it is difficult to mechanically "section" them and obtain complete useful 3-D structures.

As described in sub-section 2.7.2, OPT has a number of applications on soft organs [33, 64, 99, 104, 105, 117, 119, 123]. Since OPT can record both fluorescence and absorption profiles, these applications mostly benefit from different labelling and staining techniques. Kerwin *et al.* used the autofluorescence OPT imaging (i.e. the intrinsic fluorescence from the fixed specimens) of human embryos as the basis for the histological contrast seen in the 3-D model and tested its use as a framework onto which anatomical structures can be defined and gene expression data mapped by comparison of digital sections of OPT with physical sections stained [102]. Similarly, this section presents an exploratory investigation into the application of OPT to tissues by using autofluorescence for histopathology research, providing a label-free readout of the state of biological tissue.

6.1.2.1. Sample preparation and acquisition settings

Prior to imaging, the tissues (e.g. mouse lung, liver, kidney, female/male urogenital sinus (UGS)) were fixed and chemically cleared in BABB. The imaging system employed in this experiment was the same as in the last section (OPT macroscope system). The magnification and the NA of the optical system were adjusted according to the FOV required for each specific sample and the in-focus lateral resolution varied from 25 to 40 μm. Autofluorescence was excited in these experiments and no exogenous label was used. All specimens were scanned using two channels with the excitation at 470 ± 20 nm and 531 ± 20 nm, imaged through a 531 ± 20 nm and 600 ± 12.5 nm emission filters respectively.

6.1.2.2. Results and discussion

Figure 6.3 shows two-channel MIPs of the 3-D autofluorescence intensity reconstruction of mouse lung and heart, in which the blue channel corresponds to the excitation centred 470 nm while the green channel corresponds to the excitation centred 530 nm (see Video 6.1 for 3-D merged two-channel reconstruction). There is no significant difference, however, between these two channels although the blue channel might show more superficial information of the sample. This is due to the fact that no specific label was used and that the longer wavelength could penetrate deeper into the tissue. Longer wavelengths (excitation centred at 600 nm, 700 nm) were also tried but the signals were much weaker, resulting in a reduced SNR but still displaying similar structure.

Figure 6.4 (also seen Video 6.2) shows two-channel MIPs of the 3-D fluorescence intensity reconstruction of a female mouse UGS. This sample had a very complex shape and therefore it would be difficult to obtain a complete 3-D structure by using the traditional histopathological methods (i.e. mechanically "sectioning" and 2-D imaging). OPT has demonstrated the capability of providing the complete 3-D structures of these complex samples without physical damage or induced artefacts.

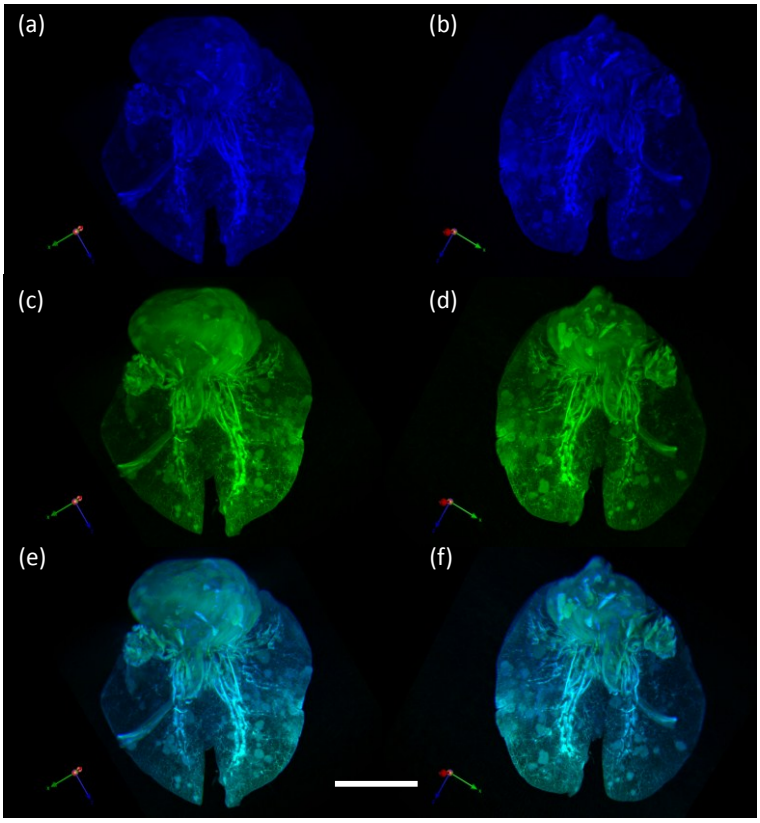


Figure 6.3: Maximum intensity projections from two opposite views of the 3-D reconstruction of a mice lung and heart with (a, b) showing blue channel (excitation centred 470 nm), (c, d) showing green channel (excitation centred 530 nm) and (e, f) showing merged two-channels (see Video 6.1). Scale bar, 5 mm.

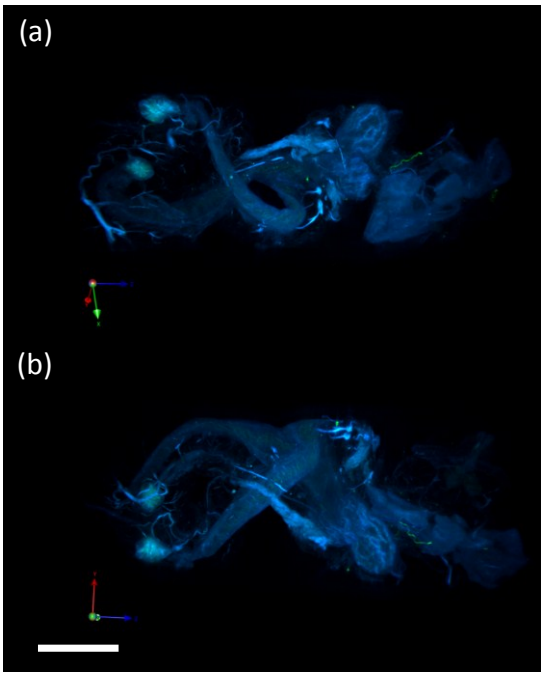


Figure 6.4: Maximum intensity projections from two views of the 3-D reconstruction of a female mouse urogenital sinus (UGS) showing merged two-channels (see Video 6.2). Scale bar, 5 mm.

Thus, the feasibility of OPT to volumetric imaging of tissue samples for histopathological research has been confirmed. Autofluorescence was used to provide a label-free readout of the state of structure of these biological tissues without the need of physical "sectioning". FLIM-OPT was also applied to the tissue samples. Unfortunately, the average fluorescence lifetime from the autofluorescence did not show significant contrast. This may be due to the numerous chemical treatments (fixing and/or clearing). However, there is the potential to apply FLIM-OPT to tissues to distinguish between different fluorescence signals, especially if the sample is extrinsically labelled (e.g. using immunohistochemical techniques).

6.2. *In vivo* imaging of zebrafish

In this study, the potential application of OPT to image live disease models was investigated. For studying disease and for drug discovery, there is an increasing demand in translating studies of biological processes at the cellular level from monolayer cell cultures to live organisms. However, the requirement of optical transparency for mesoscopic optical imaging techniques is a major limitation. For less transparent and larger organisms, it is usually necessary to employ chemical clearing to render them transparent. However, this process is inherently fatal to live organisms and thus precludes the possibility of *in vivo* imaging. In addition, it has an adverse effect on the fluorescent properties of genetically expressed fluorophores [100, 123].

It is therefore interesting to apply OPT and other optical imaging techniques to small live organisms which are sufficiently transparent – particularly those that can be genetically manipulated to serve as disease models. To date, OPT has been applied to organisms such as *D. melanogaster* [97, 106], *C. elegans* [87, 88, 107] and *Danio rerio* (zebrafish) embryos [78, 108]. For biological and pharmacological research, zebrafish are an attractive vertebrate animal model due to their short reproduction cycle, optical clarity during embryogenesis, easy drug administration and the potential manipulation using genetic and molecular approaches. One mating pair can produce up to 200 embryos a week. There are mutant lines available (e.g. the Casper and Tra/Nac lines) in which the fish do not produce melanocytes and therefore maintain transparency into adulthood [124], which is highly desirable for optical imaging. These mutant lines can be combined with transgenics that have cell types expressing fluorescent proteins (e.g. in mpx:GFP transgenics, GFP is expressed under the control of the *myeloperoxidase* promoter, resulting in expression of GFP in all neutrophils), and therefore transgenic lines can be employed to track cell migration or even monitor cell signaling via FRET. Zebrafish are widely deployed for disease model, organ function assays and on and off target effects [42, 125-132].

The different zebrafish life stages are determined their age: larval stage 3 - 30 dpf, juvenile stage 30 - 90 dpf and adult aged over 90 dpf. This section describes the applications of intensity-based OPT and FLIM-OPT to live zebrafish embryo and juvenile/adult zebrafish, including the feasibility of utilising FLIM-OPT to distinguish between multiple labels with similar spectral properties but different lifetime values, the feasibility of employing FLIM-OPT as a 3-D tomographic imaging platform for localisation of protein-

protein interactions via FRET and the feasibility of applying OPT to obtain 3-D global imaging of tumour generation and progression in juvenile/adult zebrafish (weakly scattering regime).

6.2.1. *In vivo* FLIM-OPT

OPT can provide 3-D reconstructions of the fluorescence and absorption distribution (e.g. sample structure and probe localization). However, intensity-based imaging provides mainly structural rather than functional information. Compared to intensity-based imaging, FLIM provides more robust quantitative information since lifetime measurements are less susceptible to artefacts introduced by varying fluorophore concentrations or excitation intensity fluctuations. It can provide contrast between different fluorescent species and can yield quantitative information concerning the local fluorophore environment (e.g. pH, temperature, protein-protein interactions, etc.) [1, 133, 134].

OPT can be extended to FLIM-OPT by incorporating wide-field FLIM instrumentation, as described in [77]. FLIM-OPT was realised through the wide-field acquisition of a series of time-gated fluorescence intensity images at different time delay positions with respect to the excitation pulses at each angle of projection. This technique makes the final results insensitive to intensity variations due to the ratiometric nature of FLIM. In the original experiment, FLIM was able to distinguish between the labelled fluorescence (i.e. Alexa-488-labelled neurofilament) and the autofluorescence from the heart and dorsal aorta of a mouse embryo [77]. However, *ex vivo* environments may exhibit non-physiological behaviour due to the artificial environments and therefore, there is increasing interest in more physiologically realistic engineered or *in vivo* environments. For drug discovery and many biological studies, there is an increasing demand in live disease models that can be developed in organisms, e.g. zebrafish embryos.

This sub-section presents the feasibility of applying FLIM-OPT to live animal models. The first full-body 3-D fluorescence lifetime imaging of a live LysC:GFP transgenic zebrafish embryo [78] is demonstrated, illustrating the potential of this technique to distinguish between multiple labels with similar spectral properties but different lifetime values. This also illustrates the potential of employing FLIM-OPT to live animal models for biological and pharmacological research (e.g. provide functional readouts in primary screening before the expensive mammal testing phase).

6.2.1.1. Imaging system

A schematic of our in-house developed FLIM-OPT microscope system is depicted in Fig. 6.5. When using the ultrafast fibre-laser-pumped super-continuum source for excitation, the excitation was initially incident on a rotating diffuser and then collimated. A further lens (f = 150 mm) focussed the excitation light to the back focal plane of an objective (after reflection off a dichroic cube filter) to produce collimated illumination. The fluorescence was collimated by the objective and transmitted through the dichroic filter cube. A tube lens then formed the image on the photocathode of the GOI.

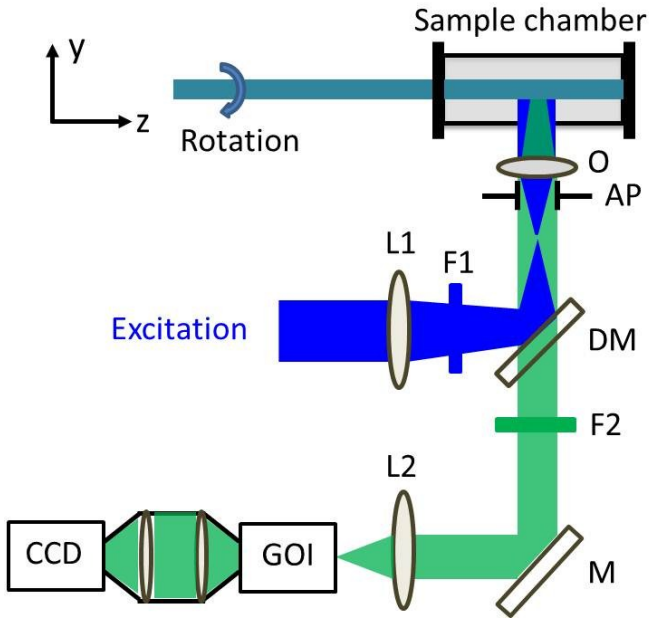


Figure 6.5: Schematic of in-house developed FLIM-OPT microscope system. O – objective, AP – aperture, L1 – condenser lens, F1 – excitation filter, DM – dichroic mirror, L2 – tube lens, F2 – emission filter, M – mirror; GOI – gated optical intensifier. (The GOI is coupled to a CCD through the use of two infinity focussed opposing camera lens of focal length of 50 mm and 35 mm.)

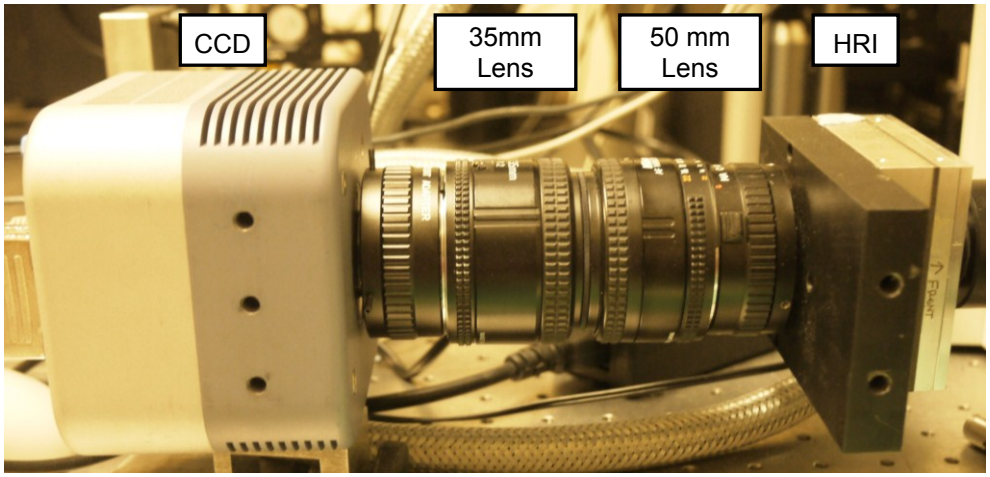


Figure 6.6: Photograph of the major components of the detection unit (GOI/HRI and CCD coupling).

In this thesis, the GOI (i.e. the imaging tube together with associated electronics and a control unit) was known as a high rate imager (HRI, Kentech Instruments, Didcot, UK). The image was coupled to a CCD (Clara, Andor Technology plc, 1040×1392, 6.45 µm pixel size) through the use of two infinity focussed opposing camera lenses of focal length of 50 mm and 35 mm (Nikkor AF, Nikon, Tokyo, Japan). Figure 6.6 shows a photograph of the major components of the detection unit (showing GOI and CCD coupling). It is noted that a high gain voltage results in increased amplification of signals but also restricts the available

dynamic range and decreases the number of detected photons [15]. The optimised gain voltage range for single-frame acquisition in this work was set between 550 and 700 V.

Figure 6.7 shows the basic features of the FLIM-OPT microscope system including spectrally filtered illumination, an electronic delay line, a rotation stage and the FLIM detection unit (i.e. a GOI coupled to a CCD). Wide-field excitation was provided by a spectrally filtered ultrafast fibre-laser-pumped super-continuum source (SC-400-2, Fianium Ltd) with an output spectral bandwidth from 450 nm to beyond 1750 nm, as shown in Fig. 6.7 (b).

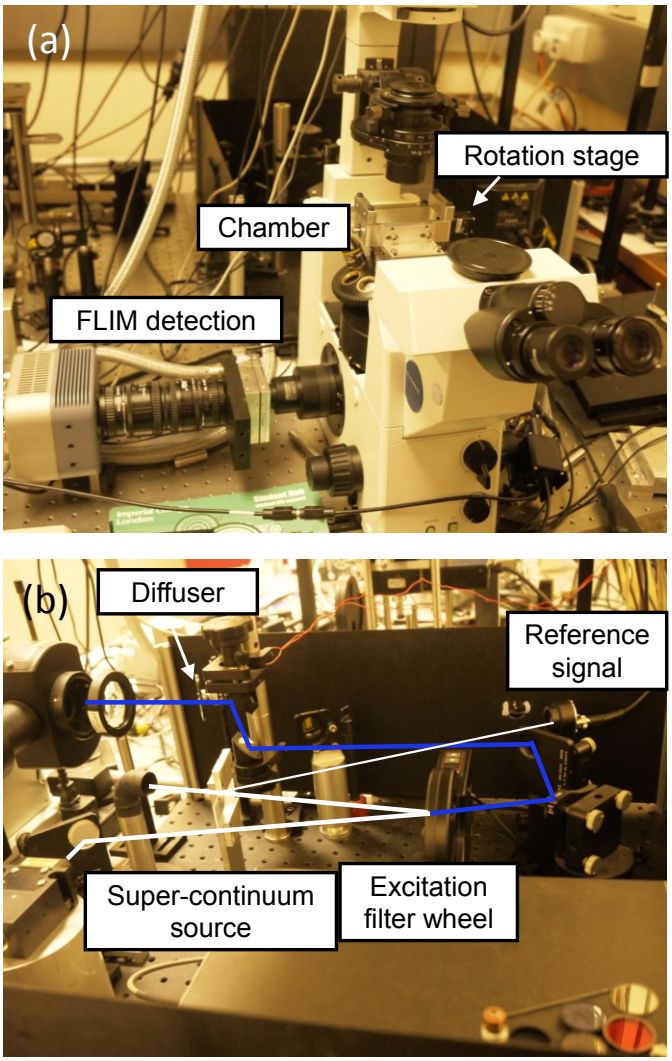


Figure 6.7: Photograph of (a) in-house developed FLIM-OPT microscope system and (b) the corresponding spectral filtered illumination based on an ultrafast fibre-laser-pumped super-continuum source.

6.2.1.2. Sample preparation

A transgenic line (LysC:GFP), which displays neutrophil specific expression of GFP, was used as an example for *in vivo* OPT imaging. Embryos were raised in embryo medium (dechlorinated system water

containing 0.0003% (vol./vol.) methylene blue and 30 μg/ml N-phenylthiourea (Sigma) to suppress melanisation).

For imaging, embryos at 3 dpf were anaesthetised and embedded in 1% low melt point agarose (Flowgen, Lichfield, UK), made from embryo media, containing 0.3 mM MS-222 (Sigma) as an anesthetic. Agarose was added to increase the viscosity of the water and prevent movement of the anaesthetized embryos.

They were then drawn into translucent FEP tubing (06406-60, Cole-Palmer), which has a refractive index similar to that of water, and the tubing then was mounted in an index matched chamber for imaging. Figure 6.8 (a) and (b) show a single projection of a live zebrafish embryo (confirmed by observing the heart beat during the acquisition) in transmission and in fluorescence respectively.

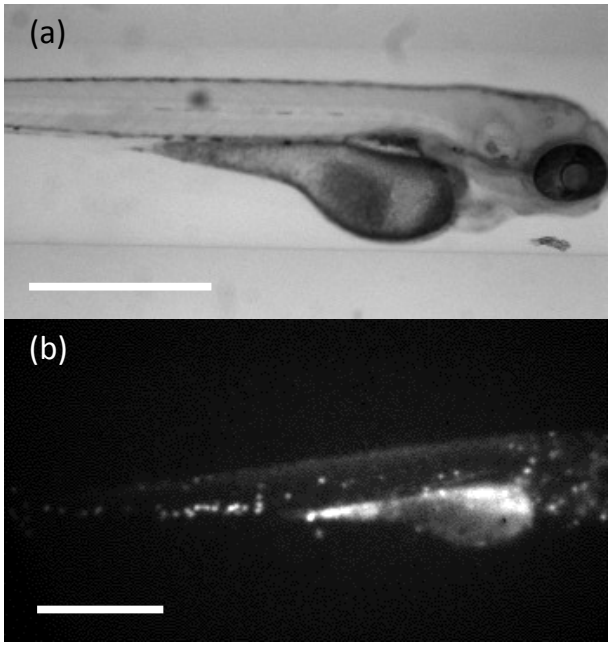


Figure 6.8: A single projection of a live LysC:GFP zebrafish embryo (confirmed by observing heart beat during acquisition) in (a) transmission and in (b) fluorescence based on the intensity-based OPT system. Scale bar, 500 μm.

6.2.1.3. Acquisition procedure

FLIM-OPT is based on the wide-field acquisition of a series of time-gated fluorescence intensity images at different time delay positions with respect to the excitation pulses at each angle of projection. Since the implementation of FLIM involves the GOI and the electronics delay line, the program starts with selecting the delay box, the rotation stage and the CCD and then initialising the hardware. During the acquisition, the GOI is triggered at the repetition rate of the pulsed laser source (40 MHz in this work) via a temporal delay box. The CCD is then triggered by the acquisition programme and integrates the fluorescence signal from the GOI for a user-defined period (i.e. integration time). After the integration, the CCD is read out and the image

is saved. Then the delay box switches to the next time delay position (i.e. time-gate shifts with respect to excitation pulses). This is repeated for a user-defined number of time-gates and then the rotation stage switches to the next angular position. The whole process is then repeated for a user-defined number of angular steps. Figure 6.9 shows a schematic of the FLIM-OPT "standard" acquisition procedure.

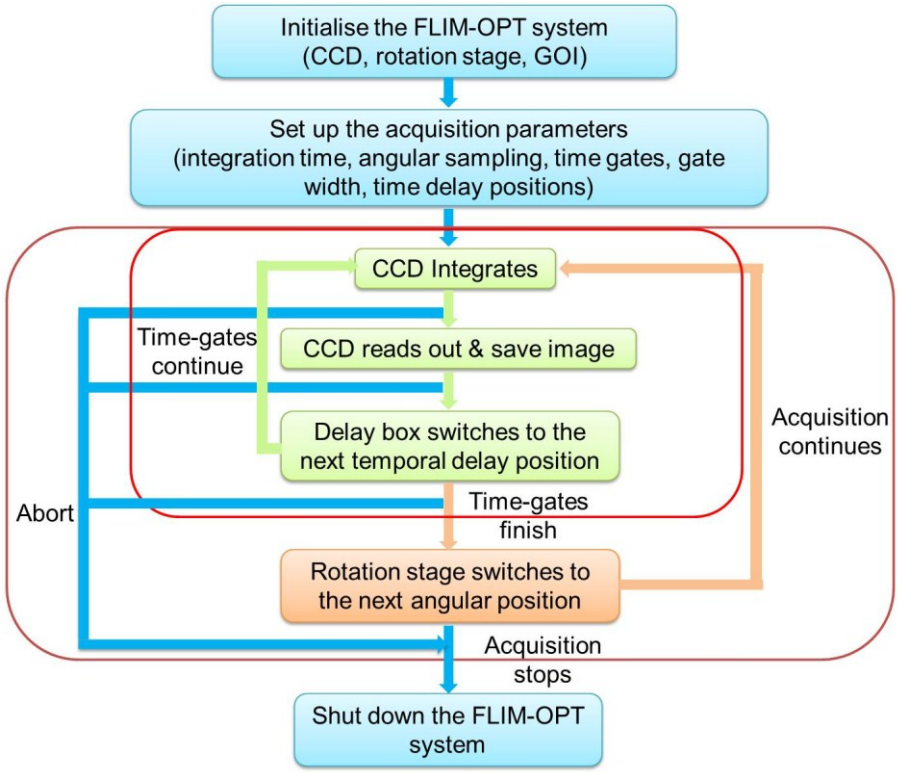


Figure 6.9: Schematic of the FLIM-OPT "standard" acquisition procedure.

Binning	Maximum frames per second
1×1	11
2×2	20
4×4	34
8×8	52.1

Table 6-1: Maximum frames per second for CCD (Clara, Andor technology plc) [135]. Full frame: 1392×1040.

As described in Chapter 2, it is noted that each gated image is actually a summation over many excitation pulses. Since the program triggers the CCD and controls the integration time, it works in an analogous way

to a full frame CCD. During the readout of the CCD, no signal is recorded although the specimen is still illuminated and the GOI is still gating. The gates are recorded in reverse order (i.e. starting from the last gate with the longest time delay and dimmest image) to reduce the effects from the previous gated signals on the next acquired frame. The effects are duo to a relatively long lifetime of phosphor, which may cause the residual signal from previous gate (if bright) comparable to the acquired signal of next gate (dim one). It is also possible to use a shutter to block the illumination when the CCD is not integrating. The maximum frame rate of the CCD (Clara, Andor Technology plc) (i.e. indicating the required readout time) depends on binning, as shown in Table 6-1.

6.2.1.4. Acquisition settings

Both epifluorescence and transmitted light imaging were utilised with a 4x objective (UPLFLN4X, Olympus UK Ltd) and a filter cube for GFP (GFP-3035B-OMF, Laser 2000 Ltd). The NA was limited to 0.07 by positioning an aperture directly behind the objective. The "standard" intensity-based OPT acquisition procedure was applied, in which fluorescence/transmitted light images were acquired at 1° intervals as the sample rotated. The transmitted light images were acquired by using the incandescent lamp through the same cube filter. Each frame had an integration time of 0.5 s for the transmitted light OPT acquisition.

For FLIM-OPT measurements, excitation was provided by a spectrally-filtered (472±15 nm) ultrafast fibre-laser-pumped super-continuum source (SC-400-2, Fianium Ltd). The emitted fluorescence was imaged onto the photocathode of the GOI (HRI, Kentech Instruments Ltd) with a gate-width of 1 ns. During the acquisition, 5 time-gated images were recorded at 1 ns relative delay positions every 4º (a total of 5×90 images were collected). Each frame had an integration time of 1 s for the time-gated acquisition. The total acquisition time for the dataset, including time-gated and transmitted light acquisitions, was ~20 minutes (comprising 630 s of photon detection and ~600 s of stage movement, temporal delay scanning, CCD set-up and readout time and switching between fluorescence and transmission modes). The in-focus lateral resolution of this FLIM-OPT system was ~13 μm due to the fact that the GOI used in this experiment had an effective pixel size of ~26 μm.

6.2.1.5. Reconstruction and fitting

3-D image reconstruction was realised based on the standard FBP algorithm. The reconstruction approach is repeated for each time-gated dataset corresponding to the time delay position. Five time-gated 3-D intensity reconstructions of the fluorescence signal were obtained, with the intensity decay contained in corresponding voxels of the time-gated reconstructions. The 3-D lifetime distribution was then determined by assuming a single exponential fluorescence decay model and using an in-house developed fitting algorithm based on non-linear least squares optimization. For visualisation purposes, the lifetime was represented on a false colour scale and merged with the integrated intensity to suppress the noise in regions with little or no signal.

6.2.1.6. Results and discussion

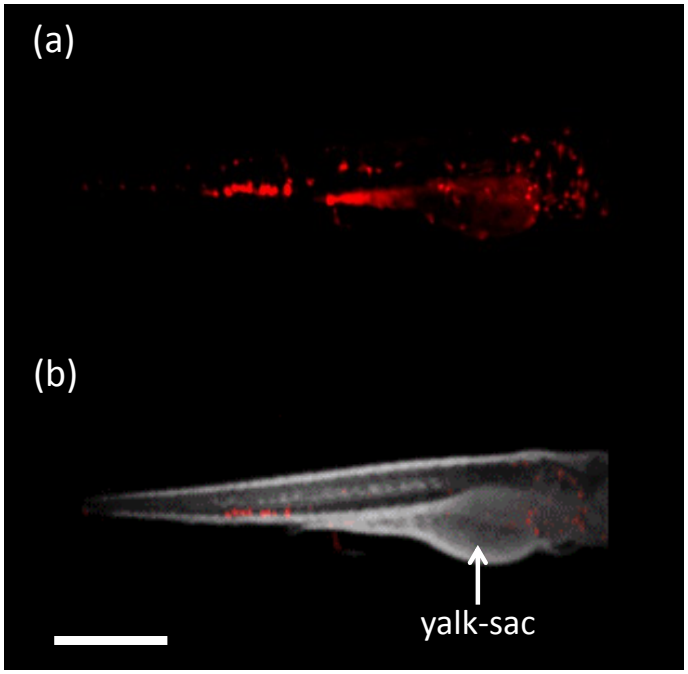


Figure 6.10: Maximum intensity projections of (a) a 3-D fluorescence intensity reconstruction and (b) the combined fluorescence (red) and absorption (grey) intensity reconstruction of a live LysC:GFP transgenic zebrafish embryo 3 dpf. Scale bar, 500 µm.

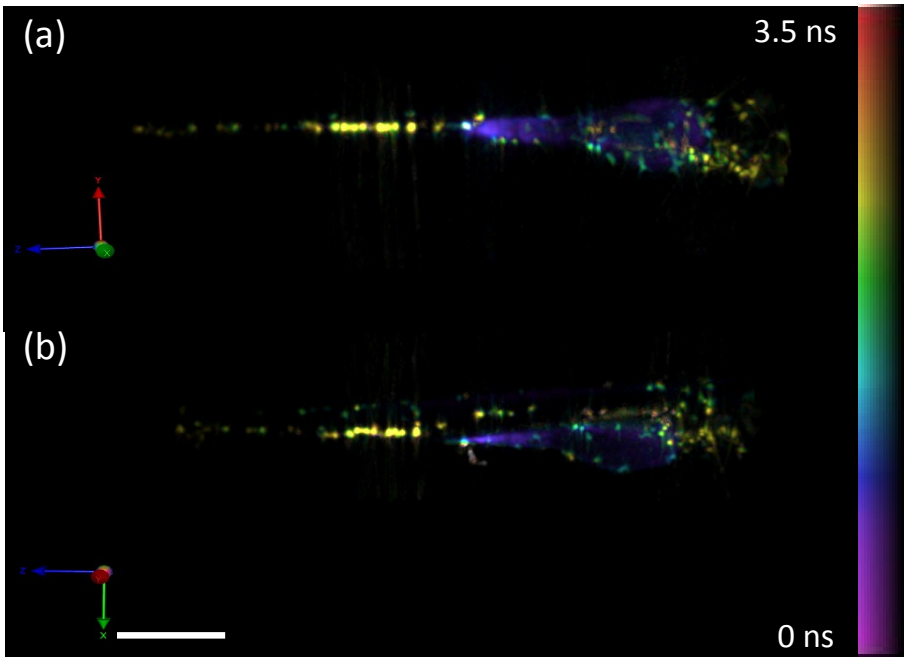


Figure 6.11: Maximum intensity projections of 3-D fluorescence lifetime reconstructions on a continuous colour scale of a live LysC:GFP transgenic zebrafish embryo 3 dpf from two orthogonal orientations. Scale bar, 500 µm.

The time-gated 3-D fluorescence intensity reconstructions at different time delay positions and the absorption reconstruction (based on the transmitted light acquisition) of a transgenic (LysC:GFP) zebrafish embryo at 3 dpf were obtained. Figure 6.10 (a) and (b) show the MIPs of a 3-D fluorescence intensity reconstruction and the combined fluorescence (red) and absorption (grey) intensity reconstruction respectively.

Since the expression of GFP was limited to neutrophils, the fluorescence intensity reconstruction was expected to illustrate the distribution of neutrophils throughout the zebrafish embryo. A significant autofluorescence signal, however, could also be observed in the raw data and the corresponding intensity reconstruction, particularly in the region of the yolk-sac. This resulted in a reduced ability to distinguish the expected fluorescent protein signal from the background fluorescence since both signals varied spatially in intensity due to the variation in expression level and the illumination and collection efficiency.

However, the GFP signal can be clearly distinguished from the background fluorescence via the fluorescence lifetime since, although the label and the background fluorescence have similar spectral properties, they have different lifetime values. The corresponding 3-D fluorescence lifetime distribution was achieved through the process described before, as shown in Fig. 6.11 (lifetime is encoded in the colour bar).

Figure 6.12 shows the fluorescence lifetime histogram, illustrating two distinct lifetime populations and confirming the correct lifetime for the GFP signal of ~2.5 ns. This separation of lifetime could be used such that the lifetime reconstruction could be viewed on a discrete colour scale, as shown in Fig. 6.13 (Video 6.3) with the GFP signal shown in green and autofluorescence shown in blue.

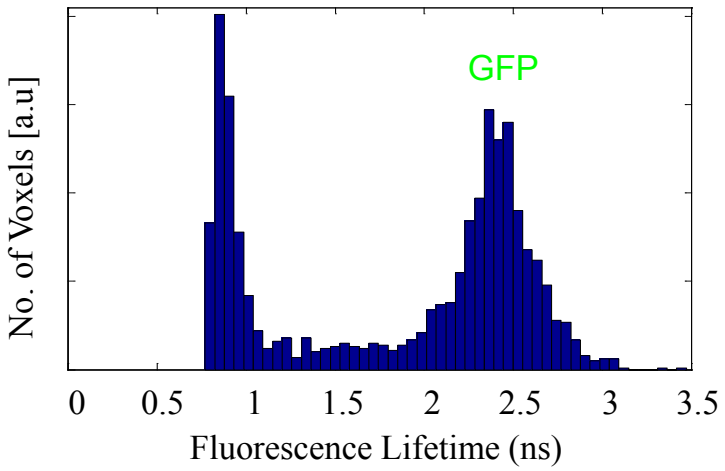


Figure 6.12: A fluorescence lifetime histogram showing two clear populations corresponding to GFP and autofluorescence.

It is noted that the total acquisition time was ~20 minutes and therefore the position and fluorescence lifetime of features that changed significantly during the acquisition time could not be accurately reconstructed. The

total acquisition time can be reduced by further developing the system (e.g. optimising the excitation powers) and modifying the acquisition program, using a similar approach described in sub-section 4.1.6.

The required processing time can be significantly reduced by employing graphic processor units (GPU) [136]. In addition, if the fluorescence lifetimes are known in advance, an optimised gating strategy can be employed for FLIM-OPT to minimise the required time-gates (e.g. 2 time-gates for a single exponential decay [12]) and therefore reduce the acquisition time and the processing time by reducing the number of recorded images and the number of 3-D intensity reconstructions required. It is also noted that the acquisition was not synchronised with the heartbeat of the zebrafish, which leads to the reconstructed structures close to the heart being compromised by the time-average motion.

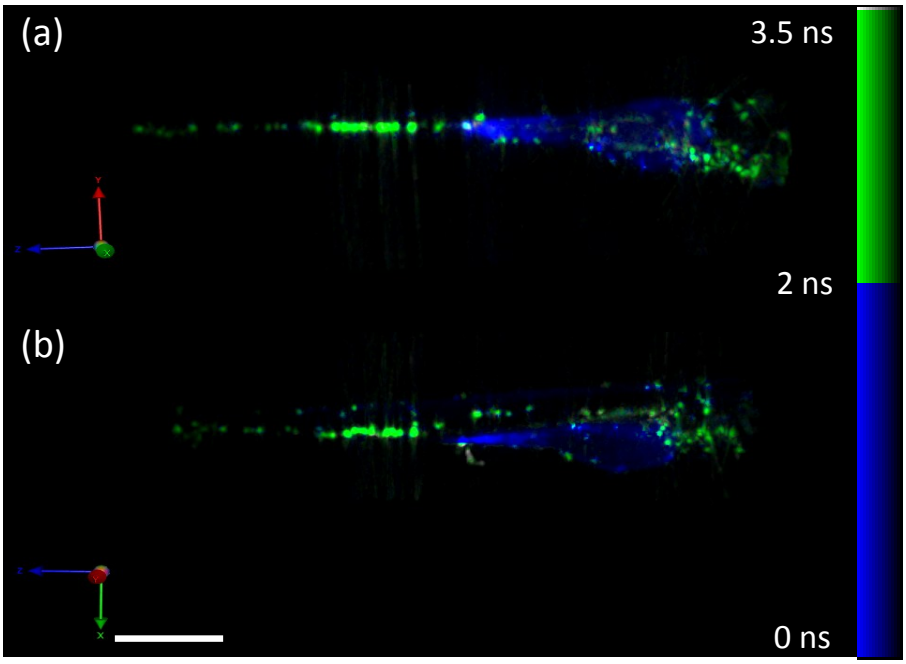


Figure 6.13: Maximum intensity projections of 3-D fluorescence lifetime reconstructions on a discrete colour scale of a live LysC:GFP transgenic zebrafish embryo 3 dpf (see Video 6.3) from two orthogonal orientations (corresponding to Fig. 6.11). Scale bar, 500 µm.

In conclusion, this work has demonstrated the application of intensity-based OPT and FLIM-OPT to live LysC:GFP transgenic zebrafish embryos to obtain the full-body 3-D fluorescence lifetime distribution for the first time. It is noted that the autofluorescence from the yolk-sac is a typical issue for zebrafish embryo imaging. This work has demonstrated that FLIM-OPT can distinguish between an expressed fluorescent protein signal and background autofluorescence (particularly in the region of the yolk-sac) with similar spectral properties but different lifetime values. It has demonstrated the potential of FLIM-OPT to map 3-D variations in local fluorophore environment (e.g. pH, calcium, protein-protein interactions via FRET, etc.).

6.2.2. FRET in zebrafish

This sub-section describes utilising FLIM-OPT as a 3-D tomographic imaging technique for localisation of protein-protein interactions via FRET. The approach is initially demonstrated by using an adapted biological FRET probe for Rac activation in live zebrafish of varying ages.

6.2.2.1. FRET probe

It is of interest to determine the activation state of relevant regulators when investigating cellular biological processes. The Rho family of GTPases is a family of small signalling GTPases that have important roles in regulation of the cell cycle and cell motility [137]. Rac1 is one member of this commonly studied family and specifically regulates cytoskeletal structure formation, including lammelipodia, focal adhesion complexes, membrane ruffles and actin polymerisation [138]. Its activation levels can be altered in disease processes that depend on cell migration such as tumour cell metastasis and inflammatory responses. It also has a critical role in the activation of transcription and apoptotic signalling, and is over-expressed in many cancers.

To detect protein activation and function, genetically encoded biosensors have been developed. As introduced in section 2.6, FRET can be used to detect and monitor interactions between proteins labelled with fluorophores (donor and acceptor), to measure conformational changes of large molecules. It is also increasingly used to read out genetically expressed biosensors for signalling molecules.

A FRET probe, called “Raichu”, designed by Yoshizaki *et al.* [139], has been employed to measure sub-cellular localisation of Rac activation [139-141]. Raichu was adapted by Kardash *et al.* for the detection of Rac activation in zebrafish [142]. This biosensor consisted of two protein functional domains - Rac1, called the “sensor”, and the CRIB domain of PAK1, called the “ligand”. Both of them could be labelled with fluorophores that act as donor and acceptor for energy transfer. In this probe, the CRIB domain of PAK1 was conjugated to SECFP (i.e. the enhanced version of Cyan Fluorescent Protein (CFP)), as the donor, while Rac1 was conjugated to YPet (i.e. the enhanced version of Yellow Fluorescent Protein (YFP)), as the acceptor. This probe is activated through the binding of Rac1 to the CRIB domain of PAK1. In other words, in response to a specific stimulus, the sensor interacts with the ligand (i.e. the activation of the biosensor) and thereby altering the relative distance between the donor and the acceptor fluorophores, which in turn alters the FRET efficiency.

The FRET efficiency was extracted from the ratiometric measurements of donor and acceptor fluorescence in separate spectral channels, but with donor excitation only (i.e. spectral FRET) [142]. The presence of FRET leads to a decrease in donor fluorescence intensity and a corresponding increase in acceptor fluorescence due to the energy transfer. However, to accurately quantify the FRET efficiency, bleedthrough of the donor fluorescence into the acceptor channel and direct excitation of the acceptor must be corrected for [142]. The donor bleedthrough can be quantified by measuring a sample with only the donor fluorophore, with the appropriate amount of donor fluorescence subtracted from the acceptor channel in the FRET experiments. Direct excitation of the acceptor will provide a map of acceptor localisation, and this can be used to estimate the directly-excited acceptor fluorescence once an acceptor-only sample has been imaged

using the donor and acceptor excitation sources in turn to determine an appropriate level of compensation. Once these effects have been compensated for, the ratio of donor to acceptor fluorescence can be used to monitor changes in FRET. This is simple in the case of a small sample such as a single cell, however, in a sample as large and complex as a fish, the wavelength-dependent effects of scattering and absorption may become significant, adding a potential source of error.

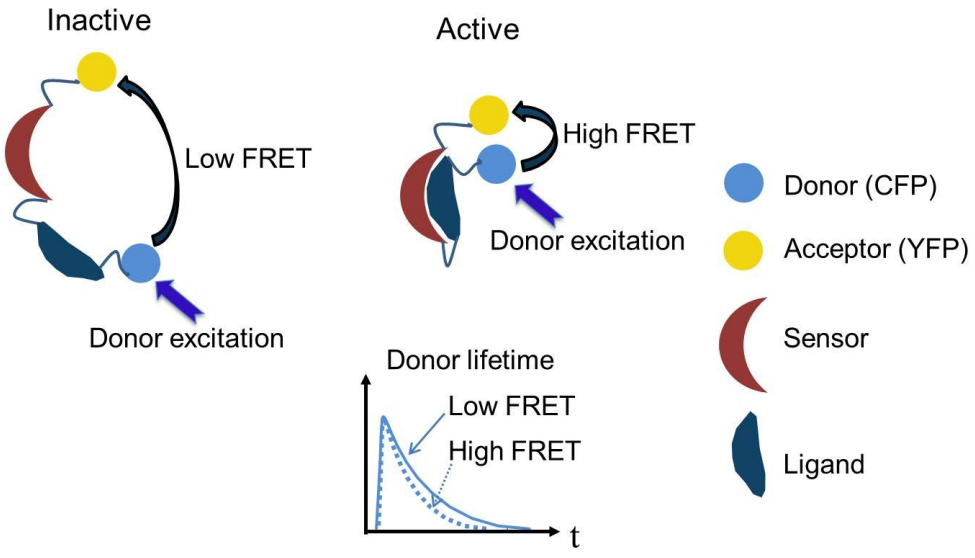


Figure 6.14: The basic structure of a single-chain FRET-based biosensor. The scheme shows the YFP and the CFP fluorophores conjugating the biosensor. Activation of ligand module results in an interaction between the sensor and the ligand. This in turn alters the FRET efficiency. The graphs illustrate the expected relative fluorescence lifetime of CFP for the inactive and active states of the biosensor.

Alternatively, FRET provides an extra de-excitation pathway for the donor and therefore the lifetime of the donor is reduced when energy transfer occurs, thus an altered FRET efficiency results in a change in the measured fluorescence lifetime of the donor fluorophore. As FLIM is only concerned with measurement of the donor lifetime, no calibration and correction at the acceptor emission wavelength is required. The basic concepts underlying the application of the FLIM FRET for measuring protein-protein interactions for this probe are shown in Fig. 6.14. A time-resolved imaging technique can then be employed to localise Rac activation based on a FRET read out using fluorescence lifetime.

This adapted biological FRET probe for Rac activation (by Kardash *et al.*) [142] was employed to initially demonstrate the feasibility of employing FLIM-OPT as a 3-D tomographic imaging technique for localisation of protein-protein interactions via FRET. In addition to one experimental probe, four control probes were employed in this experiment, as shown in Fig. 6.15. Figure 6.15 (a) shows a CFP-only probe for the non-FRET signal; (b) shows a YFP-only probe as a no donor control for background and bleedthrough monitoring; (c) shows a linked CFP/YFP probe for the High-FRET signal between the two adjoined proteins;

(d) shows a constitutively active probe that contains the Rac1 protein with a mutation in its binding site that renders it constantly active (i.e. High-FRET). The constitutively active probe is expected to illustrate the most realistic results of the experimental probe under fully active conditions since the probe will bind in the same conformation as the experimental probe while the linked CFP/YFP probe may not have the same conformation and thus could result in a slightly different FRET efficiency.

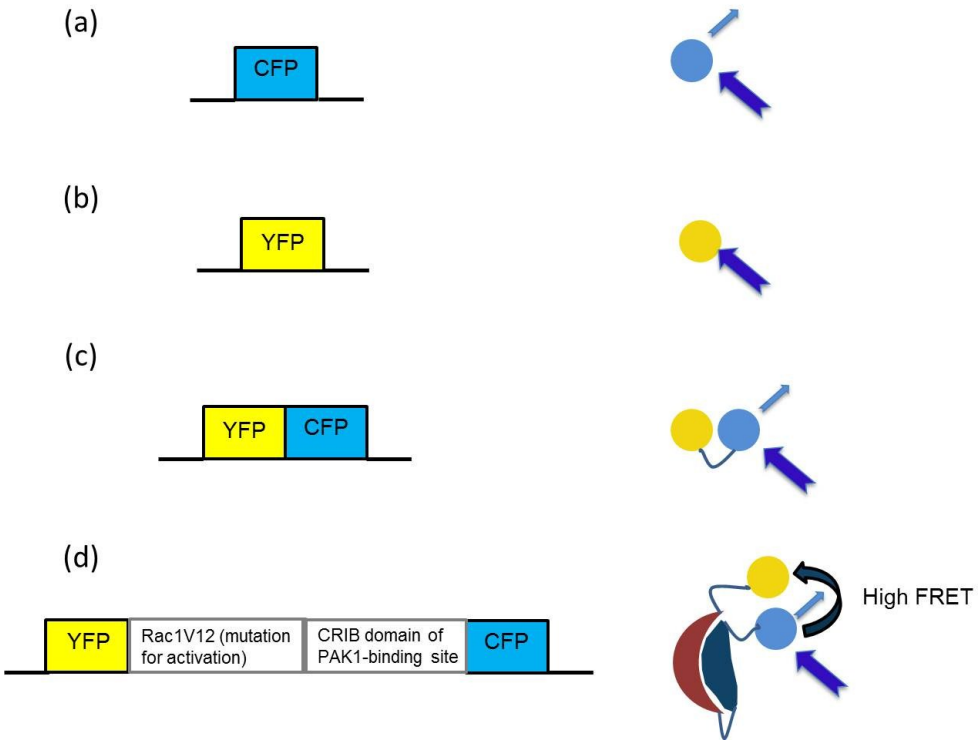


Figure 6.15: A description and a diagram of (a) the CFP-only probe for the non-FRET signal; (b) the YFP-only probe as a no donor control probe for background and bleedthrough monitoring; (c) the linked CFP/YFP probe for the High-FRET signal between the two adjoining proteins;(d) constitutively active probe that contains the Rac1 protein with a mutation in its binding site that renders it constantly active (i.e. High-FRET). The four probes here described are four control probes used in the experiment.

6.2.2.2. Sample preparation

All zebrafish used in this experiment were transparent Tra/Nac fish with reduced iridophore and melanophore numbers. To achieve uniform expression of the biosensor in zebrafish embryos, mRNA was injected into the yolk sac of embryos at the one-cell stage. Injections were performed on an injection mould consisting of 1% agarose in a solution system with methylene blue using a 12 m gauge borosilicate pipette fixed on a micro-injector. Injected embryos were then kept in a 28 ℃ incubator following standard procedures.

For imaging, embryos (24 hours post injection (hpi), 48 hpi and 72 hpi) were anaesthetised and embedded in the 1% low melt point agarose (Flowgen, Lichfield, UK), made from embryo media, containing 0.3 mM MS-

222 (Sigma) as an anesthetic. They were drawn into translucent FEP tubing (06406-60, Cole-Palmer) and mounted in an index matched chamber for imaging applications.

6.2.2.3. Imaging system and acquisition settings

The imaging system employed in this experiment was the in-house developed FLIM-OPT microscope system, as described in the last section. A 4x objective (UPLFLN4X, Olympus UK Ltd) and a filter cube for CFP (CFP-2432-OMF, Semrock) were used. The NA was limited to 0.07 by positioning an aperture directly behind the objective. For FLIM-OPT measurements, the emitted fluorescence was imaged onto the photocathode of the GOI (HRI, Kentech Instruments Ltd) with a gate-width of 1 ns. During the acquisition, 4 time-gated images were recorded at 1 ns relative delay positions every 4º (a total of 4×90 images were collected). In addition to the time-gated fluorescence images, the transmitted light images were also acquired every 1º (i.e. 360 projections) through the same cube filter. The acquisition time for each time-gated dataset was ~20 minutes with integration time varying between 1 – 2 s. Each frame for the transmitted light acquisition had an integration time of 0.1 s. The in-focus lateral resolution was ~13 μm.

6.2.2.4. Reconstruction and fitting

3-D intensity reconstruction was realised based on the standard FBP algorithm. Four time-gated 3-D intensity reconstructions of the fluorescence signal were obtained, with the intensity decay contained in corresponding voxels of the time-gated reconstructions. The 3-D lifetime distribution was then determined by assuming a single exponential fluorescence decay model and using the same in-house developed fitting algorithm used in the last sub-section. For visualisation, the lifetime for each fish was represented on the same colour scale of 500 – 3000 ps and merged with the integrated intensity to suppress the noise in regions with little or no signal.

6.2.2.5. Results and discussions

Wide-field time-gated FLIM with a higher magnification (using a 10x objective) was also employed prior to FLIM-OPT measurements to initially demonstrate the feasibility of the FRET probe. The YFP-only and control (i.e. no probe at all) group showed very weak signals and a similar lifetime, which was believed to be the lifetime of autofluorescence. The weak signals indicate the negligible bleedthrough between channels in this experiment.

Zebrafish embryos were initially screened via wide-field FLIM at 24 hpi, 48 hpi and 72 hpi. For embryos at 72 hpi, the signal was much dimmer and therefore the integration time was set to 5 s. This resulted in very long acquisition times for FLIM-OPT and therefore an increased chance of photobleaching or phototoxic effects or potential movement of the sample. Therefore, zebrafish embryos were only imaged by FLIM-OPT at 24 and 48 hpi. The weak signal is explained by the fact that the mRNA is not replicated. When injected at the one-cell stage, the mRNA diffuses into the cell and thus, every time cell division occurs the concentration within the cell is halved. Eventually, as the embryo develops the concentration of mRNA decreases thereby leading to low expression of probes.

At 24 hpi, three control groups (a CFP-only probe (non-FRET), a linked CFP/YFP probe (High-FRET) and a constitutively active probe (High-FRET)) were imaged via FLIM-OPT. Figure 6.16 (a - c) show the combined 3-D transmitted light reconstructions, fluorescence lifetime reconstructions and the fluorescence lifetime histograms for the CFP-only probe, the linked CFP/YFP probe and the constitutively active probe respectively at 24 hpi. They illustrate the difference in donor's lifetime values for these different FRET conditions. As expected, the lifetime for a CFP-only probe had the longest lifetime compared to the other two groups since there was no FRET occurring.

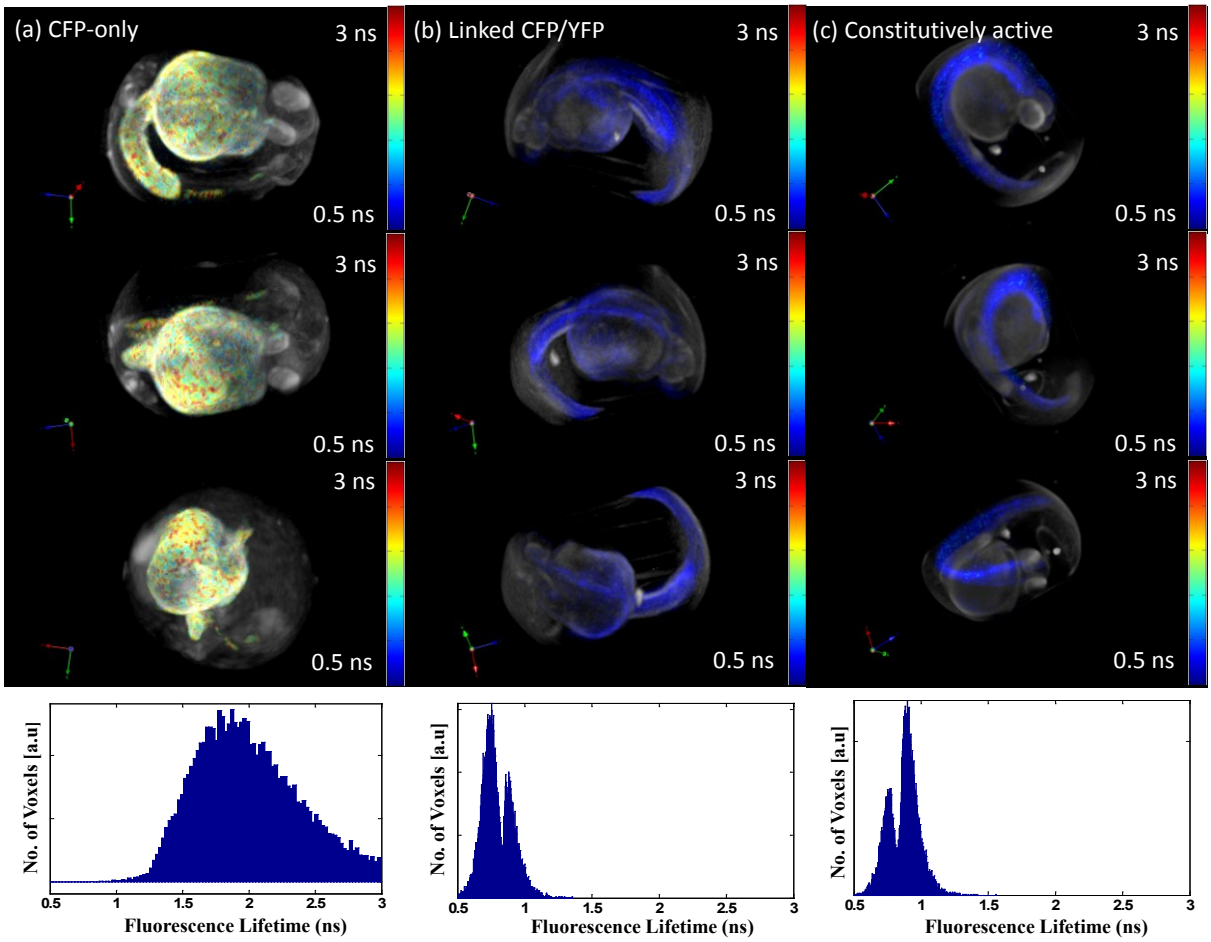


Figure 6.16: 3-D transmitted light reconstructions and the fluorescence lifetime images of 24 hpi zebrafish embryos with different control probes: (a) the CFP-only probe (no FRET); (b) the linked CFP-YFP probe (High FRET); (c) the constitutively active probe (High FRET) and their corresponding lifetime histograms.

At 48 hpi, embryos were imaged via FLIM-OPT on the three control groups and one experimental probe (FRET). Figure 6.17 shows 3-D fluorescence lifetime reconstructions and the fluorescence lifetime histograms at 48 hpi. The significant reduction in the fluorescence lifetime of the donor in three FRET groups compared to the non-FRET probe is directly visualised in the colour of the 3-D lifetime reconstruction and also highlighted in the histograms. The experimental probe shows a similar lifetime to the

constitutively active and linked CFP/YFP probes, suggesting that it is fully FRETing. As shown in the figures, the lifetime of the experimental probe is almost the same over the whole embryo. This can be explained by the fact that Rac is involved in the cell cycle and therefore in this early development stage it will be activated in every cell.

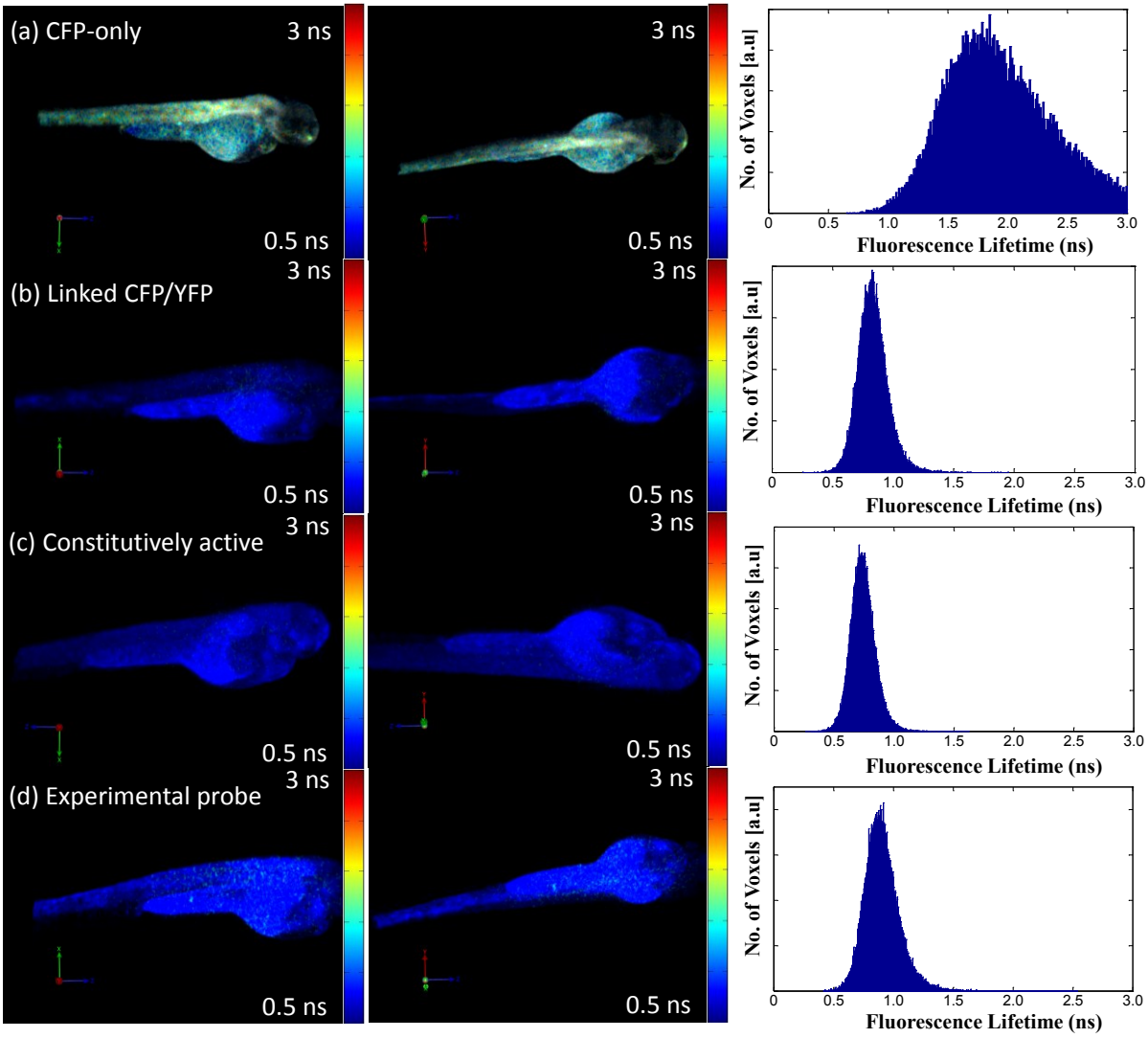


Figure 6.17: 3-D fluorescence lifetime images of 48 hpi zebrafish embryos with different probes: (a) the CFP-only probe (no FRET); (b) the linked CFP-YFP probe (High FRET); (c) the constitutively active probe (High FRET); (d) the experimental Rac probe and their corresponding lifetime histograms.

To further study Rac activation employing FLIM-OPT in older zebrafish, transgenic fish expressing the Rac probe throughout their lifetime are required. This transgenic line would allow more information surrounding the spatiotemporal localisation of Rac activation within a whole fish to be investigated. The experimental probe can be further activated or inhibited, resulting in a lifetime change of the probe. For example, Rac is

involved in wound healing and therefore a tail fin injury model can be utilised in zebrafish to show gene activation and also the cell recruitment in healing.

In conclusion, this work has demonstrated the feasibility of using FLIM-OPT as a 3-D tomographic imaging technique for localisation of protein-protein interactions via FRET by employing a Rac FRET probe in live zebrafish embryos. The significant reduction in the fluorescence lifetime of the donor in three FRET groups compared to the non-FRET probe has been observed and the experimental probe has shown highly similar lifetime as the constitutively active and linked CFP/YFP probes (High-FRET), indicating that it is fully FRETing and therefor, is high Rac activation level in this early development stage. This technique could have a significant impact in fundamental biological research and drug discovery.

6.2.3. Time-lapse global imaging of cancer in juvenile and adult zebrafish

In general, there is an increasing demand for studies in live disease models for fundamental biological research and drug discovery. One of the increasingly popular areas is the study of accurate zebrafish models of cancer since the tumours that develop in zebrafish share similarities with those that form in humans [143]. To date, however, most *in vivo* optical imaging experiments on zebrafish have been confined to embryos up to 3 dpf, which are highly transparent. All optical imaging techniques are limited by optical scattering. While OPT is also impacted, it is less severely compromised by scattering because it does not rely on focused excitation to achieve the spatial resolution unlike light sheet microscopy.

Developing OPT to provide 3-D global imaging of biological (disease) processes (e.g. for the study of cancer) in live juvenile/adult zebrafish on the cm scale is of significant interest. This is of particular importance because established imaging techniques are limited to zebrafish embryos or similar that do not present fully developed vasculature or immune systems and therefore are less relevant to human disease. To extend OPT to juvenile and adult zebrafish, the advantage of mutations such as Casper and Tra/Nac can be employed with their reduced pigmentation compared to wild-type fish.

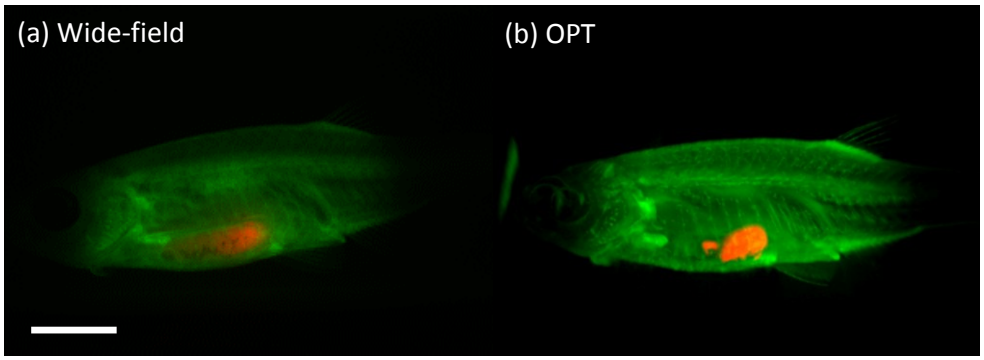


Figure 6.18: (a) Wide-field fluorescence image and (b) maximum intensity projection image of 3-D fluorescence OPT reconstruction of a live 30 dpf Casper:Fli-EGFP zebrafish with transplanted Tag-RFP U87MG tumour cells (see Video 6.4). Scale bar, 5 mm.

In order to demonstrate the feasibility of OPT to image in the weakly scattering regime with juvenile/adult zebrafish strains (Casper), a live 30 dpf Casper: Fli-EGFP zebrafish with transplanted Tag-RFP U87MG tumour cells was imaged on the OPT macroscope system. Figure 6.18 highlights the improvement in image quality and discrimination of OPT over wide-field fluorescence imaging when imaging the resulting xerografted tumour (see Video 6.4 for 3-D fluorescence reconstructions).

This sub-section describes the investigation of the feasibility of OPT to obtain 3-D global imaging of tumour generation and progression in juvenile/adult zebrafish. An initial longitudinal study of tumour progression in zebrafish is conducted, illustrating the potential of this technique to monitor and measure tumour generation and progression in live zebrafish for biological and pharmacological research.

6.2.3.1. Sample preparation

A zebrafish model of liver tumourigenesis was used as an example for *in vivo* time-lapse global imaging of cancer. For OPT measurements, the transparent mutant Casper zebrafish line crossed to the double-transgenic reporter line expressing GFP-labelled tumours and a mCherry vasculature (Tg Casper: KDR-mCherry: Tet on GFP-V12Kras [144]) was utilised.

The fish was 50 dpf on the day the longitudinal experiment began and was maintained at UCL. Doxycycline was used as the genetic inducer. Tumours were induced in the zebrafish using the Tet-on-Ras system, and the fish were then imaged at 5, 13, 20, 40, 53 days after the initial induction.

For imaging, the fish were anaesthetised by immersing in a 1X tricaine (3-amino benzoic acidethylester) solution for ~2.5 minutes (the tricaine concentration used is described in [145] and referred as 1X in this work). The anaesthetic protocol (i.e. length of time and anaesthesia concentration) for immobilisation was optimised based on the previous studies [146]. After anaesthetisation, the zebrafish was placed into a short length of translucent tubing filled with a 0.5X tricaine solution. The tubing was embedded in cold water (~ 5 °C), which was used to maintain and prolong the unconsciousness of the fish [147]. This optimised anaesthetic protocol for immobilisation of juvenile/adult zebrafish could allow up to 15 minutes imaging.

6.2.3.2. Acquisition settings

The imaging system employed in this experiment was the in-house developed OPT macroscope system, as described in sub-section 6.1.1. The magnification and the NA of the optical system were adjusted depending on the FOV required. The excitation and emission filters used for GFP detection were 472 ± 15 nm and 520 ± 17.5 nm respectively while for mCherry detection were 562 ± 20 nm and 641 ± 37.5 nm respectively.

The "standard" intensity-based OPT acquisition procedure was applied, in which fluorescence images were acquired at 3° intervals as the sample rotated. Each frame for the mCherry channel (expressing vasculature) had an integration time of 2 s for all the acquisitions and each frame for the GFP channel (expressing tumour cells) had an integration time of 0.5~2 s depending on the signal level in the acquisition. In the initial experiment, on Day 0, no OPT acquisition was acquired since the GFP (tumour) signal was extremely weak. The weak signals indicate the negligibility of the tumour volume in this initial stage of the time-lapse

experiment. As the tumour developed, the GFP signal significantly increased and consequently, the integration time for the GFP channel was reduced.

To reduce the acquisition time, the CCD was binned (2×2 binning) to ensure the total acquisition time for each sample was less than ~15 minutes (including anaesthetisation, mounting the fish, GFP and mCherry acquisitions and switching between modes). The in-focus lateral resolution of the system was ~50 μm.

6.2.3.3. Results and discussions

The Zebrafish was imaged at 5, 13, 20, 40, 53 days after the initial inducement. 3-D image reconstructions were realised by using the "standard" procedure based on the FBP algorithm. The 3-D GFP and mCherry intensity reconstructions (tumour cells and vasculature respectively) of a transgenic zebrafish at different time positions in the time-lapse process after tumour inducement were obtained, as shown in Fig. 6.19. These 3-D structures illustrate the change in tumour size and vasculature structure over the course of the experiment. As expected, there was a significant increase in tumour size as the experiment progressed. It is noted that, there was a reduction of the tumour size on Day 40, which was possibly due to an unintended reduction of doxycycline concentration at this stage.

In conclusion, this work has demonstrated the feasibility of OPT for longitudinal imaging of tumour development and progression in juvenile/adult zebrafish in 3-D. An initial longitudinal study lasted 53 days for tumour progression on an adult zebrafish with double-transgenic lines for tumour vascularisation study crossed with the transparent transgenic line (Casper), has been demonstrated, illustrating the potential of OPT for biological and pharmacological research to monitor and measure tumour generation and progression in juvenile/adult zebrafish.

Although the tumour volumes could be coarsely measured, scattering in juvenile/adult zebrafish decreased the quality of reconstructions and resulted in difficulties in accurately quantifying them. To enable quantitative evaluations of internal structures, including morphology and tumour and vasculature volume, a further development of the experimental approach could be investigated to preferentially select ballistic (unscattered) or weakly scattered photons, e.g. utilising structured illumination to reduce the cross-talk between detector pixels, implementing spatial filtering and/or polarization-gated imaging. Therefore, higher resolution images may be reconstructed, especially in parallel with the development of new tomography reconstruction algorithms addressing this increasingly scattering regime.

It is also noted that, FLIM-OPT can be employed as a 3-D tomographic imaging technique for localisation molecular interactions via FRET. Therefore, in addition to measurements of tumour volumes and generation of 3-D mapping of their localisation over time, it is also possible to study the tumour/vasculature interaction and specific signalling events by introducing fluorescent labels to vasculature and FRET biosensors to tumour cells. This would provide new insights to tumour vascularisation and new information related to the correlation of cell signalling events and larger morphological changes and could potentially provide new drug targets.

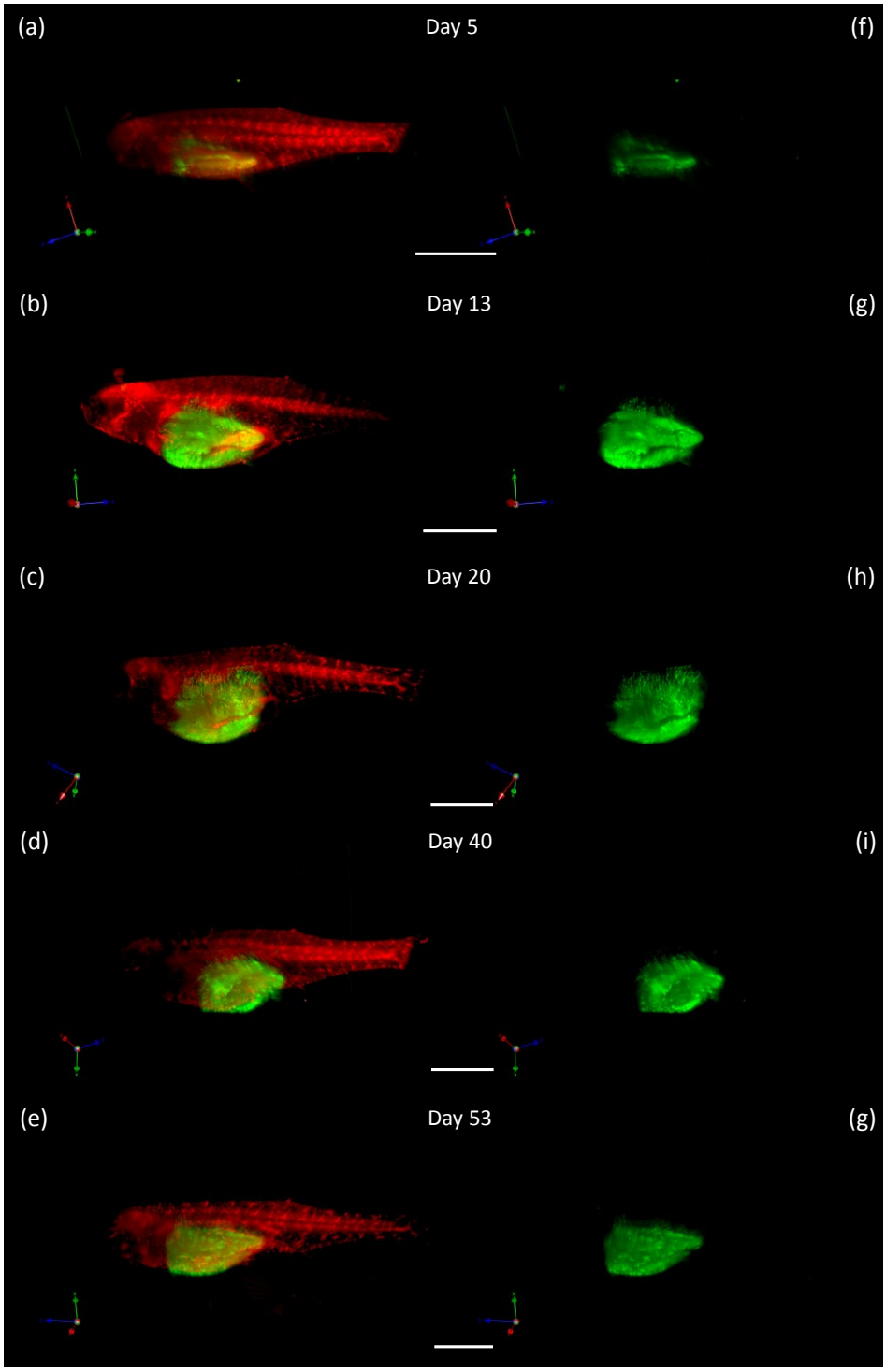


Figure 6.19: 3-D time-lapse fluorescence images of a double-transgenic zebrafish at Day (a) 5, (b) 13, (d) 20, (d) 40 and (e) 53 after the initial tumour inducement with (h-j) correspond to the corresponding separate tumour volumes at each time point. The fish was 50 dpf on the day the longitudinal experiment began (Day 0). (The transparent mutant Casper zebrafish line crossed to the double-transgenic reporter line expressing GFP-labelled tumours and a mCherry vasculature (Tg Casper: KDR-mCherry: Tet on GFP-V12Kras) was utilised.) Scale bar, 5 mm.

6.3. Conclusions

This chapter has described the application of intensity-based and FLIM-OPT to the 3-D mesoscopic biomedical imaging of tissues and live animal models (zebrafish in this work).

First, the efficacy of OPT as a tool for biomedical tissue imaging was demonstrated with a number of tissue types for morphology and histopathology applications. The application of OPT to pancreatic beta cell mass imaging has been demonstrated by providing the 3-D reconstruction at a spatial resolution of ~25 μm, in which the number and localisation of insulin-containing beta cells within the pancreas were quantified. It is noted that the existing requirement for extensive chemical treatment and the introduction of antibodies still restrict the throughput of this technique. Further development (e.g. employing red-shifted fluorescent proteins, discrimination against scattered light through a modified OPT configuration and utilising more appropriate reconstruction algorithms) could allow beta cells to be monitored prospectively and over many weeks without chemical clearing. The feasibility of applying OPT to a number of tissues for histopathology applications has also been demonstrated, using the standard technique providing intrinsic (label-free autofluorescence) contrast of different tissue pathologies. This work has illustrated the ability of OPT to directly obtain the complete 3-D structures of "volumetric" samples rather than the standard approach of mechanically slicing them, especially for the samples with complex and fragile morphology (e.g. mouse female UGS).

The efficacy of intensity-based OPT and FLIM-OPT as an imaging tool for biomedical research on live animal models was demonstrated with a number of experiments on zebrafish. The full-body 3-D fluorescence lifetime imaging of a live LysC:GFP transgenic zebrafish embryo by using FLIM-OPT has been demonstrated for the first time, using the different fluorescence lifetime values to distinguish between an expressed fluorescent protein signal and background autofluorescence with similar spectral properties (i.e. GFP > 2 ns while autofluorescence < 2 ns). This work has demonstrated that FLIM-OPT could be used to distinguish between multiple labels with similar spectral properties but different lifetime values and the feasibility of using FLIM-OPT to provide functional information for the investigation of 3-D biological process *in vivo*.

The feasibility of using FLIM-OPT as a 3-D tomographic imaging technique for localisation of protein-protein interactions via FRET has also been demonstrated, employing a Rac FRET probe in live zebrafish embryos. The significant reduction in the fluorescence lifetime of the donor in three FRET groups as compared to the non-FRET probe has been observed and the experimental probe has shown a similar lifetime to the constitutively active and linked CFP/YFP probes (High-FRET), indicating that it is fully FRETing and that there is high Rac activation level in this early development stage. This work could have a significant impact in drug discovery and fundamental biology research. It has also indicated the potential of FLIM-OPT to map other 3-D variations in local fluorophore environment (e.g. pH, calcium, etc.).

The feasibility of applying OPT to globally image tumour development and progression in the juvenile/adult zebrafish in 3-D has also been demonstrated. An initial longitudinal study lasted 53 days of tumour progression on an adult zebrafish with double-transgenic lines for tumour vascularisation study crossed with the transparent transgenic line (Casper) illustrated that OPT is able to monitor tumour generation and progression in juvenile/adult zebrafish for biological and pharmacological research. A significant increase in tumour size as the experiment progressed after tumour inducement was observed. It is noted that scattering in juvenile/adult zebrafish decreased the quality of reconstructions and resulted in difficulties to accurately quantify them. To enable quantitative evaluations of internal structures, including morphology and volume of tumour and vasculature, a further development on the experiment approach could be investigated to preferentially select ballistic (unscattered) or weakly scattered photons, e.g. utilising structured illumination to reduce the cross-talk between detector pixels, implementing spatial filtering and/or polarization-gated imaging. Thus higher resolution images may be realised, especially in parallel with the development of new tomographic reconstruction algorithms addressing this increasingly scattering regime. Furthermore, it could also able to study the tumour/vasculature interaction and specific signalling events by introducing fluorescent labels to vasculature and FRET biosensor to tumour cells and utilising FLIM-OPT. This would provide new insights to tumour vascularisation and new information related to correlation of cell signalling events and larger morphological changes and would potentially provide new drug targets.

Chapter 7: Conclusions and outlook

3-D imaging techniques are becoming increasingly important in biology and medicine as biomedical research progresses from studies of mono-layers of cells on glass to *in situ* measurements of biological systems. Recent developments in both fluorescence imaging (e.g. optical probes, spectroscopic fluorescence readouts, etc.) and 3-D imaging systems (e.g. OPT, etc.) offer the possibility to map the structural and functional information throughout samples in the mesoscopic regime (1 – 10 mm). As discussed in Chapter 2, the fluorescence signal can be analysed to extract quantitative information from such samples, for example by utilising FLIM not only to localise the fluorophore distribution but also to provide information about the local fluorophore environment including physical and chemical factors (e.g. temperature, viscosity, pH, etc.) or proximity to other fluorophores (e.g. to read out protein interactions, FRET biosensors, etc.). 3-D mesoscopic optical imaging techniques such as OPT, light sheet microscopy and SLOT have been developed to fill in the imaging gap between confocal/multiphoton LSM and established tomographic imaging techniques such as μMRI. They can be utilised to investigate many morphological and functional aspects of mesoscopic samples such as embryos, small animals, engineered tissues and plants. The focus of this thesis has been to develop and explore the potential of OPT, including FLIM-OPT, to provide 3-D imaging platforms for application in mesoscopic biomedical research, with ultimate applications including developmental biology, the study of disease mechanisms and drug discovery.

7.1. Conclusions of thesis

The discussion of the work in this thesis began by characterising the optical system through measurements of the MTF of the OPT system (the characterisation of FLIM-OPT system is shown in Appendix II). The MTFs were experimentally determined for different effective collection NAs as a function of defocus to quantify the additional spatial frequency modulation imposed by the use of focussed optical radiation in OPT. This illustrated that, as the NA decreased, the in-focus bandwidth (i.e. lateral resolution) decreased and the DOF of the optical system increased.

Typically, for tomographic reconstruction the standard FBP algorithm is employed to recover the cross-sectional images of an object from the angularly resolved projection image data. In practice, however, the use of focussed optical radiation with its associated instrumentation in OPT limits the applicability of the standard FBP algorithm, which assumes parallel-beam projection. To accommodate non-parallel light imaging, the reconstructions were modified to incorporate the measured system characteristics (i.e. the MTF) by either mask filtering or deconvolution. The MTF-mask filter realistically restricted the high frequency information to the region around the focal plane and progressively decreased the spatial frequency bandwidth with defocus. Therefore, it helped to maintain the fidelity of reconstructions when the angular sampling was reduced, thereby facilitating faster OPT acquisitions while maintaining reasonable quality reconstructions. A deconvolution filter was also employed to realistically correct for the spatial frequency modulation applied

by the imaging system, demonstrating improved resolution and contrast. A bead phantom was imaged to quantify the performances of the modified reconstruction techniques, illustrating a reduction in the average background by approximately 72% for an NA of 0.09 and by approximately 38% for an NA of 0.07 for MTF-mask filtered reconstruction compared to the standard FBP reconstruction. An improvement of ~24–28% in the reconstructed image resolution obtained for an NA of 0.07 with high-angular-sampling (i.e. 1° interval OPT acquisitions) was observed for deconvolution reconstruction compared to the non-deconvolved reconstructions (i.e. with the standard FBP and the MTF-mask filtering approach). A Fli:GFP transgenic zebrafish embryo was imaged at 3 dpf to further illustrate the impact of the modified reconstruction techniques, showing the potential for improved imaging speed using the MTF-mask filtered reconstruction and improved contrast using the deconvolution reconstruction. In practice, the deconvolution technique appears to be most appropriate for datasets acquired at a high angular sampling since it entails increased amplification of spatial frequencies approaching the cut-off frequency.

To improve the average spatial resolution while increasing the light collection efficiency, an experimental development of OPT incorporating an angular multiplexing technique was described, which permitted imaging with increased NA for a given sample thickness. This angular multiplexing OPT was initially demonstrated by employing dual optical imaging channels focused on shifted focal planes in the sample with the data being acquired simultaneously at two orthogonal angular projections. A sub-resolution bead phantom was imaged to quantify the performance of this dual axis OPT compared to the "standard" single axis OPT, which indicated a ~20% improvement in achieved resolution and ~4x increase in light collection efficiency, thereby enabling increased acquisition speed and reduced light dose. A tail section of a fluorescent Casper:Fli-EGFP transgenic zebrafish was imaged at 54 dpf to illustrate the benefits of the dual axis OPT system, demonstrating the significant improvement in the signal level and contrast. The dual axis OPT system and the acquisition programme were also optimised to facilitate faster acquisition times by significantly reducing the time for switching between two cameras, the camera read out and the saving of images. An extension to four-axis OPT was also demonstrated by sequentially acquiring datasets using one camera focused at shifted planes, which showed a further ~20% potential improvement in spatial resolution and ~4x increase in light collection efficiency compared to the dual axis approach.

The configuration of the dual axis OPT system was then adapted for multiple image acquisition at orthogonal projection angles by focusing the imaging channels to a common plane. This system was shown to be able to track time-lapse feature motion at the camera frame rate by using pairs of orthogonal projection image data and ensuring consistency of the full time-lapse information. To demonstrate the feasibility of this approach, movements of independent beads were simulated in a rotating volume to illustrate the correspondence between their recovered trajectories and the original bead trajectories. An experimental model of wound inflammation of the LysC: GFP mitfa-/- roy-/- zebrafish embryo (expressing GFP in neutrophils) was then imaged at 2 dpf to illustrate the capability of the dual image acquisition system at orthogonal projection angles to map 3-D cell migration in the zebrafish embryo with a higher time resolution and significantly reduced light dose compared to time-lapse volumetric imaging.

The final chapter of this thesis presented a number of biomedical applications of OPT and FLIM-OPT involving 3-D mesoscopic imaging of tissue samples and live animal models (i.e. zebrafish). The efficacy of OPT for tissue imaging was investigated by imaging a range of mouse tissue specimens including pancreas, lung, kidney, liver and male/female UGS, which is interesting to obtain morphological data for histopathology-based research. The potential of OPT and FLIM-OPT as an imaging tool for biological and pharmacological research on live disease models was explored by conducting a number of experiments on zebrafish. Full-body 3-D fluorescence lifetime imaging of a live LysC:GFP transgenic zebrafish embryo by using FLIM-OPT was demonstrated for the first time, using fluorescence lifetime to distinguish between an expressed fluorescent protein signal and background autofluorescence with similar spectral properties. Furthermore, the feasibility of using FLIM-OPT as a 3-D tomographic imaging technique for localisation of protein-protein interactions via FRET was demonstrated, employing a genetically expressed Rac FRET biosensor in live zebrafish embryos. In addition, the feasibility of applying OPT to globally image tumour development and progression in the juvenile/adult zebrafish in 3-D was demonstrated by conducting an initial longitudinal study (i.e. 53 days) of tumour progression on an adult zebrafish with double-transgenic lines for tumour vascularisation study crossed with the transparent transgenic line (Casper).

7.2. Future work

OPT has been shown to be a practical tool for several fields of biology and medicine research. There are many prospects for future work, including the development of OPT imaging hardware and reconstruction algorithms and the exploration and development of applications of OPT-based techniques. A key issue for biological samples is the deterioration of image quality due to scattering of optical radiation. For this reason most *in vivo* optical imaging experiments on zebrafish to date have been confined to embryos up to 3 dpf, which are highly transparent. However, zebrafish embryos or similar that do not present fully developed vasculature or immune system and therefore are less relevant to human disease. It is of importance to extend OPT to adapt to more scattering specimens including live juvenile/adult zebrafish and other disease models. This may be achieved by further development of experiment approaches that preferentially select ballistic or weakly scattered photons, e.g. utilising structured illumination to reduce the cross-talk between detector pixels, implementing spatial filtering or polarization-gated imaging. The development of new tomographic reconstruction algorithms could also improve the performance of OPT in this increasingly scattering regime. As described in Chapter 4, the measured characteristics of the OPT system can be incorporated to modify the standard FBP reconstruction. This characteristics could also be incorporated in other reconstruction techniques, e.g. algebraic reconstruction techniques [82]. Furthermore, an automated system for moderate throughput [148] could be developed for user-friendly deployment.

Publications

1. **L. Chen**, N. Andrews, S. Kumar, P. Frankel, J. McGinty, and P. M. W. French, "*Simultaneous angular multiplexing optical projection tomography at shifted focal planes*," Opt. Lett. **38**(6), 851-853 (2013).

2. G. da Silva Xavier, A. Mondragon, G. Sun, **L. Chen**, J. A. McGinty, P. M. French, and G. A. Rutter, "*Abnormal glucose tolerance and insulin secretion in pancreas-specific Tcf7l2-null mice*," Diabetologia **55**(10), 2667–2676 (2012).

3. **L. Chen**, J. McGinty, H. B. Taylor, L. Bugeon, J. R. Lamb, M. J. Dallman, and P. M. W. French, "*Incorporation of an experimentally determined MTF for spatial frequency filtering and deconvolution during optical projection tomography reconstruction*," Opt. Express. **20**(7), 7323-7337(2012).

4. J. McGinty, H. B. Taylor, **L. Chen**, L. Bugeon, J. R. Lamb, M. J. Dallman, and P. M. W. French, "*In vivo fluorescence lifetime optical projection tomography*," Biomed. Opt. Express. **2**(5), 1340-1350 (2011).

Presentations

1. **L. Chen**, N. Andrews, S. Kumar, P. Frankel, H. B. Taylor, L. Bugeon, J. R. Lamb, M. J. Dallman, J. McGinty, and P. M. W. French, "*Advances in optical projection tomography*," 2013 Multidimensional fluorescence imaging and metrology (MDFIM) workshop, poster (2013).

2. **L. Chen**, S. Kumar, M. Topping, N. Andrews, M. Katan, L. Bugeon, M. J. Dallman, Paul Frankel, J. McGinty, and P. M. W. French, "*Rapid Optical Projection Tomography for longitudinal studies of cancer and inflammation in live adult zebrafish*," 2013 Multidimensional fluorescence imaging and metrology (MDFIM) workshop, poster (2013).

3. N. Andrews, **L. Chen**, S. Kumar, J. McGinty, L. Bugeon, M. J. Dallman and P. M. W. French, "*FLIM and FRET in Live Zebrafish*," 2013 Multidimensional fluorescence imaging and metrology (MDFIM) workshop, poster (2013).

4. **L. Chen**, N. Andrews, S. Kumar, P. Frankel, J. McGinty, and P. M. W. French, "*Angular multiplexed optical projection tomography*," 2013 European Conferences on Biomedical Optics (ECBO) meeting, paper 1650088 (2013).

5. **L. Chen**, J. McGinty, H. B. Taylor, L. Bugeon, J. R. Lamb, M. J. Dallman, and P. French, "*Improved OPT reconstructions based on the MTF and extension to FLIM-OPT*," Conference on Biomedical Optics and 3-D Imaging, paper 1311757 (2012).

6. J. McGinty, **L. Chen**, H. B. Taylor, L. Bugeon, O. E. Pardo, J. R. Lamb, M. J. Dallman, and P. M. W. French, "*in vivo fluorescence lifetime optical projection tomography*," EMBO /EMBL Symposia 2011- Seeing is Believing, paper 96 (2011).

References

[1] J.R. Lakowicz, Principles of Fluorescence Spectroscopy, 3 ed., Springer, New York, 2006.

[2] G. Cox, Optical Imaging Techniques in Cell Biology, CRC Press / Taylor & Francis, 2006.

[3] F. Festy, S.M. Ameer-Beg, T. Ng, K. Suhling, Imaging proteins in vivo using fluorescence lifetime microscopy, Mol. Biosyst., 3 (2007) 381-391.

[4] R.A. Neher, E. Neher, Applying spectral fingerprinting to the analysis of FRET images, Microsc Res Tech, 64 (2004) 185-195.

[5] R.A. Schultz, T. Nielsen, J.R. Zavaleta, R. Ruch, R. Wyatt, H.R. Garner, Hyperspectral imaging: a novel approach for microscopic analysis, Cytometry, 43 (2001) 239-247.

[6] M.A. Digman, V.R. Caiolfa, M. Zamai, E. Gratton, The phasor approach to fluorescence lifetime imaging analysis, Biophys J, 94 (2008) L14-16.

[7] K. Dowling, M.J. Dayel, S.C.W. Hyde, P.M.W. French, M.J. Lever, J.D. Hares, A.K.L. Dymoke-Bradshaw, High resolution time-domain fluorescence lifetime imaging for biomedical applications, J Mod Optic, 46 (1999) 199-209.

[8] K. Dowling, S.C.W. Hyde, J.C. Dainty, P.M.W. French, J.D. Hares, 2-D fluorescence lifetime imaging using a time-gated image intensifier, Optics Communications, 135 (1997) 27-31.

[9] D.S. Elson, J. Requejo-Isidro, I. Munro, F. Reavell, J. Siegel, K. Suhling, P. Tadrous, R. Benninger, P. Lanigan, J. McGinty, C. Talbot, B. Treanor, S. Webb, A. Sandison, A. Wallace, D. Davis, J. Lever, M.A.A. Neil, D. Phillips, G.W. Stamp, P.M.W. French, Time-domain fluorescence lifetime imaging applied to biological tissue, Photochem Photobiol Sci, 3 (2004) 795-801.

[10] K. Suhling, P.M.W. French, D. Phillips, Time-resolved fluorescence microscopy, Photochem Photobiol Sci, 4 (2005) 13-22.

[11] A.V. Agronskaia, L. Tertoolen, H.C. Gerritsen, High frame rate fluorescence lifetime imaging, Journal of Physics D - Applied Physics, 36 (2003) 1655-1662.

[12] R.M. Ballew, J.N. Demas, An error analysis of the rapid lifetime determination method for the evaluation of single exponential decays, Analytical Chemistry, 61 (1989) 30-33.

[13] J. Philip, K. Carlsson, Theoretical investigation of the signal-to-noise ratio in fluorescence lifetime imaging, J Opt Soc Am A, 20 (2003) 368-379.

[14] J. McGinty, Development of wide-field fluorescence lifetime imaging for biomedical applications, in: Photonics group, Imperial College London, 2007.

[15] J. McGinty, J. Requejo-Isidro, I. Munro, C.B. Talbot, P.A. Kellett, J.D. Hares, C. Dunsby, M.A.A. Neil, P.M.W. French, Signal-to-noise characterization of time-gated intensifiers used for wide-field time-domain FLIM, J Phys D Appl Phys, 42 (2009) 135103.

[16] T. Forster, Zwischenmolekulare energiewanderung und fluoreszenz, Annals. Phys, 2 (1948) 55-75.

[17] E.A. Jares-Erijman, T.M. Jovin, FRET imaging, Nat Biotechnol, 21 (2003) 1387-1395.

[18] L. Stryer, Fluorescence energy transfer as a spectroscopic ruler, Annual review of biochemistry, 47 (1978) 819-846.

[19] M. Kleemola, M. Toivonen, J. Mykkanen, O. Simell, K. Huoponen, K.M. Heiskanen, Heterodimerization of y(+)LAT-1 and 4F2hc visualized by acceptor photobleaching FRET microscopy, Biochimica et biophysica acta, 1768 (2007) 2345-2354.

[20] A. Hoppe, K. Christensen, J.A. Swanson, Fluorescence resonance energy transfer-based stoichiometry in living cells, Biophys. J., 83 (2002) 3652-3664.

[21] J. van Rheenen, M. Langeslag, K. Jalink, Correcting confocal acquisition to optimize imaging of fluorescence resonance energy transfer by sensitized emission, Biophys. J., 86 (2004) 2517-2529.

[22] M.A. Rizzo, D.W. Piston, High-contrast imaging of fluorescent protein FRET by fluorescence polarization microscopy, Biophys. J., 88 (2005) L14-L16.

[23] S. Nagl, R. Bauer, U. Sauer, C. Preininger, U. Bogner, M. Schaeferling, Microarray analysis of protein-protein interactions based on FRET using subnanosecond-resolved fluorescence lifetime imaging, Biosens. Bioelectron., 24 (2008) 397-402.

[24] S. Pelet, M.J. Previte, P.T. So, Comparing the quantification of Forster resonance energy transfer measurement accuracies based on intensity, spectral, and lifetime imaging, J Biomed Opt, 11 (2006) 34017.

[25] J.A. Conchello, J.W. Lichtman, Optical sectioning microscopy, Nat Methods, 2 (2005) 920-931.

[26] W. Denk, J.H. Strickler, W.W. Webb, Two-Photon Laser Scanning Fluorescence Microscopy, Science, 248 (1990) 73-76.

[27] F. Helmchen, W. Denk, Deep tissue two-photon microscopy, Nat Methods, 2 (2005) 932-940.

[28] S. Lindek, C. Cremer, E.H.K. Stelzer, Confocal theta fluorescence microscopy using two-photon absorption and annular apertures, Optik, 102 (1996) 131-134.

[29] S. Lindek, C. Cremer, E.H.K. Stelzer, Confocal theta fluorescence microscopy with annular apertures, Appl Optics, 35 (1996) 126-130.

[30] S. Lindek, N. Salmon, C. Cremer, E.H.K. Stelzer, Theta-Microscopy Allows Phase Regulation in 4pi(a)-Confocal 2-Photon Fluorescence Microscopy, Optik, 98 (1994) 15-20.

[31] S. Lindek, T. Stefany, E.H.K. Stelzer, Single-lens theta microscopy - a new implementation of confocal theta microscopy, J Microsc-Oxford, 188 (1997) 280-284.

[32] S. Lindek, E.H.K. Stelzer, Confocal Theta Microscopy and 4pi-Confocal Theta-Microscopy, Three-Dimensional Microscopy: Image Acquisition and Processing, 2184 (1994) 188-194.

[33] J. Sharpe, U. Ahlgren, P. Perry, B. Hill, A. Ross, J. Hecksher-Sorensen, R. Baldock, D. Davidson, Optical projection tomography as a tool for 3D microscopy and gene expression studies, Science, 296 (2002) 541-545.

[34] J. Huisken, J. Swoger, F. Del Bene, J. Wittbrodt, E.H.K. Stelzer, Optical sectioning deep inside live embryos by selective plane illumination microscopy, Science, 305 (2004) 1007-1009.

[35] H.U. Dodt, U. Leischner, A. Schierloh, N. Jahrling, C.P. Mauch, K. Deininger, J.M. Deussing, M. Eder, W. Zieglgansberger, K. Becker, Ultramicroscopy: three-dimensional visualization of neuronal networks in the whole mouse brain, Nat Methods, 4 (2007) 331-336.

[36] R.A. Lorbeer, M. Heidrich, C. Lorbeer, D.F.R. Ojeda, G. Bicker, H. Meyer, A. Heisterkamp, Highly efficient 3D fluorescence microscopy with a scanning laser optical tomograph, Opt Express, 19 (2011) 5419-5430.

[37] A.H. Voie, D.H. Burns, F.A. Spelman, Orthogonal-Plane Fluorescence Optical Sectioning - 3-Dimensional Imaging of Macroscopic Biological Specimens, J Microsc-Oxford, 170 (1993) 229-236.

[38] D. Huber, M. Keller, D. Robert, 3D light scanning macrography, J Microsc-Oxford, 203 (2001) 208-213.

[39] E. Fuchs, J.S. Jaffe, R.A. Long, F. Azam, Thin laser light sheet microscope for microbial oceanography, Opt Express, 10 (2002) 145-154.

[40] J. Huisken, D.Y.R. Stainier, Selective plane illumination microscopy techniques in developmental biology, Development, 136 (2009) 1963-1975.

[41] M. Weber, J. Huisken, Light sheet microscopy for real-time developmental biology, Current opinion in genetics & development, 21 (2011) 566-572.

[42] J. Swoger, M. Muzzopappa, H. Lopez-Schier, J. Sharpe, 4D retrospective lineage tracing using SPIM for zebrafish organogenesis studies, J Biophotonics, 4 (2011) 122-134.

[43] K. Becker, N. Jahrling, E.R. Kramer, E. Schnorrer, H.U. Dodt, Ultramicroscopy: 3D reconstruction of large microscopical specimens, J Biophotonics, 1 (2008) 36-42.

[44] V. Ermolayev, M. Friedrich, R. Nozadze, T. Cathomen, M.A. Klein, G.S. Harms, E. Flechsig, Ultramicroscopy Reveals Axonal Transport Impairments in Cortical Motor Neurons at Prion Disease, Biophys J, 96 (2009) 3390-3398.

[45] P. Silthampitag, I. Klineberg, A.S. Jones, B. Austin, K.Y. Zee, C. Wallace, S. Scholz, A. Naim, K. Zoud, Ultramicroscopy of Bone at Oral Implant Sites: A Comparison of ED and Control Patients. Part 1-Defining the Protocol, Int J Prosthodont, 24 (2011) 147-154.

[46] P.J. Keller, A.D. Schmidt, J. Wittbrodt, E.H. Stelzer, Reconstruction of zebrafish early embryonic development by scanned light sheet microscopy, Science, 322 (2008) 1065-1069.

[47] T.F. Holekamp, D. Turaga, T.E. Holy, Fast three-dimensional fluorescence imaging of activity in neural populations by objective-coupled planar illumination microscopy, Neuron, 57 (2008) 661-672.

[48] J. Huisken, D.Y.R. Stainier, Even fluorescence excitation by multidirectional selective plane illumination microscopy (mSPIM), Opt Lett, 32 (2007) 2608-2610.

[49] U. Krzic, S. Gunther, T.E. Saunders, S.J. Streichan, L. Hufnagel, Multiview light-sheet microscope for rapid in toto imaging, Nat Methods, 9 (2012) 730-733.

[50] R. Tomer, K. Khairy, F. Amat, P.J. Keller, Quantitative high-speed imaging of entire developing embryos with simultaneous multiview light-sheet microscopy, Nat Methods, 9 (2012) 755-763.

[51] M. Tokunaga, N. Imamoto, K. Sakata-Sogawa, Highly inclined thin illumination enables clear single-molecule imaging in cells, Nat Methods, 5 (2008) 159-161.

[52] C. Dunsby, Optically sectioned imaging by oblique plane microscopy, Opt Express, 16 (2008) 20306-20316.

[53] K. Greger, J. Swoger, E.H.K. Stelzer, Basic building units and properties of a fluorescence single plane illumination microscope, Rev Sci Instrum, 78 (2007) 023705

[54] F.O. Fahrbach, A. Rohrbach, A line scanned light-sheet microscope with phase shaped self-reconstructing beams, Opt Express, 18 (2010) 24229-24244.

[55] T.A. Planchon, L. Gao, D.E. Milkie, M.W. Davidson, J.A. Galbraith, C.G. Galbraith, E. Betzig, Rapid three-dimensional isotropic imaging of living cells using Bessel beam plane illumination, Nat Methods, 8 (2011) 417-423.

[56] T.V. Truong, W. Supatto, D.S. Koos, J.M. Choi, S.E. Fraser, Deep and fast live imaging with two-photon scanned light-sheet microscopy, Nat Methods, 8 (2011) 757-760.

[57] J. Swoger, P. Verveer, K. Greger, J. Huisken, E.H.K. Stelzer, Multi-view image fusion improves resolution in three-dimensional microscopy, Opt Express, 15 (2007) 8029-8042.

[58] P.J. Verveer, J. Swoger, F. Pampaloni, K. Greger, M. Marcello, E.H. Stelzer, High-resolution three-dimensional imaging of large specimens with light sheet-based microscopy, Nat Methods, 4 (2007) 311-313.

[59] S. Preibisch, S. Saalfeld, J. Schindelin, P. Tomancak, Software for bead-based registration of selective plane illumination microscopy data, Nat Methods, 7 (2010) 418-419.

[60] M. Weber, J. Huisken, Omnidirectional microscopy, Nat Methods, 9 (2012) 656-657.

[61] A. Kaufmann, M. Mickoleit, M. Weber, J. Huisken, Multilayer mounting enables long-term imaging of zebrafish development in a light sheet microscope, Development, 139 (2012) 3242-3247.

[62] J. Swoger, P. Verveer, K. Greger, J. Huisken, E.H. Stelzer, Multi-view image fusion improves resolution in three-dimensional microscopy, Opt Express, 15 (2007) 8029-8042.

[63] P.J. Keller, F. Pampaloni, E.H. Stelzer, Life sciences require the third dimension, Curr Opin Cell Biol, 18 (2006) 117-124.

[64] J. Sharpe, Optical projection tomography as a new tool for studying embryo anatomy, J Anat, 202 (2003) 175-181.

[65] J. Sharpe, Optical projection tomography, Annu Rev Biomed Eng, 6 (2004) 209-228.

[66] J.C. Gore, M. Ranade, M.J. Maryanski, R.J. Schulz, Radiation dose distributions in three dimensions from tomographic optical density scanning of polymer gels: I. Development of an optical scanner, Phys Med Biol, 41 (1996) 2695-2704.

[67] B.J. Tarte, P.A. Jardine, T. vanDoorn, K.N. Nitschke, M.G. Poulsen, Development of a CCD array imaging system for measurement of dose distributions in doped agarose gels, Med Phys, 24 (1997) 1521-1525.

[68] N. Krstajic, S.J. Doran, Focusing optics of a parallel beam CCD optical tomography apparatus for 3D radiation gel dosimetry, Phys Med Biol, 51 (2006) 2055-2075.

[69] R.G. Kelly, K.J. Jordan, J.J. Battista, Optical CT reconstruction of 3D dose distributions using the ferrous-benzoic-xylenol (FBX) gel dosimeter, Med Phys, 25 (1998) 1741-1750.

[70] M. Oldham, J.H. Siewerdsen, S. Kumar, J. Wong, D.A. Jaffray, Optical-CT gel-dosimetry I: basic investigations, Med Phys, 30 (2003) 623-634.

[71] M. Oldham, J.H. Siewerdsen, A. Shetty, D.A. Jaffray, High resolution gel-dosimetry by optical-CT and MR scanning, Med Phys, 28 (2001) 1436-1445.

[72] K.T. Islam, J.F. Dempsey, M.K. Ranade, M.J. Maryanski, D.A. Low, Initial evaluation of commercial optical CT-based 3D gel dosimeter, Med Phys, 30 (2003) 2159-2168.

[73] J.G. Wolodzko, C. Marsden, A. Appleby, CCD imaging for optical tomography of gel radiation dosimeters, Med Phys, 26 (1999) 2508-2513.

[74] M.A. Bero, W.B. Gilboy, P.M. Glover, J.L. Keddie, Three-dimensional radiation dose measurements with ferrous benzoic acid xylenol orange in gelatin gel and optical absorption tomography, Nucl Instrum Meth A, 422 (1999) 617-620.

[75] S.J. Doran, K.K. Koerkamp, M.A. Bero, P. Jenneson, E.J. Morton, W.B. Gilboy, A CCD-based optical CT scanner for high-resolution 3D imaging of radiation dose distributions: equipment specifications, optical simulations and preliminary results, Phys Med Biol, 46 (2001) 3191-3213.

[76] A.C. Kak, M. Slaney, Principles of computerized tomographic imaging, Society for Industrial and Applied Mathematics, Philadelphia, 2001.

[77] J. McGinty, K.R. Tahir, R. Laine, C.B. Talbot, C. Dunsby, M.A.A. Neil, L. Quintana, J. Swoger, J. Sharpe, P.M.W. French, Fluorescence lifetime optical projection tomography, J Biophotonics, 1 (2008) 390-394.

[78] J. McGinty, H.B. Taylor, L. Chen, L. Bugeon, J.R. Lamb, M.J. Dallman, P.M.W. French, In vivo fluorescence lifetime optical projection tomography, Biomedical Optics Express, 2 (2011) 1340-1350.

[79] J.A. Davies, J.E. Armstrong, The anatomy of organogenesis: novel solutions to old problems, Progress in histochemistry and cytochemistry, 40 (2006) 165-176.

[80] M.T. Ke, S. Fujimoto, T. Imai, SeeDB: a simple and morphology-preserving optical clearing agent for neuronal circuit reconstruction, Nature neuroscience, 16 (2013) 1154-1161.

[81] K. Chung, J. Wallace, S.Y. Kim, S. Kalyanasundaram, A.S. Andalman, T.J. Davidson, J.J. Mirzabekov, K.A. Zalocusky, J. Mattis, A.K. Denisin, S. Pak, H. Bernstein, C. Ramakrishnan, L. Grosenick, V. Gradinaru, K. Deisseroth, Structural and molecular interrogation of intact biological systems, Nature, 497 (2013) 332-337.

[82] M.A. Haidekker, Optical transillumination tomography with tolerance against refraction mismatch, Computer methods and programs in biomedicine, 80 (2005) 225-235.

[83] J.R. Walls, J.G. Sled, J. Sharpe, R.M. Henkelman, Correction of artefacts in optical projection tomography, Phys Med Biol, 50 (2005) 4645-4665.

[84] U.J. Birk, A. Darrell, N. Konstantinides, A. Sarasa-Renedo, J. Ripoll, Improved reconstructions and generalized filtered back projection for optical projection tomography, Appl Optics, 50 (2011) 392-398.

[85] A. Darrell, H. Meyer, K. Marias, M. Brady, J. Ripoll, Weighted filtered backprojection for quantitative fluorescence optical projection tomography, Phys Med Biol, 53 (2008) 3863-3881.

[86] C. Vinegoni, D. Razansky, J.L. Figueiredo, M. Nahrendorf, V. Ntziachristos, R. Weissleder, Normalized Born ratio for fluorescence optical projection tomography, Opt Lett, 34 (2009) 319-321.

[87] U.J. Birk, M. Rieckher, N. Konstantinides, A. Darrell, A. Sarasa-Renedo, H. Meyer, N. Tavernarakis, J. Ripoll, Correction for specimen movement and rotation errors for in-vivo Optical Projection Tomography, Biomedical Optics Express, 1 (2010) 87-96.

[88] S. Zhu, D. Dong, U.J. Birk, M. Rieckher, N. Tavernarakis, X. Qu, J. Liang, J. Tian, J. Ripoll, Automated motion correction for in vivo optical projection tomography, IEEE Trans Med Imaging, 31 (2012) 1358-1371.

[89] W. Xia, R.M. Lewitt, P.R. Edholm, Fourier correction for spatially variant collimator blurring in SPECT, IEEE Trans Med Imaging, 14 (1995) 100-115.

[90] J.R. Walls, J.G. Sled, J. Sharpe, R.M. Henkelman, Resolution improvement in emission optical projection tomography, Phys Med Biol, 52 (2007) 2775-2790.

[91] L. Chen, J. McGinty, H.B. Taylor, L. Bugeon, J.R. Lamb, M.J. Dallman, P.M. French, Incorporation of an experimentally determined MTF for spatial frequency filtering and deconvolution during optical projection tomography reconstruction, Opt Express, 20 (2012) 7323-7337.

[92] M. Fauver, E.J. Seibel, J.R. Rahn, M.G. Meyer, F.W. Patten, T. Neumann, A.C. Nelson, Three-dimensional imaging of single isolated cell nuclei using optical projection tomography, Opt Express, 13 (2005) 4210-4223.

[93] Q. Miao, J. Hayenga, M.G. Meyer, T. Neumann, A.C. Nelson, E.J. Seibel, Resolution improvement in optical projection tomography by the focal scanning method, Opt Lett, 35 (2010) 3363-3365.

[94] L. Chen, N. Andrews, S. Kumar, P. Frankel, J. McGinty, P.M. French, Simultaneous angular multiplexing optical projection tomography at shifted focal planes, Opt Lett, 38 (2013) 851-853.

[95] A. Bassi, D. Brida, C. D'Andrea, G. Valentini, R. Cubeddu, S. De Silvestri, G. Cerullo, Time-gated optical projection tomography, Opt Lett, 35 (2010) 2732-2734.

[96] L. Fieramonti, A. Bassi, E.A. Foglia, A. Pistocchi, C. D'Andrea, G. Valentini, R. Cubeddu, S. De Silvestri, G. Cerullo, F. Cotelli, Time-gated optical projection tomography allows visualization of adult zebrafish internal structures, Plos One, 7 (2012) e50744.

[97] C. Vinegoni, C. Pitsouli, D. Razansky, N. Perrimon, V. Ntziachristos, In vivo imaging of Drosophila melanogaster pupae with mesoscopic fluorescence tomography, Nat Methods, 5 (2008) 45-47.

[98] V.Y. Soloviev, S.R. Arridge, Optical Tomography in weakly scattering media in the presence of highly scattering inclusions, Biomed Opt Express, 2 (2011) 440-451.

[99] M. Oldham, H. Sakhalkar, Y.M. Wang, P. Guo, T. Oliver, R. Bentley, Z. Vujaskovic, M. Dewhirst, Three-dimensional imaging of whole rodent organs using optical computed and emission tomography, J Biomed Opt, 12 (2007) 014009.

[100] H.S. Sakhalkar, M. Dewhirst, T. Oliver, Y. Cao, M. Oldham, Functional imaging in bulk tissue specimens using optical emission tomography: fluorescence preservation during optical clearing, Phys Med Biol, 52 (2007) 2035-2054.

[101] T. Alanentalo, C.E. Loren, A. Larefalk, J. Sharpe, D. Holmberg, U. Ahlgren, High-resolution three-dimensional imaging of islet-infiltrate interactions based on optical projection tomography assessments of the intact adult mouse pancreas, J Biomed Opt, 13 (2008) 054070.

[102] J. Kerwin, M. Scott, J. Sharpe, L. Puelles, S.C. Robson, M. Martinez-de-la-Torre, J.L. Ferran, G. Feng, R. Baldock, T. Strachan, D. Davidson, S. Lindsay, 3 dimensional modelling of early human brain development using optical projection tomography, Bmc Neurosci, 5 (2004) 27.

[103] M.E. Fisher, A.K. Clelland, A. Bain, R.A. Baldock, P. Murphy, H. Downie, C. Tickle, D.R. Davidson, R.A. Buckland, Integrating technologies for comparing 3D gene expression domains in the developing chick limb, Dev Biol, 317 (2008) 13-23.

[104] K. Koshiba-Takeuchi, A.D. Mori, B.L. Kaynak, J. Cebra-Thomas, T. Sukonnik, R.O. Georges, S. Latham, L. Beck, R.M. Henkelman, B.L. Black, E.N. Olson, J. Wade, J.K. Takeuchi, M. Nemer, S.F. Gilbert, B.G. Bruneau, Reptilian heart development and the molecular basis of cardiac chamber evolution, Nature, 461 (2009) 95-99.

[105] S. Wedden, L. Mitchell, G. Boyd, J. Sharpe, K. Robertson, Multispectral analysis of unstained human tissue using optical projection tomography, Am J Clin Pathol, 126 (2006) 633-634.

[106] L. McGurk, H. Morrison, L.P. Keegan, J. Sharpe, M.A. O'Connell, Three-Dimensional Imaging of Drosophila melanogaster, Plos One, 2 (2007).

[107] M. Rieckher, U.J. Birk, H. Meyer, J. Ripoll, N. Tavernarakis, Microscopic Optical Projection Tomography In Vivo, Plos One, 6 (2011).

[108] A. Bassi, L. Fieramonti, C. D'Andrea, M. Mione, G. Valentini, In vivo label-free three-dimensional imaging of zebrafish vasculature with optical projection tomography, J Biomed Opt, 16 (2011) 100502.

[109] J. McGinty, D.W. Stuckey, K.B. Tahir, R. Laine, J.V. Hajnal, A. Sardini, P.M.W. French, tomoFLIM - fluorescence lifetime projection tomography, Three-Dimensional and Multidimensional Microscopy: Image Acquisition and Processing Xvii, 7570 (2010) 268.

[110] M. Kellner, M. Heidrich, R. Beigel, R.A. Lorbeer, L. Knudsen, T. Ripken, A. Heisterkamp, H. Meyer, M.P. Kuhnel, M. Ochs, Imaging of the mouse lung with scanning laser optical tomography (SLOT), Journal of applied physiology, 113 (2012) 975-983.

[111] F.F. Yin, M.L. Giger, K. Doi, Measurement of the presampling modulation transfier function of film digitizers using a curve fitting technique, Med Phys, 17 (1990) 962-966.

[112] J.M. Boone, J.A. Seibert, An analytical edge spread function model for computer fitting and subsequent calculation of the LSF and MTF, Med Phys, 21 (1994) 1541-1545.

[113] S. Gundy, W. Van der Putten, A. Shearer, D. Buckton, A.G. Ryder, Determination of the modulation transfer function for a time-gated fluorescence imaging system, J Biomed Opt, 9 (2004) 1206-1213.

[114] Q. Miao, J. Yu, J.R. Rahn, M.G. Meyer, T. Neumann, A.C. Nelson, E.J. Seibel, Dual-mode optical projection tomography microscope using gold nanorods and hematoxylin-stained cancer cells, Opt Lett, 35 (2010) 1037-1039.

[115] M. Guizar-Sicairos, S.T. Thurman, J.R. Fienup, Efficient subpixel image registration algorithms, Opt Lett, 33 (2008) 156-158.

[116] J. Bernsen, Dynamic Thresholding of Grey-Level Images, Proc. of the 8th Int. Conf. on Pattern Recognition, (1986).

[117] T. Alanentalo, C.E. Loren, A. Larefalk, J. Sharpe, D. Holmberg, U. Ahlgren, High-resolution three-dimensional imaging of islet-infiltrate interactions based on optical projection tomography assessments of the intact adult mouse pancreas, J Biomed Opt, 13 (2008) -.

[118] J. Kerwin, M. Scott, J. Sharpe, L. Puelles, S.C. Robson, M. Martinez-de-la-Torre, J.L. Ferran, G.J. Feng, R. Baldock, T. Strachan, D. Davidson, S. Lindsay, 3 dimensional modelling of early human brain development using optical projection tomography, Bmc Neurosci, 5 (2004).

[119] T. Alanentalo, A. Hornblad, S. Mayans, A.K. Nilsson, J. Sharpe, A. Larefalk, U. Ahlgren, D. Holmberg, Quantification and Three-Dimensional Imaging of the Insulitis-Induced Destruction of beta-Cells in Murine Type 1 Diabetes, Diabetes, 59 (2010) 1756-1764.

[120] G. Sun, A.I. Tarasov, J. McGinty, A. McDonald, G.D. Xavier, T. Gorman, A. Marley, P.M. French, H. Parker, F. Gribble, F. Reimann, O. Prendiville, R. Carzaniga, B. Viollet, I. Leclerc, G.A. Rutter, Ablation of AMP-activated protein kinase alpha 1 and alpha 2 from mouse pancreatic beta cells and RIP2.Cre neurons suppresses insulin release in vivo, Diabetologia, 53 (2010) 924-936.

[121] G. da Silva Xavier, A. Mondragon, G. Sun, L. Chen, J.A. McGinty, P.M. French, G.A. Rutter, Abnormal glucose tolerance and insulin secretion in pancreas-specific Tcf7l2-null mice, Diabetologia, 55 (2012) 2667-2676.

[122] X. Shu, A. Royant, M.Z. Lin, T.A. Aguilera, V. Lev-Ram, P.A. Steinbach, R.Y. Tsien, Mammalian expression of infrared fluorescent proteins engineered from a bacterial phytochrome, Science, 324 (2009) 804-807.

[123] M. Oldham, H. Sakhalkar, T. Oliver, G. Allan Johnson, M. Dewhirst, Optical clearing of unsectioned specimens for three-dimensional imaging via optical transmission and emission tomography, J Biomed Opt, 13 (2008) 021113.

[124] R.M. White, A. Sessa, C. Burke, T. Bowman, J. LeBlanc, C. Ceol, C. Bourque, M. Dovey, W. Goessling, C.E. Burns, L.I. Zon, Transparent adult zebrafish as a tool for in vivo transplantation analysis, Cell Stem Cell, 2 (2008) 183-189.

[125] C. Parng, W.L. Seng, C. Semino, P. McGrath, Zebrafish: A preclinical model for drug screening, Assay Drug Dev Techn, 1 (2002) 41-48.

[126] C.G. Burns, D.J. Milan, E.J. Grande, W. Rottbauer, C.A. MacRae, M.C. Fishman, High-throughput assay for small molecules that modulate zebrafish embryonic heart rate, Nat Chem Biol, 1 (2005) 263-264.

[127] A.J. Hill, H. Teraoka, W. Heideman, R.E. Peterson, Zebrafish as a model vertebrate for investigating chemical toxicity, Toxicol Sci, 86 (2005) 6-19.

[128] D. Beis, D.Y.R. Stainier, In vivo cell biology: following the zebrafish trend, Trends Cell Biol, 16 (2006) 105-112.

[129] G. Kari, U. Rodeck, A.P. Dicker, Zebrafish: An emerging model system for human disease and drug discovery, Clin Pharmacol Ther, 82 (2007) 70-80.

[130] R.J. Bryson-Richardson, S. Berger, T.F. Schilling, T.E. Hall, N.J. Cole, A.J. Gibson, J. Sharpe, P.D. Currie, FishNet: an online database of zebrafish anatomy, Bmc Biol, 5 (2007) 34.

[131] T.P. Barros, W.K. Alderton, H.M. Reynolds, A.G. Roach, S. Berghmans, Zebrafish: an emerging technology for in vivo pharmacological assessment to identify potential safety liabilities in early drug discovery, Brit J Pharmacol, 154 (2008) 1400-1413.

[132] K. Dooley, L.I. Zon, Zebrafish: a model system for the study of human disease, Current opinion in genetics & development, 10 (2000) 252-256.

[133] K. Suhling, J. Siegel, D. Phillips, P.M. French, S. Leveque-Fort, S.E. Webb, D.M. Davis, Imaging the environment of green fluorescent protein, Biophys J, 83 (2002) 3589-3595.

[134] R.K. Benninger, Y. Koc, O. Hofmann, J. Requejo-Isidro, M.A. Neil, P.M. French, A.J. DeMello, Quantitative 3D mapping of fluidic temperatures within microchannel networks using fluorescence lifetime imaging, Anal Chem, 78 (2006) 2272-2278.

[135] Andor, Clara Interline CCD Instruction Manual

[136] D.C. Diez, H. Mueller, A.S. Frangakis, Implementation and performance evaluation of reconstruction algorithms on graphics processors, J Struct Biol, 157 (2007) 288-295.

[137] E. Kardash, M. Reichman-Fried, J.L. Maitre, B. Boldajipour, E. Papusheva, E.M. Messerschmidt, C.P. Heisenberg, E. Raz, A role for Rho GTPases and cell-cell adhesion in single-cell motility in vivo, Nature cell biology, 12 (2010) 47-53; sup pp 41-11.

[138] A.J. Ridley, Rho GTPases and actin dynamics in membrane protrusions and vesicle trafficking, Trends Cell Biol, 16 (2006) 522-529.

[139] H. Yoshizaki, Y. Ohba, K. Kurokawa, R.E. Itoh, T. Nakamura, N. Mochizuki, K. Nagashima, M. Matsuda, Activity of Rho-family GTPases during cell division as visualized with FRET-based probes, J Cell Biol, 162 (2003) 223-232.

[140] M. Sabouri-Ghomi, Y. Wu, K. Hahn, G. Danuser, Visualizing and quantifying adhesive signals, Curr Opin Cell Biol, 20 (2008) 541-550.

[141] P. Timpson, E.J. McGhee, K.I. Anderson, Imaging molecular dynamics in vivo - from cell biology to animal models, J Cell Sci, 124 (2011) 2877-2890.

[142] E. Kardash, J. Bandemer, E. Raz, Imaging protein activity in live embryos using fluorescence resonance energy transfer biosensors, Nature protocols, 6 (2011) 1835-1846.

[143] J.F. Amatruda, J.L. Shepard, H.M. Stern, L.I. Zon, Zebrafish as a cancer model system, Cancer Cell, 1 (2002) 229-231.

[144] A.T. Nguyen, A. Emelyanov, C.H.V. Koh, J.M. Spitsbergen, S. Parinov, Z.Y. Gong, An inducible kras(V12) transgenic zebrafish model for liver tumorigenesis and chemical drug screening, Dis Model Mech, 5 (2012) 63-72.

[145] https://wiki.zfin.org/display/prot/TRICAINE, in.

[146] W.C. Huang, Y.S. Hsieh, I.H. Chen, C.H. Wang, H.W. Chang, C.C. Yang, T.H. Ku, S.R. Yeh, Y.J. Chuang, Combined Use of MS-222 (Tricaine) and Isoflurane Extends Anesthesia Time and Minimizes Cardiac Rhythm Side Effects in Adult Zebrafish, Zebrafish, 7 (2010) 297-304.

[147] J.M. Wilson, R.M. Bunte, A.J. Carty, Evaluation of rapid cooling and tricaine methanesulfonate (MS222) as methods of euthanasia in zebrafish (Danio rerio), Journal of the American Association for Laboratory Animal Science : JAALAS, 48 (2009) 785-789.

[148] C. Pardo-Martin, T.Y. Chang, B.K. Koo, C.L. Gilleland, S.C. Wasserman, M.F. Yanik, High-throughput in vivo vertebrate screening, Nat Methods, 7 (2010) 634-636.

[149] Fianium, WhiteLase Supercontinuum System SC-400-2 Instruction Manual.

[150] J.C. Travers, Controlling nonlinear optics with dispersion in photonic crystal fibres, in: Department of Physics, Imperial College London, 2008.

Appendix I: Excitation sources for fluorescence intensity and lifetime imaging

Fluorescence imaging requires the specimen to be illuminated at an appropriate excitation wavelength and the subsequent fluorescence emission imaged onto a detector. The excitation light must be sufficiently bright to excite adequate fluorescence and also have an appropriate spectral profile (i.e. near ultraviolet (UV) and visible wavelengths) for single photon excitation. For time-domain FLIM, the excitation sources have to provide sufficiently short pulses, i.e. a pulse duration that is relatively short compared to fluorescence lifetime of the sample. This simplifies the analysis because the temporal profile of the excitation pulse need not be taken into account.

Mercury arc lamp

Arc sources are incoherent white-light sources that can be spectrally filtered. In this thesis, a mercury arc lamp (U-RFL-T, Olympus UK Ltd) was used. It contains mercury under high pressure when it is in operation. The output spectrum is mix of strong discrete lines and a background [2]. The excitation light is then provided by the combination of the lamp and appropriate filtering techniques (e.g. optical filter, acousto-optic tunable filter (AOTF), etc.).

Super-continuum source

Although arc sources or some other incoherent white light sources (e.g. thermal sources) can be spectrally filtered to cover this spectral region, they cannot provide sub 100 ps pulses. The main source which has the full visible and near UV coverage used for the wide-field fluorescence lifetime measurements is the super-continuum source. It can be generated in fibres which have high nonlinearity (e.g. photonic crystal fibres, micro-structured fibres, highly-nonlinear optical fibres, etc.) via nonlinear effects. It also requires high power (often amplified) infrared pulsed sources (e.g. Ti:Sapphire laser, Ytterbium doped fibre laser, etc.).

Configuration of the super-continuum source in the OPT system

The super-continuum source used in this thesis was an ultrafast fibre-laser-pumped super-continuum source (SC-400-2, Fianium Ltd) operating at the central wavelength of 1060 nm, with an output spectral bandwidth from 450 nm to beyond 1750 nm. It generates pulses of duration less than 10 ps, operating at 40 MHz repetition rate. The broadband channel provides in excess of 2 W average output power. This super-continuum source consists of three main sub-systems: a passively mode-locked Ytterbium doped fibre laser master source, a high power cladding pumped fibre amplifier and a high nonlinearity super-continuum generator [149], as depicted in Fig. 8.1.

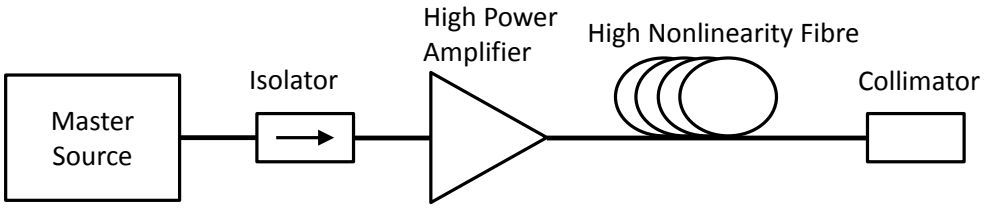


Figure 8.1: Schematic of ultrafast fibre-laser-pumped super-continuum source (SC-400-2, Fianium Ltd) [149].

The master source is a passively self-started mode-locked fibre laser based on a core-pumped, Ytterbium doped fibre operating at a repetition rate of approximately 40 MHz. It provides transform limited pulses of ~ 4 ps with acceptable pulse-to-pulse stability. The high power amplifier is based on a double-clad Ytterbium doped fibre pumped by a high power, multi-emitter laser diode pump module, which is air-cooled with inlet and outlet fans. The super-continuum generator consists of a length of highly-nonlinear optical fibre, with dispersion and length tailored to the high power picosecond pump pulses. The pulses experience large spectral broadening within the nonlinear fibre and generate a super-continuum covering the spectrum from below 450 nm to beyond 1750 nm with an average output power > 2W. This results in a useful (spatially coherent) source for fluorescence imaging (e.g. intensity, fluorescence lifetime), especially for such fluorescent probes with excitation profiles away from available laser lines (e.g. Ar^+ lines, etc.).

Physics process behind super-continuum generation

A large number of studies have been developed to understand the physical processes leading to super-continuum generation. The details include the full set of nonlinear processes in fibres, such as self-phase modulation, intra-pulse Raman scattering, four-wave mixing (FWM), modulation instability (MI) and cross-phase modulation. In the set-up used in this thesis, the super-continuum mechanism operates in a modulation instability regime [150].

MI is a phenomenon in nonlinear, anomalously (i.e. in the negative dispersion region, low-frequency components travel with lower group velocity than high frequency components) dispersive medium and is considered as a formalism of FWM. FWM allows the generation of new frequency components in spectral regions without previous spectral overlap with the pump pulse, following the below equation

$$\omega_3 + \omega_4 = \omega_1 + \omega_2 \qquad 7\text{-}1$$

where ω_1 and ω_2 are pump frequencies, ω_3 and ω_4 Stokes and anti-Stokes frequencies. In addition, the phase mismatch must be zero due to momentum conservation between the four photons, given by

$$\Delta k = \beta(\omega_1) + \beta(\omega_2) - \beta(\omega_3) - \beta(\omega_4) + 2\gamma P_0 = 0 \qquad 7\text{-}2$$

Where γ is the nonlinear coefficient, P_0 the soliton power, the last term, $2\gamma P_0$, accounts for nonlinear phase shift from the intensity dependent refractive index.

MI only occurs under certain circumstances. The most important condition is that the pump frequency is in the anomalous dispersion region, where the nonlinear contribution to the phase matching condition is dominant. High power, nonlinearity and low dispersion lead to a broad sideband separation. It is the initial stage of most super-continua with powerful pump pulses longer than 1 ps.

After pumping the pulse (i.e. a train of solitons) into the fibre with high nonlinearity, two main mechanisms are available to broaden the field into a continuum. Firstly, intra-pulse Raman scattering of the solitons leads to a red-shift in the solitons' central frequencies (i.e. the red edge of a solitons can be pumped by the blue edge, leading to a mean frequency shift). This forms a smooth continuum to longer wavelengths. The more significant mechanism in this case is FWM. If the pump frequency is adequately close to the zero dispersion wavelength of the fibre with high nonlinearity, the MI side-lobes can then develop an effective field in the normal dispersion regime. FWM, in this case, can widely separate Stokes and anti-Stokes generation because of the phase matching of the waveguide. Therefore, in the MI regime, continuum generation can be understood as a group of FWM processes. It starts with MI and then develops into the normal dispersion region which leads into a spectral broadening over a wide frequency range.

It is noted that since the MI mechanism is stochastic, the super-continuum spectra in this regime are relatively smooth and flat compared to the super-continuum spectra in the soliton fission regime (i.e. an ultra-short pulse <500 fs pumping in the anomalous dispersion region close to a zero dispersion wavelength). It is also noted that the MI continuum process will only occur if the pumped pulse and the parameters of the fibre with high non-linearity lead to a breakup of the pump pulse via MI in a shorter fibre length rather than high order soliton effects and soliton fission. In other words, relatively long pulses (> 1 ps) and low dispersion lead to the MI mechanism while ultra-short pulses (< 500 fs) and high dispersion at the pump wavelength lead to the soliton fission mechanism.

Appendix II: FLIM-OPT microscope system characterisation

To determine the MTFs for the different effective collection NAs for the in-house developed FLIM-OPT microscope system, a knife-edge technique was employed. Transmitted light images of a scalpel blade mounted in the chamber filled with water were acquired. In this case, no tilt was introduced since the effective sampling of the knife-edge was adequate to produce a 1-D ESF. Average ESFs, determined from 10 bright field and 10 background images, were acquired over a focus range of 2.4 mm (i.e. up to 1.2 mm either side of the 'in-focus' image) and repeated for effective NAs in the range 0.03-0.07 and the full NA of 0.13. In the characterisation experiment, the typical settings for FLIM-OPT experiments were used by setting the GOI gain voltage to 600 V and recording 10 time-gated images at 750 ps relative time delay positions with 1ns gate width. The distance of the knife-edge from the focal plane was recorded by the same plunge dial indicator (model #398877, RS Ltd).

The same analysis method from Boone *et al.* [112] was applied. Figure 8.2 (a) illustrates the measured in-focus ESF and the resulting fit for the imaging system by the black squares and the red solid line respectively. The resultant MTF, determined using both the analytic expression and numerical differentiation and Fourier transformation are illustrated by the red solid line and the black circles respectively in Fig. 8.2 (b).

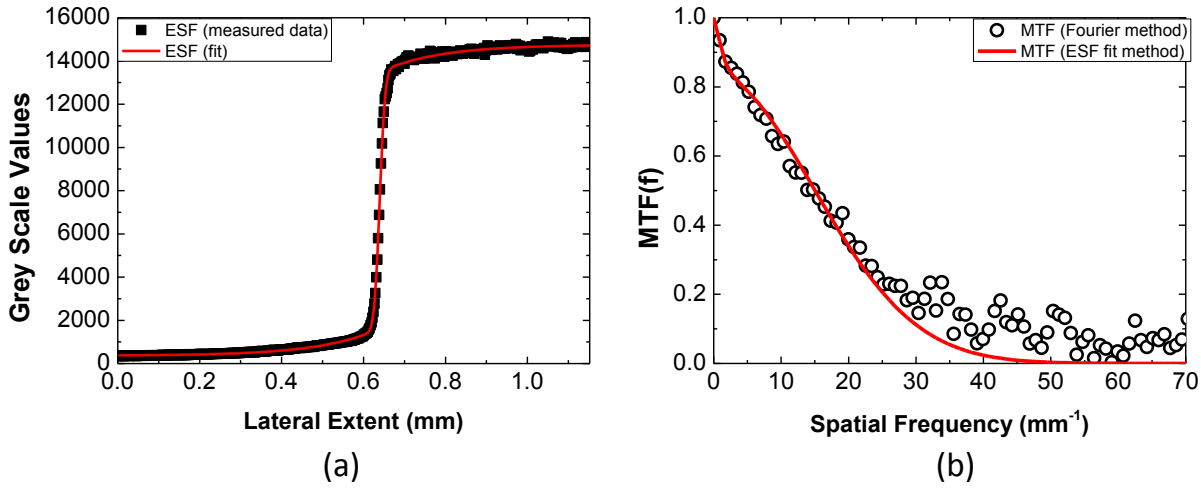


Figure 8.2: (a) The measured ESF of FLIM-OPT microscope system is plotted as discrete data points. The fit to these points is illustrated by the red solid line. The linear correlation coefficient between these two is 0.9999. (b) The corresponding MTF at this position from the analytical method, shown as the red solid line, and the numerical Fourier transform procedure, shown as data points.

To further analyse the resolution limit in the FLIM-OPT microscope system, different CCD binning parameters (1×1, 2×2 and 4×4) were analysed. Figure 8.3 shows the MTFs from the analytical method at different binning parameters for the same NA of the FLIM-OPT system (with 4x objective) almost overlapping each other. These curves illustrate that 4×4 binning provides the same spatial resolution as 1×1 binning. They indicate that the pixel size of the CCD is far smaller than that of GOI and therefore the GOI limits the resolution between these two instruments in our system. It illustrates that 4×4 binning can be employed in this system without losing frequency components and reduces the acquisition time (e.g. read out time, imaging saving time) and the consequent data size.

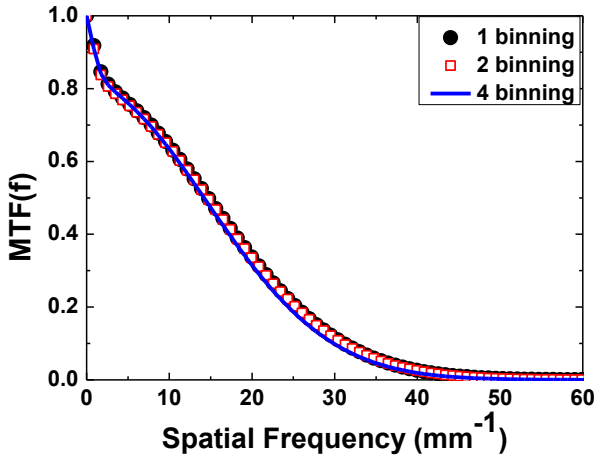


Figure 8.3: Three MTFs at different binning parameters for the same NA shown in Fig. 8.2 (a) from the analytical method, shown as the black dots for 1×1 binning, the red squares for 2×2 binning, and the blue solid line for 4×4 binning.

Figure 8.4 shows six 2-D MTFs (260×260) as a function of defocus for different effective NAs (0.13, 0.07, 0.06, 0.05, 0.04 and 0.03) of the 4×4 binning FLIM-OPT system. The pixel dimension for vertical axis (defocus distance) is 6.45 µm and for the horizontal axis (spatial frequency) is 0.596 mm^{-1} (i.e. the vertical scale -838.5 – 838.5 µm and the horizontal scale -77.48 – 77.48 mm^{-1}), where the pixel size of the CCD camera is 6.45 µm, a 4x objective (i.e. magnification of 4) and the 4×4 binning used in the system. This figure illustrates that as the NA decreases, the DOF increases but the in-focus bandwidth (i.e. lateral resolution) remains almost the same from NA 0.13 to 0.03 rather than significantly decreasing. The experimentally measured MTFs illustrates that the spatial resolution is limited by the GOI rather than the optical resolution (i.e. the NA of the optical system) for the NAs measured. This can be explained by the fact that the GOI has a relatively large effective pixel size of ~ 26 µm and therefore results in an in-focus lateral spatial resolution of the system of ~ 13 µm (when magnification is 4x). To visually compare the results for the intensity-based OPT system (i.e. without GOI) and FLIM-OPT system (i.e. with GOI), Fig. 8.5 shows the MTF (1040×1040) for the same NA (i.e. 0.07) of both systems using 1×1 binning. The in-focus bandwidths

of the MTF in FLIM-OPT system are significantly narrowed, which indicates the decreased lateral resolution. This is due to the fact that the GOI has the large pixel size and limits the resolution.

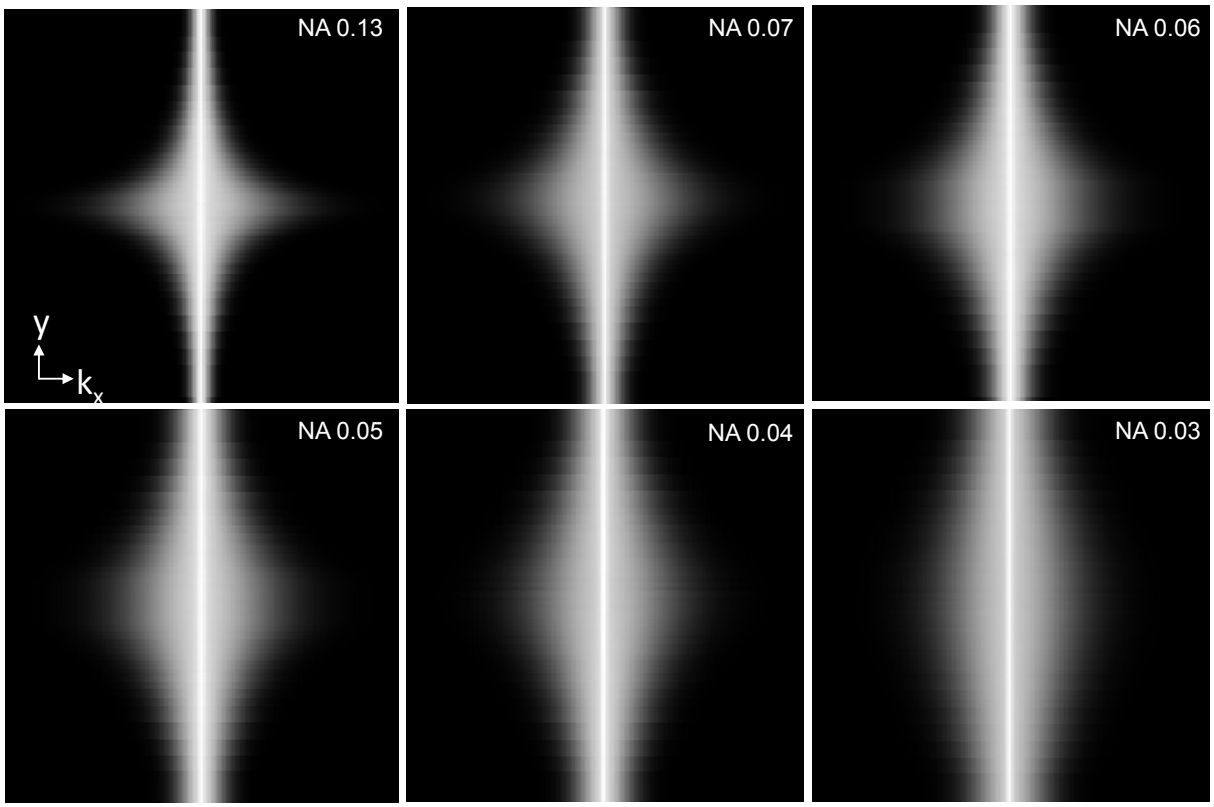


Figure 8.4: MTFs as a function of defocus (z) for different effective NAs (0.13, 0.07, 0.06, 0.05, 0.04 and 0.03) of the 4×4 binning FLIM-OPT microscope system. (260×260, Δk_x = 0.596 mm^{-1}, Δy = 6.45 µm, the vertical scale -838.5 – 838.5 µm and the horizontal scale -77.48 – 77.48 mm^{-1}).

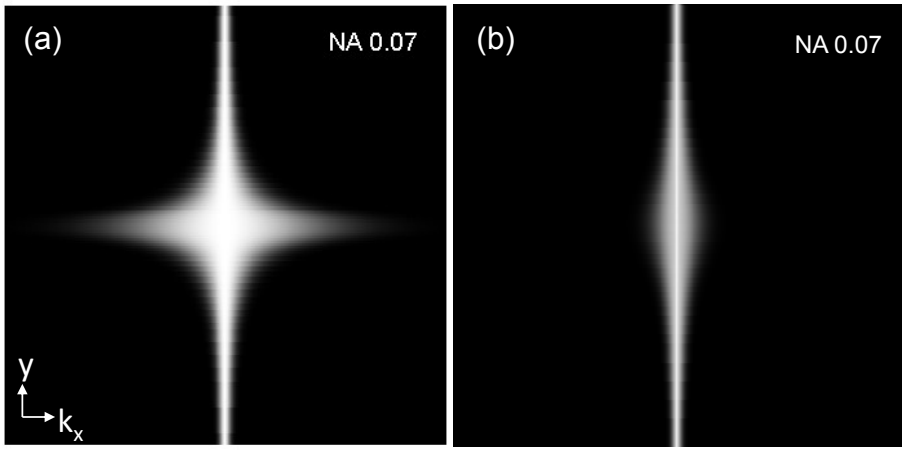


Figure 8.5: MTFs as a function of defocus (z) for (a)intensity-based OPT microscope system and (b) FLIM-OPT microscope system. (NA 0.07, 1×1 binning, 1040×1040, Δk_x = 0.596 mm^{-1}, Δy = 1.6125 µm, the vertical scale -838.5 – 838.5 µm and the horizontal scale -309.92 – 309.92 mm^{-1}).

Although the spatial resolution is not high, FLIM-OPT is still a powerful tool since it can provide an additional dimension (i.e. fluorescence lifetime) to extract quantitative information (e.g. the rate of energy transfer, the rate of excited state reactions, etc.).